Title

Two-Dimensional Semiconductor Optoelectronics

Author

Amani, Matin

Publication Date

2019

Two-Dimensional Semiconductor Optoelectronics

By

Matin Amani

A dissertation submitted in partial satisfaction of the
requirements for the degree of
Doctor of Philosophy
in
Engineering – Electrical Engineering and Computer Sciences
in the
Graduate Division
of the
University of California, Berkeley

Committee in charge:
Professor Ali Javey, Chair
Professor Ming C. Wu
Professor Daryl C. Chrzan

Spring 2019

Two-Dimensional Semiconductor Optoelectronics

Abstract

Two-Dimensional Semiconductor Optoelectronics

By

Matin Amani

Doctor of Philosophy in Engineering – Electrical Engineering and Computer Sciences

University of California, Berkeley

Professor Ali Javey, Chair

A fundamental figure of merit for high performance optoelectronic devices is their photoluminescence (PL) quantum yield (QY). This value, which accounts for the fraction of absorbed photons are re-emitted by the material governs the ultimate performance of optoelectronic devices such as light emitting diodes, photodetectors/photovoltaics, and solar cells. Two-dimensional (2D) semiconductors have emerged as a promising material system for high-performance optoelectronic and electronic applications. This class of materials possess out-of-plane van der Waals bonding, and as a result has naturally terminated surfaces, even when the material thickness is scaled to the monolayer limit. As a result, surface recombination, a dominant non-radiate pathway in most materials, can be mediated due to the naturally terminated surfaces of van der Waals materials. This offers a potentially pathway to enable near-unity PL QY at the monolayer limit.

Despite this, the room-temperature PL QY for most monolayer 2D semiconductors is extremely poor. The prototypical 2D material, MoS_2 has a maximum QY of 0.6% which indicates a considerable defect density. In the first section of this thesis we will address approaches of obtaining 2D materials with high PL QY, primarily focusing on an air-stable solution-based chemical treatment by an organic superacid which uniformly enhances the photoluminescence and minority carrier lifetime of MoS_2 monolayers by over two orders of magnitude. The treatment defect-mediated non-radiative recombination pathways, thus resulting in a final QY of over 95% with a longest observed lifetime of 10.8±0.6 nanoseconds. This treatment methodology was also extended to other 2D semiconductors such as WS_2 as well as scaled to large area films prepared by chemical vapor deposition.

Leveraging 2D materials with high brightness, the second section of this work will then discuss the development of light emitting devices. Firstly, we discuss the development of a transient electroluminescent device structure for use with monolayer 2D materials. One of the primary challenges for 2D materials scaled down to the monolayer limit has

been the efficient simultaneous injection of electrons and holes. To overcome this crucial limitation, I will discuss the development of a device which uses a single metal-semiconductor contact and a gate. Utilizing an AC potential applied to the gate, this device achieves electron and hole injection *via* tunneling. This results in excess electrons and holes present during the AC transient, which subsequently recombine to emit light. This device is then combined with the passivation methodologies presented in the first section of this thesis. Next, I will demonstrate light emitting diodes based on black phosphorous (bP). Unlike the majority of 2D semiconductors which are direct gap only at the monolayer limit, bP maintains a direct gap over all thickness. Moreover, this bandgap is thickness tunable and can be varied from 1.8 eV for a monolayer down to 0.3 eV for thick films. This property is directly leveraged to fabricate devices with an emission wavelength which can tuned over range of 960 µm to 4.1 µm with external quantum efficiencies as high as 4.4% at room temperature. Notably, bP LEDs offer high performance for emission at infrared wavelengths where the quantum efficiency traditional III-V and II-VI LEDs are limited by auger recombination. The final section of this work I will discuss the development of infrared detectors based on 2D semiconductors.

To my family and my friends

Acknowledgements

I would like to start by thanking Prof. Ali Javey, for the incredible patience, mentorship, and support he has shown me over the past five years. I was extremely fortunate that he provided me with the opportunity to join his research group and my abilities as a researcher have grown considerably from my experience in his lab. I am very grateful that he had the patience to put up with me but also help me better myself during this critical juncture of my life and career.

I would also like to thank my qualifying exam and dissertation committees, including Prof. Ming Wu, Prof. Daryl Chrzan, and Prof. Eli Yablonovitch. Their feedback and contributions during and after the exam were very helpful for the shaping of my project, and Prof. Yablonovitch has provided me with great insight on both quantitative luminescence measurements and his support for understanding the recombination pathways in 2D materials which have been integral to my work. Prof. Chrzan help was crucial in developing in an understanding of the interactions between 2D materials and their substrate. Additionally, Prof. Wu who provided me with a tremendous portion of the background knowledge I required for my research in his course as well as his insights into the mechanisms and computing the efficiency of transient electroluminescent devices. Finally, Prof. Ager also played a critical role in my studies and was a great mentor as well during my initial years as a graduate student.

Lastly, I would like to also thank the many Javey lab colleagues and mentors that have helped me develop my project and skills working alongside them. In particular, Dr. Mahmut Tosun and Prof. Tania Roy were amazing starting mentors and friends, and Dr. Der-Hsien Lien and Prof. Daisuke Kiriya who were instrumental in a large portion of my research. Prof. James Bullock, Dr. Sujay Desai, Dr. Chaoliang Tan, and Geun Ho Ahn were great colleagues and friends to work with on projects together.

There are many other coworkers and friends that have helped with experiments, discussions, and support, including Peida, Fahad, Aiden, Shiekh, Joy, Niharika, and many others too numerous to list – I would not have been able to complete a successful PhD without your help and am very grateful.

Table of Contents

Chapter 1

Introduction

Two-dimensional (2D) materials, particularly transition metal dichalcogenides (TMDCs), have been the subject of a large amount of research interest over the past several years for both electronic and optoelectronic applications.[1,2] Unlike graphene, which is a semimetal at the monolayer limit,[3] TMDCs have direct optical bandgaps in the range of 0.8 to 2.0 eV,[3-6] enabling their use as effective devices for both switching and light emission/detection. In addition, TMDCs can offer new functionalities over 3D semiconductors, such as their ability to form heterostructures free of lattice matching constraints[7] and tunable operation through the application of electric field and strain.[8,9] Valley and spin-based physics which exist in monolayers of these materials can also lead to a new classes of devices.[10,11] Tremendous progress has been made in the growth of electronic quality graphene on the wafer scale[12] as well as roll-to-roll growth[13] for use as transparent conductors. More recently research groups have been investigating techniques to grow TMDC films.[14] Numerous research groups have demonstrated the growth of various TMDCs, including MoS_2, WS_2, and WSe_2.[15-17]

The passivation of interfaces has been heavily investigated in all semiconductors. To realize high performance silicon transistors, the Si/SiO_2 interface is annealed in forming gas. This allows hydrogen to passivate dangling bonds and results in an improved subthreshold swing and reduced hysteresis.[18] In GaAs, double-heterostructures (using an AlGaAs cladding layer) are utilized to create a virtual defect-free interface.[19,20] Similarly, interfacial passivation is a requirement for 2D materials, which is partially mediated due to the natural self-termination of the 2D lattice at the surface, resulting in no dangling bonds.

The ability to mitigate the effect of defects within TMDCs is a crucial prerequisite to the realization of high-performance devices. Electronic devices such as MOSFETs, where the conduction mechanism is driven by majority carriers, are susceptible to defects. In MOSFETs, defects contribute to the interface states (D_{IT}), increasing the subthreshold swing.[19] In proposed technologies for sub-60 mV/decade switches, such as tunnel transistors (TFETs), defects contribute to sub-band gap states that result in a parasitic current pathway when the transistor is in the off-state, limiting the subthreshold swing and severely degrading the on/off ratio.[20] For optoelectronic devices where the operation is based on minority carriers, non-radiative recombination centers and pathways result in fewer photons being emitted from the device than excited states generated through either optical or electrical pumping. Hence, the removal of these non-radiative pathways in optoelectronic devices translate into a lowering of the efficiency for light emitting diodes (LEDs) and an increase in the threshold current for solid-state lasers.[21] An effective way to evaluate semiconductor quality is to study the photoluminescence (PL) quantum yield (QY), which is a ratio of the number of photons which a material emits compared to the number of photons absorbed. In chapter two, I will demonstrated that treatment using the organic superacid bis(trifluoromethane)sulfonamide (TFSI), resulted in a PL QY near 100% in exfoliated MoS_2 and WS_2 monolayers, as large area films prepared via chemical vapor deposition. The third chapter of this thesis will address the practical use of 2D semiconductors with high photoluminescence quantum yields. Realization of light emitting devices requires the simultaneous injection of both electrons and hole, however this has been a notable challenge in monolayer semiconductors, due to difficulties in forming ohmic contacts to both carriers on the same device. To overcome this limitation, a transient electroluminescent device is proposed and demonstrated. Here an alternating gate electric field is used to rapidly change the accumulated carriers in the semiconductor. Critically, carriers of opposite polarities simultaneously enter and leave the device *via* tunneling during transients facilitated by dramatic band bending and Schottky barrier thinning, resulting in light emission. Additionally, chapter three will discuss infrared light emission and detection using 2D semiconductors. Most infrared light sources operating in the mid- and long-wave infrared are based on thermal emitters, which have poor efficiency, limited brightness, and speed. Despite the drawbacks these devices are applied towards a variety of applications most notable of which is spectroscopy. Infrared LEDs can provide high speed, brightness, and narrow spectral emission, but tend to have poor quantum efficiency due to the high auger recombination velocities in narrow gap III-V and II-VI semiconductors (i.e. InSb or HgCdTe). Chapter three will discuss the utilization of black phosphorous, a 2D semiconductor where the bandgap can be tuned from 0.3 to 1.8 eV *via* thickness as a potential material for efficient infrared LEDs.

Finally, chapter four will discuss the potential of several 2D material systems for their use in infrared photodetectors. The majority of today's commercially available, high performance IR photodetectors are made using III-V and II-VI absorbers, for example, $In_{1-x}Ga_xAs$, InSb, and $Hg_{1-x}Cd_xTe$. While significant progress has greatly increased their application, several drawbacks limit wider utilization of IR photodetectors. Most notably, these devices typically rely on expensive growth methods and require active cooling to reduce thermal noise. The latter is particularly crucial for narrow bandgap absorbers operating in the mid-wave infrared (MWIR, 3-5 μm) and long wave infrared (LWIR, 8-12 μm) spectral bands where cryogenic cooling is typically required to achieve high performance. Two-dimensional materials can be thinned with no detrimental effects from surface dangling bonds. This advantage is particularly important in infrared detectors where thin absorbers can reduce noise resulting from generation-recombination, a strategy which is often not permitted in traditional semiconductors due to surface recombination. Furthermore, the ability for 2D materials to be stacked with no lattice matching constraints also enables the free formation of heterostructure devices. Utilizing these key advantages photodetectors operating in the mid-wave infrared at room temperature with a peak specific detectivity of 6×10^{10} cm $Hz^{1/2}$ W^{-1} are demonstrated.

References

1. Wu, Sanfeng; Buckley, S.; Schaibley, J. R.; Feng, L.; Yan, J.; Mandrus, D. G.; Hatami, F.; Yao, W.; Vuckovic, J.; Majumdar, A.; Xu, X. Monolayer Semiconductor Nanocavity Lasers with Ultralow Thresholds. *Nature*. **2015**, 520, 69-72.
2. Sarkar, D.; Xie, X.; Liu, W.; Cao, W.; Kang, J.; Gong, Y.; Kraemer, S.; Ajayan, P. M.; Banerjee, K. A Subthermionic Tunnel Field-Effect Transistor with an Atomically Thin Channel. *Nature*. **2015**, 526, 91-95.
3. Geim, A. K.; Novoselov, K. S. The rise of graphene. *Nat. Matter.* **2007**, 6, 183-191.
4. Splendiani, A.; Sun, L.; Zhang, Y.; Li, T.; Kim, J.; Chim, C.-Y.; Galli, G.; Wang, F. Emerging Photoluminescence in Monolayer MoS_2. *Nano Lett*. **2010**, 10, 1271-1275.
5. Zhao, W.; Ghorannevis, Z.; Chu, L.; Toh, M.; Kloc, C.; Tan, P.-H.; Eda, G. Evolution of Electronic Structure in Atomically Thin Sheets of WS_2 and WSe_2. *ACS Nano* **2013**, 7, 791-797.
6. Ruppert, C.; Aslan, O. B.; Heinz, T. F. Optical Properties and Band Gap of Single- and Few-Layer $MoTe_2$ Crystals. *Nano Lett*. **2014**, 14, 6231-6236.
7. Fang, H.; Battagli, C.; Carraro, C.; Nemsak, S.; Ozdol, B.; Kang, J.S.; Bechtel, H.A.; Desai, S.B.; Kronast, F.; Unal, A.A.; Conti, G.; Conlon, C.; Palsson, G.K.; Martin, M.C.; Minor, A.M.; Fadley, C.S.; Yablonovitch, E.; Maboudian, R.; Javey, A. Strong Interlayer Coupling in Van der Waals heterostructures Built from Single-Layer Chalcogenides. *Proc. Nat. Acad. Sci.* **2014**, 111, 6198-6202.
8. Ramasubramaniam, A.; Naveh, D.; Towe, E. Tunable Band Gaps in Bilayer Transition-Metal Dichalcogenides. *Phys. Rev. B* **2011**, 84, 205325.
9. McCreary, A.; Ghosh, R.; Amani, M.; Wang, J.; Duerloo, K.-A. N.; Sharma, A.; Jarvis, K.; Reed, E. J.; Dongare, A. M.; Banerjee, S. K.; Terrones, M.; Namburu, R. R.; Dubey, M. Effects of Uniaxial and Biaxial Strain on Few-Layered Terrace Structures of MoS_2 Grown by Vapor Transport. *ACS Nano*. **2016**, 10, 3186-3197.
10. Xiao, D.; Liu, G.B.; Feng, W.; Xu, X.; Yao, W. Coupled Spin and Valley Physics in Monolayers of MoS_2 and Other Group-VI Dichalcogenides. *Phys. Rev. Lett.* **2012**, 108, 196802.
11. Zeng, H.; Dai, J.; Yao, W.; Xiao, D.; Cui, X. Valley Polarization in MoS_2 Monolayers by Optical Pumping. *Nat. Nano.* **2012**, 7, 490-493.
12. Lee, J.-H.; Lee, E. K.; Joo, W.-J.; Jang, Y.; Kim, B.-S.; Lim, J. Y.; Choi, S.-H.; Ahn, S. J.; Ahn, J. J.; Park, M.-H.; Yang, C.-W.; Choi, B. L.; Hwang, S.-W.; Whang, D. Wafer-Scale Growth of Single-Crystal Monolayer Graphene on Reusable Hydrogen-Terminated Germanium. *Science*. **2014**, 344, 286-289.
13. Bae, S.; Kim, H.; Lee, Y.; Xu, X.; Park, J.-S.; Zheng, Y.; Balakrishnan, J.; Lei, T.; Kim, H. R.; Song, Y. I.; Kim, Y.-J.; Kim, K. S.; Ozyilmaz, B.; Ahn, J.-H.; Hong, B. H.; Iijima, S. Roll-to-Roll Production of 30-Inch Graphene Films for Transparent Electrodes. *Nat. Nano.* **2010**, 5, 574-578.
14. Najmaei, S.; Liu, Z.; Zhou, W.; Zou, X.; Shi, G.; Lei, S.; Yakobson, B.I.; Idrobo, J.-C.; Ajayan, P.M.; Lou, J. Vapour Phase Growth and Grain Boundary Structure of Molybdenum Disulphide Atomic Layers. *Nat. Matter.* **2013**, 12, 754-759.
15. Ling, X.; Lee, Y.-H.; Lin, Y.; Fang, W.; Yu, Lili, Dresselhaus, M. S.; Kong, J. Role of the Seeding Promoter in MoS_2 Growth by Chemical Vapor Deposition. *Nano Lett.* **2014**, 14, 464-472.
16. Zhou, H.; Wang, C.; Shaw, J. C.; Cheng, R.; Chen, Y.; Huang, X.; Liu, Y.; Weiss, N. O.; Lin, Z.; Huang, Y.; Duan, X. Large Area Growth and Electrical Properties of p-Type WSe_2 Atomic Layers. *Nano Lett.* **2015**, 15, 709-713.
17. Kang, K.; Xie, S.; Huang, L.; Han, Y.; Huang, P. Y.; Mak, K. F.; Kim, C.-J.; Muller, D.; Park, J. High-Mobility Three-Atom-Thick Semiconducting Films with Wafer-Scale Homogeneity. *Nature*. **2015**, 520, 656-660.
18. Wang, Q. H.; Kalantar-Zadeh, K.; Kis, A.; Coleman, J. N.; Strano, M. S. Electronics and Optoelectronics of Two-Dimensional Transition Metal Dichalcogenides. *Nat. Nano*. **2012**, 7, 699-712.
19. Martens, K.; Chui, C. O.; Brammertz, G.; Jaeger, B. D.; Kuzum, D.; Meuris, M.; Heyns, M. M.; Krishnamohan, T.; Saraswat, K.; Maes, H. E.; Groeseneken, G. On the Correct Extraction of Interface Trap Density of MOS Devices with High-Mobility Semiconductor Substrates. *IEEE Trans. Elec. Dev.* **2008**, 55, 547-556.
20. Ionescu, A.M.; Riel, H. Tunnel Field-Effect Transistors as Energy-Efficient Electronic Switches. *Nature* **2011**, 479, 329-337.
21. Ye, Y.; Wong, Z. J.; Lu, X.; Ni, X.; Zhu, H.; Chen, X.; Wang, Y.; Zhang, X. Monolayer Excitonic Laser. *Nat. Photon.* **2015**, 9, 733-737.

Chapter 2

High photoluminescence quantum yield in 2D semiconductors

2.1 – Near-unity quantum yield in monolayer MoS_2[1]

Monolayer transition metal dichalcogenide (TMDCs) have properties that make them highly suitable for optoelectronics[1,2], including the ability to form "van der Waals heterostructures" without the need for lattice matching[3,4], circular dichroism arising from the direct band gap occurring at the K and K' points of the Brillouin zone[5], and widely tunable band-structure through the application of external forces such as electric field and strain[6]. Unlike III-V semiconductors, the optical properties of TMDCs are dominated by excitons with strong binding energies (on the order of 300 meV)[7-9] and large radii (~1.6 nm)[10]. However, TMDCs have exhibited poor luminescence quantum yield (QY); i.e. the number of photons the material radiates is much lower than the number of generated electron-hole pairs. QY values ranging from 0.01% to 6% have been reported, which indicate a high density of defect states and mediocre electronic quality[11-13].

Two-dimensional (2D) monolayers are amenable to surface passivation by chemical treatments. We studied a wide range of chemical treatments and demonstrate an air-stable, solution-based, process using an organic superacid that removes the contribution of defect-mediated non-radiative recombination that acts on electronically active defect sites by uniformly passivating them, repairing them, or both. The photoluminescence (PL) in MoS_2 monolayers increased by over two orders of magnitude, resulting in a QY > 95% and a characteristic lifetime of 10.8±0.6 nanoseconds at low excitation densities.

In this study, MoS_2 monolayers were treated by a non-oxidizing organic superacid: bis(trifluoromethane)sulfonimide (TFSI). Superacids have a Hammett acidity function (H_0) that is lower than pure sulfuric acid, and are strong protonating agents. Details of the sample preparation and treatment procedure are discussed in section 2-5. The PL spectra of a MoS_2 monolayer measured before and after TFSI treatment (Fig. 2-1-1A) show a 190× increase in the PL peak intensity. The magnitude of the enhancement depended strongly on the quality of the original as-exfoliated monolayer[14]. PL imaging of a monolayer (Fig. 2-1-1B, 2-1-1C)[14] taken before and after treatment at the same illumination conditions shows that the enhancement from the superacid treatment is spatially uniform.

---

[1] Reproduced with permission from M. Amani, D.-H. Lien D. Kiriya et al., Science, 350, 1065-1068, 2015. Copyright © [2015] AAAS.

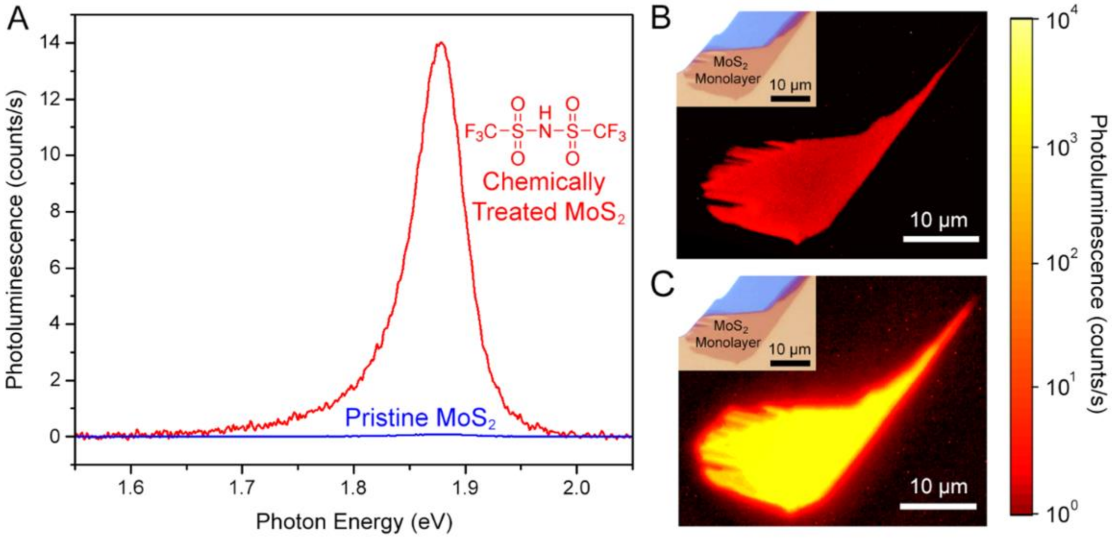

Fig. 2-1-1. **Enhancement of photoluminescence by chemical treatment.** (**A**) PL spectrum measured for both as-exfoliated and TFSI treated MoS_2 monolayers measured at an incident power of 1×10^{-2} Wcm^{-2}. (**B**) and (**C**) PL image of a MoS_2 monolayer (insert shows optical micrograph) before (**B**) and after treatment (**C**).

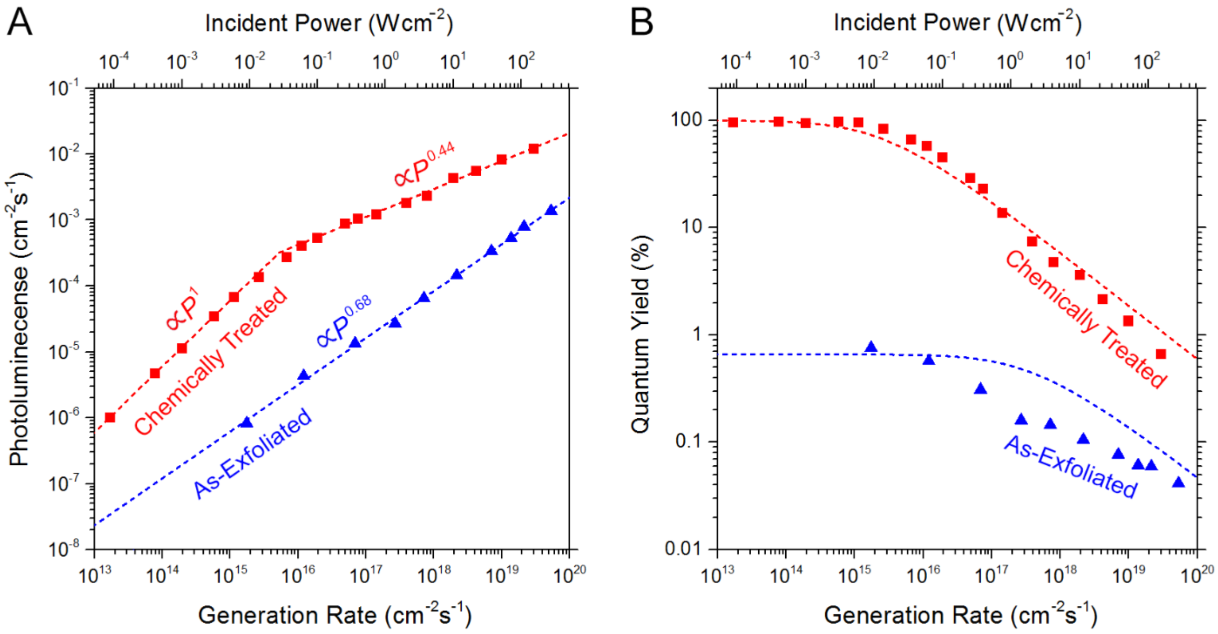

Fig. 2-1-2. Steady-state luminescence. (**A**) Pump-power dependence of the integrated photoluminescence for as-exfoliated and treated MoS_2; dashed lines show power law fits for the three dominant recombination regimes. (**B**) Pump-power dependence of the QY for as-exfoliated and treated MoS_2; dashed lines show the recombination model.

Calibrated steady-state PL measurements[14] showed that the spectral shape of the emission remained unchanged over a pump intensity dynamic range of six orders of magnitude (10^{-4} to 10^{2} W cm^{-2})[14]. From the pump-power dependence of the calibrated luminescence intensity (Fig. 2-1-2A) we extracted the QY (Fig. 2-1-2B). As-exfoliated samples exhibited low QY with a peak efficiency of 1% measured at 10^{-2} Wcm^{-2}. The absolute efficiency[12,13] and observed power law[13] are consistent with previous reports for exfoliated MoS_2. After TFSI treatment, the QY reached a plateau at low pump intensity (<10^{-2} Wcm^{-2}) with a maximum value greater than 95%. The near-unity QY suggests that within this range of incident power there was negligible non-radiative recombination occurring in the sample. Although pure radiative recombination is commonly observed for fluorescent molecules that inherently have no dangling bonds, only a few semiconductors, such as GaAs double heterostructures[15] and surface passivated quantum dots[16], show this behavior at room temperature.

At high pump-power, a sharp drop-off in the QY was observed, possibly caused by non-radiative biexcitonic recombination. We consider several models to understand the carrier density–dependent recombination mechanisms in MoS_2 before and after TFSI treatment. Here, n and p are the 2D electron and hole concentrations respectively. At high level injection, the dopant concentration is much less than the number of optically generated carriers, allowing $n = p$. The traditional interpretation without excitons[17], invokes a total recombination, R, as: $R = An + Bn^2 + Cn^3$, where A is the Shockley-Reed-Hall (SRH) recombination rate, B is the radiative recombination rate, and C is the Auger recombination rate. The QY is given as the radiative recombination over total recombination. Auger processes dominate at high carrier concentrations, while SRH recombination dominates at low carrier concentrations. In the SRH regime (i.e., low pump-power), QY increases with pump intensity. This behavior, however, was not observed in previous MoS_2 studies[12,13] nor in this work.

The standard model poorly describes our QY data[14], which is strongly influenced by bound excitons[9]. As a result, the radiative rate is proportional to the total exciton population, $\langle N \rangle$ [18]. At high exciton densities, a two body non-radiative recombination pathway is observed, which can be attributed to a bimolecular process recombination since the recombination is proportional to $\langle N \rangle^2$. This is likely a result of biexcitonic recombination, although further experiments are required to confirm this.

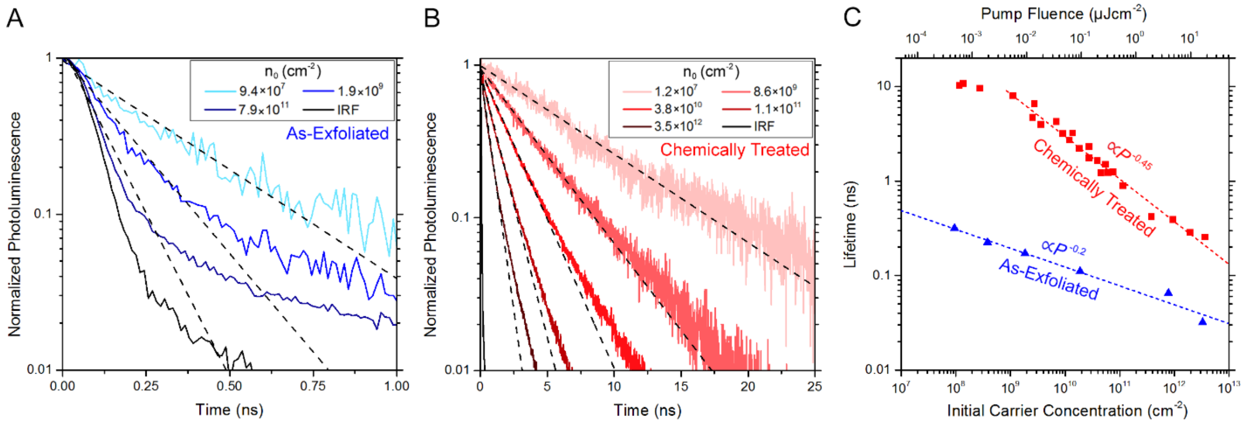

Fig. 2-1-3. Time-resolved luminescence. (**A**) Radiative decay of an as-exfoliated MoS_2 sample at various initial carrier concentrations (n_0) as well as the instrument response function (IRF). (**B**) Radiative decay of a treated MoS_2 sample plotted for several initial carrier concentrations (n_0) as well as the IRF. (**C**) Effective PL lifetime as a function of pump-fluence; the dashed line shows a power law fit for the dominant recombination regimes.

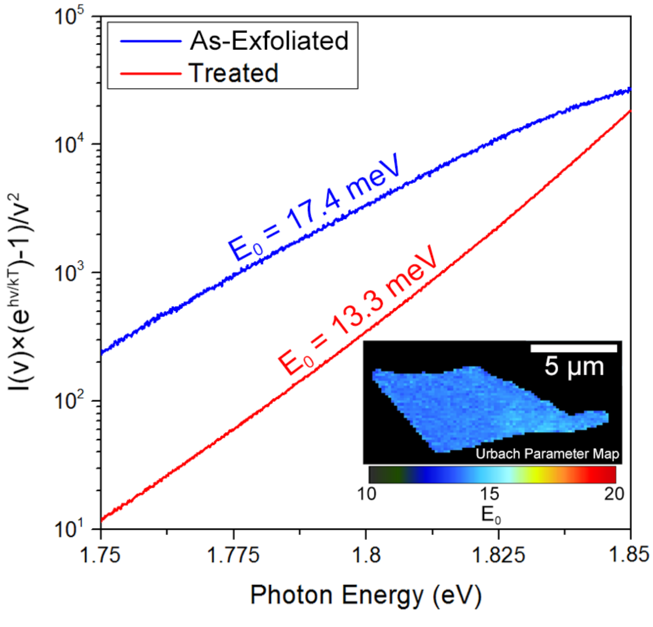

Fig. 2-1-4. Band-edge Sharpness. Band edge tails extracted from the PL spectrum using the van Roosbroeck-Shockley equation, showing the improvement of the Urbach parameter; the insert shows a spatial map of the Urbach parameter for a TFSI treated sample.

Time-resolved measurements were performed on both as-exfoliated and chemically treated samples to investigate the carrier recombination dynamics. The luminescence decay was non-exponential, but not in the standard form known for bimolecular (Bn^2) recombination (Eq. 1)[17]. As-exfoliated monolayers of MoS_2 had extremely short lifetimes on the order of 100 ps (Fig. 2-1-3A)[14], which is consistent with previous reports[18]. After treatment, we saw a substantial increase in the lifetime, which is shown at several pump-fluences in Fig. 2-1-3A. Fitting was performed with a single exponential decay that only described the initial characteristic lifetime for a given pump intensity. After the pump-pulse, the exciton population decayed, which resulted in non-exponential decay through reduced non-radiative biexcitonic recombination. At the lowest measurable pump-fluences, we observed a luminescence lifetime of 10.8±0.6 nanoseconds in the treated sample, compared to ~0.3 ns in the untreated case at a pump-fluence of 5×10^{-4} μJcm^{-2} (Fig. 2-1-3C). The contrast between Fig. 2-1-3, A and B, is consistent with the QY trend.

Urbach tails, which depict the sharpness of the band edges[22], were derived from the steady-state PL spectra via the van Roosbroeck–Shockley equation, and are plotted in Fig. 2-1-4. After the treatment, a noticeable decrease in the Urbach energy, E_0, from 17.4 to 13.3 meV was observed, indicating a reduction in the overall disorder from potential fluctuations and improved band edge sharpness[22]. A spatial map showing Urbach energy (Fig. 2-1-4)[14] further indicates that the treatment was highly uniform. The QY in air for chemically treated MoS_2 was measured daily over the course of 1 week at a constant pump-power to evaluate stability, during which the sample was stored without any passivation in ambient lab conditions (20° to 22°C, 40 to 60% relative humidity) as shown in Fig. 2-1-5[14]. The QY remained above 80% during this period of time indicating that the treatment created samples that were relatively stable.

We now turn our attention to the effect of TFSI treatment on other properties of MoS_2. The monolayer surface was imaged by atomic force microscopy (AFM) before and after treatment (Fig. 2-1-6A) from which no visible change to the surface morphology is observed. The effect of the treatment on the electrical properties of a back-gated MoS_2 transistor was also investigated. The transfer characteristics of this majority carrier device before and after treatment showed a shift in the threshold voltage toward zero, indicating that the native n-type doping in the MoS_2 was removed, while maintaining the same drive current (Fig. 2-1-6B). An improvement in the subthreshold slope suggested that the treatment reducing interface trap states. The Raman spectra of an as-exfoliated and treated monolayer (Fig. 2-1-6C) showed that there was no change in the relative intensity or peak position. Thus, the structure of MoS_2 was not altered during treatment and the lattice was not being subject to any induced strain[23]. Because absolute absorption was used in the calibration of QY, careful absorption measurements were performed using two different methods[14] both before and after treatment (Fig. 2-1-6D). At the pump wavelength, (514.5 nm), no measurable change of the absolute absorption from the treatment was observed. The strong resonances at 1.88 and 2.04 eV corresponding to the A and B excitons, respectively, are consistent with previous reports[12]. Surface-sensitive x-ray photoelectron spectroscopy (XPS) was performed on bulk MoS_2 from the same crystal used for micromechanical exfoliation. The Mo *3d* and S *2p* core levels both before and after treatment (Fig. 2-1-6E) showed no observable increase in the MoO_x peak or sulfur oxidation after the treatment. Moreover, the oxidation state and bonding of Mo and S showed no appreciable change[24]. Thus, a panoply of different materials characterization techniques show that the structure of the MoS_2 remains intact after TFSI treatment, with only the QY and lifetime being enhanced.

The exact mechanism by which the TFSI passivates surface defects is not fully understood. Exfoliated MoS_2 surfaces contain regions with a large number of defect sites in the form of sulfur vacancies, adatoms on the surface, and numerous impurities[27-28]. The calculated mid-gap energy for several defect types are shown, including a sulfur vacancy (V_s), adsorbed –OH, and adsorbed water. For all of these cases deep level traps, which contribute to defect-mediated non-radiative recombination resulting in a low QY[28], are observed. The strong protonating nature of the superacid can remove absorbed water, hydroxyl groups, oxygen and other contaminants on the surface[13]. Although these reactions will not remove the contribution of defects to non-radiative recombination, it will open the active defect sites to passivation by a second mechanism. One possibility is the protonation of the three dangling bonds at each sulfur vacancy site. However, density functional theory (DFT) calculations[14] show that this reaction is energetically unfavorable.

We have demonstrated an air-stable process by which the PL of monolayer MoS_2 can be increased by over two orders of magnitude, resulting in near-unity luminescence yield. This result sheds light on the importance of defects in limiting the performance of 2D systems, and presents a practical route to eliminate their effect on optoelectronic properties. The existence of monolayers with near ideal optoelectronic properties should enable the development of new high-performance light emitting diodes, lasers, and solar cells. These devices can fulfill the revolutionary potential of the 2D semiconductors (*1*), which require interfacial passivation, as in all classic semiconductors.

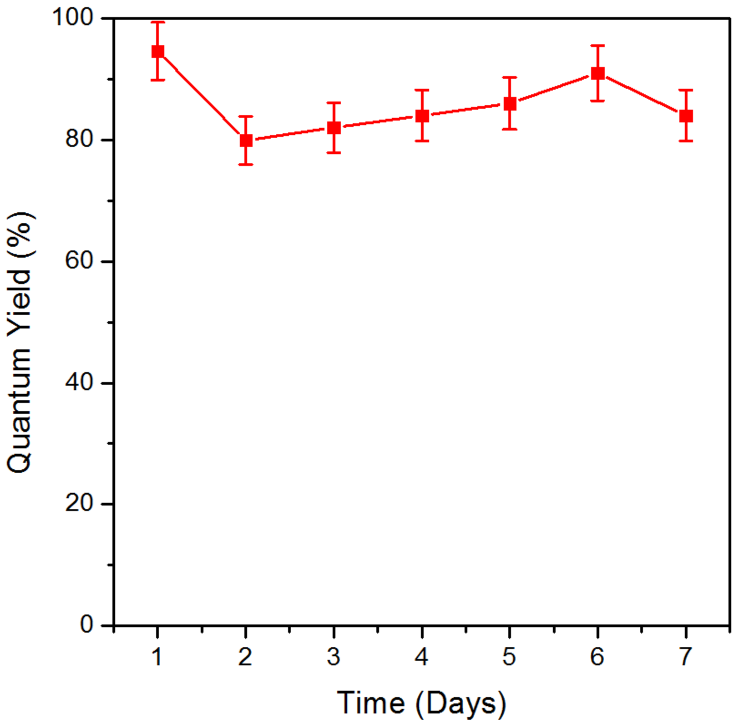

Fig. 2-1-5. Treatment Stability. QY measured at an incident power of 5×10-3 W/cm2 over one week; the sample was stored in ambient conditions (20° to 22°C, 40 to 60% relative humidity).

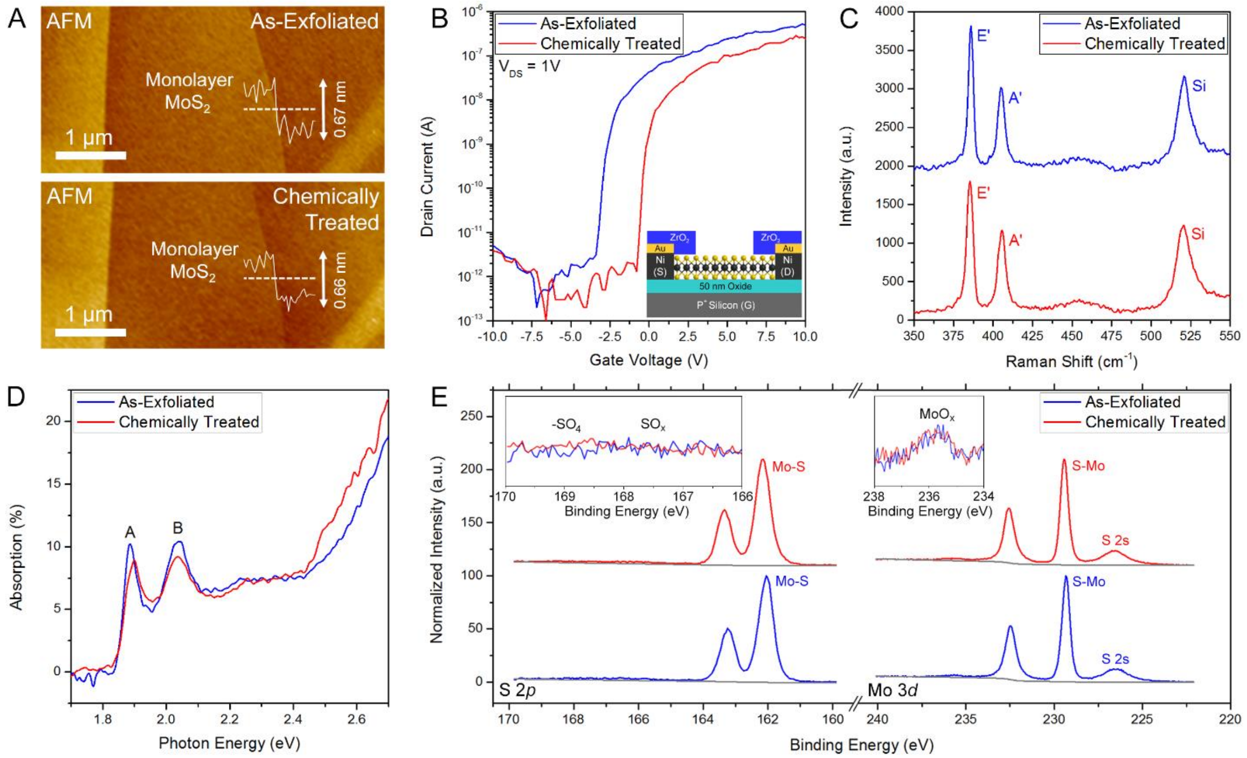

Fig. 2-1-6. Material and device characterization. (**A**) AFM images taken before and after TFSI treatment. (**B**) Transfer characteristics of a monolayer MoS_2 transistor both before and after treatment. (**C**) Raman spectrum of as-exfoliated and TFSI treated MoS_2 samples. (**D**) Absorption spectrum of the as-exfoliated and treated MoS_2 samples. (**E**) XPS spectrum of the S 2*p* and Mo 3*d* core levels before and after treatment. Inserts show that there is no appearance of SO_x or change in the MoO_x peak intensity after treatment.

References for Section 2-1

1. F. Xia, H. Wang, D. Xiao, M. Dubey, A. Ramasubramaniam, Nat. Photon. **8**, 899-907 (2014).
2. S. Wu *et al.*, Nature. **520**, 69-72 (2015).
3. H. Fang *et al.*, Proc. Nat. Acad. Sci. **111** (17), 6198-6202 (2014).
4. L. Britnell *et al.*, Science. **340**, 1311-1314 (2013).
5. K. F. Mak, K. He, J. Shan, T. F. Heinz, Nat. Nano. **7**, 494-498 (2012).
6. S. B. Desai *et al.*, Nano Lett. **14**, 4592-4597 (2014).
7. S. Tongay *et al.*, Sci. Rep. **3**, 2657 (2013).
8. A. Chernikov *et al.*, Phys. Rev. Lett. **113**, 076802 (2014).
9. H. M. Hill *et al.*, Nano Lett. **15**, 2992-2997 (2015).
10. T. C. Berkelbach, M. S. Hybertsen, D. R. Reichman, Phys. Rev. B. **88**, 045318 (2013).
11. L. Yuan, L. Huang, Nanoscale. **7**, 7402 (2015).
12. K. F. Mak, C. Lee, J. Hone, J. Shan, T. F. Heinz, Phys. Rev. Lett. **105**, 136805 (2010).
13. H. Wang, C. Zhang, F. Rana, Nano Lett. 15, 339-345 (2015).
14. Materials and methods are available as supplementary materials on Science Online.
15. I. Schnitzer, E. Yablonovitch, C. Caneau, T. J. Gmitter, Appl. Phys. Lett. **62**, 131-133 (1993).
16. Y. S. Park, *et al.*, Phys. Rev. Lett. **106**, 187401 (2011).
17. P. T. Landsberg, Phys. Stat. Sol. **41**, 457-489 (1970).
18. F. Wang, Y. Wu, M. S. Hybersten, T. H. Heinz, Phys. Rev. B. **73**, 245424 (2006).
19. H. Wang *et al.*, Phys. Rev. B. **91**, 165411 (2015).
20. C. Mai *et al.*, Nano Lett. **14** (1), 202-206 (2013).
21. T. Korn, S. Heydrich, M. Hirmer, J. Schmutzler, C. Schuller, Appl. Phys. Lett. **99**, 102109 (2011).
22. A. Iribarren, R. Castro-Rodriguez, V. Sosa, J. L. Pena, Phys. Rev. B. **58** (4), 1907-1911 (1998).
23. Z. Liu *et al.*, Nat. Comm. **5**, 5246 (2014).
24. A. Azcatl *et al.*, Appl. Phys. Lett. **104**, 111601 (2014).
25. R. Addou, L. Colombo, R. M. Wallace, Appl. Mat. Interfaces. **7** (22), 11921-11929 (2015).
26. C. P. Lu, G. Li, J. Mao, L. M. Wang, E. Y. Andrei, Nano Lett. **14**, 4628-4633 (2014).
27. S. McDonnell, R. Addou, C. Buie, R. M. Wallace, C. L. Hinkle, ACS Nano. **8**, 2880-2888 (2014).
28. R. Addou *et al.*, ACS Nano. **9** (9), 9124-9133 (2015).
29. J. Y. Noh, H. Kim, Y. S. Kim, Phys. Rev. B. **89**, 205417 (2014).
30. A. P. Nayak *et al.*, Nat. Comm. **5**, 3731 (2014).
31. M. Koppelman, Proc. Soc. Astro. Sci. **24**, 107-110 (2005).
32. H. Zeng, J. Dai, W. Yao, D. Xiao, X. Cui, Nat. Nano. **7**, 490-493 (2012).
33. S. Wu, *et al.*, 2D Mater. **1**, 011001 (2014).
34. D. Magde, R. Wong, P. G. Seybold, Photochem. Photobiol. **75** (4), 327-334 (2002).
35. E. Yablonovitch and G. D. Cody, IEEE T. Electron Dev. **29** (2), 300-305 (1982).
36. E. Yablonovitch, T. J. Gmitter, R. Bhat, Phys. Rev. Lett. **61** (22), 2546-2549 (1988).
37. W. F. Krupke, IEEE J. Quantum Electron. **10**, 450-457 (1974).
38. A. Iribarren, R. Castro-Rodriguez, V. Sosa, J. L. Pena, Phys. Rev. B. **54** (4), 1907-1911 (1998).
39. S. L. Chuang, Physics of Photonic Devices, Second Edition. A. J. Wiley & Sons, Inc. Hoboken, NJ (2009).
40. L. Yang, *et al.*, Nano Lett. **14**, 6275-6280 (2014).
41. P. Hohenberg and W. Kohn, Phys. Rev. **136**, B864 (1964).
42. W. Kohn and L. Sham, J. Phys. Rev. **140,** A1133 (1965).P. E. Blöchl, Phys. Rev. B. **50**, 17953 (1994).
43. G. Kresse and D. Joubert, Phys. Rev. B. **59**, 1758 (1999).
44. G. Kresse and J. Furthmüller, Comput. Mater. Sci.**6**,15 (1996).
45. G. Kresse and J. Furthmüller, Phys. Rev. B. **54**, 11169 (1996).
46. H. Qiu, *et al.*, Nat. Comm. **4**, 2642 (2013).
47. Y. Cai, *et al.*, Nanoscale. **6**, 1691-1697 (2014).
48. C. J. Wright and C. Sampson, J.C.S. Faraday I, **76**, 1585-1598 (1980).

2.2 – TFSI treatment of other 2D material systems[2]

Here, we expand on upon the initial results by studying the effect of TFSI treatment, in combination with combined steady-state and transient optical measurements, on several of the most optoelectronically promising TMDC monolayers[1,2] including WS_2, WSe_2, and $MoSe_2$. We find that the treatment is able to effectively passivate/repair defects in sulfur based compounds, while the selenide based materials are largely unaffected. Furthermore, we observe that all of these materials display similar recombination kinetics, *i.e.* there is no observable Shockley-Read-Hall (SRH) recombination at low injection levels while biexcitonic recombination is the likely non-radiative pathway at high injection levels.

To verify that treatment by TFSI does not damage the 2D compounds investigated in this study we performed Raman spectroscopy for each material studied both in the as-exfoliated case and after TFSI treatment. The Raman spectra of WS_2 under 514.5 nm excitation is a particularly interesting case, since under this condition there is a second order-resonance with the longitudinal acoustic mode (LA(M)) which is a result of coupling between the phonon and electronic band structures.[3] While there is no significant change in the Raman spectra for WSe_2 or $MoSe_2$ after chemical treatment, both in terms of peak position and relative intensity, as was observed for MoS_2 in our previous report,[4] we observe a strong increase in the intensity ratio of the 2LA(M) peak to the A' peak from 2.9, which is comparable to what has been previously observed for WS_2 monolayers,[5,6] to 5.3. The increased relative intensity of the resonant mode suggests that the influence of defects is reduced after chemical treatment. Furthermore, this trend is consistent with reduced 2LA(M)/A' peak intensity observed for lower quality WS_2 samples.[6]

---

[2] Reproduced with permission from M. Amani et al., Nano Letters, 16, 2786-2791, 2016. Copyright © [2016] ACS.

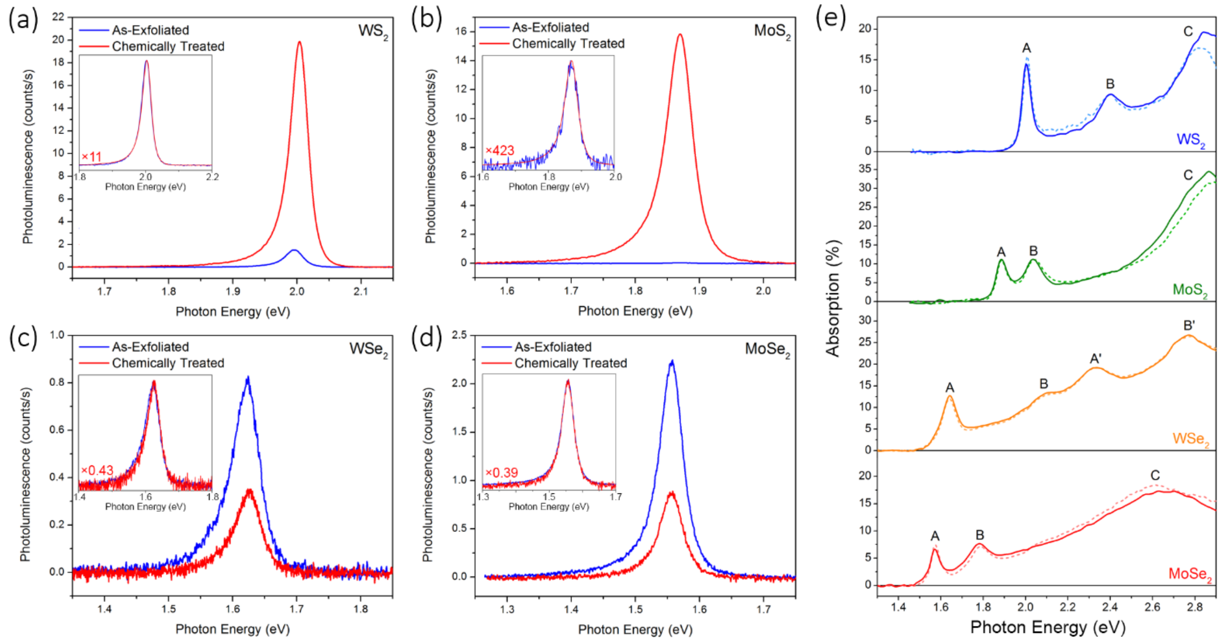

Fig. 2-2-1. PL spectra for both the as-exfoliated and TFSI treated (a) WS$_2$, (b) MoS$_2$, (c) WSe$_2$, and (d) MoSe$_2$ monolayers measured at an incident power of 1×10^{-2} Wcm^{-2}. The inset shows normalized spectra for each material. Absorption spectra of both as-exfoliated (dashed lines) and chemically treated (solid lines) WS$_2$, MoS$_2$, WSe$_2$, and MoSe$_2$ monolayers (e).

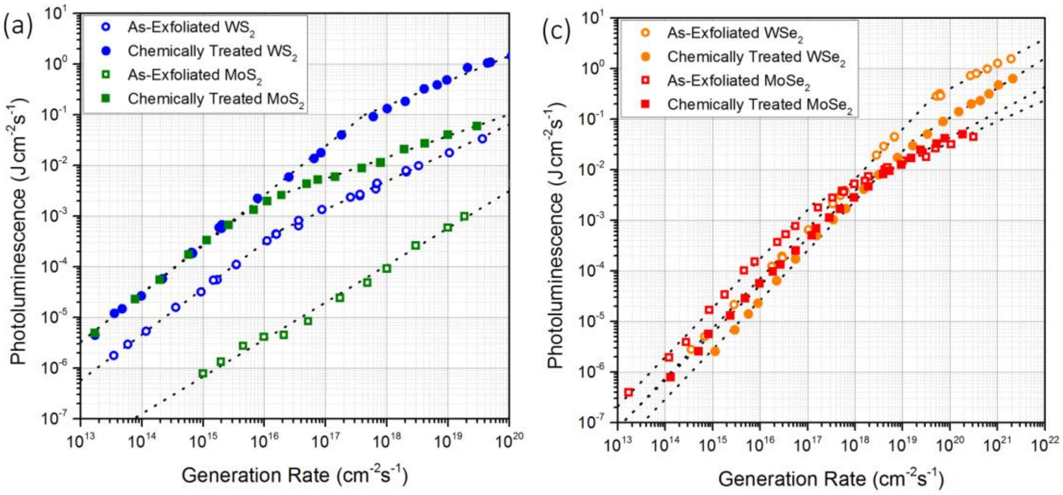

Fig. 2-2-2. Pump-power dependence of the integrated PL for as-exfoliated and treated WS$_2$ and MoS$_2$ (a). Dashed lines show power law fits for the dominant recombination regimes. Pump-power dependence of the integrated PL for as-exfoliated and treated WSe$_2$ and MoSe$_2$ (b). Dashed lines show power law fits for the dominant recombination regimes.

Steady-state calibrated PL spectra, measured at a low excitation power density of 1×10^{-2} W×cm^{-2}, for the four materials examined in this study are shown in Figure 2-2-1 a-d. We found that in addition to being able to dramatically enhance the PL of MoS_2, TFSI treatment is also effective in enhancing the PL of WS_2. As-exfoliated WS_2 has been known to show the highest quantum yield of all 2D materials which have been previously studied[7,8]; despite this we are still able to demonstrate an order of magnitude enhancement of the emission, relative to the as-exfoliated monolayer. To be able to extract the internal photoluminescence quantum yield for the different samples quantitative absorption measurements were performed for each system both before and after chemical treatment. The measurements were performed using two different methods, following the procedure described in our previous work and are plotted in Figure 2-2-1e. As was previously shown for MoS_2, there is no measurable difference in the absorption spectra as a result of TFSI treatment in WS_2, WSe_2, or $MoSe_2$. The spectral shape of the calibrated absorption spectra presented here is consistent with previously reported differential reflectance measurements on the various materials.[9]

One of the primary factors which effects the observed luminescence in 2D semiconductors is substrate induced interference and multiple reflection effects.[10] These phenomena can modulate both the effective absorption as well as the emission by increasing the number of times an incident or emitted photon can be absorbed by the 2D layer or the number of chances it has to fall within the escape cone for emission. By changing the oxide thickness on silicon substrates it was previously shown that this effect can lead to an order of magnitude modulation in the emitted light for the same monolayer,[10] indicating that this effect is independent of the materials internal PL QY. More importantly, this effect has significant wavelength dependence, and will non-linearly weight the observed luminescence for different light emitters. In the case of GaAs, by placing the sample on a highly reflective mirror substrate, it is possible to dramatically increase the probability of the emitted light escaping to ~70%.[11] In addition, complex optical environments such as Si/SiO_2, can impact the radiative lifetime through changes in the effective refractive index.[12] For our case, we utilized quartz substrates for all measurements which provides a very simple, non-wavelength dependent analysis, despite the fact that this lowers the externally measured luminescence.

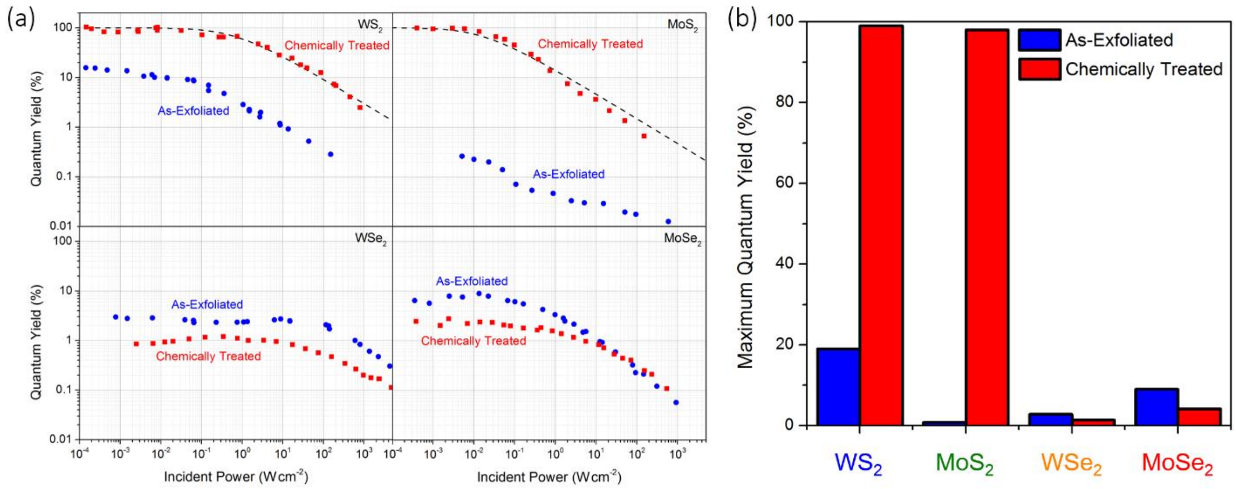

Fig. 2-2-3. Pump-power dependence of the QY for as-exfoliated and chemically treated WS_2, MoS_2, WSe_2 and $MoSe_2$ (a). Dashed lines show the recombination model for chemically treated MoS_2 and WS_2. Summary of the peak QY values for the various TMDCs obtained both before and after treatment (b).

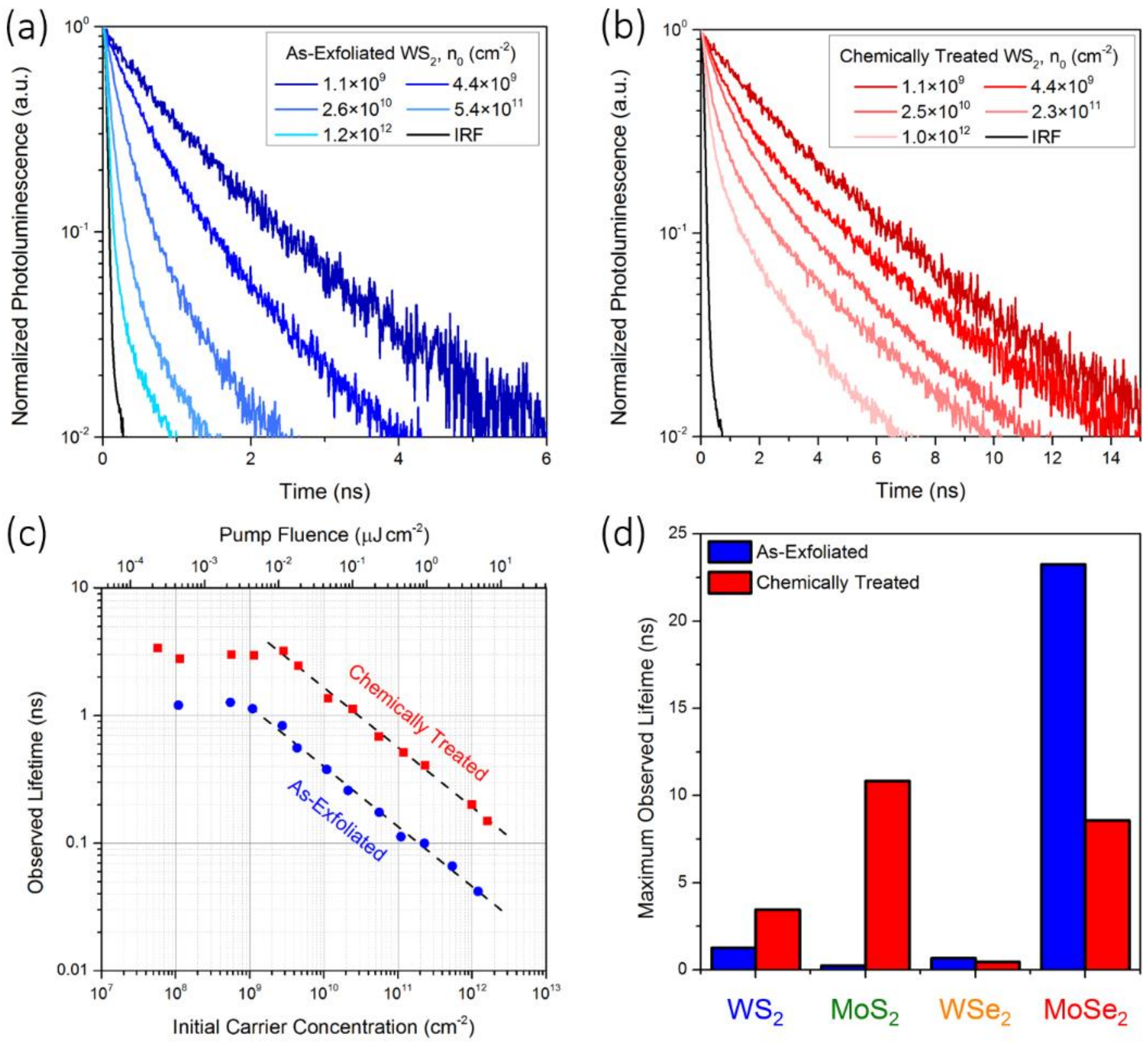

Fig. 2-2-4. Radiative decay of as-exfoliated (a) and chemically treated (b) WS_2 at various initial carrier concentrations (n_0) as well as the instrument response function (IRF). Effective PL lifetime as a function of pump-fluence for WS_2 both before and after chemical treatment; the dashed line shows a power law fit for the dominant recombination regimes (c). Summary of longest measured lifetimes for the various TMDCs obtained both before and after treatment (d).

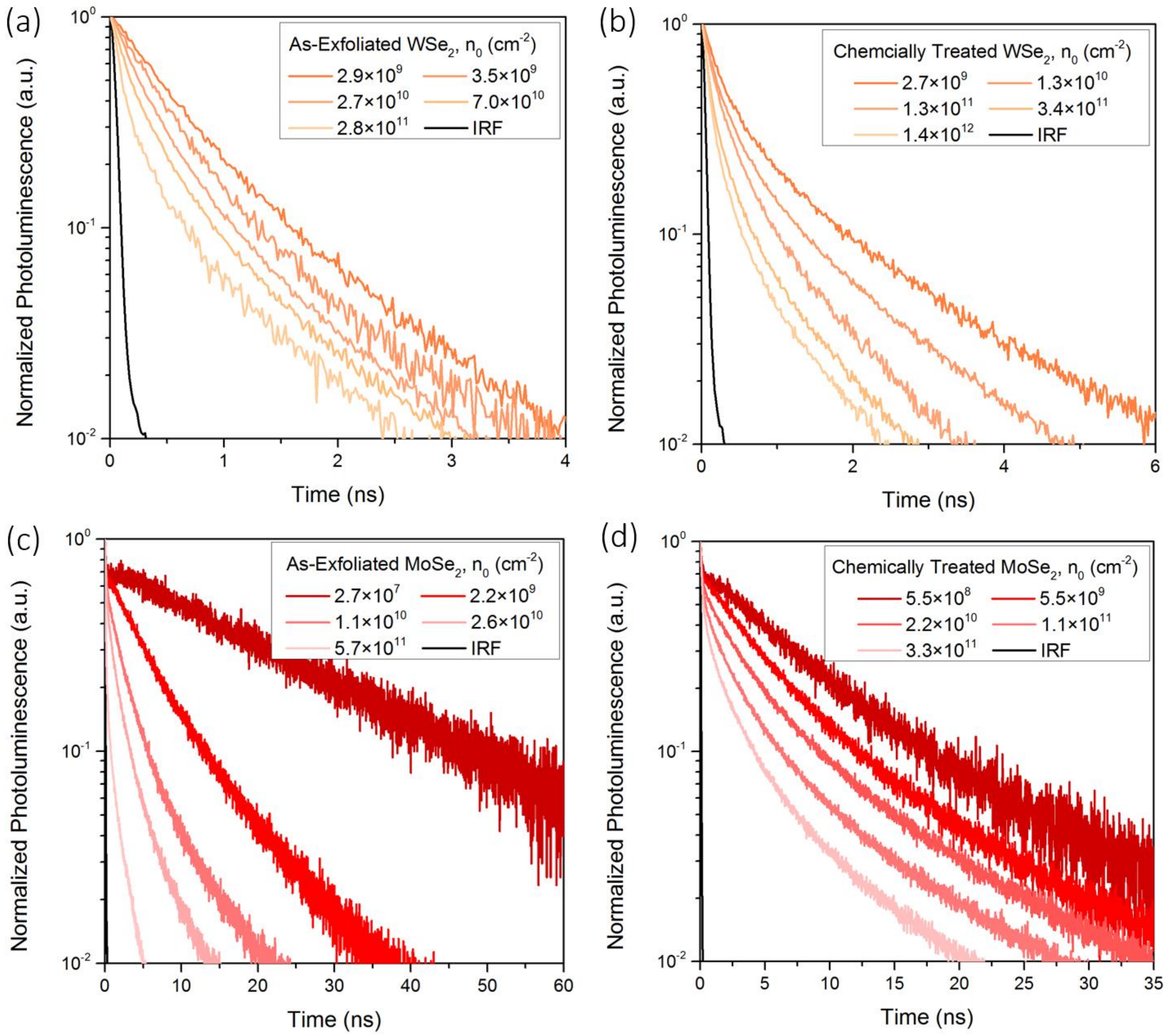

Fig. 2-2-5. Radiative decay of as-exfoliated (a) and chemically treated (b) WSe$_2$ measured at several pump fluences. Radiative decay of as-exfoliated (a) and chemically treated (b) MoSe$_2$ measured at several pump fluences.

To probe the recombination mechanisms present in the various TMDCs, we extended our PL measurements to cover a pump dynamic range of over six orders of magnitude, while avoiding incident laser powers greater than 50 µW which are known to damage as well as cause local heating effects in these materials.[13] The pump-power dependence of luminesce for the different materials is shown both before and after chemical treatment in Figure 2-2-2, as well as empirical power laws fits, given by: $I = P^n$, to the dominant recombination regimes. From these curves we extract the QY, which is plotted in Figure 2-2-3 for each material both before and after treatment. After treatment the QY for both MoS_2 and WS_2 reaches a value near-unity at low pump power, while the QY for the two selenide materials is moderately reduced as summarized in Figure 2b. At high injection levels all of the investigated materials show sub-linear dependence of the light emission, with rate-laws in the range of 0.43-0.58. The rate law is indicative of a two-body non-radiative processes and can be attributed to biexcitonic recombination (annihilation of two excitons), knowing that free electron-hole pairs in 2D materials non-reversibly form excitons due to their high binding energies.[14] In all cases, as the excitation power is reduced, the materials show saturation of the PL, *i.e.* no reduction of the luminescence yield. This is strongly in contrast with traditional semiconductors where a reduction of the PL QY is typically observed due to SRH recombination of a carrier at a defect site (one body process) as opposed to meeting an oppositely charged carrier and radiating (two body process).[15] For the excitonic case, both recombination with a defect and radiation are single body processes which leads to the observed luminescence saturation.

The dynamic luminescence behavior for the different materials, both in the as-exfoliated and chemically treated cases, was investigated to examine the carrier recombination dynamics as well as independently confirm the QY measurements. We show the decay curves for as-exfoliated and chemically treated WS_2 in Figure 2-2-4a and 2-2-4b respectively and the lifetime for both cases as a function of pump-fluence is shown in Figure 2-2-4c, and is consistent with the behavior observed in the steady state measurements. Chemically treated WS_2 shows a single exponential decay with a radiative lifetime (τ_r) of 3.4±0.3 ns as the lowest measured fluence of 2.3×10^{-4} µJ/cm^2. Similar measurements were performed on WSe_2, and $MoSe_2$ and are shown in Figure 2-2-5. Figure 2-2-4d summarizes the observed lifetimes (τ_{ob}) for the materials evaluated in this study. Despite the fact that the luminescence decay of the selenide compounds is dominated by the non-radiative lifetime, we can estimate the radiative lifetime using[15]:

$$QY = \frac{\tau_{ob}}{\tau_r} \tag{2-2-1}$$

which results in τ_r = 19.3 ns and τ_r = 116.3 ns for WSe_2 and $MoSe_2$ respectively.

2D materials are known to be host to a significant variety of defect types,[17-21] in naturally or synthesized crystals as well as monolayers grown by chemical vapor deposition.[22] In the case of both exfoliated WS_2 and MoS_2, which can achieve near-unity QY after TFSI treatment, one of the dominant defect types is likely sulfur vacancies.[10,20]

On the other hand, TFSI treatment is not able to improve the luminescence of both WSe_2 and $MoSe_2$, and typically results in a small drop from the as-exfoliated intensity. The treatment conditions for the selenium-based compounds were systematically varied; however, no TFSI based treatment condition was found to enhance the PL. High resolution TEM studies on WSe_2 have suggested that defects in this material do not simply exist as simple vacancy sites, but rather as complexes which include both missing chalcogen and metal atoms.[23]

To better understand the nature of the native defects which exist in the various crystals, scanning tunneling microscopy (STM) measurements were performed on freshly exfoliated crystals of the materials studied here. Representative STM images taken over a similar area of 100 nm × 100 nm for the different TMDC materials are shown in Figure 2-2-6; it is important to note here that the spatial variation of surface defects is high. The poor QY observed in as-exfoliated MoS_2 can be understood from the comparatively large defect density observed in STM (as high as 8 % of the imaged surface area), relative to WS_2 (~0.1-1.6 %). Dark contrast defects, predominantly observed in WS_2 and MoS_2, can be caused by missing fragments of the material as well as the presence of acceptor impurities at the vicinity of the surface region.[36-38] This is consistent with sulfur vacancies and the n-type behavior observed in WS_2 and MoS_2 field effect devices,[24,25] which do not utilize doping or extremely high work function contacts to enable p-type conduction[26,27]. The opposite behavior is seen in selenides, where a high density of bright contrast defects (>2%) that can primarily be related to donor impurities at or near the surface, are observed.[42] The interpretation of the localized imperfections were well documented for GaAs(110) and other semiconductors.[28] Our surface inspection reveals the following findings: (i) high spatial variation even across the same material with the largest imperfections density found on MoS_2, (ii) sulfide surfaces are dominated by structural defects and by acceptor impurities causing local depressions, and (iii) selenide surfaces are predominantly dominated by hillock-like structures induced by donor impurities. This drastic difference in the nature of defects may explain why sulfur based TMDC materials are more responsive to the TFSI treatment.

In summary, we have presented a comprehensive study on the recombination behavior as well as the impact of TFSI treatment on the most heavily studied direct band-gap 2D semiconductors. We show that the dominant recombination pathway at high pump-power for all of these materials is biexcitonic recombination and that there is no evidence for SRH related recombination at low injection levels. Furthermore, through the combination of lifetime and calibrated QY measurements we estimate the radiative lifetimes and provide the biexcitonic recombination coefficients for the studied systems. Our results show that sulfur based TMDCs are amenable to repair by TFSI treatment, while high QY in selenium-based compounds cannot be obtained by this method.

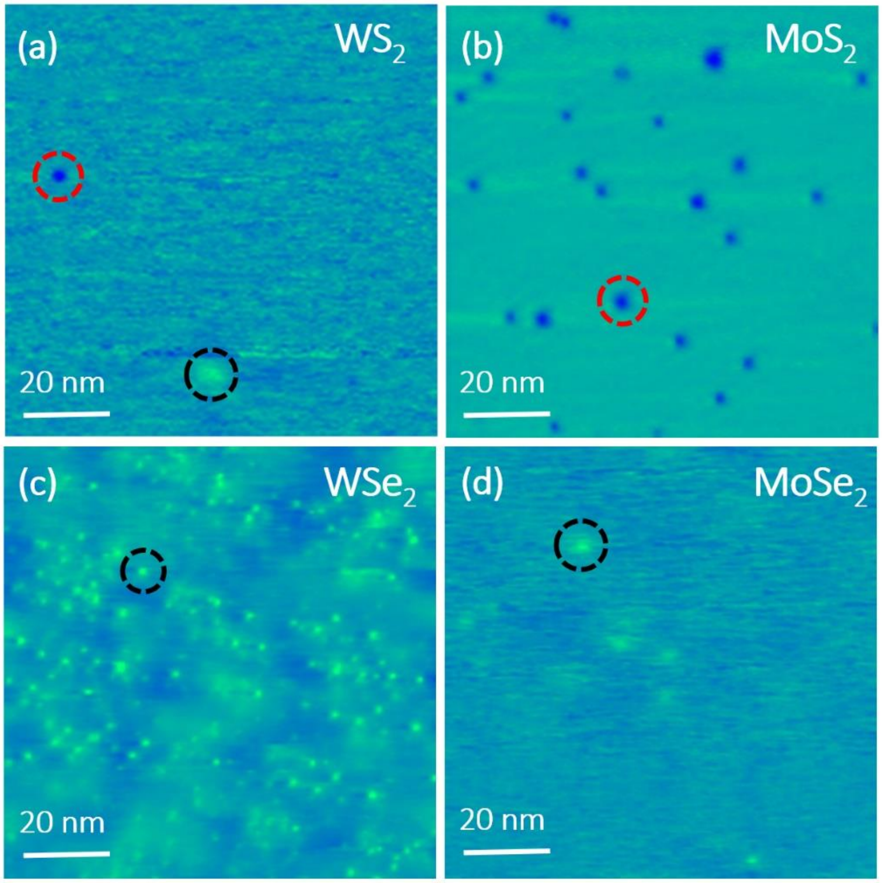

Fig. 2-2-6. Large area representative STM images (100 nm × 100 nm) measured on bulk flakes of (a) WS_2 (V_{bias} = 0.9 V, I_t = 1.0 nA), (b) MoS_2 (V_{bias} = 1.0 V, I_t = 1.0 nA), (c) WSe_2 (V_{bias} = 1.5 V, I_t = 0.5 nA), and (d) $MoSe_2$ (V_{bias} = 1.5 V, I_t = 0.5 nA). Red circles show examples of either donor impurities or missing fragments of material (dark contrast); black circles indicate show examples of acceptor impurities (bright contrast).

References for Section 2-2

1. Zhao, W.; Ghorannevis, Z.; Chu, L.; Toh, M.; Kloc, C.; Tan, P.-H.; Eda, G. *ACS Nano* **2013**, 7(1), 791-797.
2. Lezama, I.G.; Arora, A.; U. Alberto; Barreteau, C.; Giannini, E.; Potemski, M.; Morpurgo, A.F. *Nano Lett.* **2015**, 15(4), 2336-2342.
3. Liu, M.; Yin, X.; Ulin-Avila, E.; Geng, B.; Zentgraf, T.; Ju, L.; Wang, F.; Zhang, X. *Nature* **2011**, 474, 64-67.
4. Mak, K. F.; Lee, C.; Hone, J.; Shan, J.; Heinz, T. F. *Phys. Rev. Lett.* **2010**, 105, 136805.
5. Berkdemir, A.; Gutierrez, H.R.; Botello-Mendez, A.R.; Perea-Lopez, N.; Elias, A.L.; Chia, C.I.; Wang, B.; Crespi, V.H.; Lopez-Urias, F.; Charlier, J.C.; Terrones, H.; Terrones, M. *Sci. Rep.* **2013**, 3, 1755.
6. McCreary, A.; Berkdemir, A.; Wang, J.; Nguyen, M.A.; Elias, A.L.; Perea-Lopez, N.; Fujisawa, K.; Kabius, B.; Carozo, V.; Cullen, D.A.; Mallouk, T.E.; Zhu, J.; Terrones, M. *J. Matter. Res.* **2016**, advanced online publication (DOI: 10.1557/jmr.2016.47).
7. Xiao, D.; Liu, G.B.; Feng, W.; Xu, X.; Yao, W. *Phys. Rev. Lett.* **2012**, 108, 196802.
8. Zeng, H.; Dai, J.; Yao, W.; Xiao, D.; Cui, X. *Nat. Nano.* **2012**, 7, 490-493.
9. Zeng, H.; Dai, J.; Yao, W.; Xiao, D.; Cui, X. *Nat. Nano.* **2012**, 7, 490-493.
10. Lien, D.-H.; Kang, J.S.; Amani, M.; Chen, K.; Tosun, M.; Wang, H.-P.; Roy, T.; Eggleston, M.S.; Wu, M.C.; Dubey, M.; Lee, S.-C.; He, J.-H.; Javey, *Nano Lett.* **2015**, 15(2), 1356-1361.
11. Ramasubramaniam, A.; Naveh, D.; Towe, E. *Phys. Rev. B* **2011**, 84, 205325.
12. Liu, Z.; Amani, M.; Najmaei, S.; Xu, Q.; Zou, X.; Zhou, W.; Yu, T.; Qiu, C.; Birdwell, A.G.; Crowne, F.J.; Vajtai, R.; Yakobson, B.I.; Xia, Z.; Dubey, M.; Ajayan, P.M.; Lou, J. *Nat. Comms.* **2014**, 5, 5246.
13. Yablonovitch, E.; Gmitter, T.J.; Bhat, R. *Phys. Rev. Lett.* **1988**, 61(22), 2546-2549.
14. Qiu, H.; Xu, Tao, Wang, Z.; Ren, W.; Nan, H.; Ni, Z.; Chen, Q.; Yuan, S.; Miao, F.; Song, F.; Long, G.; Shi, Y.; Sun, Litao, Wang, J.; Wang, X. *Nat. Comms.* **2013**, 4, 2642.
15. Lin, Y.-C.; Bjorkman, T.; Komsa, H.-P.; Teng, P.-Y.; Yeh, C.-H.; Huang, F.-S.; Lin, K.-H.; Jadczak, J.; Huang, Y.-S.; Chiu, P.-W.; Krasheninnikov, A.V.; Suenaga, K. *Nat. Comm.* **2014**, 6, 6736.
16. Su, W.; Dou, H.; Li, J.; Hou, D.; Dai, N.; Yang, Li. *RSC Adv.* **2015**, 5, 82924.
17. Yuan, L.; Huang, L. *Nanoscale* **2015**, 7, 7402.
18. Hong, J.; Hu, Z.; Probert, M.; Li, K.; Lv, D.; Yang, X.; Gu, L.; Mao, N.; Feng, Q.; Xie, L.; Zhang, J.; Wu, D.; Zhang, Z.; Jin, C.; Ji, W.; Zhang, X.; Yuan, J.; Zhang, Z. *Nat. Comms.* **2015**, 6, 6293.
19. Najmaei, S.; Liu, Z.; Zhou, W.; Zou, X.; Shi, G.; Lei, S.; Yakobson, B.I.; Idrobo, J.-C.; Ajayan, P.M.; Lou, J. *Nat. Matter.* **2013**, 12, 754-759.
20. Addou, R.; McDonnell, S.; Barrera; Z.; Guo, Z.; Azcatl, A.; Wang, J.; Zhu, H.; Hinkle, C.L.; Quevedo-Lopez, M.; Alshareef, H.N.; Colombo, L.; Hsu, J.W.P.; Wallace, R.M. *ACS Nano* **2015**, 9, 9124-9133.
21. Addou, R.; Colombo, L.; Wallace, R.M. *ACS Appl. Mater. Interfaces* **2015**, 7, 11921-11929.
22. McDonnell, S.; Addou, R.; Buie, C.; Wallace, R.M.; Hinkle, C.L. *ACS Nano* **2014**, 8, 2880–2888.
23. Najmaei, S.; Liu, Z.; Zhou, W.; Zou, X.; Shi, G.; Lei, S.; Yakobson, B.I.; Idrobo, J.-C.; Ajayan, P.M.; Lou, J. *Nat. Matter.* **2013**, 12, 754-759.
24. Ovchinnikov, D.; Allain, A.; Huang, Y.-S.; Dumcenco, D.; Kis, A. *ACS Nano* **2014**, 8(8), 8174-8181.
25. Kiriya, D.; Zhou, Y.; Nelson, C.; Hettick, M.; Madhvapathy, S.R.; Chen, K.; Zhao, P.; Tosun, M.; Minor, A.M.; Chrzan, D.C.; Javey, A. *Adv. Func. Matter.* **2015**, 25, 6257-6264.
26. Chuang, S.; Battaglia, C.; Azcatl, A.; McDonnell, S.; Kang, J.S.; Yin, X.; Tosun, M.; Kapadia, R.; Fang, H.; Wallace, R.M.; Javey, A. *Nano Lett.* **2014**, 14, 1337-1342.
27. Whangbo, M. H.; Ren, J.; Magonov, S. N.; Bengel, H.; Parkinson, B. A.; Suna, A. *Surf. Sci.* 1995, 326, 311−326.
28. Ebert, P. *Surf. Sci.* **1999**, 33, 121-303.

2.3 – Application of TFSI treatment to synthetic and large area MoS_2 films[3]

A key unanswered question in the work presented thus far is the effectiveness of the treatment on MoS_2 grown by chemical vapor deposition (CVD). We address treatment of synthetic MoS_2 monolayers in this work and show that tensile strain present in as-grown films[1] has a dramatic effect on the treatment. We also study the effect of the sulfur precursor temperature during growth and show that this also plays a role in the ultimate quantum yield which can be achieved after treatment. As a result, we are able to achieve large-area monolayers with high quantum yield. Figures 2-3-1b and c show schematic representations of the two approaches investigated to obtain high QY synthetic MoS_2 monolayers. Samples that were grown and treated directly by TFSI (Fig. 2-3-1b) had a minimal change in the QY with peak values under 0.1%. In the second approach (Fig. 2-3-1c), the MoS_2 triangular domains and films were transferred from the growth substrate to a new substrate using HF to release MoS_2 from the original substrate. It has been previously shown that after CVD growth there an is intrinsic tensile strain present in MoS_2 monolayers,[2-5] which may be a result of the difference in thermal expansion coefficient of the Si/SiO_2 substrate and MoS_2 as the sample is cooled from the growth temperature (typically in the range of 600-800ºC) to room temperature. After the layer transfer, the strain is released, and the samples are subsequently treated by TFSI, resulting in a dramatic enhancement of the room temperature quantum yield from <1% before treatment to a final value of ~30%.

We first investigated the effect of layer transfer on the optoelectronic properties of MoS_2. For this study single MoS_2 domains were grown directly on quartz substrates and subsequently transferred to a new quartz substrate as described in section 2.1. Consistent with previous reports, we find that there is intrinsic biaxial tensile strain in the as-grown MoS_2 domains as a result of the difference in thermal expansion coefficient of the substrate and the MoS_2.[2,5] As a result we observe a shift of the in-plane Raman mode (E') of 2.4 cm^{-1} between the as-grown and transferred films, indicating that the as-grown MoS_2 is under 0.8% tensile strain (fig. 2-3-2a). The final separation of the E' and A' peaks is 18.5 cm^{-1} after transfer, which is consistent with what has been previously reported for monolayer MoS_2 produced by exfoliation.[2] We also observe a blue-shift of the PL spectra, which similarly corresponds to a release of tensile strain as shown in figure 2-3-2b.

---

[3] Reproduced with permission from M. Amani et al., ACS Nano, 10, 6535-6541, 2016. Copyright © [2016] ACS.

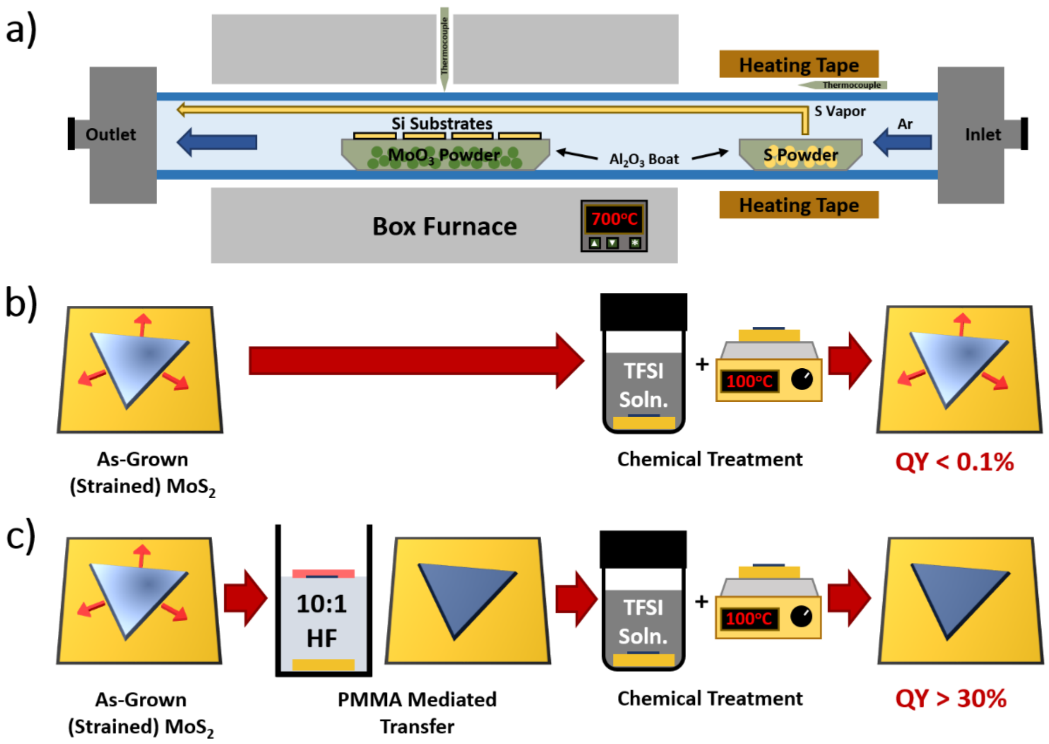

Fig. 2-3-1. (a) Configuration of the growth setup utilized to prepare the MoS2 samples for this study. The temperature of the substrate and molybdenum precursor (in the furnace hot zone) and the sulfur precursor (surrounded by heating tape) are controlled and measured independently. (b) and (c) Schematic illustrating the two primary sample preparation routes investigated in this study. As-grown MoS_2 triangular domains and films, which show tensile strain after growth were either (b) treated by TFSI directly, resulting in a small reduction in the PL QY or (c) transferred from the growth substrate using PMMA mediated transfer process releasing the strain, and subsequently treated by TFSI, resulting in a final PL QY of approximately 30%.

The dependence of the PL QY as a function of pump-power was then investigated both before and after transfer over a pump dynamic range of five orders of magnitude as shown in figure 2-3-2c, where the limits were set by either insufficient signal due to the low QY of the untreated samples or by high illumination powers (greater than 100 µW) which can lead to damage of the monolayers due to excessive local heating. The corresponding QY as a function of pump-power is plotted in figure 2-3-2d and shows that the quantum yield for the CVD samples prepared here is in the range of 0.02 to 0.5%. Interestingly, the dynamics of the PL QY as a function of pump-power change dramatically after the strain is released, as can be seen by the difference in the power law dependence for the two samples. For the transferred sample, the behavior closely matches data which has been previously reported for exfoliated films, obeying a power law of 0.72 over the measurable dynamic range (figure 2-3-2c). On the other hand, for the as-grown MoS_2 domains, the emission is linearly dependent on the incident power, with a power law of 0.98. In the unstrained case, monolayer MoS_2 shows a direct bandgap at the K point; however, upon the introduction of tensile strain (on the order of 1%) has been previously calculated that the lowest energy transition becomes K-to-Γ and is indirect.[6]

The primary implication of having an indirect as opposed to direct bandgap in semiconductors is the requirement of a phonon to observe a radiative transition. This additional requirement results in a dramatic increase in the radiative lifetime. In the case of direct band-gap GaAs, the radiative lifetime is on the order of nanoseconds, while in indirect band-gap silicon, the lifetime is on the order of milliseconds.[7,8] It is important to note here that an indirect band-gap does not imply that a material has no luminescence. In fact, high quality silicon with appropriate surface passivation can have a PL QY as high as 20%.[9] The indirect bandgap simply implies that the non-radiative lifetime must be sufficiently long (ideally much longer than the radiative lifetime) to allow carriers the opportunity to radiate. It is likely that the tensile strain present in the as-grown MoS_2 leads to the material becoming more indirect, increasing the radiative lifetime and resulting in the observed variation in the pump-power dependence of the luminescence.

The effects of chemical treatment on both as-grown and transferred samples is studied by calibrated PL measurements. For as-grown MoS_2 monolayers, treatment by TFSI surprisingly lead to a minor degradation of the luminescence (figure 2-3-3a). This behavior was consistently observed for numerous samples, and similar results were observed for samples where the growth conditions were varied as discussed later in the manuscript. Noticeably different behavior was observed after the samples were transferred as shown in figure 2-3-3b. After transfer, samples grown at an optimized sulfur precursor temperature of 200ºC were found to have an average QY value of 31±8% with TFSI treatment at low pump power. Similar pump-power dependence of PL QY was observed for a transferred MoS_2 continuous film after treatment by TFSI.

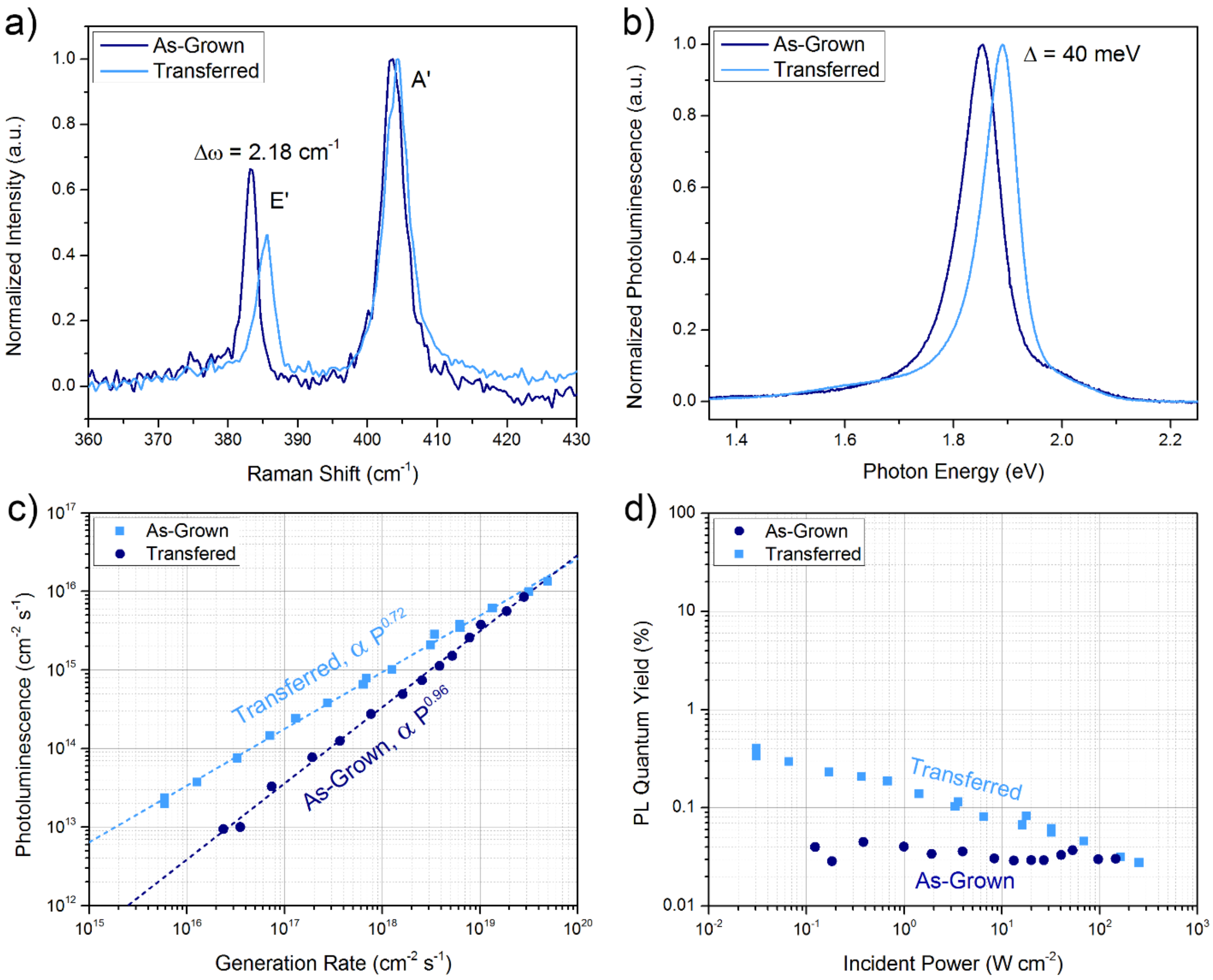

Fig. 2-3-2. (a) Raman spectra measured on as-grown and transferred MoS$_2$ single domains. (b) PL spectra of the MoS2 single domains measured before and after transfer at a laser power of 50 W/cm2. (c) Pump-power dependence of the integrated PL measured before and after transfer. Dashed lines show power law fits of the data. (d) Pump-power dependence of the QY measured before and after transfer. Samples shown here were grown directly on quartz and subsequently transferred to a new quartz substrate.

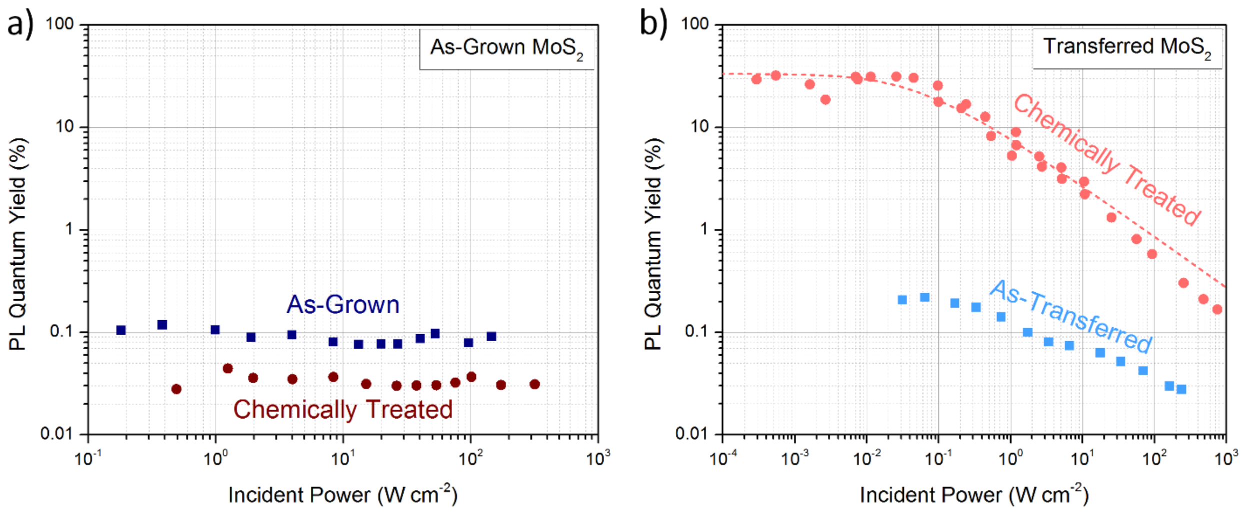

Fig. 2-3-3. (a) Pump-power dependence of the QY measured on a CVD-grown MoS_2 single domain after growth and after chemical treatment by TFSI; note that this sample was not transferred. (b) Pump-power dependence of the QY measured on a CVD-grown MoS_2 single domain after transfer and after chemical treatment by TFSI. Dashed lines show the recombination model for the treated sample.

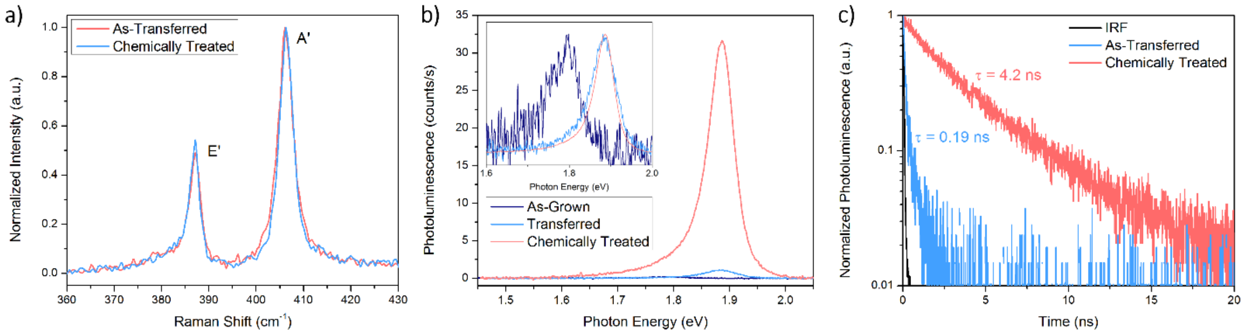

Fig. 2-3-4. (a) Raman spectra measured on transferred MoS_2 single domains before and after treatment by TFSI. (b) PL spectra obtained at a pump power of 0.1 W/cm^2 for transferred MoS_2 single domains both before and after chemical treatment by TFSI. (c) Radiative decay of transferred MoS_2 single domains obtained at a pump fluence of 5×10^{-2} μJ/cm^2 both before and after chemical treatment by TFSI, as well as the instrument response function (IRF).

To verify that the structural properties of the CVD-grown MoS_2 are unaffected due to the TFSI treatment, we performed Raman spectroscopy before and after treatment as shown in figure 2-3-4a and verify that, similar to the case of exfoliated monolayers, there is no significant change in the spectra.[2] PL spectra measured after growth, transfer, and treatment at an incident power of 0.1 W/cm^2 are shown in figure 2-3-4b. Noting that the significant spectral shift between the as-grown and transferred sample is a result of strain, we see no significant change in the spectral shape or peak-position as a result of the treatment. It is also important to note that we do not observe any change in the spectral shape of the emission over the full pump dynamic range for treated samples. Finally, to confirm the enhancement in QY by chemical treatment, we performed time resolved measurements at a low pump fluence of 5×10^{-2} μJ/cm^2. Prior to treatment, the films show an extremely short lifetime of 190 ps, which is comparable to the instrument timing resolution. After treatment, we observe a measured lifetime (τ_m) of 4.2 ns. We can estimate the quantum yield using the formula: $QY = \frac{\tau_m}{\tau_r}$, and the radiative lifetime measured in an exfoliated MoS_2 sample.[12] This results in a predicted quantum yield value of 38% and is in reasonable agreement with the steady state measurements.

While the defects in MoS_2 monolayers generated by micro-mechanical exfoliation primarily consist of sulfur vacancies,[13-16] TEM studies have shown that samples grown by CVD contain a wide variety of complex defects.[16] These include point defects such a Mo or S antisites, Mo vacancies, sulfur and disulfur vacancies, Mo and S adatoms, as well as complexes such as ring chains.[17] To obtain MoS_2 samples where the TFSI treatment, which has previously shown to have been successful in passivating exfoliated monolayers, is effective, we studied the influence of sulfur precursor temperature on the growth. Figure 2-3-5 shows the quantum yield for each condition after transfer as well as after chemical treatment by TFSI for sulfur precursor temperatures of 200ºC, 250 ºC, and 300ºC. For samples grown in sulfur rich conditions, TFSI treatment had little impact on the quantum yield. Conversely, for samples prepared in sulfur deficient conditions, a large enhancement of the PL was observed after treatment. We hypothesize that under sulfur deficient growth conditions the defects in the sample are dominated by sulfur vacancies, making them more amenable to TFSI treatment, whereas in sulfur rich conditions, the defects are primarily related to the cation and cannot be passivated by TFSI. Since the mechanism of TFSI treatment is not fully understood however, we lack sufficient evidence to make a stronger claim based on these results. Interestingly, we found that in the absence of chemical treatment, MoS_2 prepared in sulfur rich conditions show the highest emission efficiency.

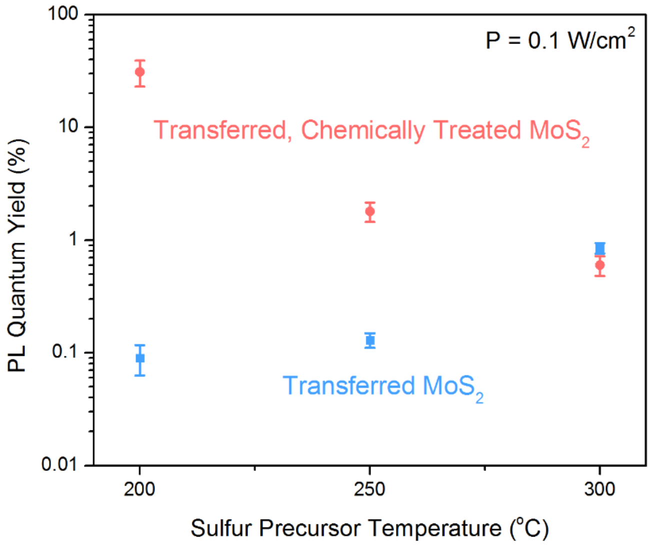

Fig. 2-3-5. Maximum quantum yield obtained on CVD-grown single domains after transfer and after subsequent treatment by TFSI as a function of the sulfur precursor temperature during the growth process. Error bars are obtained from measurements taken on 10 different locations on the same sample.

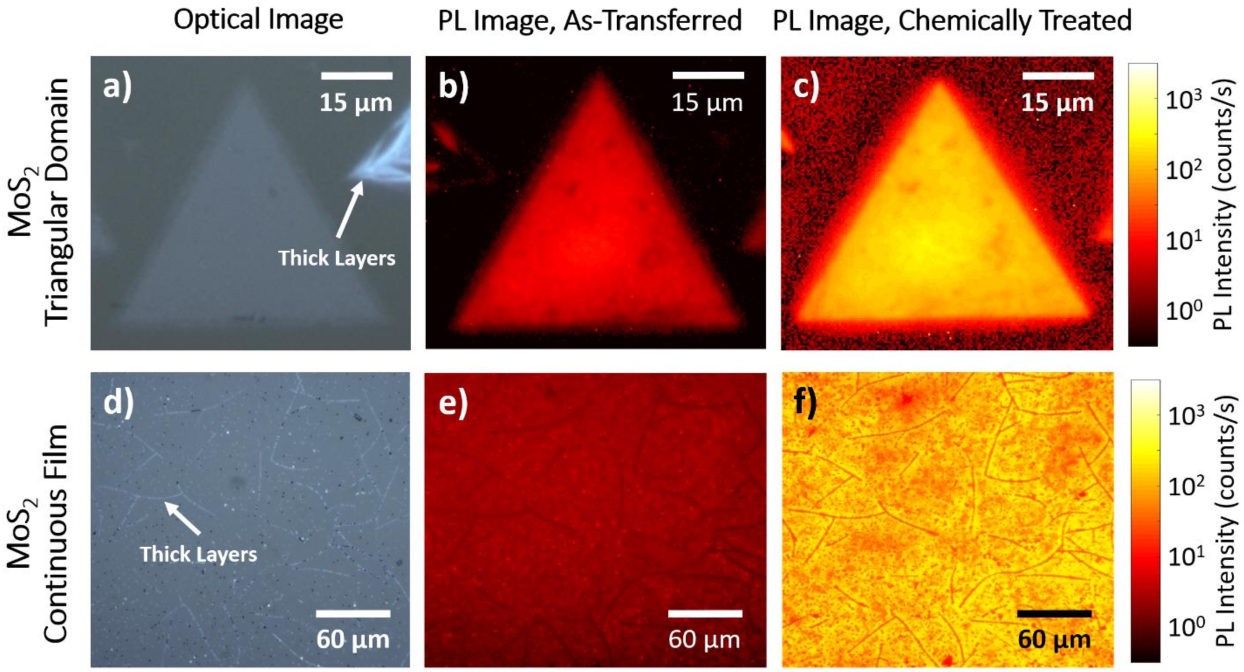

Fig. 2-3-6. (a) Optical image of a transferred MoS_2 single domains and log-scale luminescence images from the same area obtained (b) before and (c) after chemical treatment by TFSI. (d) Optical image of a transferred continuous MoS_2 film and log scale luminescence images from the same area obtained (e) before and (f) after chemical treatment by TFSI.

The uniformity of the transferred samples both before and after treatment was investigated using PL imaging. Emission from both single MoS_2 domains as well as continuous films were imaged, and the results are shown in figure 2-3-6. As a result of the transfer process, some local imperfections such as holes are generated in the samples. Additionally, since the growth process has not been optimized yet at low sulfur pressure conditions, regions of few-layered growth and overgrowth along boundary regions of the films are observed. For both films and single domains, we observed uniform enhancement of the luminescence, excluding regions where the sample was physically damaged prior to treatment and multilayer regions in the continuous film. This is in strong contrast to previous observations in CVD samples where groups have reported the observation of high PL confined to edges or other local regions of the film.[16]

Finally, we performed macro-scale imaging of the luminescence from the previously examined CVD MoS_2 film after chemical treatment by TFSI, and the results are shown in figure 2-3-7. The image was taken by a photographic camera, using a colored glass filter to block the excitation, and the sample was excited by a ultra-violet LED ($P \approx 0.2$ W/cm^2). Emission observed at the edges of the sample is due to light trapping within the high refractive index substrate. The strong, visible light emission of these monolayers coupled with their low absorption suggests that they have potential for use in transparent lighting applications.

In conclusion, we have demonstrated that treatment by TFSI can provide a highly effective and simple route to obtaining high luminescence efficiency in synthetic MoS_2. We have identified two key sample requirements for this treatment to be effective: 1) transfer of the MoS_2 film to release tensile strain of the as-grown films and 2) optimization of the sulfur precursor temperature during growth. As a result of the TFSI treatment, we obtain CVD-grown MoS_2 samples with high PL QY values around 30%. Upon TFSI treatment, the monolayer MoS_2 film grown by CVD is shown to have visible-by-eye luminescence over a large area, despite having a low absorption coefficient. These findings provide important insight into the realization of a synthetic route towards high-quality monolayer TMDCs with low trap densities.

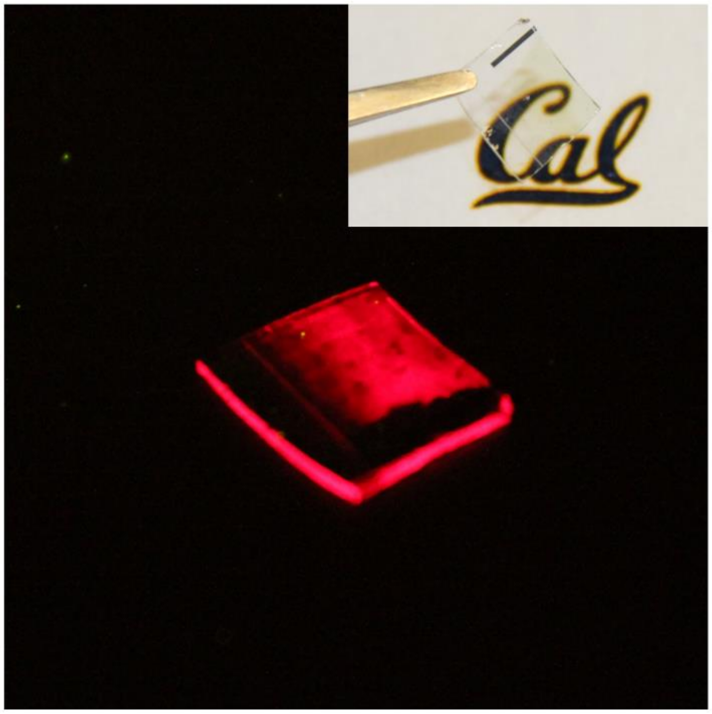

Fig. 2-3-7. Photograph of luminescence from a CVD-grown MoS_2 film transferred to a quartz substrate and subsequently chemical treated by TFSI. The MoS_2 film partially covers the sample. Inset shows a photograph of the quartz chip and the transferred MoS_2 film.

References for Section 2-3

1. Amani, M.; Chin, M. L.; Mazzoni, A. L.; Burke, R. A.; Najmaei, S.; Ajayan, P. M.; Lou, J.; Dubey, M. Growth-Substrate Induced Performance Degradation in Chemically Synthesized Monolayer MoS_2 Field Effect Transistors. *Appl. Phys. Lett.* **2014**, 104, 203506.
2. Amani, M.; Lien, D.-H.; Kiriya, D.; Xiao, J.; Azcatl, A.; Noh, J.; Madhvapathy, S. R.; Addou, R.; Kc, S.; Dubey, M.; Cho, K.; Wallace, R. M.; Lee, S.-C.; He, J.-H.; Ager, J. W.; Zhang, X.; Yablonovitch, E.; Javey, A. Near-Unity Photoluminescence Quantum Yield in MoS2. *Science* **2015**, 350, 1065–1068.
3. Miller, O. D.; Yablonovitch, E.; Kurtz, S. R. Strong Internal and External Luminescence as Solar Cells Approach the Shockley-Queisser Limit. *IEEE J. Photovol*. **2012**, 2, 303-311.
4. Lien, D.-H.; Kang, J.S.; Amani, M.; Chen, K.; Tosun, M.; Wang, H.-P.; Roy, T.; Eggleston, M.S.; Wu, M.C.; Dubey, M.; Lee, S.-C.; He, J.-H.; Javey, A. Engineering Light Outcoupling in 2D Materials. *Nano Lett.* **2015**, 15, 1356-1361.
5. Liu, Z.; Amani, M.; Najmaei, S.; Xu, Q.; Zou, X.; Zhou, W.; Yu, T.; Qiu, C.; Birdwell, A.G.; Crowne, F.J.; Vajtai, R.; Yakobson, B.I.; Xia, Z.; Dubey, M.; Ajayan, P.M.; Lou, J. Strain and Structure Heterogeneity in MoS_2 Atomic Layers Grown by Chemical Vapour Deposition. *Nat. Comms.* **2014**, 5, 5246.
6. Shi, H.; Pan, H.; Zhang, Y.-W.; Yakobson, B. I. Quasiparticle band structures and optical properties of strained monolayer MoS_2 and WS_2. *Phys. Rev. B*. **2013**, 87, 155304.
7. Yablonovitch, E.; Gmitter, T. J.; Bhat, R. Inhibited and Enhanced Spontaneous Emission from Optically Thin AlGaAs/GaAs Double Heterostructures. *Phys. Rev. Lett*. **1988**, 61, 2546-2549.
8. Richter, A.; Glunz, S. W.; Werner, F.; Schmidt, J.; Cuevas, A. Imprved Quantitative Description of Auger Recombination in Crystalline Silicon. *Phys. Rev. B*. **2012**, 86, 165202.
9. Trupke, T.; Zhao, J.; Wang, A.; Corkish, R.; Green, M. A. Very Efficient Light Emission from Bulk Crystalline Silicon. *Appl. Phys. Lett*. **2003**, 82, 2996-2998.
10. Hill, H.M.; Rigosi, A.F.; Roquelet, C.; Chernikov, A.; Berkelbach, T.C.; Reichman, D.R.; Hybertsen, M.S.; Brus, L.E.; Heinz, T.F. Observation of Excitonic Rydberg States in Monolayer MoS_2 and WS_2 by Photoluminescence Excitation Spectroscopy. *Nano Lett.* **2015**, 15, 2992-2997.
11. Chernikov, A.; Berkelbach, T. C.; Hill, H. M.; Rigosi, A.; Li, Y.; Aslan, O. B.; Reichman, D. R.; Hybertsen, M. S.; Heinz, T. F. Exciton Binding Energy and Non-Hydrogenic Rydberg Series in Monolayer WS_2. *Phys. Rev. Lett*. **2014**, 113, 076802.
12. Amani, M.; Taheri, P.; Addou, R.; Ahn, G. H.; Kiriya, D.; Lien, D.-H.; Ager, J. W.; Wallace, R. M.; Javey, A. Recombination Kinetics and Effects of Superacid Treatment in Sulfur- and Selenium Based Transition Metal Dichalcogenides. *Nano Lett.* **2016**, 16, 2786-2791.
13. Qiu, H.; Xu, Tao, Wang, Z.; Ren, W.; Nan, H.; Ni, Z.; Chen, Q.; Yuan, S.; Miao, F.; Song, F.; Long, G.; Shi, Y.; Sun, Litao, Wang, J.; Wang, X. Hopping Transport Through Defect-Induced Localized States in Molybdenum Disulphide. *Nat. Comms.* **2013**, 4, 2642.
14. Hong, J.; Hu, Z.; Probert, M.; Li, K.; Lv, D.; Yang, X.; Gu, L.; Mao, N.; Feng, Q.; Xie, L.; Zhang, J.; Wu, D.; Zhang, Z.; Jin, C.; Ji, W.; Zhang, X.; Yuan, J.; Zhang, Z. Exploring Atomic Defects in Molybdenum Disulfide Monolayers. *Nat. Comms.* **2015**, 6, 6293.
15. Najmaei, S.; Amani, M.; Chin, M. L.; Liu, Z.; Birdwell, A. G.; O'Regan, T. P.; Ajayan, P. M.; Dubey, M.; Lou, J. Electrical Transport Properties of Polycrystalline Monolayer Molybdenum Disulfide. *ACS Nano*. **2014**, 8, 7930-7937.
16. Gutierrez, H.R.; Perea-Lopez, N.; Elias, A.L.; Berkdemir, A.; Wang, B.; Lv, R.; Lopez-Urias, F.; Crespi, V.H.; Terrones, H.; Terrones, M. Extraordinary Room-Temperature Photoluminescence in Triangular WS_2 Monolayers. *Nano Lett.* **2013**, 13, 3447-3454.
17. Zhou, W.; Zou, X.; Najmaei, S.; Liu, Z.; Shi, Y.; Kong, J.; Lou, J.; Ajayan, P. M.; Yakobson, B. I.; Idrobo, J.-C. Intrinsic Structural Defects in Monolayer Molybdenum Disulfide. *Nano Lett*. **2013**, 13, 2615-2622.

2.4 – Strain engineering of synthetic WSe_2 films[4]

In many 2D materials, a number of desirable properties emerge at the monolayer limit, the most notable of which being the presence of a direct bandgap. Many studies based on mechanical bending of exfoliated 2D TMDCs have been conducted on flexible substrates, and they have shown that the application of strain can tune the properties of this new class of materials[1-4]. For example, it has been demonstrated that in multilayer WSe_2, particularly in nominally indirect-gap bilayer WSe_2, application of tensile strain can result in a transition from an indirect to a direct bandgap[5]. However, studies on the effects of strain in TMDCs have been limited to mechanical bending of samples, and there has yet to be a technique which can directly realize built-in tensile and compressive strains.

Traditionally, strain engineering of semiconductors has been leveraged to tune the electronic band structure of high-performance devices, the most notable of which being to reduce intervalley scattering, increase mobility in Si transistors, and reduce the hole effective mass in III-V semiconductor lasers[6,7]. Growth on epitaxial substrates with controlled lattice constant mismatch has typically been utilized to establish built-in strain in three-dimensional semiconductors[8]. However, due to the relatively weak interaction between 2D materials and substrates, this established method of strain engineering is likely not applicable for strain-engineered growth of TMDCs. Therefore, a route towards development of large-area strained TMDCs on a practical substrate is highly desirable. Significant research efforts have been made to realize large area TMDCs, with the majority of efforts focusing on chemical vapor deposition (CVD)[9-10]. Interestingly, a number of studies employing CVD growth of 2D materials have reported apparent strain in the synthesized samples[11,12]. However, growth of high-quality 2D materials with controllable built-in strain has not been realized. Hence, properties that are difficult to probe via mechanical bending experiments such as low-temperature optical measurements and electrical performance have yet to be explored.

In this work, we demonstrate strain engineering of 2D materials directly via CVD growth while simultaneously maintaining high material quality, through utilizing the thermal coefficient of expansion (TCE) mismatch between the TMDC and the growth substrate. Electron diffraction of strained monolayers grown directly onto transmission electron microscopy (TEM) windows is utilized to unambiguously quantify strain. Using WSe_2 as a model system, we show that it is possible to obtain both tensile (of approximately 1%) and compressive (0.2%) strained 2D semiconductors over large areas on rigid substrates. Furthermore, in the WSe_2 model system we show indirect-to-direct optical transition in tensile strained WSe_2 bilayers as well as removal of dark exciton quenching in WSe_2 monolayers.

---

[4] Reproduced with permission from G.H. Ahn, M. Amani et al., Nature Communications, 8, 608, 2017. Copyright © [2017] Springer Nature.

Due to the high growth temperatures used to synthesize TMDCs, the thermal coefficient of expansion mismatch between the substrate and the 2D semiconductor can be utilized to control the strain in the synthesized 2D material, as shown schematically in Fig. 2-4-1. The theoretical upper limit for the strain, assuming no relaxation, can be calculated using the difference in lattice constant of the substrate and 2D semiconductor at room temperature and synthesis temperature:

$$\varepsilon(T_{\mathrm{g}}) = \frac{a_{\mathrm{2D}}(T_{\mathrm{g}}) - a_{\mathrm{2D}}(25°\mathrm{C})}{a_{\mathrm{2D}}(25°\mathrm{C})} - \frac{a_{\mathrm{Sub}}(T_{\mathrm{g}}) - a_{\mathrm{Sub}}(25°\mathrm{C})}{a_{\mathrm{Sub}}(25°\mathrm{C})} \tag{2-4-1}$$

where a_{2D} is the in-plane lattice constant for the 2D material being grown, a_{Sub} is the in-plane lattice constant of the substrate, and T_{g} is the growth temperature. (1) More generally, this can be calculated using the temperature dependent thermal expansion coefficient for the 2D material (α_{2D}) and substrate (α_{Sub}) according to:

$$\varepsilon(T_{\mathrm{g}}) = \int_{25°\mathrm{C}}^{T_{\mathrm{g}}} \alpha_{\mathrm{2D}}(T)\,\mathrm{d}T - \int_{25°\mathrm{C}}^{T_{\mathrm{g}}} \alpha_{\mathrm{Sub}}(T)\,\mathrm{d}T \tag{2-4-2}$$

In order to retain the strain generated from TCE-mismatch, the bonding between the 2D layer and the substrate must be sufficiently strong and corrugated to maintain the nonslip condition that transmits strain to the layer. While one expects strains of this magnitude to arise during epitaxial growth, it is difficult to see how a similar strain can arise for films bound by van der Waals forces to an amorphous substrate. Experimentally, the corrugation in the film must be large enough to retain the strain upon cooling. To estimate the magnitude of the corrugation necessary to sustain the strain, we analyzed a 2D Frenkel-Kontorova model[14]. This model suggests that atomic binding energy variations of as little as 14 meV over the range of the unit cell are capable of retaining strains of the magnitude of those observed experimentally. This variation is roughly 1% of a typical covalent bond strength, and very near to the typical strength of a van der Waals bond. Though a more detailed theory needs to be developed, especially to understand the surface chemistry immediately prior to growth to determine the nature of the bonding, this simple analysis suggests that thermal-expansion mismatch can strain a film, even in the case of weak binding between the film and the substrate. It should be noted that in a previous study, local heating of MoS_2 using a laser was used to generate strains of up to 0.2% arising from the TCE-mismatch of MoS_2 with the substrate[17]. Although this method does not generate built-in strains (strain is released once the laser is turned off), it suggests that the MoS_2-substrate bonding is strong enough to enable TCE-mismatched induced strain engineering [15].

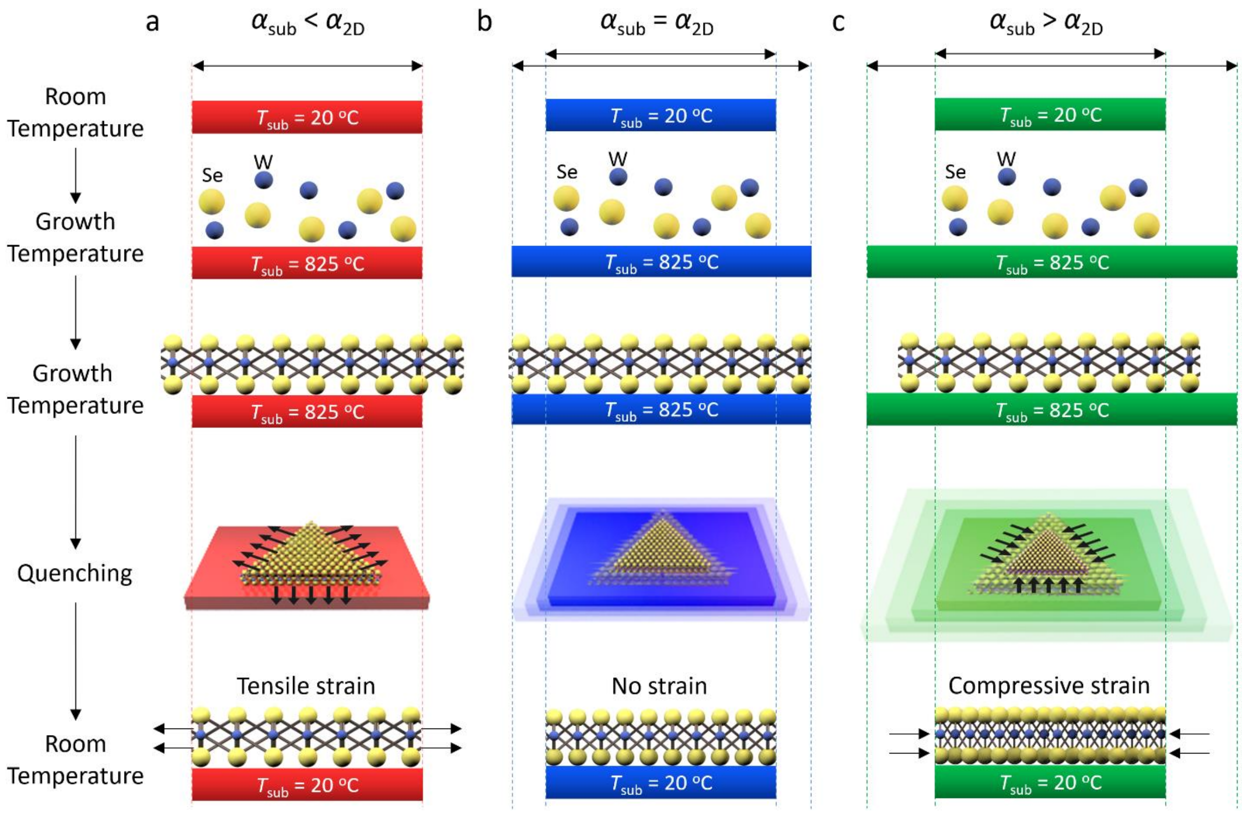

Fig. 2-4-1 | Strain-engineered growth of WSe$_2$ using TCE-mismatch. Schematic of the process through which strain is realized during the growth of 2D materials via mismatch in substrate and TMDC thermal expansion coefficient. (**a**) Tensile strain is achieved when the TCE of the substrate is less than that of the 2D material, (**b**) relaxed samples are achieved when the TCE of the substrate and TD material match, and (**c**) compressive strain is achieved when the TCE of the substrate is greater than that of the 2D material.

To demonstrate strain-engineered CVD growth of WSe_2, four substrates were chosen which have a range of TCEs. Fused silica and aluminum nitride (AlN) have a TCE of 0.55 ppm and 5.5 ppm, respectively, much smaller than that of WSe_2 (9.5±3.2 ppm), and would be expected to induce tensile strain[1,16-20]. In contrast, sapphire has a TCE closely matched to WSe_2 and would be expected to produce relaxed samples and strontium titanate (STO) with a TCE of 12 ppm should yield compressively strained samples[18,21,23]. The sample was rapidly quenched after growth to limit relaxation in the WSe_2. It is important to note that the rapid quenching process was found to be important in maintaining the presence of strain, and delay of the quenching step can result in partial relaxation of the 2D material.

To characterize the strain present in the as-grown material multiple characterization methods were utilized. First, electron diffraction was performed on WSe_2 as-grown on SiO_2 TEM grids and WSe_2 transferred to SiO_2 TEM grids. The resulting diffraction patterns are shown in Fig. 2-4-2 (a-c). In all TEM diffraction measurements on WSe_2, the camera length and lens aberrations of the imaging systems were calibrated using polycrystalline aluminum and single crystal aluminum calibration samples (Ted Pella), and the microscope lens settings were left constant for all subsequent measurements. By comparing the lattice constant extracted from the diffraction patterns of strained (as-grown) and unstrained (transferred) WSe_2, utilizing the center of mass for 75 diffraction spots from each pattern, we calculate that a 1.39±0.28% tensile strain is present in the as-grown sample. Error bars represent standard deviation in lattice constant value over 75 measured diffraction spots. Raman spectroscopy shown in Figure 2-4-2 (d), reveals a shift of E’ in plane Raman mode of 1.5±0.2 cm^{-1} between as-grown and transferred WSe_2. We note that the strain measured here is biaxial, not uniaxial, in contrast to mechanical bending studies and thus we do not observe splitting of the E’ mode. Therefore, the theoretically calculated value for the Grüneisen parameter of WSe_2 is used to calculate the expected peak shift according to: $\omega(\varepsilon) = \omega_0 + \chi\varepsilon$, which is consistent with the approximately 1% tensile strain measured via diffraction[23-25]. It should also be noted that after transfer the E’ mode shows no shift relative to samples prepared either by exfoliation or as-grown onto sapphire. High resolution Raman mapping was performed and is shown in Figure 2-4-2 (e) and (f) for WSe_2 crystals as-grown on fused silica and transferred to a new fused silica substrate respectively. We observe uniform shift throughout the full WSe_2 domain for both samples indicating that the strain is uniformly distributed within the sample on the scale of the Raman spot size.

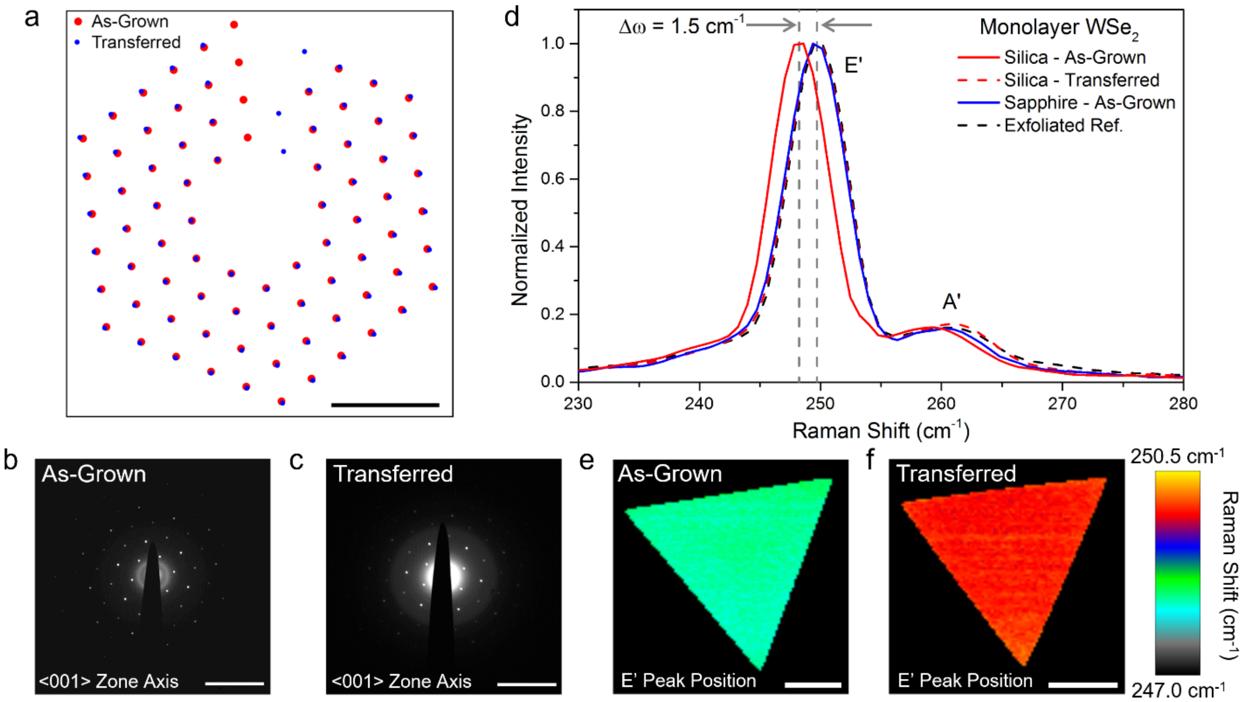

Fig. 2-4-2 | Transmission electron microscopy images and Raman spectroscopy of monolayer WSe_2. (**a**) Overlay of diffraction spots for as-grown and transferred monolayer WSe_2, showing a 1.39±0.28% strain in samples grown directly on the TEM membrane. Scale bar is 10 nm^{-1}. (**b**) Electron Diffraction patterns of tensile strained WSe_2 monolayer grown directly on an 8 nm SiO_2 TEM membrane and (**c**) a WSe_2 monolayer transferred to the same thickness membrane. Scale bar is 10 nm^{-1}. (**d**) Raman spectra of WSe_2 monolayers grown on various substrates. (**e** and **f**) Raman mapping of E’ peak position for a (**e**) tensile strained WSe_2 monolayer as-grown on fused silica and a (**f**) WSe_2 monolayer transferred to release strain; data is plotted using the same false color scheme. Scale bar is 20 μm.

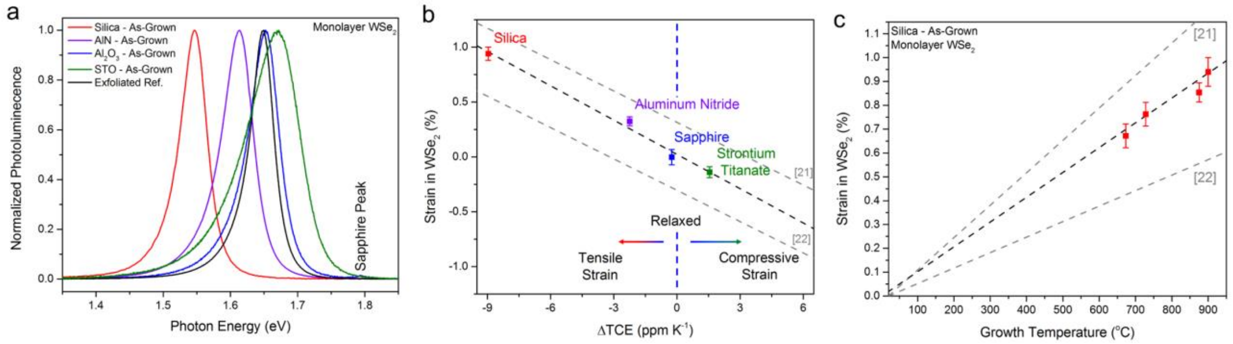

Fig. 2-4-3 | Strain engineering of 2D materials. (**a**) PL spectra for monolayer WSe_2 as-grown on substrates with a range of thermal coefficient of expansion mismatches. (**b**) Estimated strain which can be achieved in 2D materials based on the mismatch between the substrate and TMDC thermal coefficient of expansion; data points show measured strain for substrates with a range of thermal expansion coefficient mismatch; dashed grey lines are based on TCE values for WSe_2 obtained from references 21 and 22, dashed black line shows fit to experimental data. Error bars represent the standard deviation of strain measured over fifteen samples. (**c**) Estimated strain realized in WSe_2 as-grown on fused silica at various substrate temperatures; dashed grey lines are based on TCE values for WSe_2 obtained from references 21 and 22, dashed black line shows fit to experimental data. Error bars represent the standard deviation of strain, measured over fifteen samples.

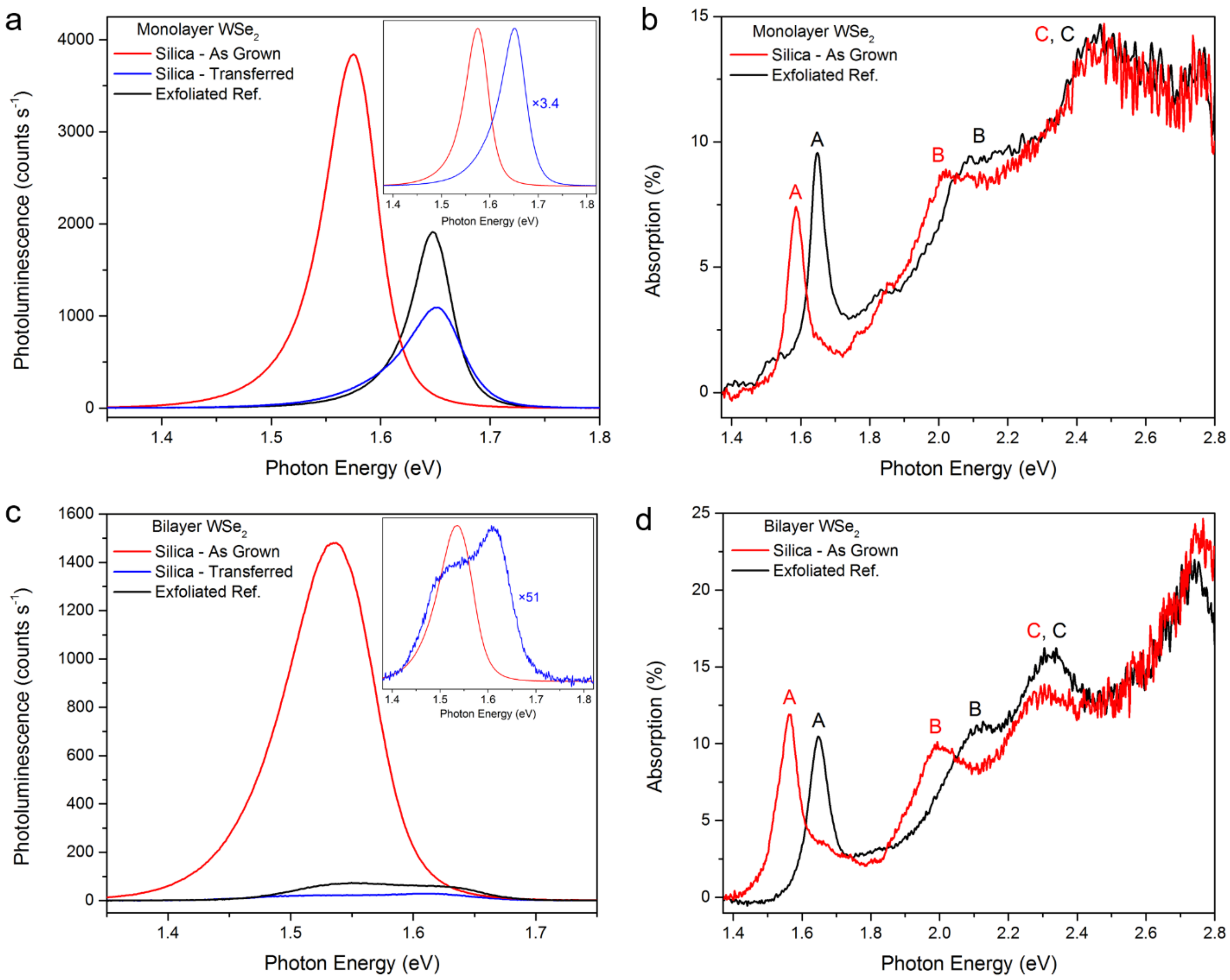

Fig. 2-4-4 | Photoluminescence of strain-engineered monolayer and bilayer WSe$_2$. (**a**) Photoluminescence spectra of as-grown and transferred monolayer WSe$_2$ as well as exfoliated reference. Inset shows normalized spectra. (**b**) absorption spectra of as-grown and exfoliated monolayer WSe$_2$. (**c**) Photoluminescence spectra of as-grown and transferred bilayer WSe$_2$ as well as exfoliated reference; inset shows normalized PL spectra of as-grown and transferred bilayer WSe$_2$. (**d**) Absorption spectra of as-grown and exfoliated bilayer WSe$_2$.

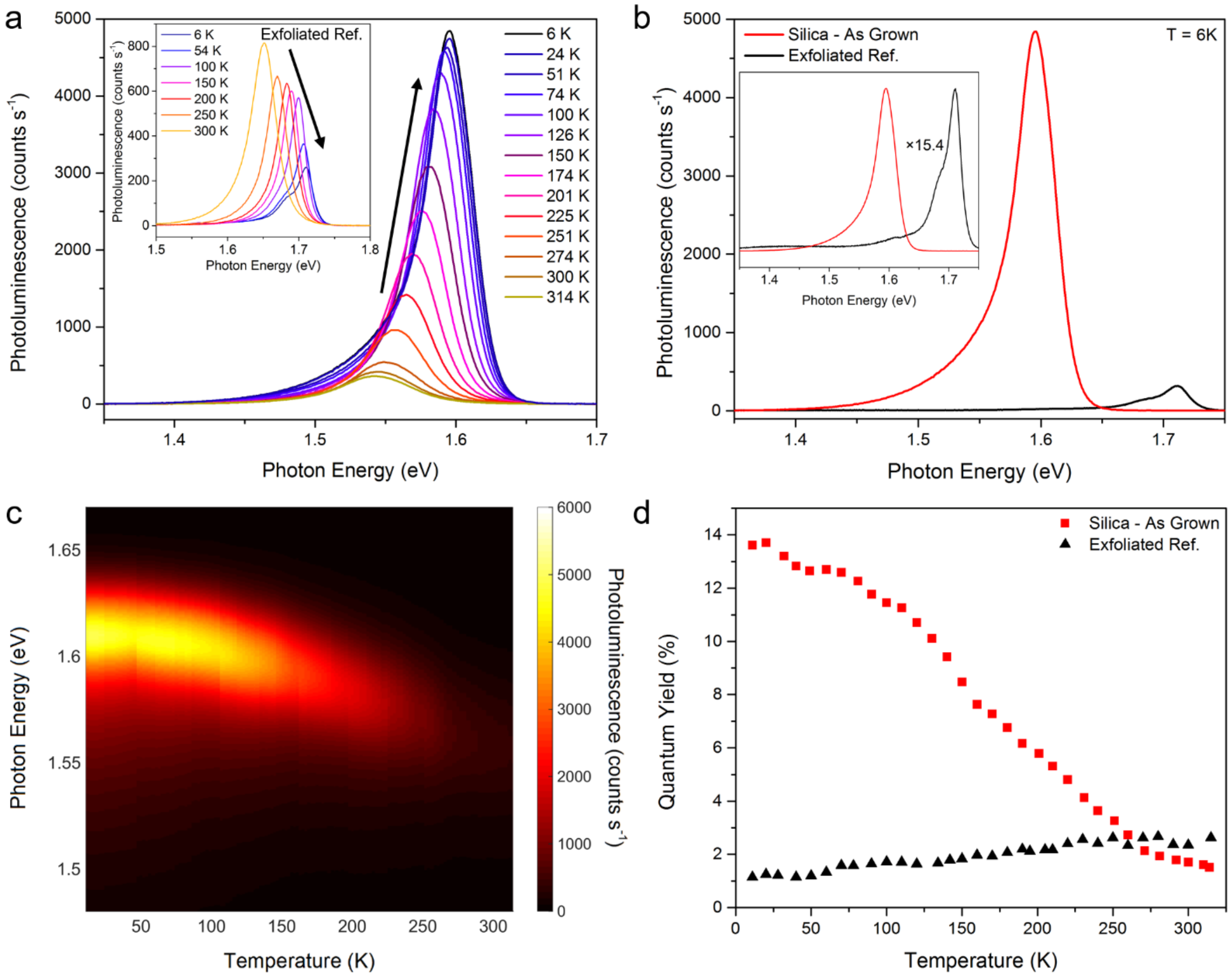

Fig. 2-4-5 | Low-temperature photoluminescence of strain-engineered monolayer WSe_2. (**a**) Temperature dependent photoluminescence spectra of as-grown monolayer WSe_2 (tensile strained), inset shows the same measurement on an exfoliated monolayer WSe_2 sample. (**b**) Photoluminescence spectra of as-grown (tensile strained) WSe_2 and exfoliated WSe_2 measured at 6K, inset shows normalized spectra. (**c**) Two dimensional plots of photoluminescence spectra and intensity of as-grown (tensile strained) monolayer WSe_2. (**d**) Temperature dependence of the PL QY for as-grown (tensile strained), and exfoliated WSe_2 as a function of temperature.

PL measurements were employed to measure the bandgap as a function of strain. Figure 2-4-3 (a) shows photoluminescence spectra of samples grown on all substrates investigated in this work as well as an exfoliated reference. There is a large spectral shift of 120 meV between samples grown on fused silica with near zero TCE and STO which has the highest TCE of all substrates investigated in this work. Figure 2-4-3 (b) shows the estimated strain from photoluminescence peak shift as a function of predicted strain in WSe_2, as a function of lattice mismatch between the substrate and TMDC lattice constant. Strain values are determined from the experimental measured PL peak position (error bars are calculated from variation in peak position and spectrometer error from measurements on 15 different crystals) and theoretically calculated bandgap as a function of strain extracted from references 1 and 25. It is important to note that we utilized the difference in peak position relative to an unstrained sample, to eliminate effects from absolute bandgap error from theoretical calculations. We performed an analysis of the expected strain due lattice parameter misfit to rule out the influence of epitaxial strain between the substrate and WSe_2. From this calculation, the expected strain from lattice mismatch shows the opposite trend of what we observe experimentally. We find that our experimentally realized strain per ΔTCE of -0.10±0.01 % per ppm K^{-1}) is in excellent agreement with the theoretical value of -0.09 % per ppm K^{-1}. In order to verify that the substrate does not affect the photoluminescence peak shape or position of monolayer WSe_2, samples were transferred to the four substrates used in this study and no shift of the PL peak was observed. The impact of growth temperature to tune the strain was also studied using fused silica as the substrate. Figure 2-4-3 (c) shows the tensile strain in monolayer WSe_2 grown at different temperatures, estimated using PL peak position. We can tune the strain from 0.94±0.06% to 0.67±0.05% as the growth temperature is changed from 900°C to 673°C.

Calibrated PL measurements were used to provide a gauge of material quality. We find that strained WSe_2 monolayers as-grown on fused silica show comparable PL intensity to exfoliated WSe_2, demonstrating that strain engineering of 2D materials can be achieved without compromising material performance. Specifically, as-exfoliated samples show a typical quantum (QY) yield of 2.3±0.4%, while samples grown on fused silica show a typical QY of 1.9±0.6%. Upon transfer, the strain within the as-grown material is released, and its emission peak shifts to 1.65 eV, closely matching that of exfoliated samples, as shown in Fig. 2-4-4 (a). In addition to emission, the absorption spectrum of as-grown monolayer was measured and is shown in Fig. 2-4-4 (b). The absorption spectra clearly show that A and B exciton resonances are red-shifted with presence of tensile strain, and are consistent with the observed shift in the emission. Interestingly, the absorption of the C exciton peak shows no shift between the as-grown and exfoliated samples, which is consistent with previously reported mechanical bending experiments on exfoliated monolayers, although it should be noted that in these experiments the strain was uniaxial[28].

More interestingly, it has been previously demonstrated using bending experiments that under the application of a uniaxial strain of approximately 1.5% bilayer WSe_2 undergoes an indirect-to-direct bandgap transition[5]. This effect is caused by an increase in the energy level of the indirect valley at the Σ-point as well as a corresponding decrease in the energy level of the direct valley at the K point[5]. While it is important to note these results are obtained under uniaxial strain, similar trends between uniaxial and biaxial strain have been observed in theoretical studies on other 2D material systems[27]. Figure 2-4-4 (c) depicts the PL spectra of as-grown, exfoliated and transferred bilayer WSe_2. In the as-grown strained bilayer, we observe a single sharp PL peak as oppose to a broader spectrum corresponding to emission from both the indirect and direct bandgaps, as observed in the unstrained exfoliated and transferred samples. Moreover, the intensity of PL is reduced by approximately fifty times upon transfer and resultant release of tensile strain as shown in Fig. 2-4-4 (c). This phenomenon can possibly be attributed to the optical transition from indirect-to-direct in bilayer WSe_2 in the presence of tensile strain. This is in a good agreement of previous reports on indirect-to-direct optical transition of WSe_2 through bending experiments, although these previous studies utilized uniaxial strain[5]. The normalized PL spectra for bilayer WSe_2 grown on fused silica after transfer, as well as unstrained samples grown on sapphire and prepared by exfoliation show very similar spectral shape. Absorption of WSe_2 bilayer samples was also measured and is shown in Fig. 2-4-4 (d).

To further characterize WSe_2 monolayers, we performed low temperature PL measurements. Numerous studies have experimentally observed that the photoluminescence of monolayer WSe_2 is quenched at reduced temperatures. This behavior is unusual for a direct bandgap semiconductor and has been attributed to the formation of dark excitons with an energy level approximately 30 meV below the bright state[30,31]. It has been hypothesized that at low temperatures the bright exciton is allowed to relax to the lower energy level resulting in a reduction of the PL QY. Conversely, both theoretical and experimental studies have suggested that un-strained monolayer WSe_2 is an indirect-gap semiconductor, with a small ($< 3kT$) energy difference between the indirect and direct gaps[30,31]. Upon cooling of exfoliated monolayer WSe_2 samples we observe similar results to what has been previously reported as shown in the inset of Fig. 2-4-5 (a), that is a reduction in PL emission at low temperatures. However, for the case of tensile strained monolayer WSe_2 as-grown on fused silica we observe the opposite trend (Fig. 2-4-5). As the temperature is reduced from 300K to 6K the PL intensity increases by over an order of magnitude, resulting in a final PL QY of 14% as shown in Fig. 2-4-5 (d). The nature of the physical mechanism for the dramatic difference in temperature dependent behavior can be directly attributed to band structure modification due to the presence of strain. However, it remains unclear if this is due to an indirect-to-direct bandgap transition or an increase in the energy level of the dark state.

In summary, we have demonstrated controlled and stable strain engineering of 2D materials by growth, realized through thermal coefficient of expansion mismatch between the substrate and 2D material. The demonstrated strain engineering allows for dramatic modulation of the physical properties of 2D materials. Using WSe_2 as a model system, we have achieved a strain induced indirect-to-direct optical transition in directly grown WSe_2 bilayer, resulting in an amplification of the PL intensity by over fifty times. We have also shown tunable PL emission of WSe_2 monolayer, while maintaining its high performance.

Notably, in the monolayer case under tensile strain, we observed increasing luminescence at reduced temperatures, in stark contrast with what has been reported in the un-strained exfoliated material, suggesting that strain can be utilized to brighten the dark exciton. This practical route for the direct realization of strain engineering in 2D materials can allow for the characterization of device properties as a function of strain as well as enable optical measurements that are not accessible to samples strained by physical bending or stretching. Our work depicts that biaxial strains of 1% tensile to 0.2% compressive can be obtained by using readily achievable differences in the thermal expansion coefficients by choosing an appropriate growth substrate. By expanding upon this method, it may be possible to obtain uniaxial strain via growth on substrates with anisotropic thermal expansion coefficients or obtain significantly higher strain values via growth on piezoelectric substrates[34, 35].

References for Section 2-4

1. Chang, C.-H., Fan, X., Lin, S.-H., Kuo, J.-L. Orbital analysis of electronic structure and phonon dispersion in MoS_2, $MoSe_2$, WS_2, and WSe_2 monolayers under strain. *Phys. Rev. B* **88**, 195420 (2013).
2. Shi, H.; Pan, H.; Zhang, Y.-W., Yakobson, B. I. Quasiparticle band structures and optical properties of strained monolayer MoS_2 and WS_2. *Phys. Rev. B* **87**, 155304 (2013).
3. Duerloo, K.-A. N., Li, Y. Reed, E. J. Structural phase transitions in two-dimensional Mo- and W-dichalcogenide monolayers. *Nat. Comm.* **5** 4214 (2014).
4. Zhu, H. *et. al*. Observation of piezoelectricity in free-standing monolayer MoS_2. *Nat. Nano.* **10**, 151-155 (2015).
5. Desai, S. B. *et. al*. Strain-induced indirect to direct bandgap transition in multilayer WSe_2. *Nano Lett.* **14** (8), 4592-4597 (2014).
6. Thompson, S. E. *et. al*. 90-nm logic technology featuring strained-silicon. *IEEE Trans. Electron Dev.* **5** (11), 1790-1797 (2004).
7. Yablonovitch, E., Kane, E. O. Band structure engineering of semiconductor lasers for optical communications. *J. of Lightwave Technol.* **6** (8), 1292-1299 (1988).
8. Alamo, J. A. Nanometre-scale electronics with III-V compound semiconductors. *Nature* **479** 317-323 (2011).
9. Zande, A. M. *et. al*. Grains and grain boundaries in highly crystalline monolayer molybdenum disulphide. *Nat. Mat.* **12**, 554-561 (2013).
10. Yu, J., Li, J., Zhang, W., Chang, H. Synthesis of high quality two-dimensional materials via chemical vapor deposition. *Chem. Sci.* **6**, 6705-6716 (2015).
11. Kang, K. *et. al*. High-mobility three-atom-thick semiconducting films with wafer-scale homogeneity. *Nature* **520**, 656-660 (2015).
12. Liu, Z. *et. al*. Strain and structure heterogeneity in MoS_2 atomic layers grown by chemical vapour deposition. *Nat. Comms.* **5**, 5246 (2014).
13. Amani, M. *et. al*. Growth-substrate induced performance degradation in chemically synthesized monolayer MoS_2 field effect transistors. *Appl. Phys. Lett.* **104**, 203506 (2014).
14. Braun, O. M., Kivshar, Y. *The Frenkel-Kontorova Model- Concepts, Method, and Applications*. Springer, Berlin (2004).
15. Plechinger, G. *et. al.* Control of biaxial strain in single-layer molybdenite using local thermal expansion of the substrate. *2D Mater.* **2** (1), 015006 (2015).
16. Roy, R., Agrawal, D. K., McKinstry, H. A. Very low thermal expansion coefficient materials. *Annu. Rev. Mater. Sci.* **19**, 59-81 (1989).
17. Slack, G. A., Bartram, S. F. Thermal expansion of some diamondlike crystals. *J. Appl. Phsy.* **46** (1), 89-98 (1975).
18. Reeber, R. R., Wang, K. Lattice parameters and thermal expansion of important semiconductors and their substrates. *Mat. Res. Soc. Symp.* **662**, T6.35.1-6 (2000).
19. El-Mahalawy, S. H., Evans, B. L. The thermal expansion of 2H-MoS_2, 2H-$MoSe_2$, and 2H-WSe_2 between 20 and 800°C. *J. Appl. Cryst.* **9**, 403-406 (1976).
20. Ding, Y.; Xiao, B. Thermal expansion tensors, Grüneisen parameters and photon velocities of bulk MT_2 (M = W and Mo; T = S and Se) from first principle calculations. *RSC Adv.* **5**, 18391-18400 (2015).
21. Yim, W. M., Paff, R. J. Thermal expansion of AlN, sapphire, and silicon. *J. Appl. Phys.* **45** (3), 1456-1457

(1974).
22. Ligny, D., Richet, P. High temperature heat capacity and thermal expansion of $SrTiO_3$ and $SrZrO_3$ perovskites. *Phys. Rev. B* **53** (6), 3013-3022 (1996).
23. Late, D. J.; Shirodkar, S. N.; Waghmare, U. V.; Dravid, V. P.; Rao, C. N. R. Thermal expansion, anharmonicity and temperature dependent Raman spectra of single- and few-layer $MoSe_2$ and WSe_2. *Chem. Phys. Chem.* **15**, 1592-1598 (2014).
24. Sahin, H. *et. al*. Anomalous Raman spectra and thickness-dependent electronic properties of WSe_2. *Phys. Rev. B* **87**, 165409 (2013).
25. Johari, P.; Shenoy, V. B. Tuning the electronic properties of semiconducting transition metal dichalcogenides by applying mechanical strains. *ACS Nano*. **6** (6), 5449-5456 (2012).
26. Schmidt, R. *et. al.* Reversible uniaxial strain tuning in atomically thin WSe_2. *2D Mat.* **3**, 021011 (2016).
27. Dong, L., Namburu, R. R., O'Regan, T. P., Dubey, M., Dongare, A. M. Theoretical study on strain-induced variation in electronic properties of MoS_2. *J. Mat. Sci.* **49** (19), 6762-6771 (2014).
28. Zhang, X.-X. *et. al.* Experimental evidence for dark excitons in monolayer WSe_2. *Phys. Rev. B* **115**, 257403 (2015).
29. Ye, Z. *et. al*. Probing excitonic dark states in single-layer tungsten disulphide. *Nature* **513**, 214-218 (2014).
30. Ramasubramaniam, A. Large excitonic effects in monolayers of molybdenum and tungsten dichalcogenides. *Phys. Rev. B* **86**, 115409 (2012).
31. Zhang, C. *et. al. Nano Lett.* Probing critical point energies of transition metal dichalcogenides: surprising indirect gap of single layer WSe_2. *Nano Lett.* **15**, 6494-6500 (2015).
32. Li, J., Bi, W., Ki, W., Huang, X., Reddy, S. Nanostructured crystals: Unique hybrid semiconductors exhibiting nearly zero and tunable uniaxial thermal expansion behavior. *J. Am. Chem. Soc.* **129**, 14140-14141 (2007).
33. Chaix-Pluchery, O., Chenevier, B., Robles, J. J. Anisotropy of thermal expansion in $YAlO_3$ and $NdGaO_3$. *Appl. Phys. Lett.* **86** (25), 251911 (2005).
34. Li, S. *et. al*. Halide-assisted atmospheric pressure growth of large area WSe_2 and WS_2 monolayer crystals. *Appl. Matt. Today* **1** (1), 60-66 (2015).
35. Chen, J. *et. al*. Chemical vapor deposition of large-sized hexagonal WSe_2 crystals on dielectric substrates. *Adv. Matter.* **27** (42), 6722-6727 (2015).
36. Amani, M. *et. al*. Recombination kinetics and effects of superacid treatment in sulfur- and selenium based transition metal dichalcogenides. *Nano Lett.* **16** (4), 2786-2791 (2016).

2.5 – Experimental and theoretical methods

Calibrated Luminescence Efficiency Measurements

The PL (photoluminescence) data presented here was obtained with a custom built micro-PL system using the 514.5 nm line of an Ar ion laser (Lexel 95) for excitation. The laser power was adjusted using various neutral density (ND) filters. An overview of the configuration used for measurement and the calibration of the instrument is shown in Fig. 2-5-1. The power of the excitation beam was measured during the duration of the measurement (130 times greater than the incident power on the sample) and was calibrated at high illumination intensity using a photodiode power meter (ThorLabs S120C). However, in order to accurately measure low (< 100 pW) excitation power, lock-in detection from the output of a calibrated photodiode was used (noise equivalent power of 1.7×10^{-13} WHz$^{-1/2}$). These values were carefully cross calibrated before all measurements at multiple laser powers to ensure the incident power was accurately measured. The laser beam was focused onto the sample using a 60× ultra-long working distance (ULWD) objective lens (NA = 0.7) which resulted in a measured spot size of 3.8 μm^2. PL was collected by the same microscope objective, passed through a 550 nm dielectric longpass filter to remove the excitation signal, dispersed by an f = 340 mm spectrometer with either a 150 g/mm or 600 g/mm grating, and detected by a Si CCD camera (Andor iDus BEX2-DD). The CCD background was obtaining by collecting a spectrum before each measurement at the same integration time without the laser on and was subsequently subtracted from the PL spectrum. We calculated the error in the integrated counts using:

$$\delta N = \frac{N}{\sqrt{N + n_{pix}\left(1 + \frac{n_{pix}}{n_b}\right)N_{RO}^2}} \tag{2-5-1}$$

where δN is signal to noise ratio, N is the total PL counts, n_{pix} is the number of pixels, n_b is the uncertainty from the background estimation, and N_{RO} is the readout noise.

Prior to measuring, the entrance slit of the spectrometer was opened until the maximum number of PL counts was obtained. All measurements were performed using linearly polarized excitation, negating any effects from intervalley scattering by maintaining equivalent population in two valleys.

The spectrometer wavelength was calibrated using the atomic emission peaks from Ar and Kr lamps (Newport). The systems' relative sensitivity versus wavelength (instrument function) was evaluated by measuring the response of a virtual Lambertian black body light source created under the objective via illumination from a temperature stabilized lamp (ThorLabs SLS201) imaged onto a diffuse reflector (> 1 cm thick spectralon) surface. The system efficiency was calibrated immediately after each measurement by removing the 550 nm long pass filter and measuring the response of the excitation laser focused on the diffuse reflector (> 1 cm thick spectralon). This is a reasonable simulation of the PL source, as the emission profile of 2D materials has recently been experimentally measured and is approximately Lambertian. The pump-power dependence is converted to external quantum efficiency (EQE) by dividing by the absorbed pump power (P), i.e.: $QY = PL / P$.

Two independent approaches were used to verify the system calibration. First, to remove the possibility of errors due to the confocal nature of the spectral measurement, which is strongly dependent on the objective focus and the solid angle covered by the collection cone, we cross-calibrated using a calibrated silicon photodiode which was able to view a fraction of the luminescence but is independent of microscope optical path as depicted in Fig. 2-5-1; due to the relatively low sensitivity of the photodiode, these measurements were only performed at higher excitation power (> 10 W/cm^2). Calibrations were also performed using a sample with a known QY close to 100% (rhodamine 6G in methanol) using a procedure which has previously been used to measure the QY of 2D materials. These three methods were found to be in good agreement with each other (< 15% error). For measurements taken against the spectralon reference the percent of generated photons which are able to escape from the sample was calculated using $1/4n^2$, where n is the refractive index of the medium, this was used to determine the QY from the measured EQE.

The error in the QY measurements was calculated from the uncertainty in the laser power measurement, CCD signal, and the absorption coefficient. The overall error bounds for the measurement are given by:

$$\delta QY = QY\sqrt{\left(\frac{\delta P}{N}\right)^2 + \left(\frac{\delta N}{N}\right)^2 + \left(\frac{\delta \alpha}{N}\right)^2} \qquad (2\text{-}5\text{-}2)$$

where, P and δP is the measured laser power and the corresponding uncertainty, N and δN is the measured CCD counts and corresponding uncertainty, and α and $\delta\alpha$ is the absorption coefficient at 514.5 nm and the corresponding uncertainty.

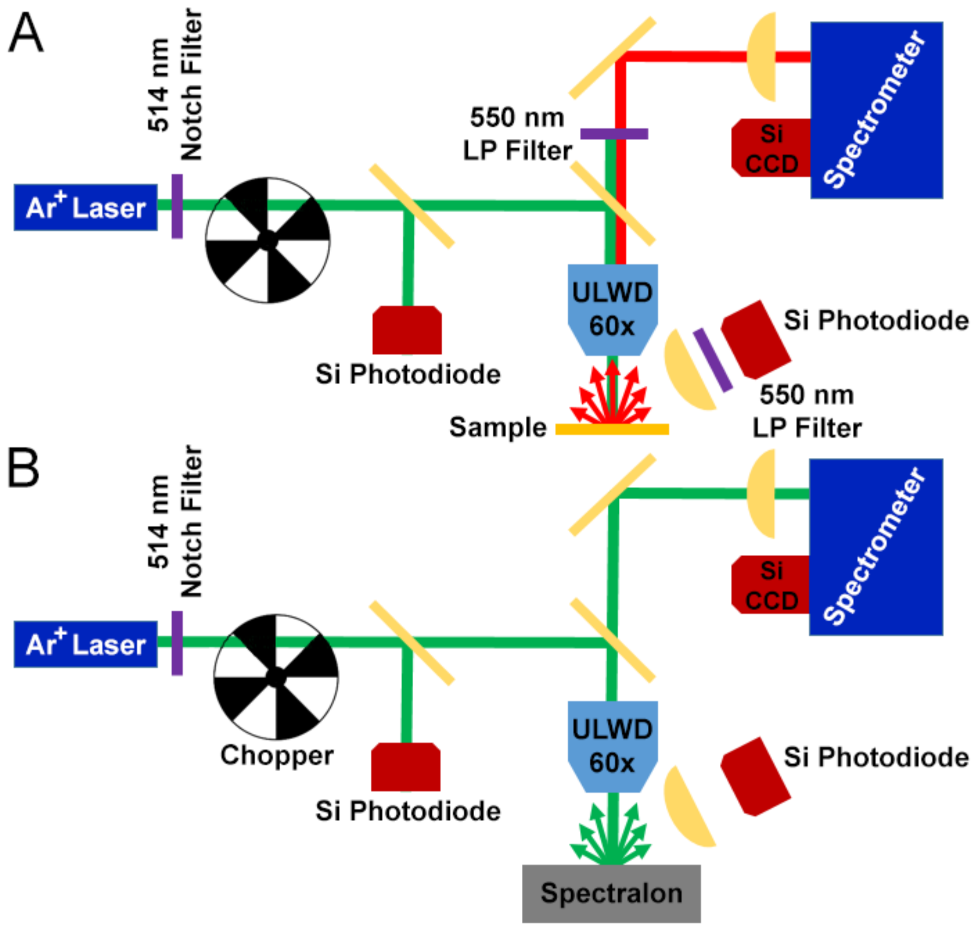

Fig. 2-5-1. Schematic of the optical setup used to measure external quantum efficiency. (**A**) Optical setup used to measure PL spectrum as well as calibration via a R6G film. (**B**) Optical setup used for calibrating the absolute collection efficiency via a near ideal diffuse reflector.

Micro-Absorption and Reflection Measurements

Two sets of absorption/reflection measurements were performed for monolayer MoS_2 on quartz substrates both before and after treatment. First the absolute absorption at the PL excitation wavelength (514.5 nm) was measured using lock-in detection; a schematic of the setup is shown in Fig. 2-5-2A. The extracted absorption value of 7.53±0.23% is used for the QY calculations. Illumination from a supercontinuum laser source (Fianium WhiteLase SC-400) was used to obtain an absorption spectrum (total incident power << 1 W/cm^2). Either the reflected or transmitted light was guided to a spectrometer to analyze the full spectrum. A schematic of the setup is shown in Fig. 2-5-2B. In both cases the light was focused on the sample using a 50× objective, the reflected light was collected via the same objective and the transmitted light was collected by a 20× objective. The system was calibrated using quartz and silver as reference transmission and reflectance standards. The reported generation rates (steady-state measurements) and initial carrier densities (time-resolved measurements) are calculated from the number of incident photons per unit area and the absorption.

Other Optical Methods

All measurements were taken starting from the lowest laser power and were stopped at a maximum power (10 μW) approximately one order of magnitude lower than what was found to cause sample degradation. The TFSI treated samples in particular were found to be sensitive to high illumination powers. An important consideration for MoS_2 is that the thickness of the sample (0.7 nm) is significantly less than the emission wavelength, thus the refractive index of the surrounding medium will determine the optical mode density and influence the measured lifetime according to the Füchtbauer-Ladenburg equation:

$$\frac{1}{\tau_r} = 8\pi n^2 c \int \frac{\sigma_{em}(\lambda)}{\lambda^4} d\lambda \qquad \text{(2-5-3)}$$

which is an extension of the Einstein *A* and *B* coefficients where τ_r is the radiative lifetime, n is the refractive index of the medium, c is the speed of light in vacuum, σ_{em} is the emission cross-section, and λ is the wavelength of spontaneous emission. Therefore, we utilized quartz substrates for all measurements where an absolute QY and/or radiative lifetime is reported. It is important to note that in the case of samples with low luminescence (< 10% QY) the measured lifetime will be dominated by the non-radiative lifetime (τ_{nr}) and therefore approximately equal to τ_{nr}, ergo this effect will not play a dominant role.

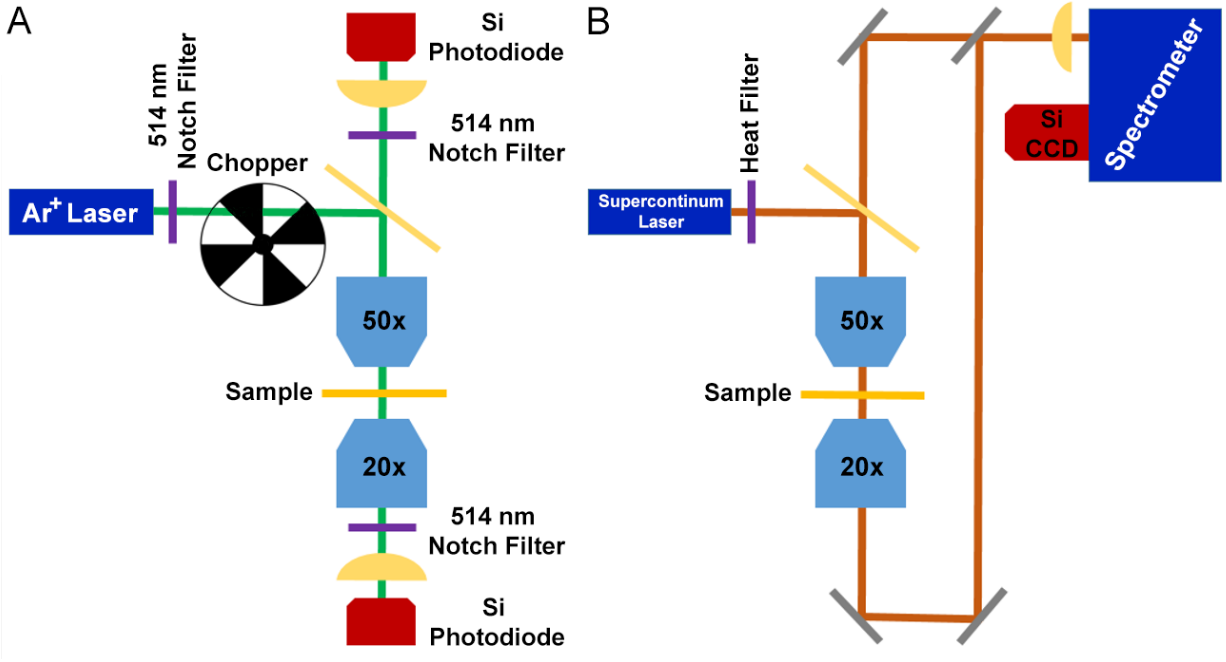

Fig. 2-5-3. Schematic of the optical setup used to measure absorption. (**A**) Optical setup used to measure the absorption at 514.5 nm. (**B**) System configuration used to measure the full absorption spectrum via separately measuring the transmitted and reflected light from a white laser source.

Raman spectra was measured with a triple spectrometer configured in subtractive mode with a 2400 g/mm grating in the final stage and using the 514.5 nm line of the Ar ion laser as the excitation source. PL imaging was performed using a florescence microscopy setup with a 470 nm LED excitation source (operating at 200 mA) and a CCD detector (Andor Luca). The background counts were subtracted from the PL images and cosmic rays were removed using a software filter; the images were then normalized by integration time. High resolution PL mapping was performed using a WITec Alpha 300RA equipped with a piezo electric scanning stage. The sample was excited using the 532 nm line of a frequency-doubled Nd:YAG laser as the excitation source and focused on the sample using a 100× objective.

For time-resolved photoluminescence performed on treated MoS_2, the sample was excited pulsed light at 5 MHz generated by a supercontinuum laser source (Fianium WhiteLase SC-400) (20-30 ps pulse width). A wavelength of 514 nm (2 nm measured bandwidth) was selected with a monochrometer and was subsequently sent through a bandpass filter to remove any stray leakage light. The excitation was linearly polarized and focused on the sample with a 60× objective. The signal was detected with a low dark count avalanche photodiode operating in single photon counting mode (IDQuantiqe) and analyzed using a time correlated single photon counting module (TCSPC) (Becker-Hickl GmbH). The instrument response was 110 ps and the data was fit by deconvolution from the instrument response to a single exponential decay; the reported errors are the uncertainty from fitting. Due to the extremely short lifetime of as-exfoliated MoS_2 monolayers, time-resolved measurements were also performed via a synchroscan streak camera (Hamamatsu) with an overall time resolution of 2 picoseconds as shown in Fig. 2-5-3. The sample was excited by 560 nm light generated by an optical parametric oscillator (Spectra Physics, Inspire HF 100) pumped by a mode-locked Ti:sapphire oscillator. The laser pulse width was 200 femtoseconds, and the repetition rate was 80 MHz. The linearly polarized excitation light was guided to an inverted microscope and focused on the sample by a 50× objective. The emission signal was detected in the back scattering configuration using emission filters to block the excitation laser prior to collection.

The band edge tail $D(v)$ (also known as the Urbach tail) can be related to the photon emission rate per unit energy at steady-state conditions by the van Roosbroeck-Schockley equation:

$$D(\nu) \propto \frac{I(\nu)\left(e^{h\nu/kT} - 1\right)}{n_r^2 \nu^2} \qquad \text{(2-5-4)}$$

where, h is the Plank constant, k is the Boltzmann constant, T is temperature, and n_r is the real part of the refractive index. From this we can extract the Urbach parameter, E_0 (characteristic width of the absorption edge) using:

$$D(h\nu) = D_0 e^{(h\nu - E_g)/E_0} \tag{2-5-5}$$

where E_g is the bandgap.

Sample Preparation and Solution Treatment Procedure

MoS_2 (SPI Supplies), WS_2, WSe_2, and $MoSe_2$ (HQ Graphene) was mechanically exfoliated on either quartz for quantum yield (QY), lifetime, and absorption measurements or on SiO_2/Si substrates for imaging, electrical, and Raman characterization. Monolayers were identified by optical contrast and atomic force microscopy (AFM). The treatment procedure with bis(trifluoromethane)sulfonimide (TFSI) is as follows: 20 mg of TFSI, (Sigma-Aldrich) was dissolved in 10 ml of 1,2-dichloroethane (DCE) (Sigma-Aldrich) to make a 2 mg/ml solution. The solution is further diluted with 1,2-dichlorobenzene (DCB) (Sigma-Aldrich) or DCE to make a 0.2 mg/ml TFSI solution. The exfoliated sample was then immersed in the 0.2 mg/ml solution in a tightly closed vial for 10 min on a hotplate (100°C). The sample was removed and blow dried with nitrogen without rinsing and subsequently annealed at 100°C for 5 min. Depending on the initial optical quality of the sample, the treatment sometimes needed to be repeated to obtain > 95% QY. As a control experiment we studied N-phenyl-bis(trifluoromethane)sulfonimide (Ph-TFSI) which was prepared using the following procedure: 25 mg of Ph-TFSI (Sigma-Aldrich) was dissolved in 10 ml of DCE (Sigma-Aldrich) to make a 2.5 mg/ml solution. The solution is further diluted with DCB (Sigma-Aldrich) to a 0.25 mg/ml solution. The exfoliated sample was immersed in the 0.25 mg/ml solution in a tightly capped vial for 10 min on a hotplate (100 °C). The sample was removed and blow dried with nitrogen without rinsing and subsequently annealed at 100°C for 5 min. Prior to treatment, samples were annealed in forming gas (5% H_2, 95% N_2) at 300°C for 3 hours; while this does not significantly affect the QY after treatment it was found to significantly improve the long term stability of the sample. It is important to note that there is a large variation in the QY of as-exfoliated monolayer samples (with peak QY ranging from 0.1% to 1%). All data taken on as-exfoliated monolayers in this manuscript are representative of samples with a peak QY close to 1%.

MoS_2 Film Growth

Monolayer MoS_2 triangular domains and films were grown, either on quartz or SiO_2/Si substrates, by atmospheric pressure CVD. Prior to growth, the substrates were cleaned in a piranha for 15 minutes followed by a 5 minute soak in dionized (DI) water, acetone, and isopropyl alcohol. Afterwards, 40 μL of perylene-3,4,9,10-tetracarboxylic acid tetrapotassium salt (PTAS) was spin coated on each sample as a seeding layer for the growth. A schematic of the CVD furnace used to grow the films is shown in figure 2-3-1a. The sulfur precursor (15-33 mg) was loaded in an alumina boat and placed in a region outside of the furnace, where the temperature could be controlled by a heating tape. The sulfur precursor temperature was varied from 200ºC-300ºC to grow the various triangular domains and films investigated in this study. MoO_3 powder (18-20 mg) was added to a second alumina boat and four PTAS-coated substrates were placed on top of the alumina boat facing up. This boat was loaded into the center of the furnace for growth. The growth process was performed in a tube furnace at a sample temperature of 700ºC for growth involving SiO_2/Si substrates and 750ºC for quartz. The growth was carried out for 10 minutes, during which argon (5 sccm) was used as a carrier gas. An argon flow rate of 200 sccm was used before the growth to purge the tube and after to quench the growth process.

The resulting MoS_2 was transferred from the original growth substrate to a quartz substrate using poly(methyl methacrylate) (PMMA) mediated transfer. A film of 495 PMMA A11 was spun onto the samples and was allowed to dry in air overnight. The PMMA at the edges of the samples was then removed and the samples were placed in diluted hydrofluoric acid (10:1) to etch the oxide. After the substrate was either etched or released (the total etch time varied from 1-10 hours), the PMMA/MoS_2 film was placed in several subsequent water baths, and was ultimately transferred to the final quartz substrate. The film was allowed to dry for 12 hours, and then the PMMA was removed in hot acetone and the substrate was rinsed with isopropyl alcohol.

WSe_2 Film Growth

WSe_2 was grown on several substrates with varying thermal expansion coefficients using chemical vapor deposition. Substrates were first cleaned by sonication in acetone and isopropyl alcohol for 10 minutes. The growth was carried out using a two-heating zone furnace (DaePoong Industry, 50602). The cleaned substrates were loaded into the downstream zone, and a ceramic boat containing mixture of WO_3 and KBr was then placed next to the substrates. KBr was mixed with WO_3 at a ratio of 1:2, with the KBr acting as a promoter for the growth. This is similar to methods described in reference 32; however, we found that several salts can be used, and play a significant role in determining the ultimate sample morphology. A ceramic boat containing 500 mg Se powder was placed in the center of the upstream zone. After loading, the quartz tube was evacuated, and Ar was introduced at 60 sccm resulting in a pressure of 2.6 Torr. The temperature of upstream zone was then ramped to 100°C, and the downstream furnace was subsequently ramped to a setpoint of 825°C. The set point of the upstream zone was adjusted such that the residual heat from the downstream zone results in vaporization of Se. Once the temperature of downstream furnace was stabilized, hydrogen was introduced at a flow rate of 40 sccm (total pressure of 3 Torr). This initiates the growth as the presence of hydrogen is required to decompose and vaporize WO_x[33]. The typical growth time used was 15 minutes. Once the growth is complete, hydrogen flow was stopped, and the furnace was opened to rapidly cool the sample. Specific growth conditions were tuned to optimize the photoluminescence quantum yield of the as-grown samples and to either promote growth of bilayer or monolayer domains. It should be noted that for growths where the substrate temperature was varied the WO_3/KBr boat was placed in the center of the first heating zone and the Se boat was placed at the edge of the first heating zone. The substrates were placed in the center of the second heating zone. The position of Se boat was adjusted to control the temperature. Transfer of grown WSe_2 is done using a HF based wet transfer technique with PMMA as the transfer medium.

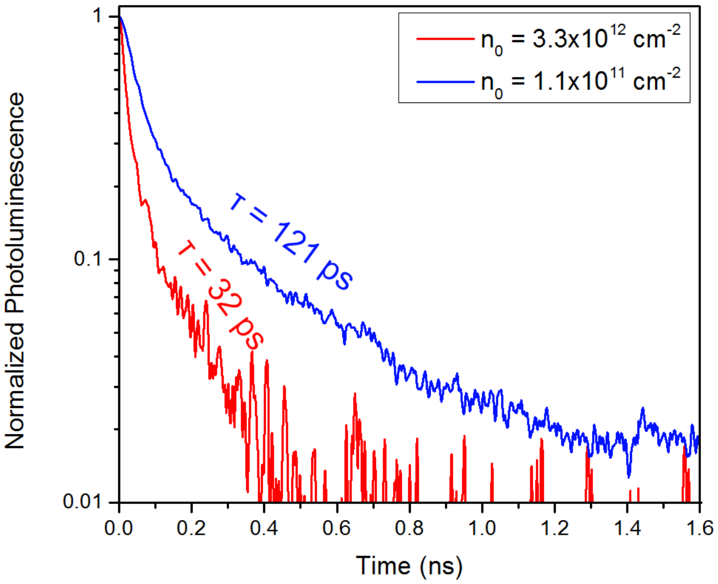

Fig. 2-5-3. As-exfoliated MoS_2 time-resolved luminescence. Photoluminescence decay spectrum for as-exfoliated MoS_2 measured at multiple excitation powers using a streak camera (2 ps time resolution).

Chapter 3

Light emitting devices based on 2D semiconductors

3.1 – Pulsed electroluminescence in monolayer semiconductors[5]

A key limitation in previously demonstrated steady-state monolayer light emitting devices is the restrictions posed by Schottky contacts or requirement of complex heterostructures to achieve injection of electrons and holes. We demonstrate a transient-mode electroluminescent device based on transition-metal dichalcogenide monolayers (MoS_2, WS_2, $MoSe_2$ and WSe_2) to overcome these problems. Electroluminescence from this dopant-free two-terminal device is obtained by applying an AC voltage between the gate and the semiconductor. Notably, the electroluminescence intensity is weakly dependent on the Schottky barrier height or polarity of the contact. We fabricate a monolayer seven-segment display and achieve the first transparent and bright millimeter-scale light emitting monolayer semiconductor device.

Transition metal dichalcogenides (TMDCs) such as WSe_2 and MoS_2 are semiconducting analogues of graphene, and are candidate materials for next generation optoelectronic and electronic devices[1-5]. Their unique properties include naturally terminated surfaces at the monolayer limit (~0.7 nm), which when coupled with appropriate passivation of defect sites can result in near-unity photoluminescence (PL) quantum-yield (QY)[3,6]. In addition, monolayer TMDCs display a myriad of attractive and unique physical properties including the lack of inversion symmetry, chiral light emission, and the ability to form heterostructures without the need for lattice matching[7-9]. Recent advances in the synthesis of high quality TMDCs *via* chemical vapor deposition (CVD) demonstrate their potential for scalability[10,11]. The high PL QY and sub-nanometer thickness of TMDCs can be leveraged to develop large-area, transparent and efficient light emitting devices[3,6]. However, despite their exceptional material properties, a key challenge for TMDC light emitting devices to date has been the formation of ohmic contacts to electrons and holes in the same device. Ohmic contacts in traditional light emitting diodes (LEDs) are essential to minimize resistive losses and achieve high injection levels[12]. In previous works, steady-state electroluminescence (EL) was obtained in TMDCs using *p-n* junctions formed *via* electrostatic or chemical doping[13-15]. More recently, EL from complex quantum well heterostructures utilizing graphene with hexagonal boron-nitride tunnel barriers has been demonstrated[16,17]. However, the lack of suitable bipolar ohmic contacts remains to be a significant issue, ultimately limiting the performance of TMDC light emitting devices[1].

---

[5] Reproduced with permission from D.-H. Lien, M. Amani, S.B. Desai et al., Nature Communications, 9, 1229, 2018. Copyright © [2018] Springer Nature.

Inspired by the first electroluminescent device, the light-emitting-capacitor[18-21], we achieve efficient bipolar carrier injection and light emission in TMDCs *via* transient mode operation using a single metal-semiconductor contact (source). In this two-terminal device, the source is grounded and an AC voltage is applied to the gate electrode. Alternating electron and hole populations are injected into the monolayer TMDC from the source contact. Notably, the carrier injection is weakly dependent on the Schottky barrier height (φ_B) (*i.e.* polarity of the contact) because of the large tunneling currents present at the source during the gate voltage (V_g) transients. The transient-electroluminescent (t-EL) device achieves bright EL at high injection levels. We demonstrate a millimeter scale device with bright EL (peak power of 193 $\mu W\ cm^{-2}$) from a ~0.7 nm thick monolayer in ambient room lighting. Finally, we show a large area device fabricated on a quartz substrate, which is transparent in the off-state by using indium tin oxide (ITO) electrodes.

Figure 3-1-1a shows a schematic of the t-EL device, consisting of a monolayer TMDC on a heavily doped silicon substrate (gate) with a 50 nm thick SiO_2 layer as the gate oxide. The TMDC is contacted with one metal electrode (source), and a bipolar square wave is applied between the gate and source. As shown in Fig. 3-1-1b, EL is only observed near the source contacts and the emission region laterally extends from the contact edge by ~3 μm. We fabricated devices based on four of the most heavily studied monolayer TMDCs by employing this generic device structure, specifically: WS_2, MoS_2, WSe_2 and $MoSe_2$[22,23]. All four of the studied materials show EL, with the spectral emission shape closely matching their respective PL (Fig. 3-1-1c).

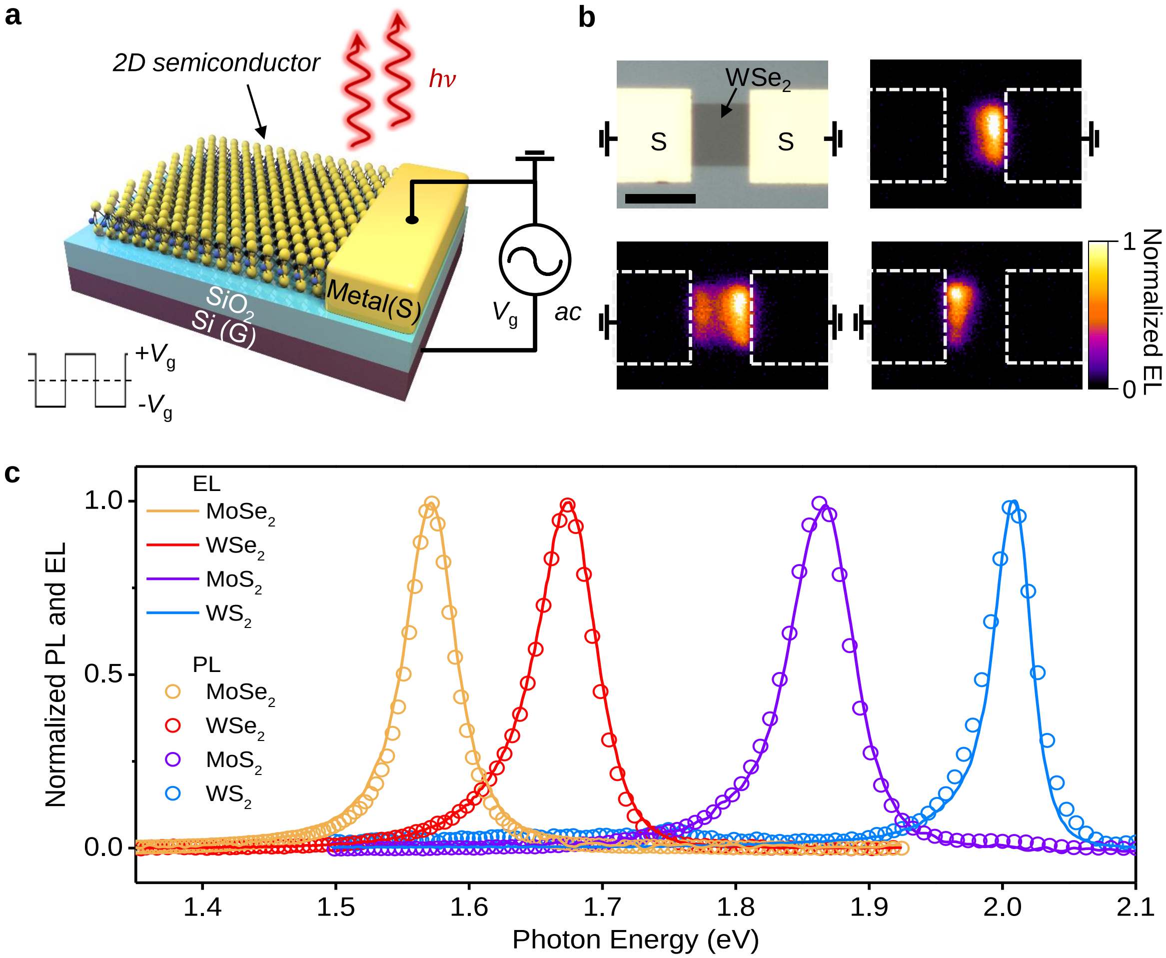

Fig. 3-1-1 Transient EL in TMDCs. a Schematic of the t-EL device. An AC voltage is applied between the gate and source electrodes and emission occurs near the source contact edge. **b** Optical and EL image of a WSe_2 device, showing that emission is only observed near the grounded source contacts. Scale bar is 10 μm. **c** EL and PL spectra measured for $MoSe_2$, WSe_2, MoS_2 and WS_2 monolayer devices.

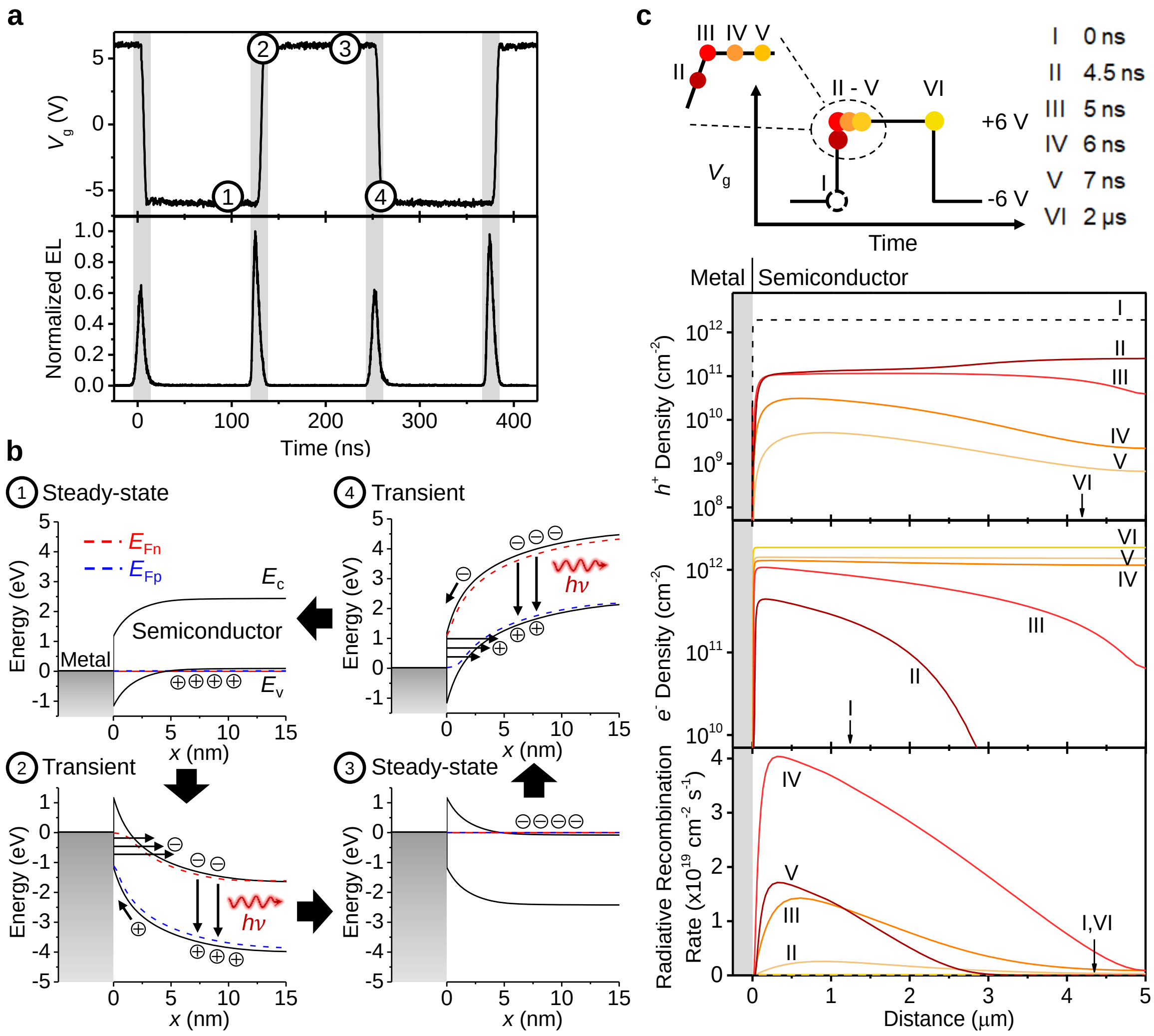

Fig. 3-1-2 Operation mechanism. a Time-resolved electroluminescence and the corresponding V_g, showing that EL occurs at the V_g transients (time points 2 and 4). **b** Band diagrams at different times during the operation cycle, corresponding to panel A. E_{Fn} and E_{Fp} indicate the quasi-Fermi levels for electrons and holes respectively. **c** V_g pulse applied to the simulated device and the corresponding electron/hole density and radiative recombination rate. Simulations were performed for material parameters corresponding to WSe_2 using a 50 nm thick gate oxide and $V_g = \pm 6$ V.

We performed time-resolved electroluminescence (TREL) measurements to understand the dynamic performance and the mechanism of light emission in the t-EL device. The measured TREL from a WSe_2 device and the corresponding V_g square wave are shown in Fig. 3-1-2a. Pulsed EL is observed at each V_g transition and has a full width half maximum of 8 ns. EL emission in the device increases linearly with frequency (f), with no changes in spectral shape. Note that the EL is stable with a variation (~±25%) in intensity over time. The emission mechanism can be elucidated from the sequence of simulated energy band diagrams shown in Fig. 3-1-2b, as well as the carrier densities and radiative recombination rate shown in Fig. 3-1-2c. When V_g is held at -6 V, the hole density in the semiconductor is large and approaches its steady-state value ($p_0 \sim 1.9\times10^{12}$ cm^{-2}). When V_g is switched to +6 V the field across the capacitive component of the device (*i.e.* SiO_2 gate dielectric) cannot change instantaneously. As a result, the applied voltage is dropped across the resistive parts of the device including the semiconductor and the source contact, but is dominated by the latter. The large voltage drop and the steep energy band bending at the Schottky contact lead to large transient tunneling currents. Injected electrons diffuse inward while holes exit the semiconductor through the contact or recombine with incoming electrons. Thus, the hole density shows a continuous decrease whereas the electron density in the semiconductor increases until it reaches its steady-state value ($n_0 \sim 1.9\times10^{12}$ cm^{-2}). At steady-state, the band bending in the semiconductor and at the contact decreases and the tunneling currents subside. The excess electron and hole populations simultaneously present (large quasi-Fermi level splitting) during the AC transient result in pulsed light emission. Similarly, this mechanism can also explain the emission from the device during a -6 V to +6 V V_g transient. The large transient tunneling currents in the t-EL device allow for efficient modulation of the carrier densities in the semiconductor, surmounting the large Schottky barriers typically associated with non-ohmic contacts to TMDCs.

The impact of φ_B on transient carrier injection and light emission is further studied by fabricating WSe_2 devices with electrodes prepared by sputtering (ITO), thermal evaporation (Au, Ag, Ni, MoO_x), as well as transferred van der Waals few-layer graphene contacts. The different contacts result in ~3 orders of magnitude variation in the on-current when the device is configured as a transistor. However, the corresponding t-EL devices show a maximum variation in the integrated emission intensity of only ~4× (Fig. 3-1-3a). TCAD simulations similarly show negligible difference in integrated EL for varying φ_B over the range of ohmic ($\varphi_B = 0.05$ eV) to mid-gap ($\varphi_B = E_g/2$). The relative intensity of emission during the two V_g transients, however, does vary for devices with varying φ_B. As shown in the TREL of a hole selective contact device, the EL intensity at $+V_g$ to $-V_g$ transient is stronger than the other transient. This is consistent with simulation results and discussed in section 3.3. In addition to the effect of φ_B, we also studied the dependence of EL on varying V_g (Fig. 3-1-3b and Fig. 3-1-4). EL is observed from the device when V_g is greater than the turn-on voltage (V_t), whose precise value is dependent on the bandgap (E_g) of the material and parasitic resistances in the device. We experimentally observe a higher

V_t for WS_2 (4.1 V) as compared to WSe_2 (2.0 V) which is qualitatively consistent with the larger E_g of WS_2[24].

The efficiency in traditional light emitting devices is defined as the number of emitted photons over the total current. However, for the t-EL device, transient current measurement is challenging due to device and measurement setup parasitic capacitances as well as the high slew rate (1.6 V ns^{-1}) of the V_g square wave. Given this limitation, we define EL internal efficiency (η_i) based on the total steady-state carrier concentration, which represents the maximum number of carriers which can undergo radiative recombination in a given V_g cycle. The efficiency is thus defined as: $\eta_i = \frac{\text{photons/cycle}}{(n_o+p_o)\times\text{Area}}$. The sum of the steady-state concentrations, (n_0+p_0) is given by $C_g(2V_g\text{-}E_g\, q^{-1})q^{-1}$. Here, n_0 and p_0 are the steady-state electron and hole concentrations corresponding to a positive and negative V_g respectively, C_g (69.1 nF cm^{-2} for 50 nm SiO_2 gate oxide) is the areal gate capacitance and q is the elementary charge. The analytical value of n_0+p_0 closely matches that from simulations at sufficiently high V_g (Fig. 3-1-2c and Fig. 3-1-3). η_i approaches 100% for the case where the PL QY is unity and all the steady-state carriers present in the device undergo recombination during a V_g transient. In practice, PL QY may not be 100%, and only a fraction of the steady-state carriers will undergo recombination in the semiconductor, while the remainder exit through the contact due to the finite slew rate of the AC source. Further details on the efficiency calculation are provided in section 3-3.

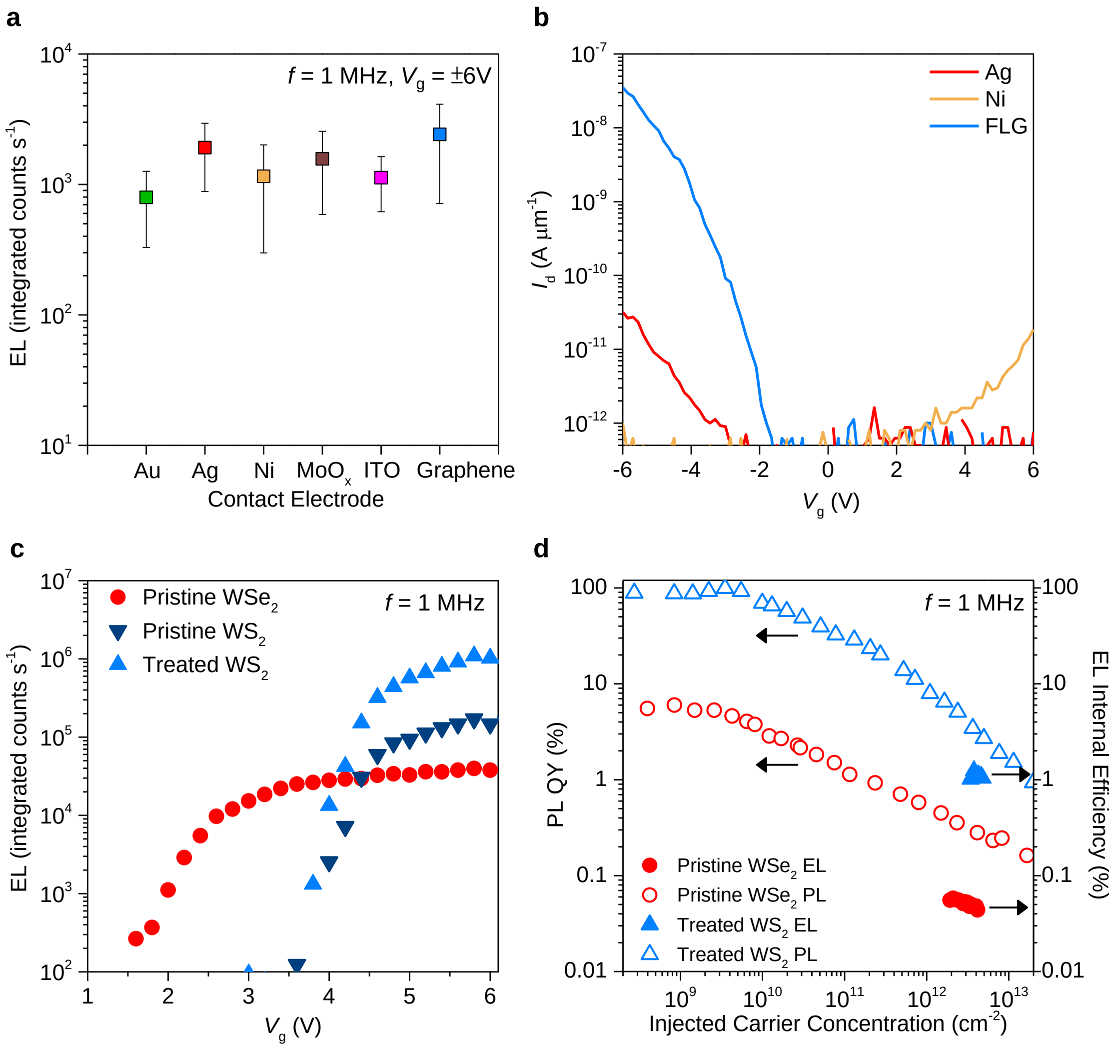

Fig. 3-1-3 Contact and voltage dependence. a EL from WSe_2 devices fabricated using various source contacts. Error bars show the standard deviation of EL intensity measured from at least five different devices. Inset shows I_d-V_g characteristics of WSe_2 devices contacted by Ag, Ni and few-layer graphene source electrodes. **b** Voltage dependence of EL for WSe_2 and WS_2 devices (WS_2 before and after superacid treatment). **c** PL QY and EL internal efficiency measured for a WSe_2 device and a superacid-treated WS_2 device as a function of injected carrier concentration.

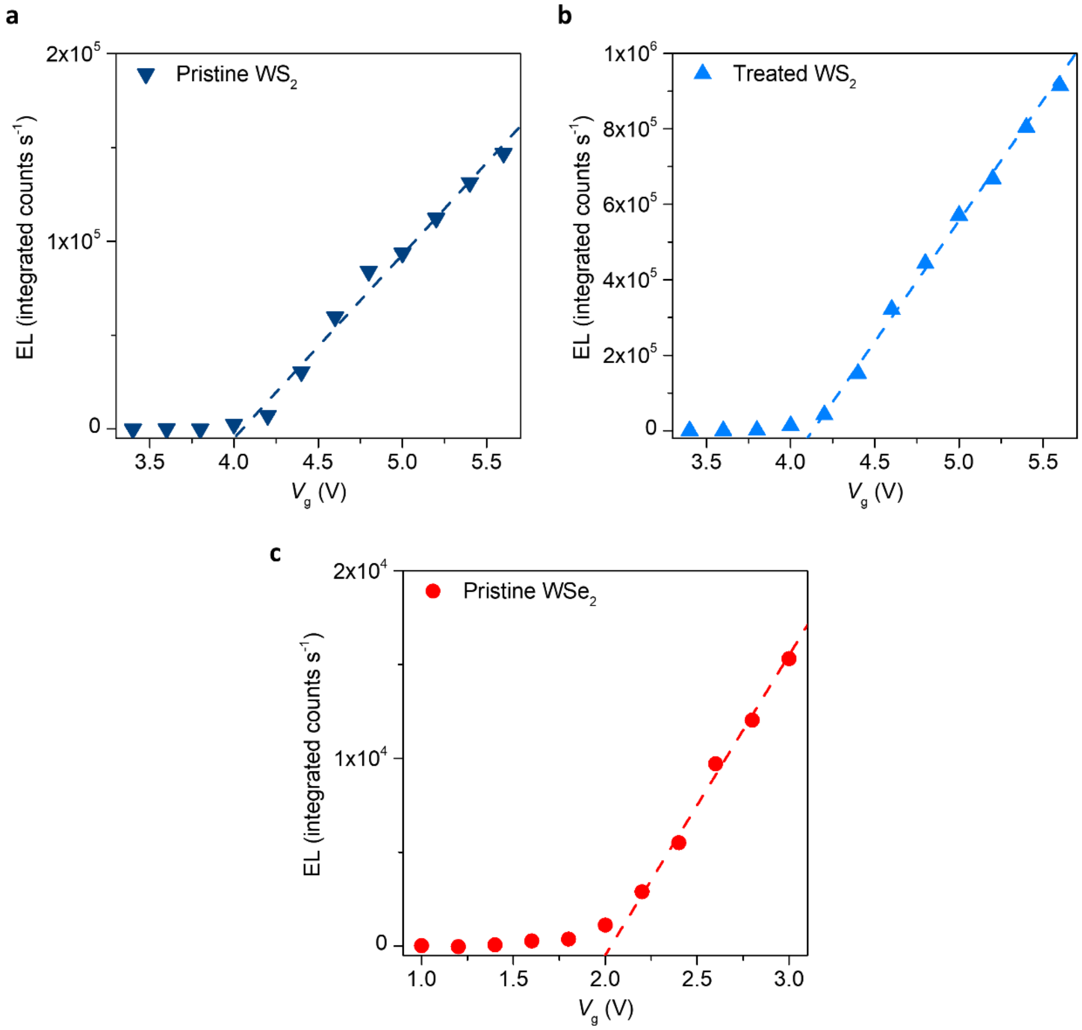

Fig. 3-1-4 V_g dependence of EL characteristics. EL measured for a WS_2 device before **(a)**, and after superacid treatment **(b)**, as well as a WSe_2 device **(c)**, as a function of injected carrier concentration. Note that V_t for the WSe_2 and WS_2 devices are 2.0 V and 4.1 V, respectively.

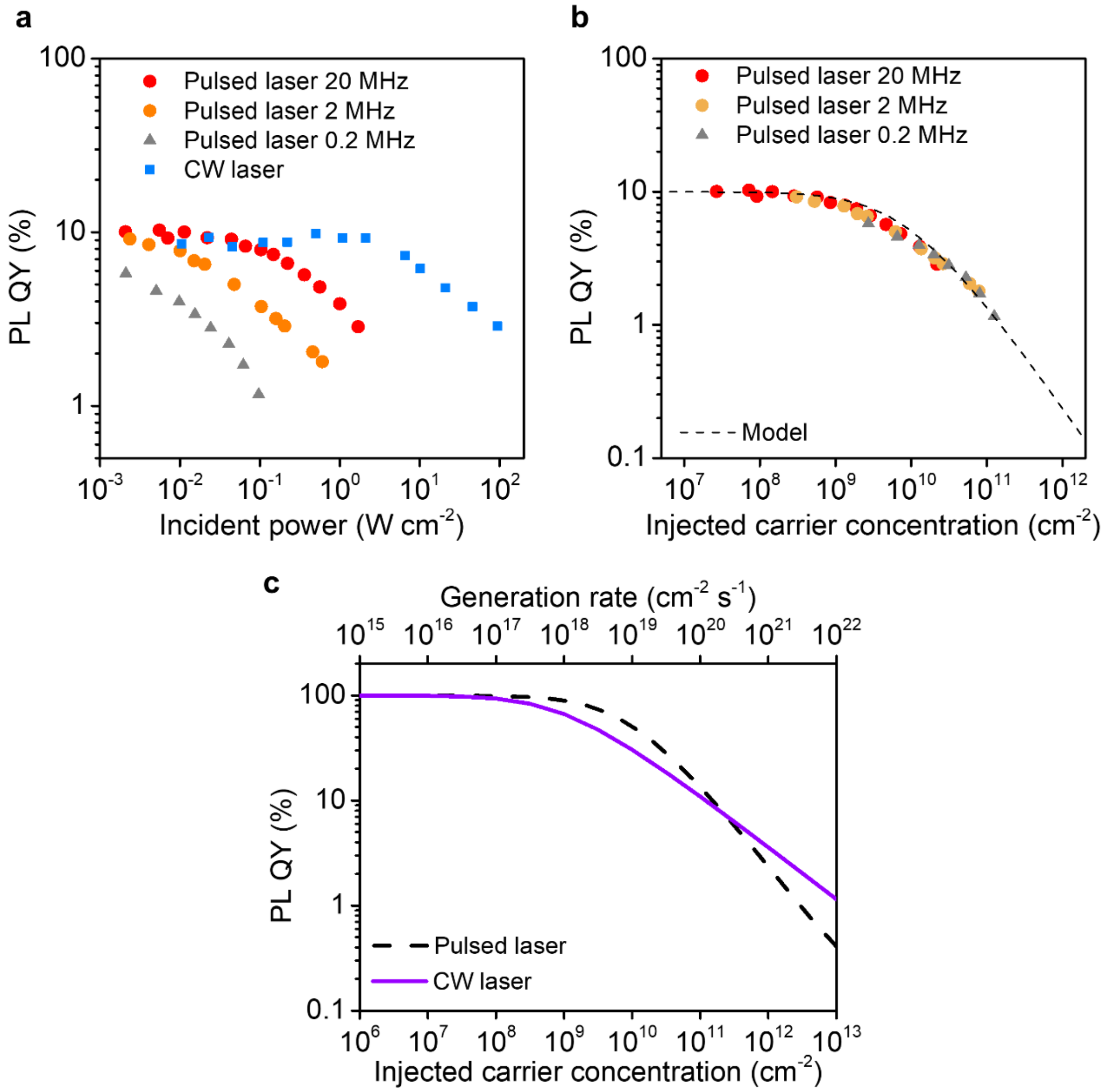

Fig. 3-1-5 Quasi-steady-state PL QY. (a) QY measured as a function of incident average power for a CW laser and a pulsed laser with repetition rates of 0.2, 2, and 20 MHz; excitation wavelength is 514 nm in all cases. **(b)** Quasi-steady-state QY as a function of incident carrier concentration from measurements shown in panel **(a)**; dashed line shows recombination model. **(c)** Modeled recombination for steady state (purple) and quasi-steady-state (black) excitation.

The WSe_2 t-EL device at $n_0+p_0 = 2.1\times10^{12}$ cm^{-2} (calculated for $V_g = 3.2$ V and $E_g = 2.34$ eV) has an EL external efficiency (η_e) of 0.01%[24]. The η_i of this device is extracted from η_e by considering the escape cone and optical interference from the Si substrate with a 50 nm SiO_2 layer[3,25]. Using this method, we calculate η_i of ~0.06%. To contrast the performance of the t-EL device relative to the PL QY of the material, the steady-state and quasi-steady-state PL are measured using a continuous-wave and pulsed laser respectively (Fig. 3-1-3c and Fig. 3-1-5). The droop observed in PL QY at high injection levels has been previously attributed to biexcitonic recombination in 2D semiconductors[3,6]. The calculated η_i for WSe_2 ~ 0.06% has an upper bound equal to the PL QY of the material (~ 0.3%) (Fig. 3-1-3c). The efficiency of the device can be improved by utilizing a material with a high PL QY. We fabricated WS_2 devices where the semiconductor surface is passivated using a non-oxidizing organic superacid: bis(trifluoromethane)sulfonimide, which has been shown to enhance the PL QY at low injection levels ($< 10^9$ cm^{-2}) to > 95%[3,6]. In this superacid-treated device, we obtain a peak η_e of ~0.27% at n_0+p_0 ~3.8×10^{12} cm^{-2} (calculated for $V_g = 5.8$ V and $E_g = 2.88$ eV), corresponding to η_i ~1.2%[24]. We note that the η_i is still significantly limited by the PL QY droop at high injection levels (3.4%) (Fig. 3-1-3c). The effect of biexcitonic recombination on the PL QY is shown in Fig. 3-1-5. This indicates that for pump levels in the range of 10^{12} cm^{-2}, WS_2 which has a C_{bx} of ~0.1 cm^2 s^{-1}, η_e can be improved to ~40% by sufficiently lowering C_{bx}. The next phase for improving the efficiency involves engineering the radiative lifetime and biexcitonic recombination rate by properly selecting the substrate and/or top coating. Similar efforts are made in III-V thin film devices, where the radiative recombination rate is highly dependent on the optical mode density and refractive index of the medium[26].

To demonstrate the versatility of this transient injection mechanism, we fabricated the first display using TMDCs as the light emitting material. A seven-segment display was fabricated using monolayer WSe_2 with Ni contacts. An optical image and the corresponding PL image of the display are shown in Fig. 3-1-6a and 3-1-6b respectively. By grounding the source electrodes of individual elements in the display sequentially, we show that we can dynamically display the letters C-A-L. Furthermore, we show that the t-EL device can be readily scaled to millimeter dimensions by using large-area monolayer films of WSe_2 grown by CVD[11]. In order to maximize the light emitting area, a Ni electrode is patterned in a grid structure with a line spacing of 8 μm (corresponding to ~2× of the emission FWHM). As a result, the EL from each contact edge fills the active area as shown schematically in Fig. 3-1-4d. The final device was then packaged in a standard chip carrier. Figure 3-1-6e and 3-1-6f show photographs of a 3 mm × 2 mm device in operation under room-lights. The average and peak output power of the device operating at $f = 400$ kHz, was measured directly using a power meter to be 0.62 μW cm^{-2} and 193 μW cm^{-2} respectively. This shows that a monolayer semiconductor has the potential to be used in display and lighting applications. Finally, we demonstrate that the device can be made transparent as shown in Fig. 3-1-6g. This device is fabricated on a fused quartz substrate, utilizing ITO as the gate and source electrodes and Al_2O_3 as the gate dielectric. Photographs of a transparent device in the off- and on-state are shown in Fig. 3-1-6h,i respectively.

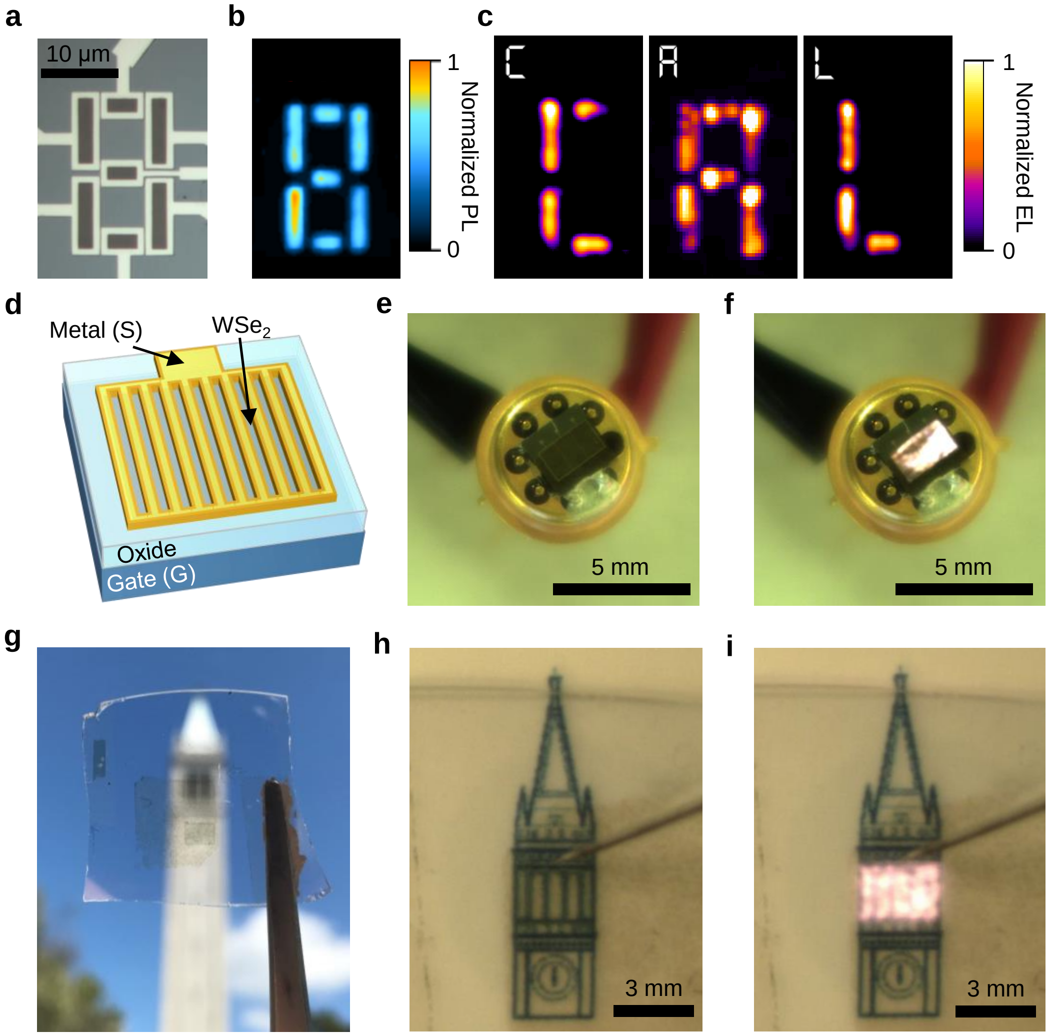

Fig. 3-4-6 Seven-segment display and millimeter-scale t-EL device. a Optical microscope image and **b**, photoluminescence image of a seven-segment t-EL display. **c** Operation of the seven-segment display showing EL in the shape of C-A-L. **d** Schematic of a millimeter-scale device, showing the grid source electrode structure to increase active emission area. **e**, **f** Photograph of a packaged, 3 mm × 2 mm, device in the off- (**e**) and on- (**f**) state. **g** Photograph of a millimeter-scale transparent device. **h**, **i** Photograph of a large area (3 mm × 2 mm) transparent device in the off- (**h**) and on- (**i**) state.

In summary, we have demonstrated bright EL at high injection levels using transient mode operation *via* a simple dopant-free device which does not require complex heterostructures to achieve light emission. EL from this device is weakly dependent on the Schottky barrier height or polarity. The transient EL concept demonstrated in this work can be extended to large bandgap materials in the future, for which achieving ohmic contacts to both carrier types is particularly challenging. We show that this device structure can be scaled-up to obtain light emission on millimeter length scales. The ability to realize large-scale light emission from monolayer semiconductors opens numerous potential opportunities in the field of 2D materials and can lead to the realization of transparent displays. Our results also suggest that the main factors limiting the performance of the t-EL device is PL QY droop due to biexcitonic recombination. The device performance can be further improved through engineering of the optical medium[3,25]. Finally, unlike traditional LEDs, the exposed light emitting surface of these devices also permits for the direct integration of plasmonic structures, nano-antennas, and photonic crystals, which could allow for the fabrication of high-speed devices or the development of electrically pumped 2D lasers[27-29].

References for Section 3-1

1. Xia, F., Wang, H., Xiao, D., Dubey, M. & Ramasubramaniam, A. Two-dimensional material nanophotonics. *Nat. Photon.* **8**, 899-907 (2014).
2. Mak, K. F., Lee, C., Hone, J., Shan, J. & Heinz, T. F. Atomically thin MoS_2: A new direct-gap semiconductor. *Phys. Rev. Lett.* **105**, 136805 (2010),
3. Amani, M. *et. al*. Near-unity photoluminescence quantum yield in MoS_2. *Science* **350**, 1065-1068 (2015).
4. Radisavljevic, B., Radenovic, A., Brivio, J., Giacometti, V. & Kis, A. Single-layer MoS_2 transistors. *Nat. Nanotechnol.* **6**, 147-150 (2011).
5. Desai, S. B. *et. al*. MoS_2 transistors with 1-nanometer gate lengths. *Science* **354**, 99-101 (2016).
6. Amani, M. *et. al*. Recombination kinetics and effects of superacid treatment in sulfur- and selenium-based transition metal dichalcogenides. *Nano Lett.* **16**, 2786-2791 (2016).
7. Wu, Wenzhuo *et. al.* Piezoelectricity of single-atomic-layer MoS_2 for energy conversion and piezotronics. *Nature* **514**, 470-474 (2014).
8. Zhang, Y. J., Oka, T., Suzuki, R., Ye, J. T. & Iwasa, Y. Electrically switchable chiral light-emitting transistor. *Science* **344**, 725-728 (2014).
9. Fang, H. *et. al.* Strong interlayer coupling in van der Waals heterostructures built from single-layer chalcogenides. *Proc. Nat. Acad. Sci.* **111**, 6198-6202 (2014).
10. Kang, K. *et. al.* High-mobility three-atom-thick semiconducting films with wafer-scale homogeneity. *Nature* **520**, 656-660 (2015).
11. Ahn, G. H. *et. al.* Strain-engineered growth of two-dimensional materials. *Nature Commun.* **8**, 608 (2017).
12. Nakamura, S., Senoh, M . S. & Mukai, T. High-power InGaN/GaN double-heterostructure violet light emitting diodes. *Appl. Phys. Lett.* **62,** 2390-2392 (1993).
13. Ross, J. S. *et. al.* Electrically tunable excitonic light-emitting diodes based on monolayer WSe_2 p-n junctions. *Nat. Nanotechnol.* **9**, 268-272 (2014).
14. Baugher, B. W. H., Churchill, H. O. H., Yang, Y. & Jarillo-Herrero, P. Optoelectronic devices based on electrically tunable p-n diodes in a monolayer dichalcogenide. *Nat. Nano.* **9**, 262-267 (2014).
15. Pospischil, A., Furchi, M. M. & Mueller, T. Solar-energy conversion and light emission in an atomic monolayer p-n diode. *Nat. Nanotechnol.* **9**, 257-261 (2014).
16. Withers, F. *et. al.* Light-emitting diodes by band-structure engineering in van der Waals heterostructures. *Nat. Mater.* **14**, 301-306 (2015).
17. Withers, F. *et. al.* WSe_2 Light-Emitting Tunneling Transistors with Enhanced Brightness at Room Temperature. *Nano Lett.*, **15**, 8223–8228 (2015)
18. Butler, K. H., Jerome, C. W. & Waymouth, J. F. The electroluminescent lamp: A new light source. *Electr. Eng.*

73, 524-528 (1954).

19. Wood, V. *et. al.* Electroluminescence from nanoscale materials *via* field-driven ionization. *Nano. Lett.* **11**, 2927-2932 (2011).
20. Cho, S. H. *et. al.* High performance AC electroluminescence from colloidal quantum dot hybrids. *Adv. Mater.* **24**, 4540-4546 (2012).
21. Xu, J., Carroll, D. L. Smith, G. M., Dun, C. & Cui, Y. Achieving high performance in AC-field driven organic light sources. *Sci. Rep.* **6**, 24116 (2016).
22. Gutierrez, H. R. *et. al.* Extraordinary room-temperature photoluminescence in triangular WS_2 monolayers. **13**, 3447-3454 (2013).
23. Tonndorf, P. *et. al.* Photoluminescence emission and Raman response of monolayer MoS_2, $MoSe_2$, and WSe_2. *Opt. Express* **21**, 4908-4916 (2013).
24. Ramasubramaniam, A. Large excitonic effects in monolayers of molybdenum and tungsten dichalcogenides. *Phys. Rev. B* **86**, 115409 (2012).
25. Lien D.-H. *et. al.* Engineering Light Outcoupling in 2D Materials. *Nano Lett.* **15**, 1356-1361 (2015).
26. Yablonovitch, E., Gmitter, T. J. & Bhat, R. Inhibited and enhanced spontaneous emission from optically thin AlGaAs/GaAs double heterostructures. *Phys. Rev. Lett.* **61**, 2546-2549 (1988).
27. Ciraci, C. *et. al.* Probing the ultimate limits of plasmonic enhancement. *Science* **337**, 1072-1074 (2012).
28. Eggleston, M. S., Messer, K., Zhang, L., Yablonovitch, E. & Wu, M. C. Optical antenna enhanced spontaneous emission. *Proc. Nat. Acad. Sci.* **112**, 1704-1709 (2014).
29. Wu, S. *et. al.* Monolayer semiconductor nanocavity lasers with ultralow thresholds. *Nature* **520**, 69-72 (2015).
30. Ma, D. *et. al.* A universal etching-free transfer of MoS_2 films for applications in photodetectors. *Nano Res.* **8**, 3662-3672 (2015).

3.2 – Tunable black phosphorous light emitting diodes

Unlike the majority of 2D materials, which are only direct bandgap at the monolayer limit, black phosphorous (bP) maintains a direct bandgap for all thicknesses, which ranges from 1.4 to 0.3 eV[1-6]. In this work we leverage this property to demonstrate the first light emitting diodes (LEDs) based on bP/MoS_2 heterostructures. We show that the emission wavelength of bP/MoS_2 LEDs can be tuned from 0.94 to 4.5 µm by varying bP thickness. This efficient and tunable emission enables the use of bP/MoS_2 LEDs in non-dispersive-infrared (NDIR) gas sensors. Furthermore, we obtain a peak external quantum efficiency (EQE) of 4.4% and internal quantum efficiency (IQE) of 19.3% at an emission wavelength of 3.7 µm. Notably this is the highest EQE for an LED reported in the mid-wave infrared[7-9] and is enabled due to the low Auger recombination coefficient of bP compared to other small bandgap III-V semiconductors.

Most infrared light sources operating in the mid- and long-wave infrared are based on thermal emitters, which have poor efficiency, limited brightness, and modulation speed. Despite such drawbacks, these devices find use in a variety of applications, the most notable of which is spectroscopy. In the search for an alternative, significant research has been performed on solid-state infrared light sources, the most notable of which are quantum/interband cascade lasers QCL/ICLs[10-12] and LEDs[7-9]. These devices provide tunable, bright, and spectrally narrow emission which can be modulated at high frequencies. While recent works have shown dramatic improvements in the efficiencies of QCLs and ICLs (with wall plug efficiencies approaching 30% at room temperature)[11] their wide spread use is limited due to the stringent requirements concerning the growth of the semiconductor materials on which they are based, which lead to exceptionally high costs. Infrared LEDs have dramatically lower costs than QCL/ICLs while still providing high speed, brightness, and narrow spectral emission, but tend to have poor EQE[13]. This is due to the high Auger recombination velocities in the narrow gap III-V and II-VI semiconductors (i.e. InSb or HgCdTe)[13] employed for these devices. Non-traditional material systems such as quantum dots have also been used for infrared light emitters, but these devices have only been demonstrated for wavelengths up to 2 µm, and do not cover longer wavelengths[14-16].

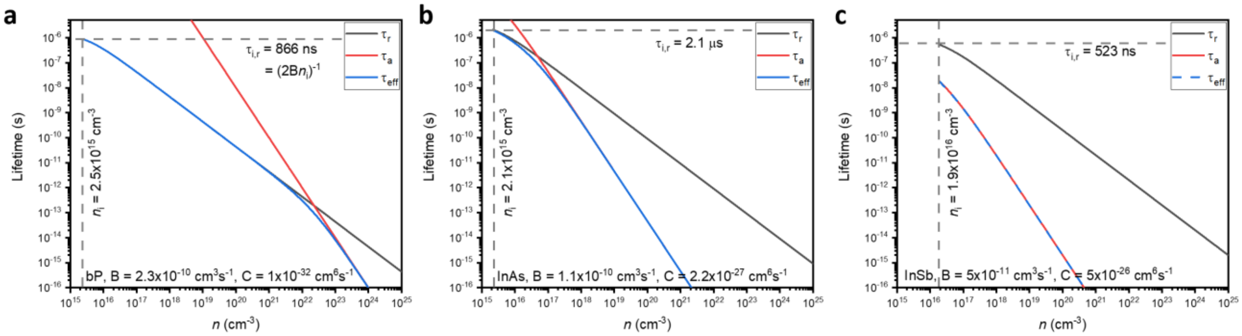

Fig. 3-2-1. Auger and radiative lifetimes as a function of carrier concentration ($n = n_\mathrm{i}+\Delta n$) for **a**, bP, **b**, InAs, and **c**, InSb. The intrinsic carrier concentration as well as the intrinsic radiative lifetime is indicated in the figures for each material.

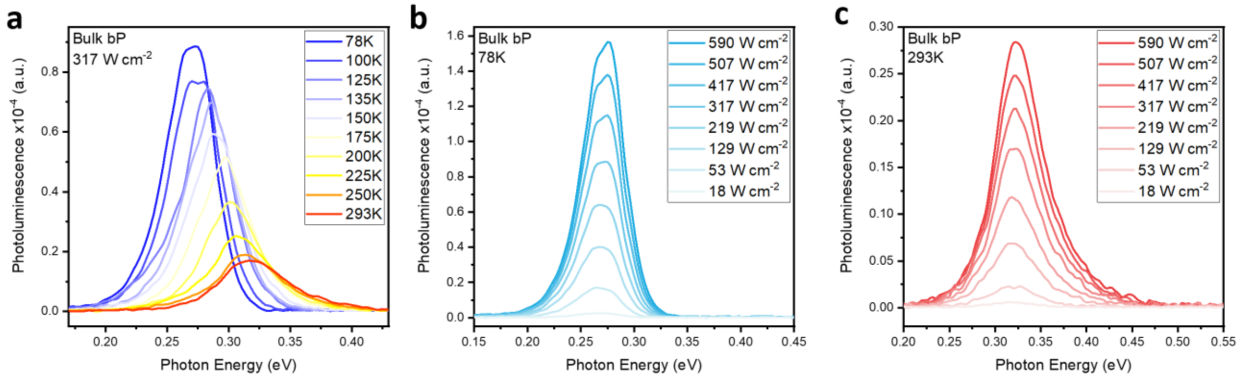

Fig. 3-2-2. a, Temperature dependent photoluminescence spectra of a bulk bP crystal (~220 nm thick) at an excitation power of 317 W cm^{-2}. **b**, PL measured as a function of pump fluence at 293K. **c**, PL measured as a function of pump fluence at 78K.

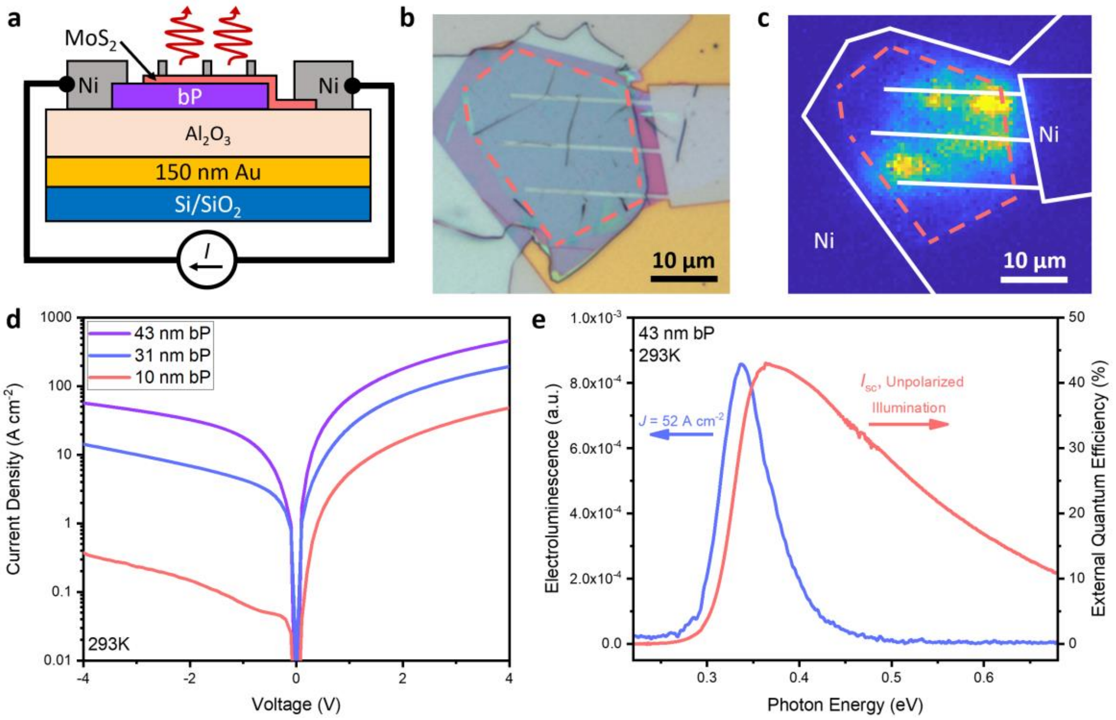

Fig. 3-2-2 Mid-infrared bP/MoS_2 light emitting diodes. **a**, schematic of device configuration, showing the bP/MoS_2 heterojunction and Au/Al_2O_3 back reflector structure. **b**, Optical micrograph of a completed device. The bP/MoS_2 heterojunction is outlined for clarity. **c**, EL image of the device shown in panel **b**, obtained using a 128×128 MCT focal plane array coupled to an infrared microscope at a forward current density of 118 A cm^{-2}. **d**, Typical *J*-*V* characteristics obtained from various bP/MoS_2 diodes with varying bP thickness. The R_0A product for all devices investigated here as a function of bP thickness studied is shown in Fig. 3-2-2. **e**, Measured EL and photoresponse spectrum for a bP/MoS_2 heterojunction with a 43 nm thick bP layer.

Some of the drawbacks in III-V/II-VI infrared LEDs can potentially be overcome by 2D materials. Unlike their three-dimensional counterparts, 2D systems possess no surface dangling bonds as their surfaces are covalently terminated, minimizing the impact of surface recombination and leading to high photoluminescence (PL) quantum-yields (QY)[3]. This property provides 2D materials with a distinct advantage for applications such as electronics, where thinner semiconductor layers permit extreme device scalability[4], and optoelectronics, where the dramatic reduction in surface recombination velocity can allow for PL QY approaching unity[3]. One of the most exciting 2D materials which has been studied extensively over the past several years is bP[5,6,17]. Unlike other 2D semiconductors, *i.e.* MoS_2 or WSe_2, bP maintains a direct bandgap for all thicknesses, which can be tuned from 0.3 eV in bulk to 1.4 eV at the monolayer limit[5,17]. Furthermore, multiple studies have suggested that bP possesses Auger recombination velocities which are several orders of magnitude lower than III-V semiconductors. Auger lifetimes (τ_a) are strongly dependent on bandgap, effective masses, and temperature, and this relationship can be described by:

$$\tau_a \propto \exp\left(aE_g \mathrm{k}_b T\right) \qquad (3\text{-}2\text{-}1)$$

where a is a constant depending on the effective masses for electrons and holes (m_e^* and m_h^*, respectivly) as $(m_e^*/m_h^*)/[1+(m_e^*/m_h^*)]$. As a result Auger recombination becomes significant in small bandgap III-V semiconductors with large effective mass disparities for the two carrier types. The recombination kinetics for these narrow bandgap material systems with low exciton binding energies can be described by a traditional ABC model, where A is Schockly-Reed-Hall recombination, B is bimolecular radiatiative recombination, and C is Auger recombination. In steady state, total generation (G) is equal to recombination (R) and is balanced according to:

$$G = \mathrm{A}\frac{np-n_i^2}{n} + \mathrm{B}(np-n_i^2) + C[n(np-n_i^2)+p(np-n_i^2)] \qquad (3\text{-}2\text{-}2)$$

where, n, p, and n_i, are the excess electron, hole, and intrinsic carrier concentrations respectively. Importantly, the intrinsic carrier concentrations for narrow gap materials near room temperature are high (2.5×10^{15} cm^{-3} for bulk bP) and cannot be neglected. From the rate equations the effective radiative (τ_r) and Auger lifetimes can be calculated according to:

$$\tau_r = [\mathrm{B}(n+p+2n_i)]^{-1} \qquad (3\text{-}2\text{-}3)$$

$$\tau_a = [n\mathrm{C}(p+n_i)+p\mathrm{C}(n+n_i)]^{-1} \qquad (3\text{-}2\text{-}4)$$

and is shown in Fig. 3-2-1 for bulk bP (E_g = 320 meV), InAs (E_g = 354 meV), and InSb (E_g = 170 meV), with the respective recombination parameters and the n_i shown in Table 3-2-1. Note that the effective lifetime τ_{eff} is given by $\tau_r\ \tau_a\ /(\ \tau_r + \tau_a)$. It can be immediately observed that the room temperature recombination in InAs and InSb is dominated by the effects of Auger recombination even at low excess carrier concentrations. As a result, bP exhibits strong PL even for thick layers as shown in Fig. 3-2-2. Despite extensive previous work on bP based transistors[18,19] and photodetectors[20-22], electrically pumped light emission has yet to be realized. Here, we utilize bP/MoS_2 heterojunctions to achieve electroluminescence (EL) from bP layers of varying thickness. A schematic of the device structure and an optical image of a typical device are shown in Figure 3-2-3a and 3-2-3b, respectively. The device consists of a bP/MoS_2 heterojunction where both the MoS_2 (10-15 nm thick, which acts as the electron selective contact) and bP are contacted by Ni electrodes. To increase the current spreading over the heterojunction area and to reduces series resistance losses, additional Ni electrodes are placed over the MoS_2 on the heterojunction. Finally, the device is placed on an Au (150 nm) mirror separated by an Al_2O_3 (360 nm) dielectric spacer, which increases the fraction of light coupled from the device to free space. The impact of the current spreading electrodes can be more clearly seen in the EL image shown in Figure 3-2-3c, where much of the emission occurs in the areas defined by the electrodes.

Typical current-voltage characteristics of devices fabricated with bP thicknesses of 43, 31 and 10 nm are shown in Figure 3-2-3d. A clear reduction in the forward current and an increase in the rectification ratio can be observed with decreasing bP thickness. This can be attributed to an increase in series resistance under forward bias, and confinement of the depletion width for thinner bP layers under reverse bias[21]. The zero-bias resistance (R_0A) measured for all of the devices fabricated in this study is shown in Fig. 3-2-4, which shows an increase of ~3 orders of magnitude as the bP thickness is reduced from bulk to bilayer. The EL spectra and spectral photoresponse of a typical device with a 43 nm thick bP layer are shown in Figure 3-2-3e. A strong EL peak can be clearly observed at the band-edge of the bP layer with a peak photon energy of 0.34 eV, consistent with the PL measurements shown in Fig. 3-2-2. Additionally, the bP/MoS_2 diode shows a strong photovoltaic response which is consistent with previously reported photodetector results[21]. We next turn our attention to the detailed characterization of this bP LED (43 nm thick). Light-current curves measured for this device at 293 and 78K are shown in Figure 3-2-5, which show an expected linear increase in emission for low injection density followed by saturation at higher injection density, with peak output powers of 17 and 42 µW measured at 293 and 78K respectively. The turn-on voltage of this device can be extracted from the light-voltage curve (Figure 3-2-5b) and is found to be 350 mV and 200 mV at 293 and 78K respectively, closely matching the bandgap of the bP layer (340 meV)[17].

Material	B (cm^3s^{-1})	C (cm^6s^{-1})	n_i (cm^{-3})
bP	2.3×10^{-10}	1×10^{-32}	2.5×10^{15}
InAs	1.1×10^{-10}	2.2×10^{-27}	2.2×10^{15}
InSb	5×10^{-11}	5×10^{-26}	1.9×10^{16}

Table 3-2-1. Recombination parameters and intrinsic carrier concentrations at 293K for bP, InAs, and InSb.

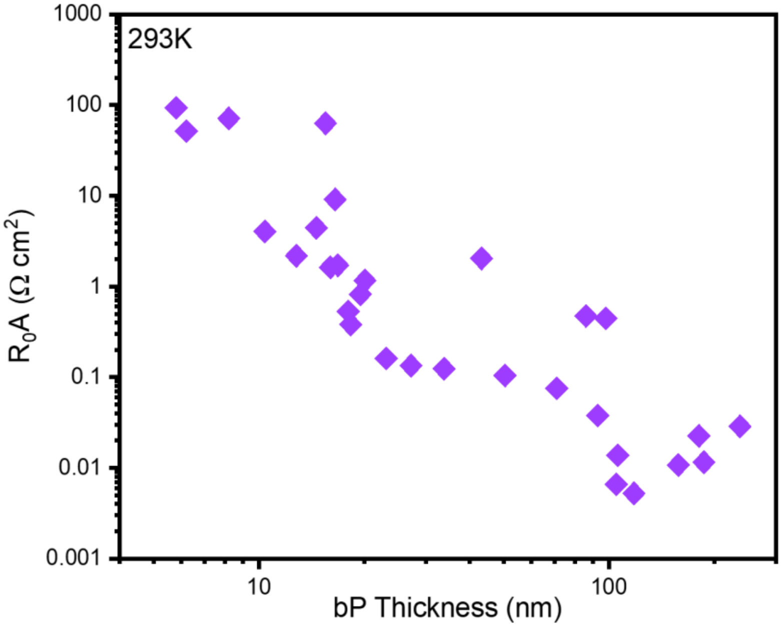

Fig. 3-2-4. Thickness dependence of zero-bias resistance area product for bP/MoS_2 heterojunctions.

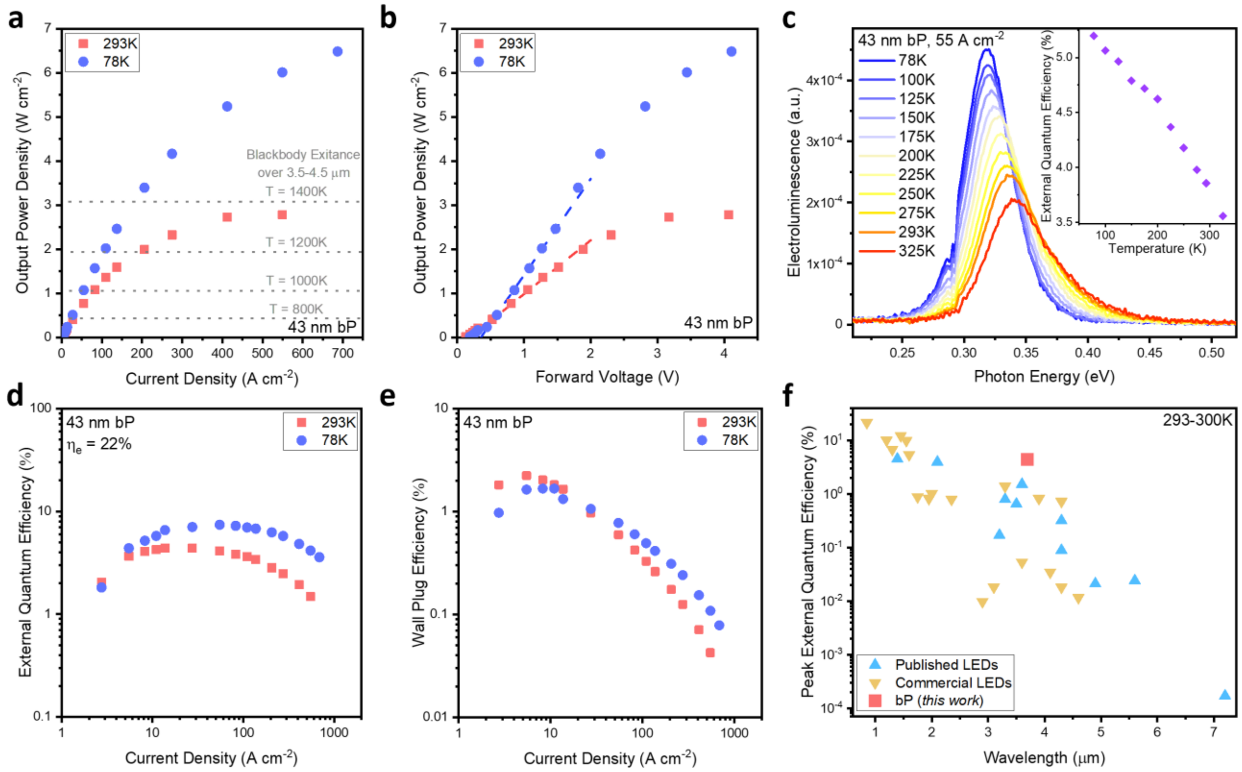

Fig. 3-2-5 Optoelectronic characteristics of bP/MoS$_2$ LEDs. a, Light-current characteristics for a typical device measured at 78K and 293K. **b**, Light-voltage characteristics for a typical device measured at 78K and 293K. Dashed lines show the fits used to extract the turn-on voltage for the device which was found to be 0.35 V and 0.2 V at 78K and 293K, respectively. **c**, Temperature dependence of the EL spectra measured at a constant current density of 55 A cm^{-2}; inset shows the corresponding EQE as a function of temperature. Note that the feature appearing in all of the spectra at 0.29 eV is due to residual CO$_2$ present in the optical path. **d**, EQE as a function of current density measured at 78K and 293K. **e**, Wall plug efficiency as a function of current density measured at 78K and 293K. **f**, Comparison of peak external quantum efficiencies reported for bP/MoS$_2$ as well as various published and commercial infrared LEDs. Summary and references of other devices shown here are presented in Table 3-2-2.

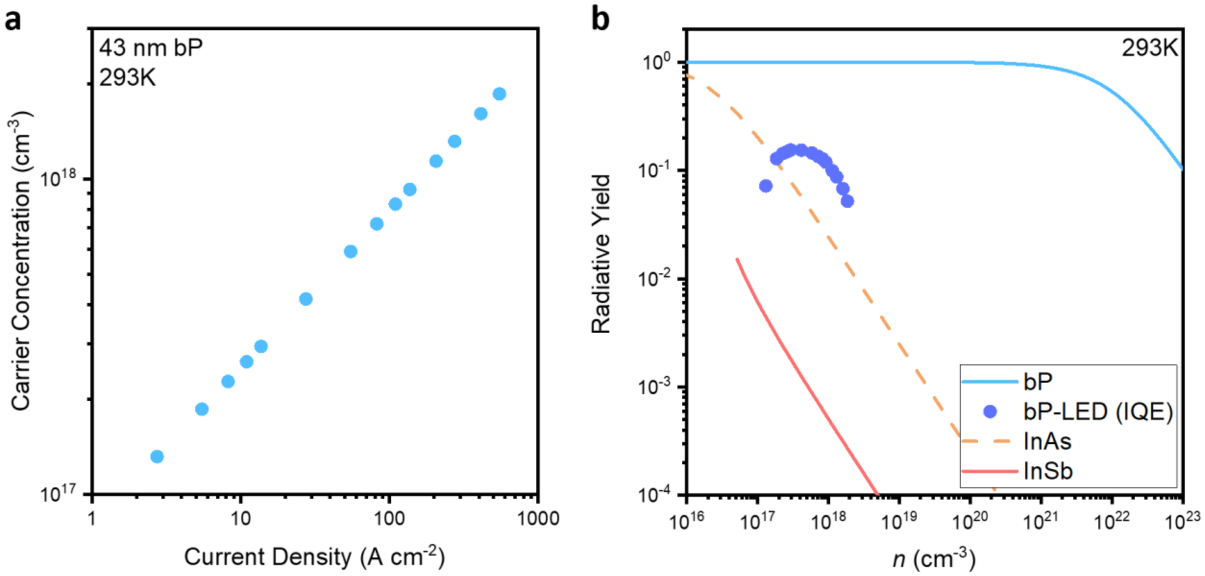

Fig. 3-2-6. a, Carrier concentration as a function of injected current density calculated for the device shown in Fig. 3-2-5d at 293K. **b**, Superimposed IQE of the bP LED shown in Fig. 3-2-5d with the theoretical quantum efficienciesof bP, InAs, and InSb calculated from the recombination parameters shown in Table 3-2-1. Note that no SRH recombination was assumed and $n = n_i + \Delta n$.

The EQE for this device is calculated according to: $q_{\mathrm{e}}P_{\mathrm{el}}I^{-1}(h\nu)^{-1}$, where q_{e} is the elementary charge, P_{el} is the externally emitted optical power, I is the operating current, h is the Planck constant, and υ is the frequency of light. The temperature dependent EQE of this device and the corresponding EL spectra measured at a constant current density of 55 A cm^{-2} are shown in Figure 3-2-5c. The emission spectra show a redshift in the bandgap at reduced temperatures that is consistent with previous demonstrations [21], and an expected increase in EQE from 3.4% to 5.6% over the temperature range of 325K to 78K. The EQE and derived wall plug efficiency ($P_{\mathrm{el}}I^{-1}V_{\mathrm{app}}^{-1}$, where V_{app} is the applied forward voltage) as a function of injected current density are shown in Figure 3-2-5d and 3-2-5e respectively. The EQE in this device peaks (4.4% and 7.7% at 293 and 78K, respectively) immediately prior to the onset of saturation. On the other hand, the wall plug efficiency approaches the EQE at low injection levels but shows a large droop at high injection levels, which can be attributed to series resistance (*i.e.* Schottky contacts) in the device. To compare the measured internal efficiency as a function of injection current we can calculate the instantaneous carrier concentration in the bP layer. Assuming the concentration is uniform over the full bP thickness and area, self-consistently solving the recombination equation yields the effective lifetime in bP as shown in Fig. 3-2-6a. The resulting IQE can be plotted over the theoretical quantum yield for bP as well as other III-V materials as shown in Fig. 3-2-6, and indicates that these bP devices are not limited by Auger recombination. This is consistent with the small temperature dependence on EQE observed in Fig. 3-2-5, and is in stark contrast to InAs based LEDs which show an improvement in EQE of over an order of magnitude at cryogenic temperatures. A comparison of this bP/MoS_2 LED to other published and commercially available infrared light emitting diodes is shown in Figure 3-2-5f and is summarized in Table 3-2-2. While this device is considerably less efficient than LEDs operating in the visible and near-infrared spectrum which typically have EQEs in the range of 10-30%, the measured room temperature EQE of 4.4% from bP exceeds the highest reported values for mid-wave light emitting devices based on highly developed III-V and II-VI materials (Ref. 7-9 and Table 3-2-2) and the IQE of bP LEDs is greater than the theoretical maximum IQE of InAs at moderate to high injection levels.

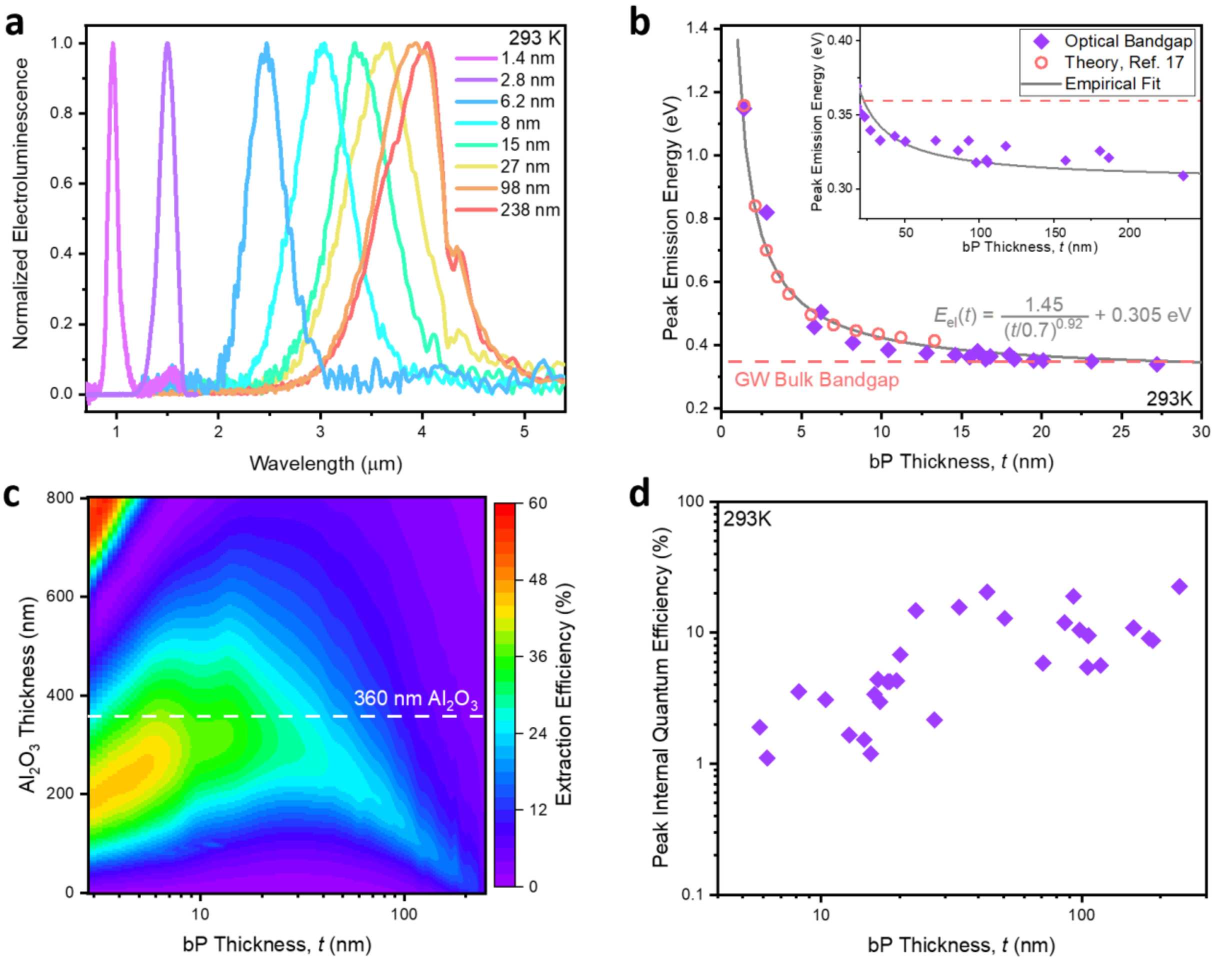

Fig. 3-2-7. Thickness tunable EL spectra. a, Room temperature EL spectra measured for selected bP/MoS_2 heterojunctions with varying bP thickness in the range of 1.4 to 238 nm. **b**, Peak emission wavelength as a function of bP thickness for 27 devices as well as the theoretically calculated bandgap for varying thickness bP (taken from Ref. 17). **c**, Simulated photon extraction efficiency as a function of both bP and Al_2O_3 thickness; note that a constant MoS_2 thickness of 10 nm was used for all simulations and the dashed line indicates an Al_2O_3 thickness of 360 nm, which was used for the devices shown here. **d**, IQE calculated for the devices shown in panel **b**.

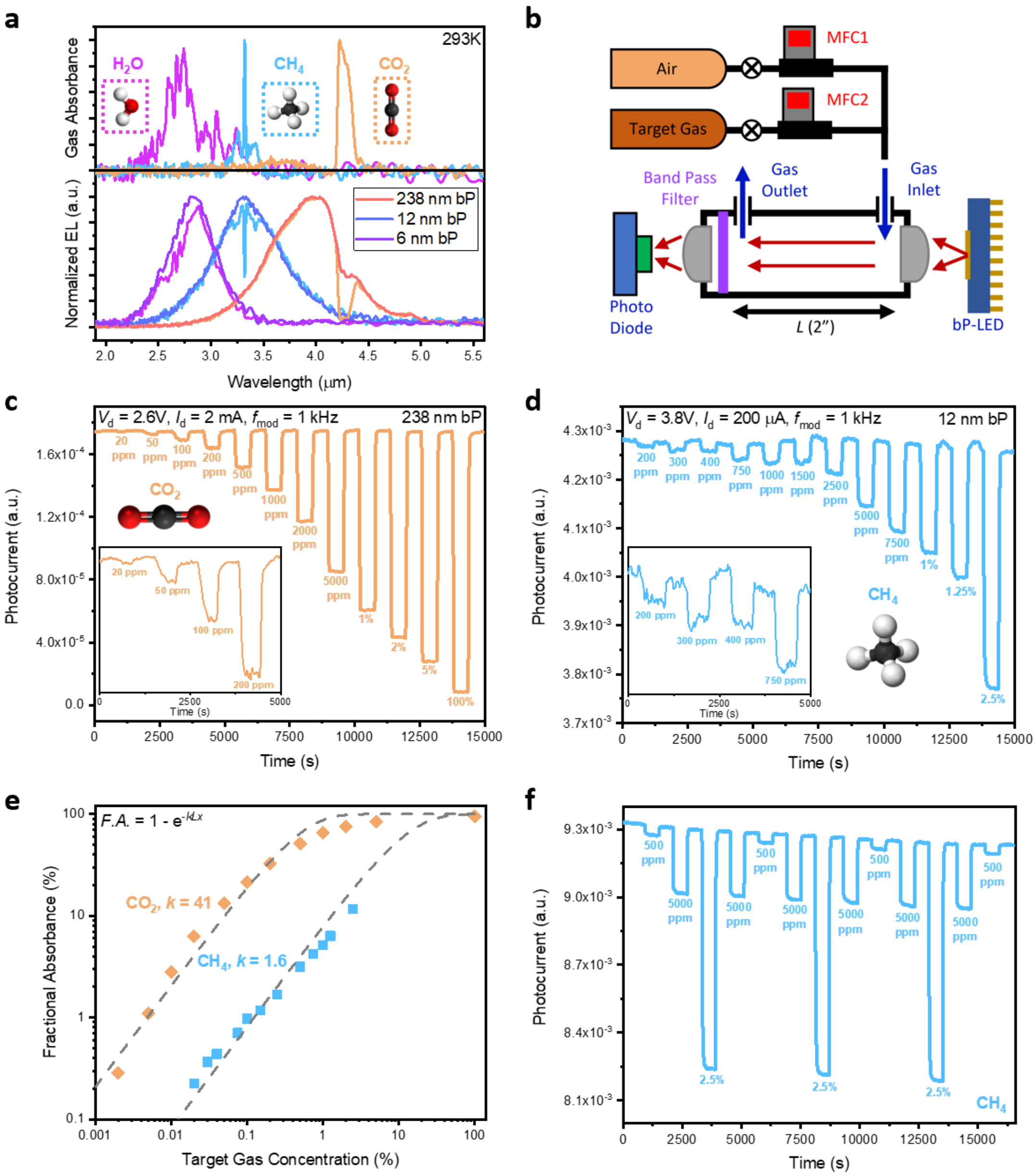

Fig. 3-2-8 Gas sensing using bP LEDs. a, Normalized EL spectra of a 238 nm, 12 nm and 6 nm thick bP/MoS_2 LEDs in the presence and absence of CO_2, CH_4, and H_2O gas respectively and the absorption spectra of the gases measured using the bP/MoS_2 LEDs. **b**, Schematic of experimental setup used for measurements consisting of a bP/MoS_2 LED and a commercial photodetector, coupled through a gas mixing chamber. **c**, Measured photocurrent from a 238 nm bP/MoS_2 LED with varying concentrations of CO_2 present in the optical path. **d**, Measured photocurrent from a 12 nm bP/MoS_2 LED with varying concentrations of CH_4 present in the optical path. **e**, Fractional absorbance of CO_2 and CH_4 as a function of concentration. **f**, CH_4 concentration cycling for gauging hysteresis for the bP LEDs operating in an NDIR sensor. Drift measurements for the devices shown in panel **c** and **d** over an 8-hour period are shown in Fig. 3-2-8.

One of the unique properties of bP is its widely thickness tunable bandgap in a mono-elemental material system[5,6,17]. This property can be directly leveraged in light emitting devices where the bP layer thickness is varied as shown in Figure 3-2-7a. By utilizing bP layers with thickness ranging from 1.4 nm (*i.e.* bilayer bP) to 238 nm, we show that the peak emission wavelength can be tuned over 960 nm to 4 µm. The peak emission energy (E_{el}) measured on 32 different devices is shown in Figure 3-2-7b, where the bandgap as a function of thickness can be described by:

$$E_{el}(t) = \frac{1.45}{(t/0.7)^{0.92}} + 0.305\ eV \tag{3-2-5}$$

where t is bP thickness. This is in excellent agreement with the theoretically calculated bandgap of bP as a function of thickness. We performed finite-difference time-domain simulations to determine the light extraction efficiency (η_{e}) of these devices[23]. Figure 3-2-7c shows the simulated extraction efficiency as a function of dielectric spacer thickness and bP thickness. Note that these simulations are performed at the bP peak emission wavelength, which is calculated for each thickness using equation 1. The dashed line represents a 360 nm Al_2O_3 spacer thickness which was used in the devices fabricated here. This structure takes advantage of the non-epitaxial nature of bP, and notably can achieve very high extraction efficiencies in the range of 30-45%. The internal quantum efficiency (IQE) as a function of bP thickness is then calculated according to EQE $\eta_{\mathrm{e}}^{-1}$and is shown in Figure 3-2-7d. For devices thicker than 30 nm, the calculated IQE falls in the range of in 5-20%, while a reduction is observed for thinner layers which can likely be attributed to degradation of the active bP layer during fabrication[24].

Finally, we demonstrate a potential application of our bP/MoS_2 LEDs by utilizing them as light sources for NDIR gas sensing, which leverages the infrared absorption bands of different target gas molecules[25-26]. These devices typically utilize thermal emitters, which cannot be rapidly modulated and require high power to operate[26]. To enable the use of NDIR sensors for internet-of-things applications which need a battery life on the order of years, it is necessary to have devices that can be rapidly modulated and have high efficiency[27]. Figure 3-2-8a shows measured EL spectra of bP/MoS_2 LEDs with thicknesses of 6, 12, and 238 nm. These devices were selected because they possess large spectral overlap with dominant absorption peaks of water vapor (H_2O, 2.7 µm), methane (CH_4, 3.3 µm), and carbon dioxide (CO_2, 4.3 µm), respectively. The absorption of these gasses was then directly measured using the bP/MoS_2 LEDs *via* measuring the EL spectra with the target gas present in the optical path. A gas cell, mimicking commercially available NDIR sensors was then constructed as shown in Figure 3-2-8b, using 238 and 12 nm bP in conjunction with a commercial photodetector and bandpass filters to detect CO_2 and CH_4 as shown in Figure 3-2-8c-e. Experiments showed highly sensitive detection of up to 100% CO_2 and 2.5% (50% of the lower explosive limit, LEL) CH_4 with the devices. Measurements revealed lower limit of detection (LOD) as low as 20 ppm with a sensitivity of ±30 ppm for CO_2, and LOD of 100 ppm and sensitivity of ±150 ppm for CH_4, with minimal hysteresis and high consistency as shown in Figure 3-2-8e and f. Additionally, stability measurements of these two devices, performed with the device under continuous 50% duty cycle operation for a period of eight hours showed negligible drift (< 1.3%) and are shown in Fig. 3-2-9.

While other technologies exist in this spectral regime, their adoption is impeded either due to low efficiency or high costs. The first demonstration of efficient electrically pumped infrared light emission from bP provides an exciting new application space for 2D materials which can overcome many of the key limitations in existing technologies. Specifically, we have demonstrated that LEDs based on bP/MoS_2 heterostructures can be utilized to obtain tunable EL over a wide spectral range (940 nm to 4.5 µm) and that these devices can show EQE and IQE as high as 4.4% and 19.3% respectively. This is enabled by the low Auger recombination velocity of bP, which allows us to observe IQEs which are higher than what is theoretically possible in III-V semiconductors such as InAs. Furthermore, utilizing the thickness dependent emission from bP, we have demonstrated that these devices can be employed in NDIR gas sensors targeting CO_2, CH_4, and H_2O. Unlike III-V and II-VI based devices, the non-epitaxial nature of 2D materials can allow for these devices to be integrated with silicon devices, potentially allowing for integration with silicon photonics or multi-modal gas sensors.

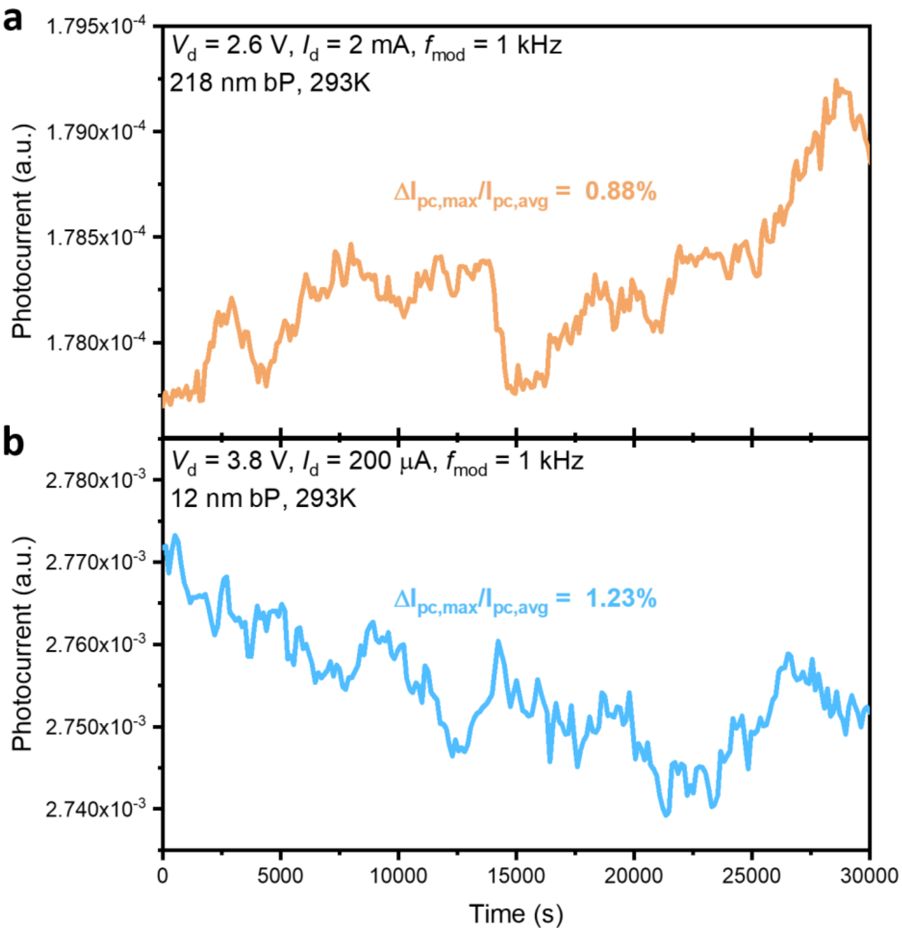

Fig. 3-2-9 a, Stability measurements taken on the device shown in Fig. 3b, taken over a period of 8-hours, showing a maximum drift of 0.88%. **b**, Stability measurements taken on the device shown in Fig. 3d, taken over a period of 8-hours, showing a maximum drift of 1.23%.

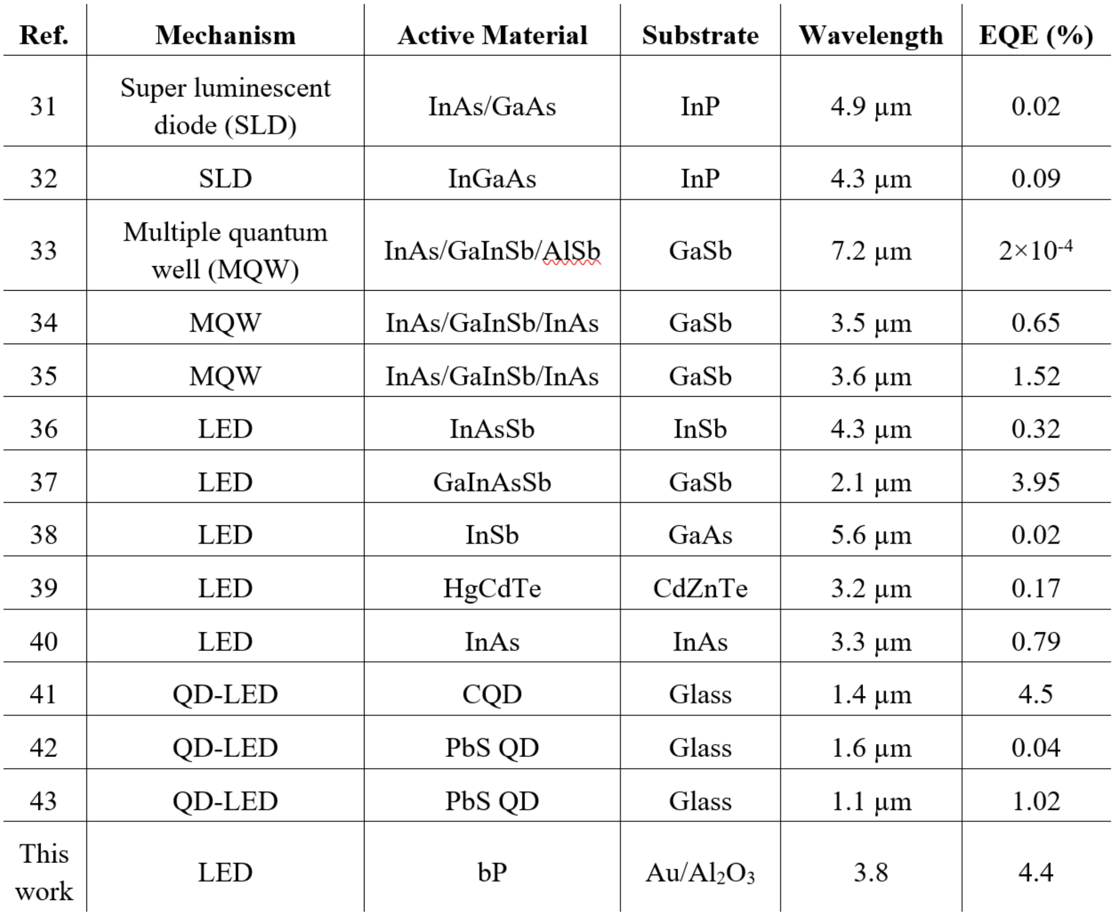

Ref.	Mechanism	Active Material	Substrate	Wavelength	EQE (%)
31	Super luminescent diode (SLD)	InAs/GaAs	InP	4.9 μm	0.02
32	SLD	InGaAs	InP	4.3 μm	0.09
33	Multiple quantum well (MQW)	InAs/GaInSb/AlSb	GaSb	7.2 μm	2×10^{-4}
34	MQW	InAs/GaInSb/InAs	GaSb	3.5 μm	0.65
35	MQW	InAs/GaInSb/InAs	GaSb	3.6 μm	1.52
36	LED	InAsSb	InSb	4.3 μm	0.32
37	LED	GaInAsSb	GaSb	2.1 μm	3.95
38	LED	InSb	GaAs	5.6 μm	0.02
39	LED	HgCdTe	CdZnTe	3.2 μm	0.17
40	LED	InAs	InAs	3.3 μm	0.79
41	QD-LED	CQD	Glass	1.4 μm	4.5
42	QD-LED	PbS QD	Glass	1.6 μm	0.04
43	QD-LED	PbS QD	Glass	1.1 μm	1.02
This work	LED	bP	Au/Al_2O_3	3.8	4.4

Table 3-2-2. Overview of published infrared light emitting diodes shown in Figure 3-2-4f. Efficiencies for commercial devices are taken from datasheets by Hamamatsu, Roithner, and ThorLabs.

References for Section 3-1

1. Xia, F., Wang, H., Xiao, D., Dubey, M., Ramasubramaniam, A. Two-dimensional material nanophotonics. *Nat. Photon*. **2014**, 8, 899-907.
2. Tan, C., Cao, X., Wu, X.-J., He, Q., Yang, J., Zhang, X., Chen, J., Zhao, W., Han, S., Nam, G.-H., Sindoro, M., Zhang, H. Recent advances in ultrathin two-dimensional materials. *Chem. Rev.* **2017**, 117, 6225-6331.
3. Amani, M., Lien, D.-H., Kiriya, D., Xiao, J., Azcatl, A., Noh, J., Madhvapathy, S. R., Addou, R., Kc, S., Dubey, M., Cho, K., Wallace, R. M., Lee, S.-C., He, J.-H., Ager, J. W., Zhang, X., Yablonovitch, E., Javey, A. Near-Unity Photoluminescence Quantum Yield in MoS_2. *Science* **2015**, 350, 1065-1068.
4. Desai, S. B., Madhvapathy, S. R., Sachid, A. B., Llinas, J. P., Wang, Q., Ahn, G. H., Pitner, G., Kim, M. J., Bokor, J., Hu, C., Wong, H.-S. P., Javey, A. MoS_2 transistors with 1-nanometer gate lengths. *Science* **2016**, 354, 99-102.
5. Xia, F., Wang, H., Jia, Y. Rediscovering black phosphorus as an anisotropic layered material for optoelectronics and electronics. *Nat. Comm.* **2014**, 5, 4458.
6. Wang, X., Jones, A. M., Seyler, K. L., Tran, V., Jia, Y., Zhao, H., Wang, H., Yang, L., Xu, X., Xia, F. Highly anisotropic and robust excitons in monolayer black phosphorous. *Nat. Nano.* **2015**, 10, 517-521.
7. Das. N. C., Oliver, K., Towner, F., Simons, G., Shen, H. Infrared (3.8 µm) interband cascade light-emitting diode array with record high efficiency. *Appl. Phys. Lett.* **2005**, 87, 041105.
8. Popov, A. A., Stepanov, M. V., Sherstnev, V. V., Yakovlev, Y. P. InAsSb light-emitting diodes for the detection of CO_2 ($\lambda = 4.3\ \mu$m). *Tech. Phys. Lett.* **1998**, 24, 596-598.
9. Hadji, E., Bleuse, J., Magnea, N., Pautrat, J. L. 3.2 µm infrared resonant cavity light emitting diode. *Appl. Phys. Lett.* **1995**, 67, 2591.
10. Faist, J., Capasso, F., Sivco, D. L., Sirtori, C., Hutchinson, A. L., Cho, A. Y. Quantum cascade laser. *Science*. **1994**, 264, 553-556.
11. Yao, Y., Hoffman, A. J., Gmachl, C. F. Mid-infrared quantum cascade lasers. *Nat. Photon.* **2012**, 6, 432-439.
12. Bai, Y., Slivken, S., Darvish, S. R., Razeghi, M. Room temperature continuous wave operation of quantum cascade lasers with 12.5% wall plug efficiency. *Appl. Phys. Lett.* **2008**, 93, 021103.
13. Krier, A. Physics and technology of mid-infrared light emitting diodes. *Phys. Trans. R. Soc.* **2001**, 359, 599-619.
14. Gong, X., Yang, Z., Walters, G., Riccardo, C., Ning, Z., Beauregard, E., Adinolfi, V., Voznyy, O., Sargent, E. H. Highly efficient quantum dot near-infrared light-emitting diodes. **2016**, 10, 253-257.
15. Pradhan, S., Stasio, F. D., Bi, Y., Gupta, S., Christodoulou, S., Stavrinadis, A., Konstantatos, G. High-efficiency colloidal quantum dot infrared light-emitting diodes via engineering at the supra-nanocrystalline level. *Nat. Nano.* **2019**, 14, 72-79.
16. Yang, Z., Voznyy, O., Liu, M., Yuan, M., Ip, A. H., Ahmed, O. S., Levina, L., Kinge, S., Hoogland, S., Sargent, E. H. All-quantum-dot infrared light-emitting diodes. **2015**, 9, 12327-12333.
17. Rudenko, A. N., Yuan, S., Katsnelson, M. I. Toward a realistic description of multilayer black phosphorous: From GW approximation to large-scale tight-binding simulations. *Phys. Rev. B*. **2015**, 92, 085419.
18. Li, L., Yu, Y., Ye, G. J., Ou, X., Wu, H., Feng, D., Chen. X. H., Zhang, Y. Black-phosphorus field-effect transistors. *Nat. Nano.* **2014**, 9, 372-377.
19. Wang, H., Wang, X., Xia, F., Wang, L., Jiang, H., Xia, Q., Chin, M. L., Dubey, M., Han, S-J. Black phosphorus radio-frequency transistors. *Nano Lett.* **2014**, 14, 6424-6429.
20. Buscema, M., Groenendijk, D. J., Blanter, S. I., Steele, G. A., van der Zant, H. S. J. Castellanos-Gomez, A. Fast and broadband photoresponse of few-layer black phosphorus field-effect transistors. *Nano Lett.* **2014**, 14, 3347-3352.
21. Amani, M., Regan, E., Bullock, J., Ahn, G. H., Javey, A. Mid-Wave Infrared Photoconductors Based on Black Phosphorous-Arsenic Alloys. **2017**, *ACS Nano*, 11,11724-11731.
22. Bullock, J., Amani, M., Cho, J., Chen, Y.-Z., Ahn, G.H., Adinolfi, V., Shrestha, V. R., Gao, Y., Crozier, K. B., Chueh, Y.-L., Javey A. Polarization-resolved black phosphorus/molybdenum disulfide mid-wave infrared photodiodes with high detectivity at room temperature. *Nat. Photon.* **2018**, 12, 601-607.
23. Vandersteegen, P. Modeling the optical behavior of organic LEDs for illumination. **2008**, https://photonics.intec.ugent.be/download/phd_160.pdf
24. Favron, A., Gaufres, E., Fossard, F., Phaneuf-L'Herureux, A.-L., Tang, N, Y.-W., Levesque, P. L., Loiseau, A., Leonelli, R., Francoeur, S., Martel, R. Photooxidation and quantum confinement effects in exfoliated black phosphorus. *Nat. Mater.* **2015**, 14, 826-832.
25. Lee, D.-D., Lee, D.-S. Environmental gas sensors. *IEEE Sensors. J.* **2001**, 1, 214-224.
26. Dinh, T.-V., Choi, I.-Y., Son, Y.-S., Kim, J.-C. A review on non-dispersive infrared gas sensors: Improvement on sensor detection and interference correction. *Sens. Act. B.* **2016**, 231, 529-538.

27. Mehmood, Y., Ahmad, F., Yaqoob, I., Adnane, A., Imran, M., Guizani, S. Internet-of-Things-Based Smart Cities: Recent Advances and Challenges. *IEEE Comm.* **2017**, 55, 16-24.
28. Fang, H., Battaglia, C., Carraro, C., Nemsak, S., Ozdol, B., Kang, J. S., Bechtel, H. A., Desai, S. B., Kronast, F., Unal, A. A., Conti, G., Conlon, C., Palsson, G. K., Martin, M. C., Minor, A. M., Fadley, C. S., Yablonovitch, E., Maboudian, R., Javey, A. Strong interlayer coupling in van der Waals heterostructures built from single-layer chalcogenides. *Proc. Nat. Acad. Sci.* **2014**, 111, 6198-6202.
29. Das, S., Zhang, W., Demarteau, M., Hoffmann, A., Dubey, M., Roelofs, A. Tunable transport gap in phosphorene, *Nano Lett.* **2014**, 14, 5733-5739.
30. Zhang, Y. G., Gu, Y., Wang, K., Fang, X., Li, A. Z., Liu, K. H. Fourier transform infrared spectroscopy approach for measurements of photoluminescence and electroluminescence in mid-infrared. *Rev. Sci. Inst.* **2012**, 83, 053106.
31. Palik, E. D. Handbook of optical constants of solids, Academic Press, 1985.

3.3 – Experimental and theoretical methods

Transient Electroluminescence Device Fabrication

Devices based on MoS_2 (SPI supplies), WS_2 (HQ Graphene), and $MoSe_2$ (HQ Graphene) were fabricated from monolayers mechanically exfoliated onto 50 nm SiO_2/Si p^{++} substrates. The WSe_2 monolayers used in this work were synthesized by CVD with conditions tuned to optimize the PL QY of the material. Growth methods are presented in the reference[11], with the following modifications to obtain large area films: the Se boat temperature was ramped up to 130 °C and the growth time was extended to 42 minutes. The typical PL QY of synthesized WSe_2 samples at low pump powers is in the range of 5-15%. CVD WSe_2 monolayers were subsequently transferred to the desired substrate. For large area devices, WSe_2 films were transferred either to Si/SiO_2 or fused quartz/ITO/Al_2O_3 substrates. For patterning micron-scale devices on Si/SiO_2, the 2D material was first etched using XeF_2 while micron-scale devices on fused quartz/ITO/Al_2O_3 were etched using O_2/CF_4 plasma. Metal electrodes were subsequently deposited by thermal evaporation or sputtering. For graphene contacted devices, graphene flakes (3-5 layers thick) were etched and subsequently placed on the TMDC using a previously reported dry transfer technique. Due to the low PL QY of as-exfoliated MoS_2, devices were prepared using 40 nm thick Au contacts and subsequently were chemically treated using an organic superacid[3] to enhance the PL QY prior to EL measurements. All patterning was performed using electron-beam lithography with either PMMA or MMA/PMMA as the resist. In the case of devices fabricated on quartz substrates, a 10 nm Au film was thermally evaporated on the PMMA and etched post e-beam lithography using KI/I_2 etchant. For the case of superacid-treated WS_2 devices shown in this work, few-layer graphene contacts were used. This was done in order to eliminate process-induced degradation of the 2D layer, which predominantly occurs during e-beam lithography.

Visible and Near Infrared Electroluminescence Measurements

Electroluminescent devices were pumped using a bipolar square wave from an Agilent 33522A arbitrary waveform generator applied to the gate electrode, while the source contact was grounded. The PL and EL data presented in this work was measured using a custom built micro-PL instrument described in detail in reference[3]. To measure PL, either a 514.5 nm Ar^+ laser or a monochromated 514 nm line from a pulsed supercontinuum laser was used as the excitation source. PL and EL were collected using either a 50× ultra-long working distance or a 10× objective lens. The PL signal was passed through a 550 nm dielectric longpass filter to block the excitation light. Both PL and EL were dispersed by a spectrometer with a 340 mm focal length and 150 groove mm^{-1} grating, and detected using a Si CCD camera (Andor iDus BEX2-DD). Prior to each measurement, the CCD background was obtained and subsequently subtracted from the PL/EL acquisition. Time-resolved electroluminescence measurements were collected using a time-correlated single photon counting (TCSPC) module. The signal was detected with a low dark count avalanche photodiode operating in single photon counting mode (IDQuantique). The timing for the TCSPC was determined using pulses generated with the same phase/frequency as the square wave applied to the gate of the device. PL and EL imaging was performed in a florescence microscopy setup using a 470 nm LED as the excitation source and a CCD detector (Andor Luca) to acquire images. For EL imaging, the illumination source was turned off. Macroscopic photographs and videos of electroluminescence were taken using a CMOS camera with a telephoto lens; images are single exposures taken in ambient room lighting. Note that for the macroscopic EL photographs the cold filter was removed from the camera. All measurements reported in this paper are taken at room temperature, in an ambient lab environment, with no device encapsulation. Transistor I_d-V_g characteristics as well as C-f measurements of the gate oxide were taken using an Agilent B1500A semiconductor parameter analyzer.

Black Phosphorous LED Fabrication

The light emitting diodes studied here were fabricated on an Au/Al_2O_3 cavity. This was formed by atomic layer deposition of Al_2O_3 (360 nm thick) onto a patterned Ti/Au (10 nm/100 nm) back reflector. The active layer was formed using a poly(methyl methacrylate) (PMMA) mediated dry transfer process. Due to the poor stability of bP in the presence of humidity, bP flakes were exfoliated in a glove box and suitable thickness crystals were identified in a nitrogen purged AFM. An MoS_2 electron contact was then placed onto the bP, and the stack was then placed on the Au/Al_2O_3 substrate to create the final Au/Al_2O_3/bP/MoS_2 structure. Contacts to both the bP and MoS_2 layers were simultaneously formed using electron-beam lithography followed by deposition of a 40 nm thick Ni film by thermal evaporation. Liftoff was performed in a glovebox with anhydrous solvents. Finally, a 2 nm Al film was evaporated over the complete stack, which oxidizes to form Al_2O_3 in air and has been shown to improve the device stability.

Infrared Electroluminescence Measurements

Electrical measurements were performed using a 4155C Semiconductor Parameter Analyzer (Agilent). EL spectra covering the range of 2-5 µm were performed using a FTIR spectrometer (ThermoFisher) with a customized Janis cryostat equipped with a CaF_2 window. Devices were first wire bonded in a 24 pin chip carrier and evacuated to a base pressure of $< 10^{-5}$ Torr. The cryostat was then placed at the auxiliary source port of the FTIR, which was modified to include a microscope equipped with a 15× Schwarzschild objective to couple the emitted light to the interferometer and internal HgCdTe photodetector. To separate the EL from the thermal background and to increase the measurement dynamic range, a double modulation scheme was used[30]. Here, the device was operated using a voltage controlled current source (Stanford Research Systems), with the drive current modulated at a frequency of 5 kHz and the FTIR optical velocity set to 0.0657 cm s^{-1}. The resulting photocurrent was then sent to a lock-in amplifier with a reference frequency of 5 kHz. The resulting demodulated interferogram was then acquired and averaged using an oscilloscope and the EL spectra were calculated as the power spectral density of the resulting interferogram. The sample rate and acquisition window were set such that the fast Fourier transform (FFT) bin size was 1 meV, though it should be noted that for the spectra shown in Figure 3-2-4a, the acquisition window was increased to improve the spectral resolution to 0.5 meV. The spectral range covered a wavelength range of 15 to 1 µm. A schematic of the full experimental setup as well as the total and double modulated interferograms are shown in Fig. 3-3-1. It should be noted that the devices can still be measured under continuous wave operation (i.e. without double modulation. For thinner bP devices with bi-layer to quad-layer thicknesses measurements were taken using a grating spectrometer equipped with an InGaAs CCD (1.7 µm cutoff). The devices measured showed strongly polarized emission, which is consistent with previous reports on strongly polarized absorption in bP. This is characterized in the polarization resolved EL spectra, where a linear BaF_2 polarizer was placed in the optical path.

In order to calibrate the intensity of the emission, we characterized the instrument function with a blackbody held at a temperature (T) of 673K. The emitted light from the blackbody was passed through a 100 µm aperture and a chopped at a frequency of 3 kHz. The power spectral density emitted by the blackbody (F) in an FFT bin with size Δλ can be calculated using:

$$F(\lambda) = A_{app}\int_{\lambda}^{\lambda+\Delta\lambda} M_e(673K,\lambda) - M_e(293K,\lambda)\,d\lambda \qquad (3\text{-}3\text{-}1)$$

where A_{app} is the area of the aperture and M_{e} is Planck’s law for spectral exitance and given by:

$$M_e(\lambda,T) = \frac{2\pi hc^2}{\lambda^5\left(e^{hc(k\lambda T)^{-1}} - 1\right)} \qquad (3\text{-}3\text{-}2)$$

Where c is the speed of light and k is the Boltzmann constant. This in conjunction with the measured spectra can be used to find the instrument calibration function. EL imaging was performed at ALS Beamline 2.4 using a 128×128 HgCdTe focal plane array coupled to an FTIR microscope (Agilent). For these measurements the device was operated in air.

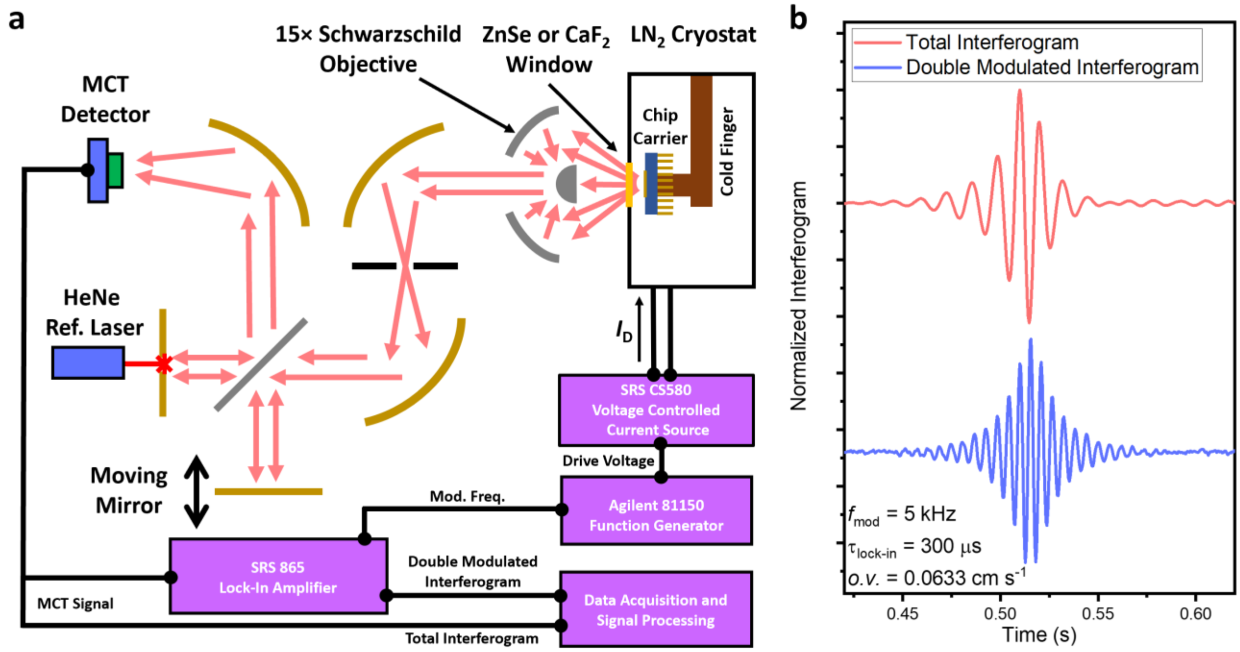

Fig. 3-3-1. **a**, Schematic of experimental setup used for the characterization bP/MoS$_2$ LEDs, consisting of a modified FTIR and electronics to perform double modulation of the emission signal. **b**, The total recorded interferogram resulting from the thermal background as well as the extracted double modulated interferogram.

Optical Simulations

FDTD simulations were performed using a commercial package (FDTD Solutions, Lumerical) using a linearly polarized dipole emitter to simulate emission. For these simulations the mesh grid was set to $\lambda_{el}/1000$, where λ_{el} is the calculated peak emission wavelength of the bP layer. Refractive index values for the band-edge of bP were taken from literature[22]. The region in the bP where the dipole power was measured was set to have a k value of zero.

NDIR Gas Sensor Measurements

The spectra in Figure 3-2-4a showing the absorption of humidity, methane and carbon dioxide were taken as the difference of two separately measured EL spectra. In the first measurement the emitted light was passed through nitrogen gas, while spectra were re-taken in the presence of the target gas/humidity. A line of nitrogen was passed through a bubbler filled with deionized water to raise the relative humidity from 5% to 60% at 22°C. Humidity and temperature were monitored by a commercial sensor Sensirion AG (Model SHT2×). To further analyze the performance of bP/MoS_2 LEDs for use in NDIR sensors, a test cell was constructed where emission from the bP LED is collected by a lens, transmitted through a commercial band pass filter designed for either CO_2 (Andover Corporation) or CH_4 (ThorLabs) NDIR gas sensors, passed through a two inch sealed optical path with feed throughs for analyte gas, and subsequently collected by a commercial InSb photodiode (Teledyne Judson). Synthetic air–diluted CH_4 gas cylinder was purchased from Cal Gas Direct Incorporated at a calibrated concentration of 2.5% and for CO_2 sensing experiment, ultrahigh purity carbon dioxide (Praxair Technology Inc.) was used. Pure dry air was used as diluent gas and was procured from Praxair Technology Inc. Gas delivery was performed using mass flow controllers (Alicat Scientific Inc.). For these measurements background air flow of 10 SLPM was used, and the target gas was delivered at flow rates ranging from 0-100 SCCM and was diluted by dry air with an appropriate flow rate to reach a particular concentration level. For these measurements the devices were directly modulated at a frequency of 1 kHz, and the signal was collected using a lock-in amplifier (Stanford Research Systems). Fractional absorbance (F.A.) of the target gas at particular concentrations was calculated according to F.A. = $(I_{pc,N2}-I_{pc,x})/\ I_{pc,N2}$, where $I_{pc,N2}$ is the photocurrent measured under a nitrogen purge and $I_{pc,x}$ is the photocurrent measured in the presence of gas at concentration x. This data was fit using a modified Beer-Lambert law model as shown in Figure 3-2-4e, where L is the chamber length, and k is a fitting constant related to the passband of the filter and absorption coefficient of the gas. Measured filter filter transmission curves overlaid with the emission spectra for the devices using in Figure 3-2-4.

Transient Electroluminescence Efficiency calculation.

The EL internal efficiency of the t-EL device can be extracted from the ratio of the total number of emitted photons per cycle to the steady-state electron (n_0) and hole (p_0) concentrations:

(3-3-3)

$$\eta_{\mathrm{i}} = \frac{\int_0^T \int_0^L R\, dx\, dt}{(n_{\mathrm{o}} + p_{\mathrm{o}})L} = \beta(\mathrm{PL\ QY})$$

Here T is the time period, L is the length of the device, R is the radiative recombination rate and β is the fraction of steady-state carriers which undergo recombination during a V_{g} transient. The value of (n_0+p_0) can be calculated using 3-3-6. During a -V_{g} to +V_{g} transient (total change of $2V_{\mathrm{g}}$), the net voltage dropped at the Schottky source contact is equal to the sum of the barrier heights to electrons and holes ($\varphi_{\mathrm{Bn}} + \varphi_{\mathrm{Bp}} = E_{\mathrm{g}}$). Thus,

$$(n_{\mathrm{o}} + p_{\mathrm{o}}) = \frac{C_{\mathrm{ox}}\left[2V_{\mathrm{g}} - \left(\varphi_{\mathrm{Bn}} + \varphi_{\mathrm{Bp}}\right) q^{-1}\right]}{q} \tag{3-3-4}$$

To achieve steady-state carrier densities, sufficient voltage must be applied to enable large band bending and thus achieve significant tunneling through the Schottky barriers. As such this equation is only valid for sufficiently high V_{g}. The integral in the numerator is equal to the total number of photons emitted per cycle. The internal efficiency is unity when the PL QY is 100% and all of the steady-state carriers undergo recombination ($\beta = 1$). Practically, due to the finite slew rate of the AC source and a finite radiative recombination rate, a fraction of the steady-state carriers exit the semiconductor through the source contact without recombining ($\beta \neq 1$). The external efficiency is given by:

$$\eta_{\mathrm{e}} = \eta_{\mathrm{i}}\, \eta_{\mathrm{ext}} \tag{3-3-5}$$

where η_{ext} is the light extraction efficiency. This is calculated using $(4n^2)^{-1}$ where n is the refractive index of the medium, as well as the optical interference from the Si substrate with a 50 nm SiO_2 layer. The enhancement factor for Si/SiO_2 is experimentally determined to enhance the light-outcoupling by 1.6× for WSe_2 and 2× for WS_2.

Chapter 4

Infrared photodetectors based on 2D semiconductors

4.1 – Photoconductive black phosphorous/black phosphorous arsenic MWIR detectors[6]

Black phosphorous (b-P), and more recently black phosphorous arsenic alloys (b-PAs), are candidate 2D materials for the detection of mid-wave and potentially long-wave infrared radiation. However, studies to date have utilized laser-based measurements to extract device performance and the responsivity of these detectors. As such, their performance under thermal radiation and spectral response has not been fully characterized. Here, we perform a systematic investigation of gated-photoconductors based on black phosphorous-arsenic alloys as a function of thickness over the composition range of 0% to 91% As. Infrared transmission and reflection measurements are performed to determine the bandgap of the various compositions. The spectrally resolved photoresponse for various compositions in this material system is investigated to confirm absorption measurements, and we find that the cut-off wavelength can be tuned from 3.9 μm to 4.6 μm over the studied compositional range. In addition, we investigated the temperature dependent photoresponse and performed calibrated responsivity measurements using blackbody flood illumination. Notably, we find that the specific detectivity (D*) can be optimized by adjusting the thickness of the b-P/b-PAs layer to maximize absorption and minimize dark current. We obtain a peak D* of 6×10^{10} cm $Hz^{1/2}$ W^{-1} and 2.4×10^{10} cm $Hz^{1/2}$ W^{-1} for pure b-P and b-PAs (91% As) respectively at room temperature, which is an order of magnitude higher than commercially available mid-wave infrared detectors operating at room temperature.

The detection of infrared (IR) light has numerous applications, including thermal imaging, gas sensing, and communication.[1-3] Thermal radiation falls in either the mid-wave (3-5 μm) or long-wave (8-14 μm) spectral bands. Research in detectors for these wavelengths has been dominated by thermal detectors such as bolometers and semiconductor detectors including indium antimonide, mercury cadmium telluride, or type-II quantum wells.[4-7] However, key challenges still exist in both detector types. Specifically, semiconductor detectors typically require cryogenic cooling and complex growth/fabrication processes leading to high costs.[8] On the other hand, while bolometers can achieve room temperature operation at significantly lower costs, they are ultimately limited by slow temporal response, limiting their applications.[7] The key challenge for semiconductor detectors operating in the mid- and long-wave IR bands is the significant thermal generation, which results from the small bandgap requirements (0.3 eV and 0.1 eV

---

[6] Reproduced with permission from M. Amani et al., ACS Nano, 11, 11724-11731, 2017. Copyright © [2017] ACS.

respectively for mid- and long-wave). This in turn results in significant dark currents due to thermal generation.

A potential route to mediate thermal generation within IR photodetectors is to minimize the thickness of the active electronic material. Two-dimensional (2D) materials have potential to accomplish this through both extreme reduction in thickness, as well as the possibility of coupling to nano-optics to increase total absorption.[9,10] Furthermore, 2D materials have naturally passivated surfaces due to the lack of out-of-plane bonding, which can result in high interface quality in the presence of suitable defect passivation and can remove the requirement for a lattice matched substrate.[11,12] Significant research has been performed in this area, with much of the initial work focused on mono- and bilayer graphene; however, these devices suffer from low intrinsic absorption and high dark current due to the absence of a bandgap.[14-16] More recently black phosphorous (b-P) and black phosphorous-arsenic (b-PAs) alloys have emerged as potential 2D semiconductors with suitable bandgaps for IR detection.[17,18] In addition, b-P has been shown to provide other attractive properties, such as high mobility, anisotropic optical properties, and a highly tunable thickness-dependent direct-bandgap over the monolayer to six-layer range.[19-21] Previous studies have demonstrated both photoconductive as well as photovoltaic b-P photodetectors, and have demonstrated that this material system shows high photoconductive gain and a strongly polarized photoresponse.[22-24]

Here, we perform a detailed characterization of gated-photoconductors based on b-P and b-PAs alloys as a function of thickness. The bandgaps of these materials were determined using absorption spectroscopy. Spectrally resolved photoresponse measurements of various compositions were performed for the first time, which are in agreement with absorption measurements. We find that while b-PAs alloys show larger bandgaps than what has been previously estimated from the extinction coefficient, this material system provides full tunability over the mid-IR band. Furthermore, we find these photoconductive detectors show a highly polarized photoresponse, with an extinction ratio greater than 100×. Finally, we measured the responsivity and specific defectivity of these gated photoconductors using flood illumination from a blackbody source and measured a peak D* of 6×10^{10} cm $Hz^{1/2}$ W^{-1} and 2.4×10^{10} cm $Hz^{1/2}$ W^{-1} for pure b-P and b-PAs (91% As) respectively at room temperature.

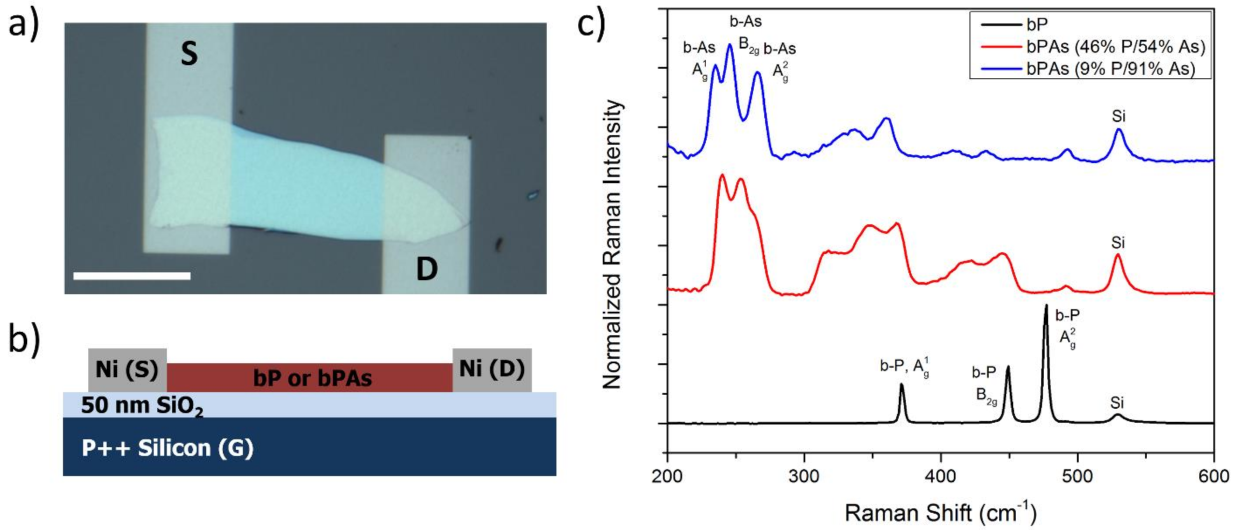

Fig. 4-1-1. (a) Optical microscope image of a typical b-P gated photoconductor with a thickness of 29 nm, the scale bar is 10 μm. (b) Cross-sectional schematic of the gated photoconductor. (c) Raman spectra measured for pure b-P as well as b-PAs alloys.

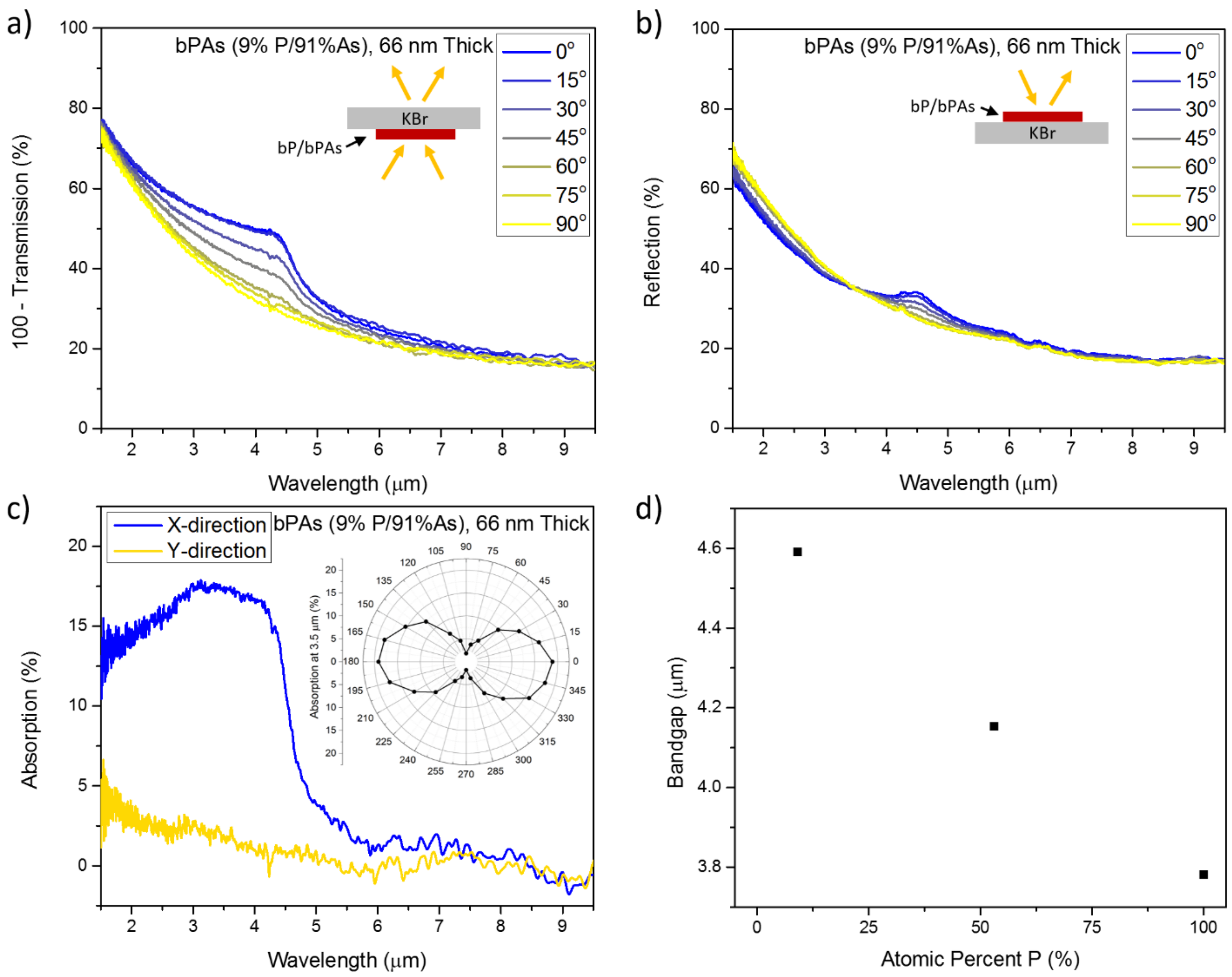

Fig. 4-1-2. (a) Polarization resolved transmission spectra measured for a 66 nm thick b-PAs crystal on a KBr substrate, inset shows the optical configuration used during measurements. (b) Polarization resolved reflection spectra measured for a 66 nm thick b-PAs crystal on a KBr substrate, inset shows the optical configuration used during measurements. (c) Absorption spectra, calculated from 100-T-R, for the b-PAs crystal shown in (a) and (b) along both crystal directions. Inset shows the polarization resolved absorption at a wavelength of 3.5 μm. (d) Bandgap of b-P and b-PAs alloys as a function of P concentration.

Fig. 4-4-1a and Fig. 4-4-1b show an optical image and cross-sectional schematic of the gated-photoconductors fabricated in this study. Multilayer b-P and b-PAs crystals with different As concentrations were exfoliated on Si/SiO_2 substrates with a 50 nm thick oxide in a N_2 glovebox and were coated with PMMA prior to removal from the nitrogen ambient. For device fabrication exposure to air was minimized and critical process steps such as lift-off were performed inside a glovebox with anhydrous solvents. Measurements shown in this work were either carried out in a purged N_2 environment or under vacuum.

Energy dispersive electron spectroscopy (EDS) was performed to verify the compositions of the materials investigated here. In addition, Raman spectroscopy was performed to verify the crystal structure and composition of the various b-PAs crystals. Raman spectra for b-P and b-PAs crystals are shown in Fig. 4-4-1c. For bP-As (91% As), we observe Raman modes at 235.7 cm^{-1}, 247.1 cm^{-1}, and 267.1 cm^{-1}, corresponding to the out-of-plane A_g^1 mode, in-plane B_{2g} mode, and out-of-plane A_g^2 mode of b-As respectively. Additionally, for b-PAs we observe additional peaks over the range of 300 cm^{-1} to 400 cm^{-1}, which have been attributed to varied P-P/As-P/P-As bonding for the alloyed materials. These spectra are consistent with the findings of Liu, *et. al*, who performed both Raman measurements as well as calculations on the expected vibrational modes of b-PAs.[18,20]

Transmission and reflection measurements were performed for crystals transferred onto KBr substrates to determine the bandgap of b-PAs alloys. Polarization resolved transmission and reflection spectra for a b-PAs (91% As) crystal, taken using a Fourier transform infrared spectrometer (FTIR) microscope, are shown in Fig. 4-1-2a and 4-1-2b respectively. The optical path was kept constant for both measurements, and reflection spectra were taken in reference to an Au mirror. From these measurements, we can obtain the absorption coefficient, calculated as 100%-Reflection-Transmission as shown in Fig. 4-1-2c. We observe strongly polarized light absorption along the perpendicular crystal direction, which is consistent with previous reports.[17] The absorption as a function of polarization angle at a wavelength of 3.5 μm is shown in the inset of Fig. 4-1-2c. The bandgap as a function of composition is extracted from the absorption spectra and shown in Fig. 4-1-2d. The bandgap (E_g) of this material system can be tuned from 3.8 μm (326 meV) for pure b-P to 4.6 μm (269 meV) for b-PAs (91% As). It is worthwhile to note that previous measurements on the extinction coefficient of b-PAs alloys suggested a potentially wider range of bandgap tunability (E_g = 150 meV for b-PAs 83% As).[18] This discrepancy can be attributed to utilizing the extinction coefficient to extract E_g, which does not account for reflected light at wavelengths below the bandgap, as can be seen in Fig. 4-1-2a.

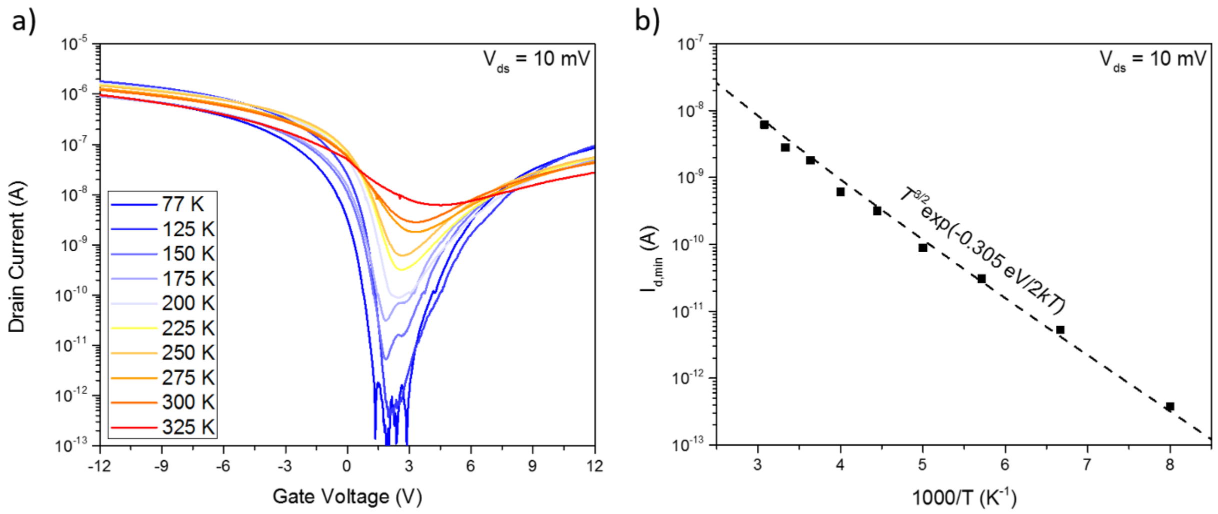

Fig. 4-1-3. (a) Transfer characteristics of an 18 nm thick b-P crystal measured as a function of temperature at a drain bias of 10 mV. Note that a cold shield was utilized for these measurements. (b) Arrhenius plot of minimum drain source current ($I_{\text{d,min}}$) as a function of temperature extracted from panel (a). Dashed line is a fit based on generation-recombination limited dark current.

A critical roadblock for IR detectors is the significant dark current arising from small bandgaps, which places a limit on the noise of the device.[25] Ultimately for mid- and long-wave IR detectors, the performance limit is set by random (4-1-1) background radiation viewed by the device.[25] A key advantage of utili material as the active detector is that the active volume which contributes to thermal generation is reduced per unit area of the device. In addition, for ultra-thin devices the background doping concentration in the semiconductor can be electrostatically tuned with the gate. To understand the source of the noise current as a function of gate voltage for b-P, we performed temperature dependent measurements of the conductance. As shown in Fig. 4-1-3a, we observe a minimum in the dark current at small, positive gate voltages, which indicates that the material is lightly p-doped. Additionally, we see that the Ni contact to these devices is ambipolar indicating that it can inject both electrons and holes. The minimum dark current, corresponding to the gate voltages where the background doping is compensated is plotted in Fig. 4-1-3b. The current from carrier generation-recombination (G-R), $I_{\text{G-R}}$, is proportional to:

$$I_{\mathrm{G-R}} \propto T^{3/2} \exp(-E_{\mathrm{g},0}/2kT)$$

where T is the temperature, $E_{g,0}$ is the effective bandgap, and k is the Boltzmann constant.[26] By fitting the $I_{d,min}$ to the G-R current we extract an effective bandgap of 305 meV. This is in reasonable agreement with values extracted from absorption measurements (326 meV), and is expected to underestimate the bandgap due to contributions from trap states.

Figure 4-1-4a and 4-1-4b show transfer characteristics of a typical 31 nm thick b-P gated photoconductor taken in the dark and under illumination by a 1000 K blackbody with the detector held at 297 K and 77 K respectively. The corresponding responsivity, R is also shown, calculated as I_l-I_d/P, where I_l current measured with the detector illuminated by a 1000 K blackbody, I_d is the current measured with the device viewing a room temperature background, and P is total incident power above the band-edge. From both the transfer characteristics and the photoresponse curves it can readily be seen that the optimum photoresponse is obtained when the device is gated to compensate the background doping electrostatically. The spectral photoresponse of the b-P photoconductor was measured using the experimental setup shown in Fig. 4-4-1. Here, illumination from the same 1000 K blackbody is modulated using a FTIR spectrometer, and the measured spectra at 77 K and 297 K (at a gate voltage of 3.8V) is shown in Fig. 4-1-4c. The gate dependent photoresponse extracted from spectral response measurements is shown in Fig. 4-1-4d and is in good agreement with the measurements shown in Fig. 4-1-4a and 4-1-4b. We can observe a clear absorption edge for the b-P detector, corresponding to the material's bandgap. The cut-off wavelength, λ_{co} (defined as wavelength at which responsivity drops by 50%), for this device at room temperature is 3.91 μm and is in very good agreement with the E_g value fitted from reflection/transmission measurements.

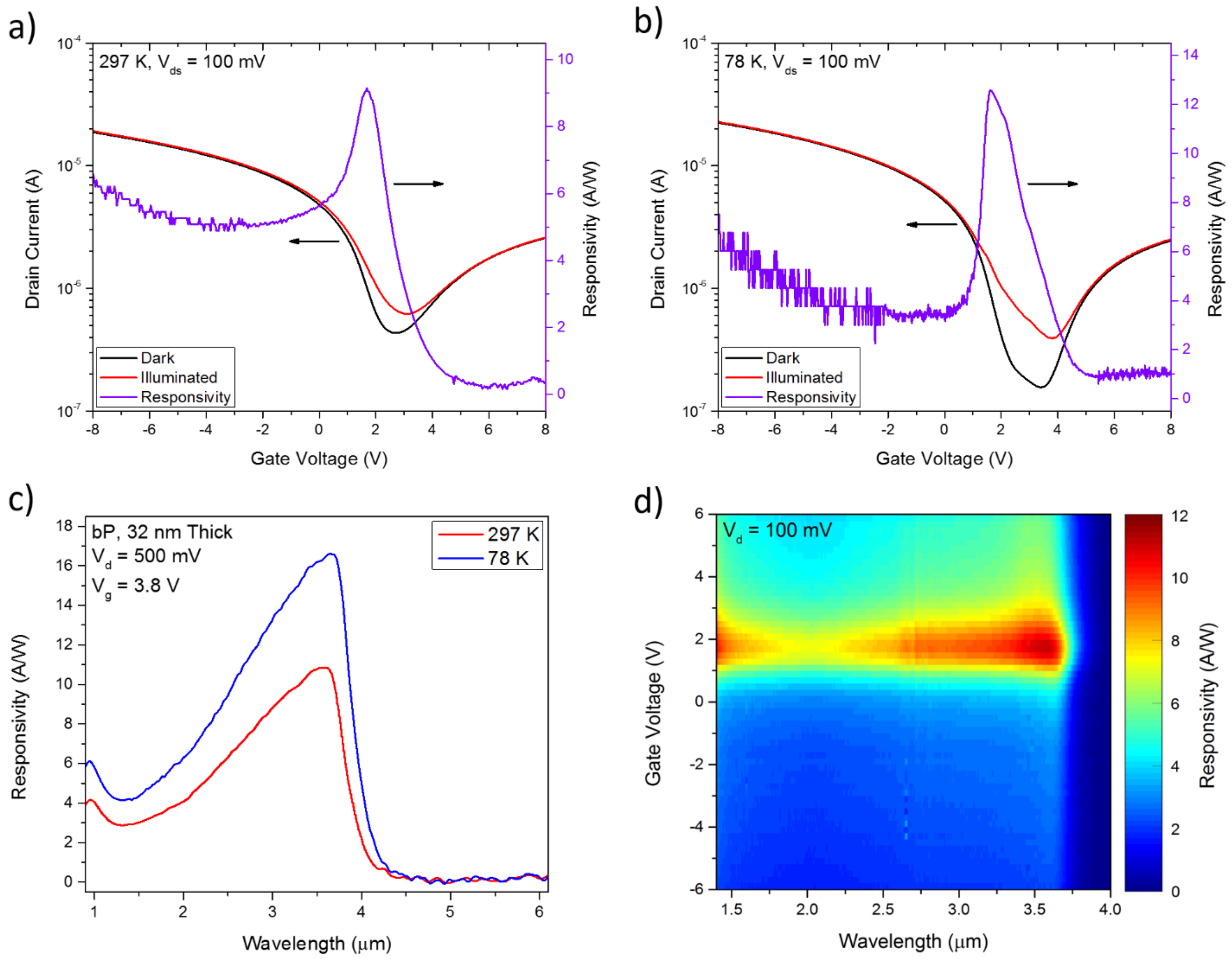

Fig. 4-1-4. (a) Transfer characteristics of a 29 nm thick b-P gated photoconductor measured under dark and illumination from a 1000 K blackbody with the device at 297 K. (b) Transfer characteristics of a 29 nm thick b-P gated photoconductor measured under dark and illumination from a 1000 K blackbody with the device at 77 K. Note that a cold shield was not present for dark measurements. (c) Broadband spectral photoresponse of the device shown in (a) and (b), measured at 297 K and 77 K. (b) Gate voltage dependence of the spectral photoresponse, measured at 297 K.

The frequency response as well as the rise and fall time were measured using a directly modulated laser diode (λ = 980 nm) and are shown in Fig. 4-1-5a and 4-1-5b. We measure a rise and fall time of 12.4 μs and 8.6 μs, respectively. The 3 dB bandwidth is extracted from Fig. 4-1-5b to be 117 kHz. From this analysis, we can estimate the photocarrier lifetime, τ_0, from $f_{\mathrm{3dB}} = 1/2\pi\tau_0$ to be 1.4 μs. Additionally, we can calculate the carrier transit time, τ_{tr}, from the field-effect mobility (μ_{fe}) for this device (596 cm^2 V^{-1} s^{-1}) which is estimated using $\mu_{\mathrm{FE}} = \left(dI_{\mathrm{d}}/dV_{\mathrm{g}}\right)(L/W)/(V_{\mathrm{d}}C_{\mathrm{ox}})$, where L, W, and C_{ox} are the length, width and oxide capacitance of the device respectively. Subsequently, the τ_{tr} is calculated to be 8.2 ns using: $\tau_{\mathrm{tr}} = L^2/(\mu_{\mathrm{FE}}V_{\mathrm{d}})$. From this we can estimate the photoconductive gain (G) to be 54 at a bias voltage of V_{d} = 100 mV.

The quantum efficiency of the device can be calculated utilizing the measured responsivity and the gain according to:

$$R(\lambda) = \frac{q\eta\lambda G}{hc} \qquad \text{(4-1-2)}$$

where q is the electron charge, η is the quantum efficiency, h is Plank's constant, and c is the speed of light.[27] We obtain a quantum efficiency of 6.4% for unpolarized incident light. This value is found to be reasonable based on reflection measurements taken on the same device, which indicates that ~8% of incident light is absorbed by the device at λ = 980 nm and is thus able to contribute to the photocurrent.

The noise current density for a typical device operated at $I_{\mathrm{d,min}}$ as a function of frequency (f) is shown at room temperature and 77 K in Fig. 4-1-5c. We can observe that the low frequency behavior (f < 150 Hz) is dominated by 1/f flicker noise both at room temperature and 77K.[27,28] This behavior is often observed in photoconductive detectors, as well as in previous b-P transistors and photoconductors and is attributed to charge trapping/de-trapping. At moderate frequencies the total noise current is the sum of contributions from Shot, G-R, and Johnson noise. For this device under low intensity illumination, Shot noise is expected to dominate (as can be seen from temperature dependent measurements in Fig. 4-1-3b) and is given as: $\langle i_{\mathrm{S}}^2\rangle = 2qI_{\mathrm{G-R}}\Delta f$, where q and $I_{\mathrm{G\text{-}R}}$ are the electron charge and G-R current respectivly.[28,29]

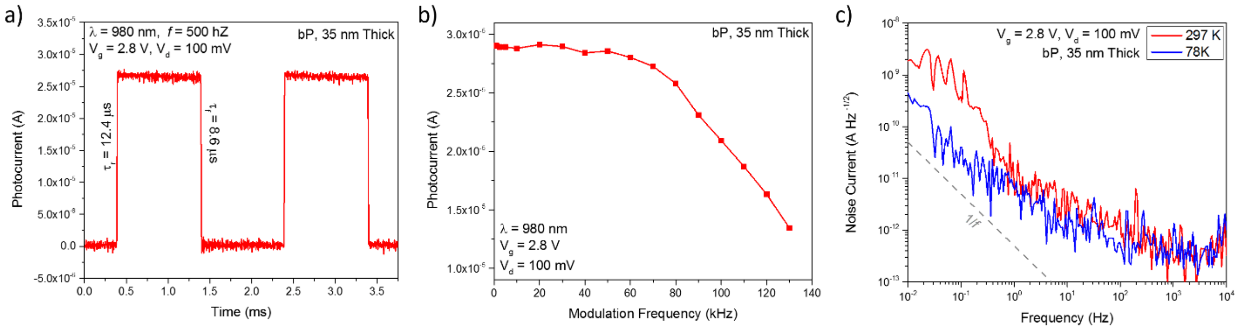

Fig. 4-1-5. (a) Room temperature temporal photoresponse of a 35 nm thick b-P photoconductor, excited by a 980 nm laser modulated at 50 kHz. (b) Photocurrent versus modulation frequency measured at an incident power of 15 nW measured at room temperature, showing a 3 dB frequency of 117 kHz. (c) Noise spectrum measured for a 35 nm thick b-P photoconductor at room temperature and 77 K; dashed line shows a reference 1/*f* curve.

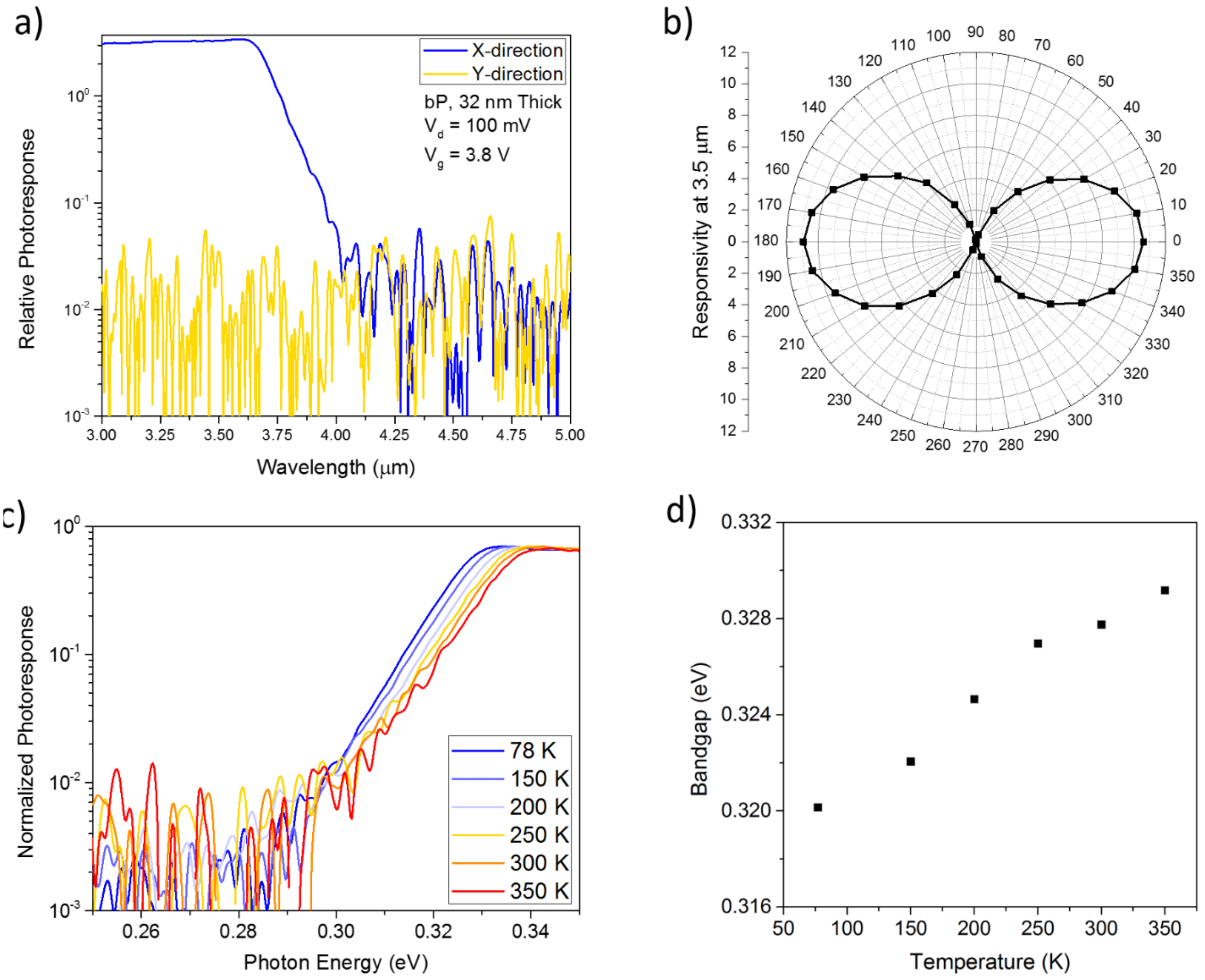

Fig. 4-1-6. (a) Relative response of a b-P photoconductor measured for incident light polarized along (x-direction, arm-chair) and perpendicular to (y-direction, zig-zag) the absorbing axis of the b-P crystal. (b) Responsivity of the device shown in panel (a) as a function of polarizer angle. (c) Normalized photoresponse of a b-P photodetector measured as a function of temperature. (d) Extracted bandgap from the spectral photoresponse as a function of device temperature.

As shown previously in Fig. 4-1-2c, b-P shows a highly polarized absorption, and previous studies have shown that under visible illumination b-P photoconductors show a preferential response to light polarized along the x-direction (arm-chair direction).[20,22,23] We measured the polarization dependence of a b-P gated-photoconductor by placing a linear BaF_2 wire-grid polarizer in the FTIR beam path directly in front of the b-P gated-photoconductor. As expected from the highly polarized absorption spectra of b-P, there is strong anisotropicity in the photoresponse for polarization aligned to and against the crystal orientation of the b-P. We find that the polarization ratio between the two crystal orientations at mid-infrared wavelengths is over 100×. It is important to note that this value is limited by the dynamic range of the FTIR and is approaching the extinction ratio of the polarizer used in this study. The polarization resolved photoresponse measured for 3.5 μm incident light is shown in Fig. 4-1-6a and 4-1-6b. The spectral photoresponse, measured as a function of temperature for a b-P photoconductor is shown in Fig. 4-1-6c. Interestingly, we observe that the cut-off wavelength of the device extends to lower photon energies as the temperature is reduced. While this is the opposite from the behavior typically observed in most semiconductors, it is consistent with the calculated bandgap for b-P which has been predicted to show decreasing E_g with temperature due to its negative pressure coefficient and strong electron-photon coupling.[30,31] The extracted bandgap values from the spectral photoresponse are shown in Fig. 4-1-6d.

Finally, we investigated the specific detectivity of b-P and b-PAs photoconductors. The generic expression for specific detectivity is given by:

$$D^* = \frac{\sqrt{A\Delta f}}{NEP} = \frac{R\sqrt{A\Delta f}}{i_\mathrm{n}} \tag{4-1-3}$$

where A is the detector area, Δf is the integration time, NEP is noise equivalent power, and i_n is the noise current.[27,32] In the ideal case for photoconductors, the i_n is limited by shot noise and can be calculated from dark resistance of the device. However, this generally provides a strong overestimation of D*. For the purpose of this work we utilized the experimentally measured noise current for all D* calculations, which are taken at a modulation frequency of 150 Hz to minimize the contribution of $1/f$ noise. The specific detectivity measured for b-P as a function of thickness under illumination by a 673 K blackbody using the setup shown in Fig. 4-4-3 is shown in Fig. 4-1-7a. We found that the optimum thickness for maximizing D* was 25-35 nm thick, which balanced the increased absorption for thicker layers and the reduced dark current and thermal- thinner layers. The thickness dependence of D* can be understood from equation 4, which assumes a constant device area, that responsivity is directly proportional to absorption in the material, and the photoconductive gain is thickness independent.

$$D^* \propto \frac{signal}{noise} \propto \frac{(1 - e^{-\alpha t})}{\langle i_\mathrm{S}^2 \rangle + \langle i_\mathrm{J}^2 \rangle + N_e} \tag{4-1-4}$$

Here, α is the absorption coefficient, t is the thickness, $\langle i_J^2 \rangle$ is the Johnson noise, and N_e is excess noise. In the ideal case $\langle i_\mathrm{S}^2 \rangle$ and $\langle i_\mathrm{J}^2 \rangle$ are proportional to the active semiconductor thickness; however, in practice the excess noise contribution dominates in the limit case when t approaches zero, leading to an optimal device thickness. Figure 4-1-7b shows the specific detectivity as a function of wavelength for b-P and b-PAs gated photoconductors, fabricated with the optimized thickness. We obtain a peak room temperature D* of 6×10^{10} cm $\mathrm{Hz}^{1/2}$ W^{-1} and 2.4×10^{10} cm $\mathrm{Hz}^{1/2}$ W^{-1} for pure b-P and b-PAs (91% As) respectively from the measured noise current.

In summary, we have investigated the spectral performance of b-P and b-PAs gated-photoconductors as a function of thickness and composition. We find that the specific detectivity of these devices can be significantly improved by tuning the thickness. For optimized devices, with a thickness of ~28 nm, we obtain peak D* of 6×10^{10} cm $\mathrm{Hz}^{1/2}$ W^{-1} for b-P and 2.4×10^{10} cm $\mathrm{Hz}^{1/2}$ W^{-1} for b-PAs (91% As) at room temperature with a bandwidth of 117 kHz. This detectivity is an order of magnitude greater than commercial devices operating at room temperature.[1-3,32] In addition these devices show very strong sensitivity to the polarization of incident light, with an extinction ratio >100× which is comparable to traditional polarization optics. However, we found from both transmission/reflection and spectrally resolved photoresponse measurements that the bandgap tunability of the b-PAs material system is smaller than what was initially estimated and is limited to midwave-IR spectral band.[18] As such, other techniques of reducing the bandgap in b-PAs or new 2D materials still need to be investigated to achieve longwave-IR photodetection.

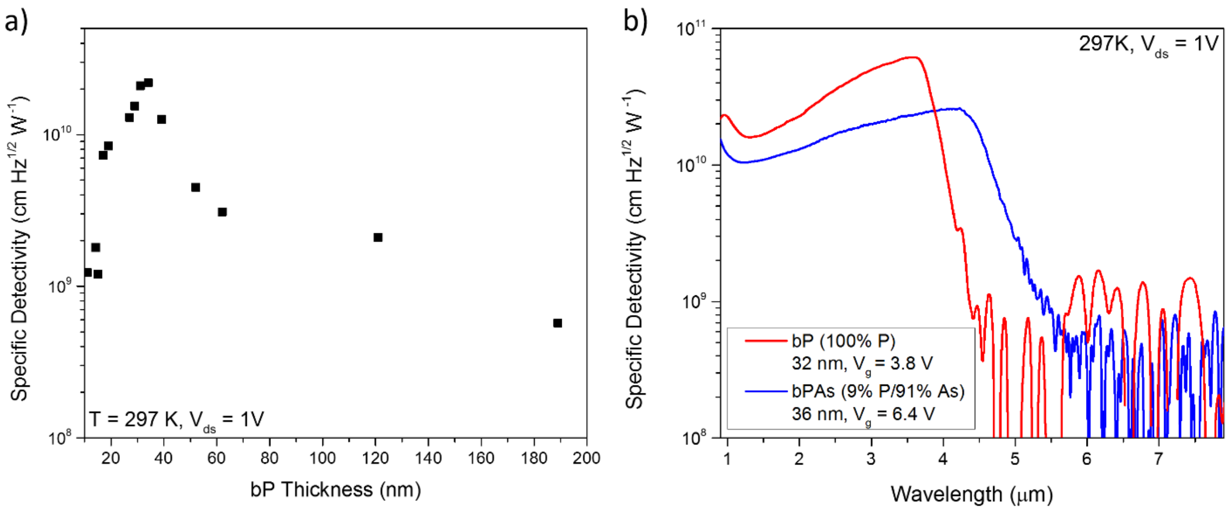

Fig. 4-1-7. (a) Specific detectivity of b-P photoconductors as a function of layer thickness; measurements were performed under gating conditions which maximized the detectivity for the specific device at room temperature. (b) Specific detectivity of b-P and b-PAs photoconductors with optimized thickness; measurements were performed under gating conditions which maximized detectivity for the specific device at room temperature.

References for Section 4-1

1. Razeghi, M.; Nguyen, B.-H. Advances in Mid-Infared Detection and Imaging: A Key Issues Review. *Rep. Prog. Phys.* **2014**, 77, 082401.
2. Barve, A. V.; Lee, S. J.; Noh, S. K.; Krishna, S. Review of Current Progress in Quantum Dot Infrared Photodetectors. *Laser Photon. Rev.* **2009**, 4, 738-750.
3. Piotrowski, J.; Rogalski, A. Uncooled Long Wavelength Infrared Photon Detectors. *Infar. Phys. Technol.* **2004**, 46, 115-131.
4. Kimukin, I.; Biyikli, N.; Ozbay, E. InSb High-Speed Photodetectors Grown on GaAs Substrates. *Apl. Phys. Lett.* **2003**, 94, 5414-5416.
5. Norton, P. HgCdTe Infrared Detectors. *Opto-Electron. Rev.* **2002**, 10, 159-174.
6. Hoang, A. M.; Dehzangi, A.; Adhikary, S.; Razeghi, M. High Performance Bias-Selectable Three-Color Short-Wave/Mid-Wave/Long-Wave in Infrared Photodetectors Based on Type-II InAs/GaSb/AlSb Superlattices. *Sci. Rep.* **2016**, 6, 24144.
7. Niklaus, F.; Vieider, C.; Jakobsen, H. MEMS-Based Uncooled Infrared Bolometer Arrays – A Review. **2007**, 6836, 68360D-1.
8. Rogaloski, A. HgCdTe Infrared Detector Material: History, Status and Outlook. *Rep. Prog. Phys.* **2005**, 68, 2267-2336.
9. Xia, F.; Wang, H.; Xiao, D.; Dubey, M.; Ramasubramaniam, A. Two-Dimensional Material Nanophononics. **2014**, 8, 899-907.
10. Lin, Z.; McCreary, A.; Briggs, N.; Subramanian, S.; Zhang, K.; Sun, Y.; Li, X.; Borys, N. J.; Yuan, H.; Fullerton-Shirey, S. K.; Chernikov, A.; Zhao, H.; McDonnell, S.; Lindenberg, A. M.; Xiao, K.; LeRoy, B. J.; Drndic, M.; Hwang, J. C. M.; Park, J.; Chhowalla, M.; *et al.* 2D Materials Advances: From Large Scale Synthesis and Controlled Heterostructures to Improved Characterization Techniques, Defects and Applications. *2D Mater.* **2016**, 3, 042001.
11. Amani, M.; Lien, D.-H.; Kiriya, D.; Xiao, J.; Azcatl, A.; Noh, J.; Madhvapathy, S. R.; Addou, R.; Kc, S.; Dubey, M.; Cho, K.; Wallace, R. M.; Lee, S.-C.; He, J.-H.; Ager, J. W.; Zhang, X.; Yablonovitch, E.; Javey, A. Near-Unity Photoluminescence Quantum Yield in MoS_2. *Science* **2015**, 350, 1065–1068.
12. Amani, M.; Taheri, P.; Addou, R.; Ahn, G. H.; Kiriya, D.; Lien, D.-H.; Ager, J. W.; Wallace, R. M.; Javey, A. Recombination Kinetics and Effects of Superacid Treatment in Sulfur- and Selenium Based Transition Metal Dichalcogenides. *Nano Lett.* **2016**, 16, 2786-2791.
13. Koppens, F. H. L.; Mueller, T.; Avouris, P. H.; Ferrari, C.; Vitiello, M. S.; Polini, M. Photodetectors Based on Graphene, Other Two-Dimensional Materials, and Hybrid Systems. *Nat. Nanotechnol.* **2014**, 9, 780-793.
14. Zhang, Y.; Liu, T.; Meng, B.; Li, X.; Liang, G.; Hu, X.; Wang, Q. J. Broadband High Photoresponse from Pure Monolayer Graphene Photodetector. *Nat. Comm.* **2013**, 4, 1811.
15. Liu, C.-H.; Chang, Y.-C.; Norris, T. B.; Zhong, Z. Graphene Photodetectors with Ultra-Broadband and High Responsivity at Room Temperature. *Nat. Nanotechnol.* **2014**, 9, 273-278.
16. Yan, J.; Kim, M.-H.; Elle, J. A.; Sushkov, A. B.; Jenkins, G. S.; Milchberg, H. M.; Fuhrer, M. S.; Drew, H. D. Dual-Gated Bilayer Graphene Hot-Electron Bolometer. *Nat. Nanotechnol.* **2012**, 7, 472-478.
17. Ling, X.; Wang, H.; Huang, S.; Xia, F.; Dresselhaus, M. S. The Renaissance of Black Phosphorus. *Proc. Nat. Acad. Sci.* **2015**, 112, 4523-4530.
18. Liu, B.; Kopf. M.; Abbas, A. N.; Wang, X.; Guo, Q.; Jia, Y.; Xia, F.; Weihrich, R.; Bachhuber, F.; Pielnhofer, F.; Wang, H.; Dhal, R.; Cronin, S. B.; Ge, M.; Fang, X.; Nilges, T.; Zhou, C. Black Arsenic-Phosphorus: Layered Anisotropic Infrared Semiconductors with Highly Tunable Compositions and Properties. *Adv. Mat.* **2015**, 27, 4423-4429.
19. Qiao, J.; Kong, X.; Hu, Z.-X.; Yang, F.; Ji, W. High-Mobility Transport Anisotropy and Linear Dichroism in Few-Layer Black Phosphorous. *Nat. Comms.* **2014**, 5, 4475.
20. Wang, X.; Jones, A. M.; Seyler, K. L.; Tran, V.; Jia, Y.; Zhao, H.; Wang, H.; Yang, L.; Xu, X.; Xia, F. Highly Anisotropic and Robust Excitons in Monolayer Black Phosphorus. *Nat. Nanotechnol.* **2015**, 10, 517-521.
21. Tran, V.; Soklaski, R.; Liang, Y.; Yang, L. Layer-Controlled Band Gap and Anisotropic Few-Layer Black Phosphorous. *Phys. Rev. B.* **2014**, 89, 235319.
22. Guo, Q.; Pospischil, A.; Bhuiyan, M. Jiang, H.; Tian, H.; Farmer, D.; Deng, B.; Li, C.; Han, S.-J.; Wang, H.; Xia, Q.; Ma, T.-P. Mueller, T.; Xia, F. Black Phosphorus Mid-Infrared Photodetectors with High Gain. *Nano Lett.* **2016**, 16, 4648-4655.
23. Yuan, H.; Liu, X.; Afshinmanesh, A.; Li, W.; Xu, G.; Sun, J.; Lian, B.; Curto, A. G.; Ye, G.; Hikita, Y.; Shen, Z.; Zhang, S.-C.; Chen, X.; Brongersma M.; Hwang, H. Y.; Cui, Y. Polarization-Sensitive Broadband Photodetector

using a Black Phosphorus Vertical p-n Junction. *Nat. Nanotechnol.* **2015**, 10, 707-713.

24. Miao, J.; Zhang, S.; Cai, L.; Wang, C. Black Phosphorus Schottky Diodes: Channel Length Scaling and Application as Photodetectors. *Adv. Electron. Mat.* **2016**, 2, 1500346.
25. Piotrowski, J.; Gawron, W. Ultimate Performance of Infrared Photodetectors and Figure of Merit of Detector Material. *Infar. Phys. Technol.* **1997**, 38, 63-68.
26. Martyniuk, P.; Antoszewski, J.; Martyniuk, M.; Faraone, L.; Rogalski, A. New Concepts in Infrared Photodetector Designs. *Appl. Phys. Rev.* **2014**, 1, 041102.
27. Petritz, R. L. Theory of Photoconductivity in Semiconductor Film. *Phys. Rev.* **1956**, 104, 1508-1516.
28. Beck, W. A. Photoconductive Gain and Generation-Recombination Noise in Multiple-Quantum-Well Infrared Detectors. *Appl. Phys. Lett.* **1993**, 63, 3589-3591.
29. Ye, Z.; Campbell, J. C.; Chen, Z.; Kim, E.-T., Madhukar, A. Noise and Photoconductive Gain in InAs Quantum-Dot Infrared Photodetectors. *Appl. Phys. Lett.* **2003**, 83 (6), 1234-1236.
30. Villegas, C. E. P.; Rocha, A. R.; Marini, A. Anomalous Temperature Dependence of the Band Gap in Black Phosphorus. *Nano Lett.* **2016**, 16, 5095-5101.
31. Villegas, C. E. P.; Rodin, A. S.; Carvalho, A.; Rocha, A. R. Two-Dimensional Exciton Properties in Monolayer Semiconducting Phosphorus Allotropes. *Phys. Chem. Chem. Phys.* **2016**, 18, 27829.
32. Vincent, J. D. Fundamentals of Infrared Detector Operation and Testing. Wiley, New York (1990).

4.2 – Photovoltaic black phosphorous MWIR detectors[7]

We utilize bP / MoS_2 heterostructures to fabricate photodiodes and optimize the devices for detection of MWIR light intensity and polarization at room temperature. To optimize the collection of light, we perform in-depth characterization of bP, and report, for the first time, the complex refractive index of this material in a wavelength range that encompasses the MWIR. This information is used to design and fabricate a simple optical structure which deliberately utilizes destructive interference to efficiently couple in a narrow band of MWIR light – permitting the demonstration of a high quantum efficiency bP / MoS_2 photodiode. Finally, we demonstrate a bias-selectable polarization resolved bP photodetector, utilizing two orthogonally aligned bP / MoS_2 photodiodes, monolithically integrated to create a device which directly measures both the intensity and polarization of incoming MWIR light.

Two primary figures of merit for photodetectors are their external quantum efficiency (η_e) and specific detectivity (D^*).[1-5] These parameters are optimized by increasing the percentage of incident photons which generate photocurrent as well as via reduction of the electronic noise. As such, simultaneous optimization of η_e and D^* requires consideration of both optical and electrical design. A schematic showing the structure of the heterojunction photodiodes fabricated in this work as well as an example optical micrograph are shown in Fig. 4-2-1a and 4-2-1b, respectively. The device consists of a bP / MoS_2 heterojunction where a thin (~10-20 nm) n-type MoS_2 layer acts as an electron selective-contact and MWIR window. Holes are contacted via a rear Au pad, which simultaneously acts as a MWIR back reflector. As shown schematically in the simulated band diagram of Fig 4-2-1c, the MoS_2 heterojunction provides asymmetric band offsets with the bP, allowing the flow of electrons to the MoS_2 contact while blocking the flow of holes. A false colored transmission electron micrograph (TEM) of a completed device is shown in Fig. 4-2-1d. In addition, high resolution TEM images of the bP / MoS_2 and bP / Au interfaces are shown in Fig. 4-2-1e and 4-2-1f, respectively. The layered structure of bP and MoS_2 can be seen with corresponding monolayer thicknesses of 5.5 Å and 6 Å, respectively. A thin amorphous layer can also be observed at both interfaces, most prominently at the bP / Au interface. This is attributed to PO_x from surface oxidation, which forms during periods of atmospheric exposure while fabricating devices.[6] This layer could introduce adverse effects to the device performance particularly to collection efficiency, as it obscures the selective contacts, and its response time, due to the defective nature of the PO_x layer.

---

[7] Reproduced with permission from J. Bullock, M. Amani et al., Nature Photonics, 12, 601-607, 2018. Copyright © [2018] Springer Nature.

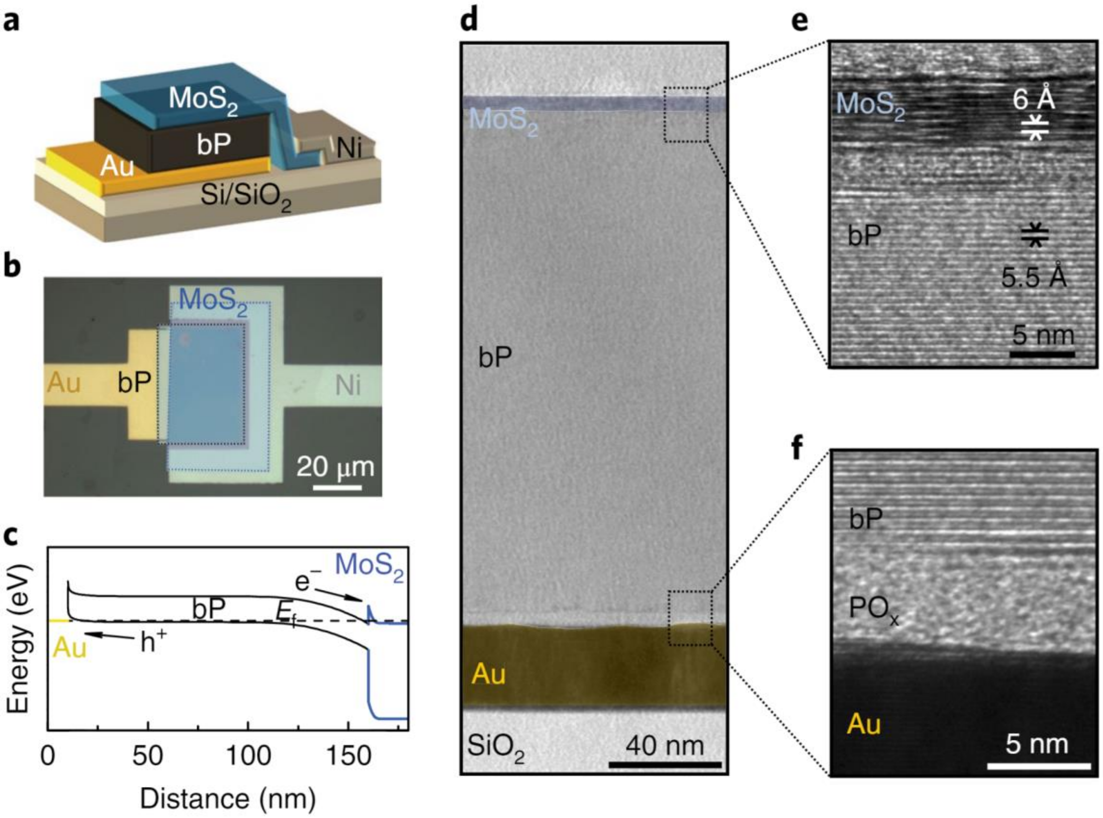

Fig. 4-2-1 bP/MoS$_2$ heterojunction photodiode concept. a, Schematic of device configuration, showing the heterojunction and contact configuration. b, Optical micrograph of a completed device, regions containing bP and MoS$_2$ are outlined for clarity. c, Simulated energy band diagram of the device under equilibrium. d, Cross-sectional TEM image of a completed photodiode. e, High resolution cross-sectional TEM image showing the bP/MoS$_2$ interface. f, High resolution cross-sectional TEM image showing the bP/Au interface.

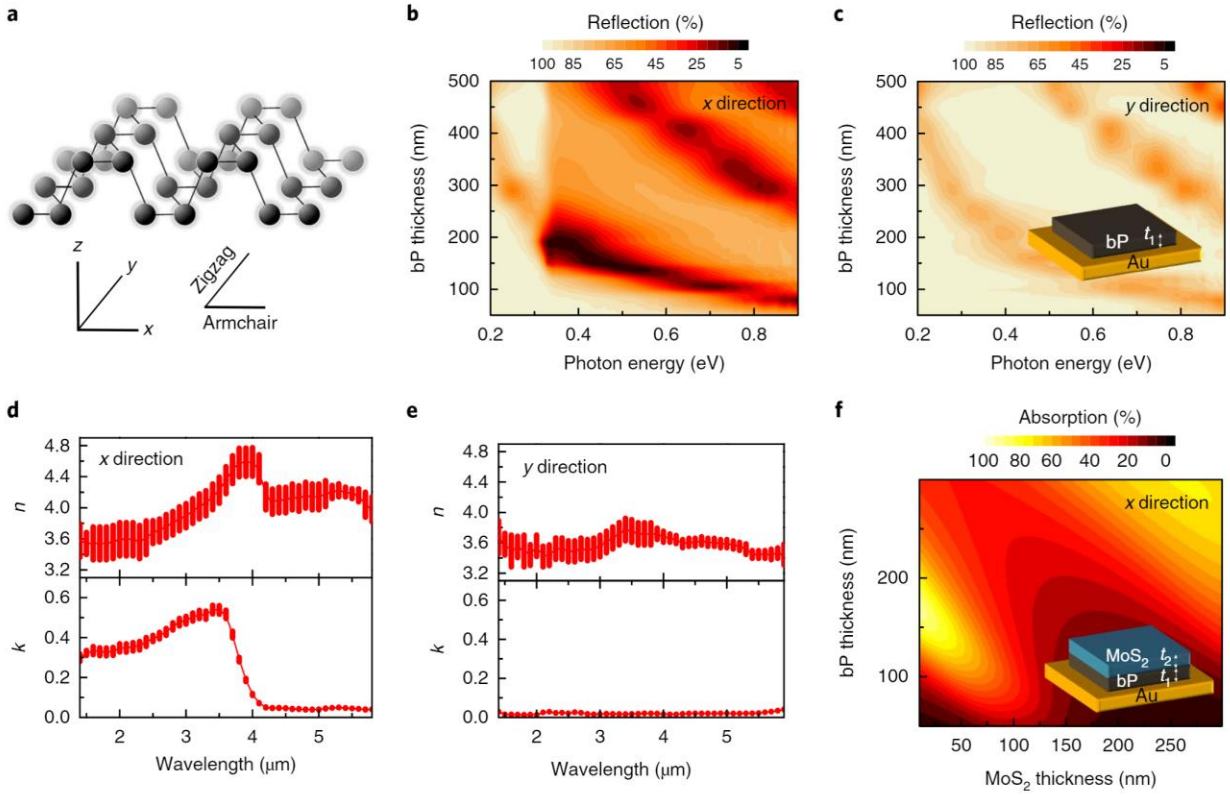

Fig. 4-2-2 Infrared optical constants of bP. a, Schematic diagram of bP crystal structure, b, Reflection of bP on Au, measured for crystals with thickness ranging from 50 nm to 500 nm with the polarizer aligned in the *x*-direction. c, Reflection of bP on Au, measured for crystals with thickness ranging from 50 nm to 500 nm with the polarizer aligned in the *y*-direction. d, Extracted complex refractive index of bP in the *x*-direction. e, Extracted complex refractive index of bP in the *y*-direction. Error bars in d and e are based on the deviation between the modelled and measured reflection at each wavelength. f, Modelled absorption in bP layer, for a bP / MoS_2 stack on Au, as a function of the bP and MoS_2 layer thicknesses.

Losses due to reflection limit the fraction of incident light that can be absorbed and are a strong function of both the bP and MoS_2 layer thicknesses. The reflection and absorption in the device can be modelled utilizing the complex refractive index (n, k) of the two materials. While broadband values of n and k have been reported for MoS_2, only the visible refractive index has been characterized for bP to date.[7-17] The anisotropic crystalline structure of bP, shown in Fig 4-2-2a, results in polarization dependent optical properties (referred to as linear dichroism). Light impinging with an electrical field parallel to the x-axis, or arm-chair direction, sees a sharp absorption onset at the bulk bP band edge of ~0.31 eV.[6,7,18] Absorption of polarised light aligned to the y-axis or zig-zag direction, however, is symmetry-forbidden at the ~0.31eV band edge and substantially weaker at higher energy wavelengths.[7,8,19] This has been confirmed experimentally for bulk bP from MWIR to visible wavelengths.[5,7,20] To extract an effective n and k for the x-and y-directions in bP, polarized IR reflection measurements were performed on bP crystals with varying thickness, ranging from 50 nm to 500 nm, on Au substrates. The combined interpolation of these polarized reflection measurements is shown in Fig. 4-2-2b and 4-2-2c for incident polarizations aligned along the x- and y-axis of bP, respectively.

For polarized illumination aligned to the x-direction, a clear drop in reflection can be seen at photon energies above 0.31 eV for all thicknesses. This is a result of the onset of absorption at the band edge of bP. As expected, no such sharp step is seen for the y-direction in Fig. 4-2-2c. Refractive index values are obtained using the transfer matrix method,[21] to fit a model of the thickness (t) dependent reflection $R_{\text{model}}(t)$ to the measured reflection $R_{\text{meas}}(t)$ at each wavelength. The model is based on a bP / Au stack and assumes that the refractive index is thickness independent across the measured thickness range (50 – 500 nm). This assumption is based on the predicted saturation of the layer dependent band-structure of bP above ~8 layers,[6] and also further demonstrated by fitted reflection measurements. The extracted n and k values for the x-direction and y-direction are provided in Fig. 4-2-2d and 4-2-2e, respectively. For light polarized in the x-direction a pronounced step in the extinction coefficient, k, is observed at $\lambda = 3.8$ μm which corresponds well to the expected band edge of bP.

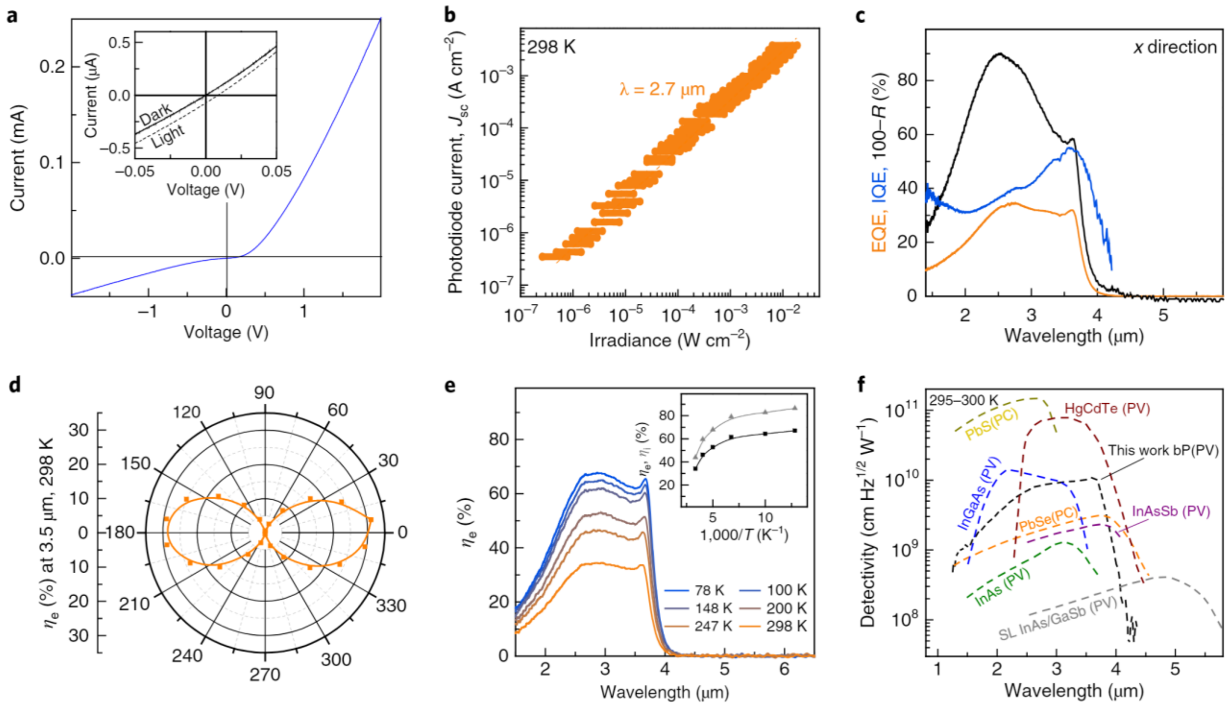

Fig. 4-2-3 Photoresponse and detectivity. a, *IV* curve of a bP/MoS_2 heterojunction photodiode; inset shows measurement taken in the dark and under illumination by a 1000 K blackbody source. b, Measured photocurrent as a function of incident illumination intensity. Excitation is performed with a λ = 2.7 μm laser diode. Error bars are based on the uncertainty in the laser spot size, c, spectrally dependent η_e, η_i and 100%-*R* for a bP / MoS_2 heterojunction photodiode, d, measured η_e at λ=3.5 μm as a function of polarisation angle, e, Spectral η_e as a function of temperature. Inset shows η_e and η_i at λ=3 μm as a function of temperature. f, Specific detectivity as a function of wavelength measured for a bP / MoS_2 heterojunction at room temperature as well as various commercially available and reported MWIR photodetectors. All FTIR and laser diode characterisation was performed at a bias of 0 V.

With these n and k values, we use the transfer matrix method to simulate the absorption of the photodiode in the x-direction. Ideally from an electrical standpoint, the thickness of the bP layer should be minimized in order to reduce noise resulting from generation-recombination as well as to improve the carrier extraction efficiency. However, from an optical perspective, absorption within the bP layer, which is small for very thin layers, should be maximized. To obtain a compromise between these two requirements, the bP absorption, averaged between λ = 2.5-3.8 μm, is simulated as a function of the bP and MoS_2 layer thicknesses. A contour plot of the modelled absorption is provided in Fig. 4-2-2f. The periodic absorption behavior is associated with changes in front surface reflection due to thickness dependent constructive and destructive interference of MWIR light. A local maximum in absorption is seen for bP layers with a thickness of 170 nm on Au, with an MoS_2 thickness of zero. This corresponds to the expected quarter wavelength minima in reflection, and hence interference effects can be used to provide a compromise between minimizing thickness and maximizing absorption. Given that an MoS_2 layer with sufficient lateral conductivity is required to collect electrons, we choose an optimum device configuration of bP (~150 nm) / MoS_2 (15 nm). With this optical design ~80% of incident light polarized in the x-direction at λ = 3 μm can be absorbed in the bP layer. We emphasize that, in terms of device thickness, this detector bridges the gap between conventional 2D material photodetectors and traditional bulk semiconductor detectors. Resultantly, it inherits benefits from both of these two detector classes, such as increased absorption as well as being free of surface dangling bonds.

The *IV* characteristics of a typical bP / MoS_2 heterojunction photodiode, measured at 300 K with no illumination, is provided in Fig. 4-2-3a and shows the expected rectifying behavior of a diode formed using a narrow bandgap material. The inset of Fig. 4-2-3a compares the measured *IV* behavior with and without illumination from a 1000 K unpolarized blackbody source. The generation of photocarriers shifts the *IV* curve downwards, resulting in an open circuit voltage V_{oc} and short circuit current I_{sc}, confirming that the device is operating in the photovoltaic mode. Figure 4-2-3b shows the relationship between the short circuit current density J_{sc} and incident optical power density from a λ = 2.7 μm laser diode source. The device shows the expected linear increase in photocurrent as a function of incident light power density over the full measurement range, which spans five orders of magnitude. Similar results are found using a λ = 1.6 μm illumination source.

The quantum efficiency of the device is measured under x-direction polarized illumination using a calibrated Fourier transform infrared spectrometer (FTIR), the setup of which is described in section 4-4. As shown in Fig 4-2-3c, the bP / MoS_2 photodiode shows an external quantum efficiency η_e of ~30-35% from λ=2.5-3.5 μm. These are the highest η_e values reported for bP in this range at room temperature and correspond to current responsivity values of ~0.9 A/W. Also presented in Fig 4-2-3c is the measured reflection R, plotted as 100%-R. The narrow spectral band of MWIR light coupled into the absorber corresponds to the targeted quarter wavelength interference feature with its peak occurring just below λ=3 μm. From η_e and R, the internal quantum efficiency (η_i) can also be calculated according to: $\eta_i(\lambda) = \eta_e(\lambda)/(100 - R(\lambda))$, yielding a value of 40-50% at room temperature. The polarization dependence of η_e at λ = 3.5 μm, as a function of polarization angle, is provided in the polar plot of Fig. 4-2-3d. It can be seen that as the polarization angle is changed from 0^o (aligned with the *x*-axis) to 90^o (aligned to the *y*-axis) a decrease in η_e, from greater than 30% to less than 1%, is measured. That the η_e for *x*-polarized light is substantially higher than for *y*-polarized light is consistent with the anisotropic absorption discussed in Fig. 4-2-2 and is in alignment with previous responsivity measurements of bP photodetectors at shorter wavelengths.[7]

As shown in Fig. 4-2-3e, the η_e shows no significant changes in spectral shape as a function of temperature, apart from a small red-shift in the absorption edge, attributed to a decrease in the bandgap with decreasing temperature. This anomalous temperature dependence of the bandgap has been previously predicted and experimentally observed in bP.[18,19] However, η_e increases as the temperature is decreased, reaching a value of 63% at 78 K. This is further illustrated in the inset of Fig 4-2-3c, with η_e and η_i (measured at $\lambda = 3$ μm) plotted as a function of inverse temperature, showing that η_i reaches a peak value of 84% at 100 K. This is most likely a result of an increase in the minority carrier diffusion length at lower temperatures, which in turn increases the collection efficiency of the back contact. A previously measured increase in bP's mobility at low temperatures ($\mu_{h,300k} \approx 750$ $cm^2V^{-1}s^{-1}$, $\mu_{h,77k} \approx 3{,}800$ $cm^2V^{-1}s^{-1}$).[24], can partially account for this predicted increasing diffusion length.

To directly compare the performance of the bP / MoS_2 photodiode to conventional photodetectors, we extract its specific detectivity D^*. This is achieved utilizing two independent approaches, which are discussed in detail in section 4-4 section. Firstly, D^* is calculated, following the approach suggested in Ref[3] for a photodiode under 0 V bias, from η_e and the zero-bias resistance area product (R_0A):

$$D^* = \frac{\eta_e \lambda q}{hc}\left[\frac{4kT}{R_0A} + 2q^2\eta_e\Phi_b\right]^{-1/2} \tag{1}$$

where λ is the wavelength, q is the elementary charge, c is the speed of light in vacuum, T is the detector temperature, Φ_b is the background flux density and h and k are the Planck and Boltzmann constants. The second term in the parenthesis accounts for contributions to noise from fluctuations in the thermal background and is negligible in this case, since $4kT/R_0A > 2q^2\eta_e\Phi_b$. Figure 4-2-3f shows $D^*(\lambda)$ extracted from this approach at room temperature compared against the current state-of-the-art room temperature photodiodes,[21,22] many of which are commercially available. It can be seen that the bP photodiode outperforms more established technologies in the MWIR region, with a peak D^* of 1.1×10^{10} $cmHz^{1/2}W^{-1}$ at $\lambda = 3.8$ μm. It should be noted that the MoS_2 / bP photodiode presented in Figure 4-2-3 has been characterized at 0 V bias, unlike many of the detectors presented in Figure 4-2-3f, which require an applied bias to obtain the reported values. To verify the MoS_2 / bP photodiode D^* values, the noise equivalent power (NEP) was measured for this device under flood illumination from a blackbody source as described in section 4-4. In this approach the incident power density is calculated using geometrical considerations, the temperature of the source and an integration of the total irradiance to the band edge.[23] Additionally, the noise is directly measured allowing D^* to be calculated as $\sqrt{A\Delta f}/\mathrm{NEP}$, where Δf is the integration time (1 second) and A is the area. From this measurement, we find a room temperature D^* value of 7×10^9 cmHz$^{1/2}$W^{-1}. This value is in good agreement with the spectral D^*, calculated from the device R_0A shown in Fig. 4-2-3f.

The frequency response and noise current for the bP / MoS_2 heterojunction photodiodes is characterized in Fig. 4-2-4. As shown in Fig. 4-2-4a no observable baseline drift in photoresponse is observed under modulated laser diode illumination (λ = 2.7 μm). In addition, the rise and fall times, measured under λ = 2.7 μm illumination at 0 V bias, are found to be 3.7 μs and 4 μs, respectively as shown in Fig. 4-2-4b. These values are among the fastest reported for bP based photoconductors and photodiodes.[14,16,28] While this is slower than commercially available MWIR photodiodes,[29] these values are promising given the early stage of device development and are faster than common photoconductive and thermal detectors. Improvements in response time could be achieved by reducing the bP bulk trap concentration during crystal growth and eliminating defective PO_x interfacial layers, by developing an oxidant free fabrication procedure. The dashed purple lines in Fig. 4-2-4b, measured from a commercially available InAs photodiode, are included to provide a reference of the instrument response. Similar rise / fall times are found when an illumination source of λ = 1.6 μm is used. Figure 4-2-4c shows the measured frequency response, with the 3 dB point at approximately 100 kHz using a λ = 1.6 μm illumination source. Figure 4-2-4d shows the measured noise current spectrum of the bP / MoS_2 photodiode. The shape it exhibits is commonly seen in systems dominated by generation-recombination noise and notably $1/f$ noise behavior is not observed at low frequencies since the device is operated in photovoltaic mode at zero bias.[30] The measured low-frequency noise has a value of 4×10^{-13} A Hz$^{-1/2}$. This is similar but higher than that reported previously for photodiodes fabricated using bPAs which exhibit low-frequency noise of ~7×10^{-14} A Hz$^{-1/2}$. This difference can be attributed to the thicker absorber layer (~150 nm) used in this work in comparison with devices in Ref.[31] (5-20 nm), which results in lower generation recombination noise.

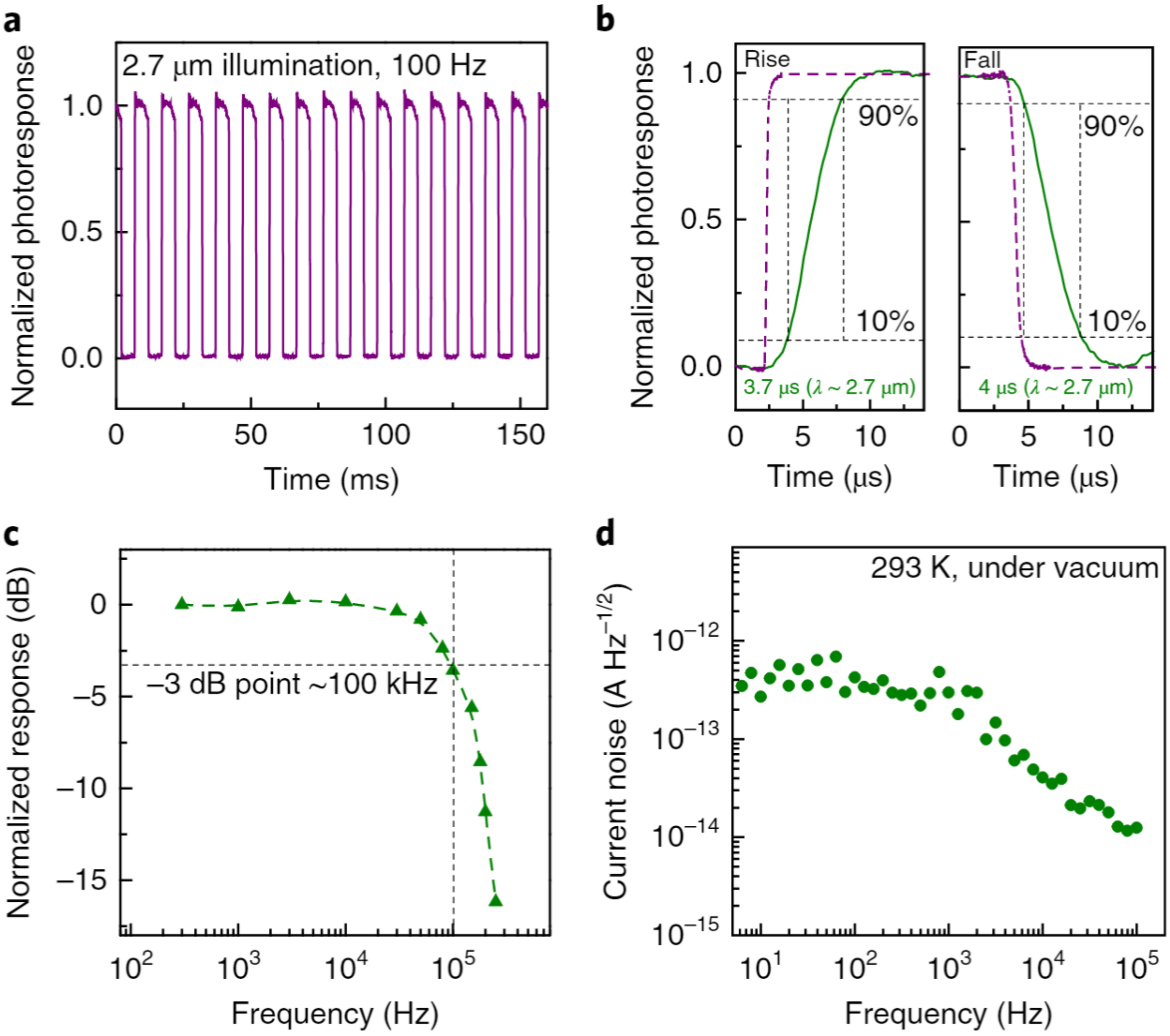

Fig 4-2-4 Frequency response and noise. a, Photocurrent measured from a bP / MoS_2 photodiode under a modulated illumination source (λ= 2.7 μm). b, 90%-10% rise and fall times measured with a λ= 2.7 μm illumination source (~10 mW/cm^2). Green solid lines are representative of the bP / MoS_2 photodiode and the purple dotted lines show the instrument response (measured using a commercial InAs photodiode, Judson J12D). c, Frequency response of a bP / MoS_2 photodiode, showing a 3-dB frequency of 100 kHz (λ=1.6 μm). d, Spectral noise density of a bP / MoS_2 photodiode. All device photoresponse and noise characterization was performed at a bias of 0 V.

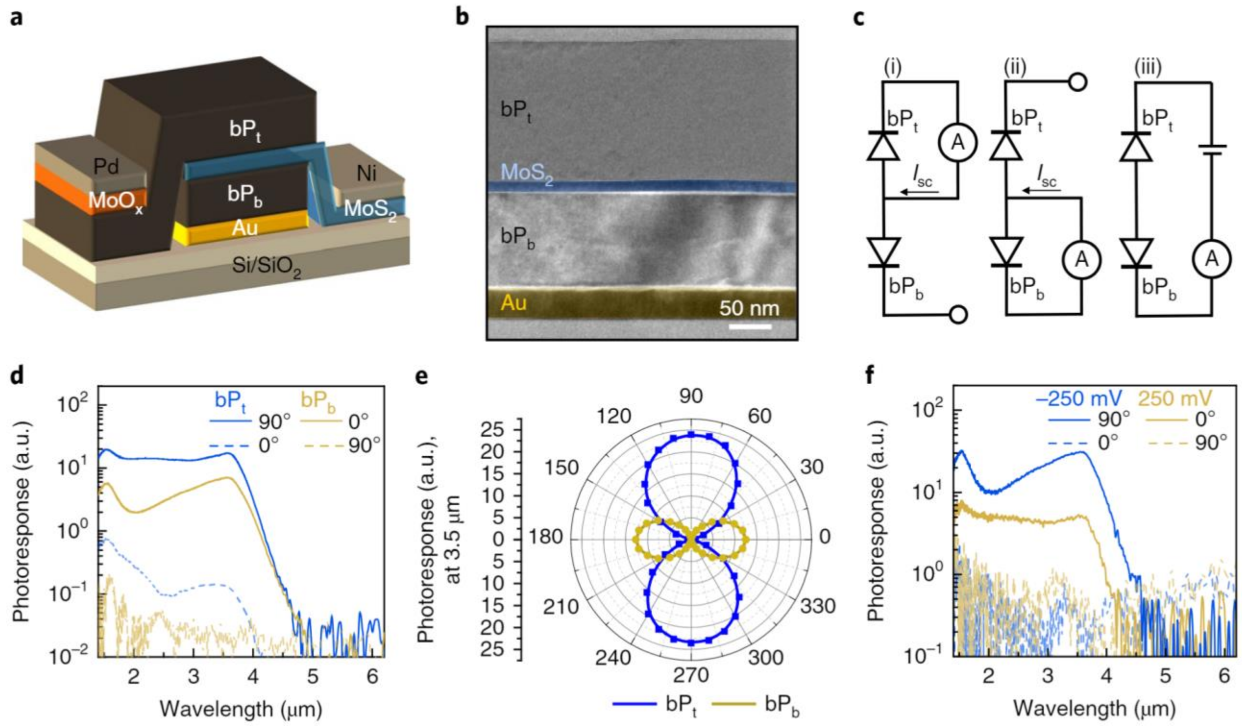

Fig 4-2-5 Polarization resolved bP/MoS$_2$ heterojunction photodiode. a, Schematic of polarization resolved bP/MoS$_2$ heterojunction photodiode, showing the heterojunction and contact configuration. b, Cross-sectional TEM image of a completed polarization resolved bP/MoS$_2$ heterojunction photodetector, showing the various layers in the device. c, Electrical configurations used to measure: photoresponse from bP$_t$ (i), photoresponse from bP$_b$ (ii), and photoresponse from the top or bottom mode using the bias selectable mode (iii). d, Spectrally resolved photoresponse measured from bP$_t$ and bP$_b$ under linearly polarized illumination normal and perpendicular to the device. e, Measured photoresponse under linearly polarized illumination at $\lambda = 3$ μm in bP$_t$ and bP$_b$ as a function of polarizer angle. f, spectrally resolved photoresponse of the device in the bias selectable mode under four different conditions: ±250 mV for polarization aligned to the x-axis of the top and bottom devices.

Finally, we leverage this device structure and the anisotropic optical properties of bP to develop a polarization resolved detector. A schematic of the polarization resolved detector developed in this study is shown in Fig. 4-2-5a and a false colored TEM cross-section of a fabricated device is shown in Fig. 4-2-5b. The device consists of two vertically stacked bP layers arranged so that their crystal orientations are perpendicular to one another. These two bP layers are separated by a common MoS_2 electron contact and each bP layer has an isolated hole contact. This configuration is similar to two-color back-to-back photodiodes which have been previously demonstrated with III-V semiconductors.[32] The bottom bP layer utilizes a full-area Au hole contact, similar to the photodiodes presented above, while the top bP layer collects holes through a MoO_x / Pd hole contact adjacent to the back reflector. The MoO_x / Pd stack has been shown to be an effective hole contact to a number of semiconductor materials,[33,34] owing to its large work function.

To demonstrate the performance of this device, spectrally resolved photoresponse measurements are taken individually on the top and bottom bP photodetectors using the circuit configuration shown in Fig 4-2-5c *i* and *ii*, respectively. Each device is measured under two conditions: linearly polarized light aligned to the x-axis of the top device (90^o) and, linearly polarised light aligned to the x-axis of bottom device (0^o). All four measurements are provided in Fig. 5d. The performance of this device can be quantified by an extinction ratio r_e for each layer, defined as the photoresponse measured with x-polarized illumination divided by photoresponse for y-polarized illumination. For both the top and bottom devices r_e values of ~100:1 are calculated at $\lambda = 3.5$ μm, which is on the order of the extinction ratio of the polarizer used in this study. These results are further corroborated by the polar plot of Fig. 4-2-5e, which shows the photoresponse as a function of polarizer angle at $\lambda = 3.5$ μm. In separate measurements, it is shown that the device is also able to simultaneously detect the two linear polarization components when illuminated with unpolarized light. Furthermore, the response from the individual detectors can be accessed in a bias-selectable (*i.e.* two-terminal configuration) as depicted in the circuit schematic of Fig 4-2-5c *iii*. By applying a bias of ±250 mV across the outer contacts one device is reverse biased (where the photocurrent is collected), and the other forward biased (contributing negligibly to the photocurrent). Note that for these measurements the MoS_2 contact was electrically disconnected. The functionality of this configuration is clearly seen in Fig. 4-2-5f by the exclusive collection of only 0^o or 90^o linear polarized MWIR light under negative or positive biasing, respectively. A bias of ±250 mV was chosen as it was the minimum value at which photocurrent from the two detectors could be effectively separated. Higher biases were avoided to minimize noise due to dark current in the device. The unbalanced photocurrent from the top and bottom bP layers can be attributed to a combination of device variation and differences in absorption arising from the layer thicknesses and their position within the device stack. An optical structure, which couples in and absorbs an equal proportion of perpendicularly polarized light in the two bP absorbers, can be realised by controlling the bP and MoS_2 layer thicknesses and integrating an antireflection layer.

In summary, we have designed and fabricated MWIR bP / MoS_2 heterojunction photodiodes with high performance at room temperature. By determining the complex refractive index in the IR, we have designed a simple optical structure for the bP / MoS_2 photodiode that achieves high MWIR absorption via interference. This allows the use of a moderately thin bP layer (~150 nm), which reduces noise while still permitting high absorption (in excess of ~80%) within a narrow band in the MWIR region. These devices display impressive room temperature η_e and D^* values of 35% and 1.1×10^{10} $\mathrm{cmHz}^{1/2}\mathrm{W}^{-1}$, respectively. Finally, we utilize the anisotropic optical properties of bP to demonstrate a bias-selectable polarization-resolved monolithic photodetector, which is capable of simultaneously detecting orthogonally polarized light without the use of external optics. This could further be expanded upon to create polarimetry focal plane arrays which do not rely on moving parts or additional optical components.

References for Section 4-2

1. Xia, F., Wang, H., Xiao, D., Dubey, M. & Ramasubramaniam, A. Two-dimensional material nanophotonics. *Nat. Photon.* 8, 899–907 (2014).
2. Jakšić, Z. *Micro and Nanophotonics for Semiconductor Infrared Detectors*. (Springer-Verlag, 2014).
3. Rogalski, A., Adamiec, K. & Rutkowski, J. *Narrow-Gap Semiconductor Photodiodes*. (SPIE Press, 2000).
4. Wang, X., Cheng, Z., Xu, K., Tsang, H. K. & Xu, J.-B. High-responsivity graphene/silicon-heterostructure waveguide photodetectors. *Nat. Photon.* 7, 888–891 (2013).
5. Xia, F., Wang, H. & Jia, Y. Rediscovering black phosphorus as an anisotropic layered material for optoelectronics and electronics. *Nat. Commun.* 5, 5458 (2014).
6. Ling, X., Wang, H., Huang, S., Xia, F. & Dresselhaus, M. S. The renaissance of black phosphorus. *Proc. Natl. Acad. Sci.* 112, 4523–4530 (2015).
7. Yuan, H. *et al.* Polarization-sensitive broadband photodetector using a black phosphorus vertical p–n junction. *Nat. Nanotechnol.* 10, 707–713 (2015).
8. Qiao, J., Kong, X., Hu, Z.-X., Yang, F. & Ji, W. High-mobility transport anisotropy and linear dichroism in few-layer black phosphorus. *Nat. Commun.* 5, 5475 (2014).
9. Hong, T. *et al.* Anisotropic photocurrent response at black phosphorus–MoS2 p–n heterojunctions. *Nanoscale* 7, 18537–18541 (2015).
10. Deng, Y. *et al.* Black Phosphorus–Monolayer MoS_2 van der Waals Heterojunction p–n Diode. *ACS Nano* 8, 8292–8299 (2014).
11. Ye, L., Li, H., Chen, Z. & Xu, J. Near-Infrared Photodetector Based on MoS2/Black Phosphorus Heterojunction. *ACS Photonics* 3, 692–699 (2016).
12. Chen, P. *et al.* Gate tunable WSe2–BP van der Waals heterojunction devices. *Nanoscale* 8, 3254–3258 (2016).
13. Shim, J. *et al.* Phosphorene/rhenium disulfide heterojunction-based negative differential resistance device for multi-valued logic. *Nat. Commun.* 7, 13413 (2016).
14. Huang, M. *et al.* Broadband Black-Phosphorus Photodetectors with High Responsivity. *Adv. Mater.* 28, 3481–3485 (2016).
15. Youngblood, N., Chen, C., Koester, S. J. & Li, M. Waveguide-integrated black phosphorus photodetector with high responsivity and low dark current. *Nat. Photon.* 9, 247–252 (2015).
16. Guo, Q. *et al.* Black Phosphorus Mid-Infrared Photodetectors with High Gain. *Nano Lett.* 16, 4648–4655 (2016).
17. Mao, N. *et al.* Optical Anisotropy of Black Phosphorus in the Visible Regime. *J. Am. Chem. Soc.* 138, 300–305 (2016).
18. Liu, H. *et al.* Phosphorene: An Unexplored 2D Semiconductor with a High Hole Mobility. *ACS Nano* 8, 4033–4041 (2014).
19. Tran, V., Soklaski, R., Liang, Y. & Yang, L. Layer-controlled band gap and anisotropic excitons in few-layer black phosphorus. *Phys. Rev. B* 89, 235319 (2014).
20. Li, D. *et al.* Polarization and Thickness Dependent Absorption Properties of Black Phosphorus: New Saturable Absorber for Ultrafast Pulse Generation. *Sci. Rep.* 5, 15899 (2015).
21. Macleod, A. *Thin-Film Optical Filters*. (CRC Press, 2010).

22. Villegas, C. E. P., Rocha, A. R. & Marini, A. Anomalous Temperature Dependence of the Band Gap in Black Phosphorus. *Nano Lett.* 16, 5095–5101 (2016).
23. Villegas, C. E. P., Rodin, A. S., Carvalho, A. & Rocha, A. R. Two-dimensional exciton properties in monolayer semiconducting phosphorus allotropes. *Phys. Chem. Chem. Phys.* 18, 27829–27836 (2016).
24. Li, L. *et al.* Quantum Hall effect in black phosphorus two-dimensional electron system. *Nat. Nanotechnol.* 11, 42 (2016).
25. Martyniuk, P., Kopytko, M. & Rogalski, A. Barrier infrared detectors. *Opto-Electron. Rev.* 22, 127–146 (2014).
26. Dhar, N. K., Dat, R. & Sood, A. K. Advances in Infrared Detector Array Technology. in *Optoelectronics - Advanced Materials and Devices* (InTech, 2013).
27. Amani, M., Regan, E., Bullock, J., Ahn, G. H. & Javey, A. Mid-Wave Infrared Photoconductors Based on Black Phosphorous-Arsenic Alloys. *ACS Nano* (2017). doi:10.1021/acsnano.7b07028
28. Buscema, M. *et al.* Fast and Broadband Photoresponse of Few-Layer Black Phosphorus Field-Effect Transistors. *Nano Lett.* 14, 3347–3352 (2014).
29. Martyniuk, P. & Rogalski, A. HOT infrared photodetectors. *Opto-Electron. Rev.* 21, 239–257 (2013).
30. Yau, L. D. & Sah, C.-T. Theory and experiments of low-frequency generation-recombination noise in MOS transistors. *IEEE Trans. Electron Devices* 16, 170–177 (1969).
31. Long, M. *et al.* Room temperature high-detectivity mid-infrared photodetectors based on black arsenic phosphorus. *Sci. Adv.* 3, e1700589 (2017).
32. Haddadi, A., Dehzangi, A., Chevallier, R., Adhikary, S. & Razeghi, M. Bias–selectable nBn dual–band long–/very long–wavelength infrared photodetectors based on InAs/InAs 1−x Sb x /AlAs 1−x Sb x type–II superlattices. *Sci. Rep.* 7, 3379 (2017).
33. Bullock, J., Cuevas, A., Allen, T. & Battaglia, C. Molybdenum oxide MoOx: A versatile hole contact for silicon solar cells. *Appl. Phys. Lett.* 105, (2014).
34. Chuang, S. *et al.* MoS2 P-type Transistors and Diodes Enabled by High Work Function MoOx Contacts. *Nano Lett.* 14, 1337–1342 (2014).
35. Low, T. *et al.* Tunable optical properties of multilayer black phosphorus thin films. *Phys. Rev. B* 90, 075434 (2014).
36. Morita, A. Semiconducting black phosphorus. *Appl. Phys. A* 39, 227–242 (1986).

4.3 – Photoconductive SWIR detectors based on tellurium[8]

Two-dimensional (2D) materials, particularly black phosphorous (bP), have demonstrated themselves to be excellent candidates for high-performance infrared photodetectors and transistors. However, high-quality bP can be only obtained *via* mechanical exfoliation from high temperature- and high-pressure-grown bulk crystals and degrades rapidly when exposed to ambient conditions. Here, we report solution-synthesized and air-stable quasi-2D tellurium (Te) nanoflakes for short-wave infrared (SWIR) photodetectors. We perform comprehensive optical characterization *via* polarization-resolved transmission and reflection measurements, and report the absorbance and complex refractive index of Te crystals. It is found that this material is an indirect semiconductor with a bandgap of 0.31 eV. From temperature-dependent electrical measurements, we confirm this bandgap value and find that 12 nm thick Te nanoflake show high hole mobilities of 450 and 1430 $cm^2 V^{-1} s^{-1}$ at 300K and 77K, respectively. Finally, we demonstrate that despite its indirect bandgap, Te can be utilized for high-performance SWIR photodetectors by employing optical cavity substrates consisting of Au/Al_2O_3 to dramatically increase the absorption in the semiconductor. By changing the thickness of the Al_2O_3 cavity, the peak responsivity of Te photoconductors can be tuned from 1.4 μm (13 A/W) to 2.4 μm (8 A/W) with a cut-off wavelength of 3.4 μm, fully capturing the SWIR band. An optimized room temperature specific detectivity (D*) of 2×10^9 cm $Hz^{1/2} W^{-1}$ is obtained at a wavelength of 1.7 μm.

Narrow bandgap semiconductors, with bandgaps in the range of 0.7 to 0.3 eV, have been heavily investigated for numerous applications. These include high-speed and high-performance transistors, which typically require materials with high mobility and low effective mass.[1,2] Additionally, photodetectors and light sources which can operate in the short-wave infrared (SWIR, 1.4 μm – 3 μm) band are heavily utilized for imaging and optical communication.[3-5] This area has typically been dominated by III-V semiconductors such as indium gallium arsenide (InGaAs) and indium gallium arsenide phosphide (InGaAsP), which have excellent performance but require complex growth and fabrication procedures.[6,7] Numerous research groups have investigated techniques to achieve III-V semiconductors through non-epitaxial growth on silicon or by layer transfer.[8-11] However, these techniques still introduce significant complexity and may require high growth temperature. Moreover, key limitations still exist in InGaAs-based devices; an example being edge-recombination in scaled InGaAs photodiodes which limits pixel sizes in focal plane arrays to dimensions of 5-6 μm, well above the diffraction limit.[12] As such, there is a pressing need to find suitable materials that can either improve the performance and/or reduce the costs of these devices.

---

[8] Reproduced with permission from M. Amani, C. Tan, et al., ACS Nano, 12, 7253-7263, 2018. Copyright © [2017] ACS.

One such potential material system is two-dimensional (2D) materials, which have been heavily studied over the past decade. One of the key advantages of 2D materials, which enables their high performance, is their naturally terminated surfaces; *i.e.* since the out-of-plane bonds in these materials are van der Waals rather than covalent.[13,14] As such, they do not suffer from the surface-induced performance degradation commonly observed in three-dimensional (3D) semiconductors, which require surface passivation (typically in the form of cladding layers). This has enabled extraordinary electronic and optical properties of these materials such as photoluminescence quantum yields approaching unity and their exceptional thickness scalability down to the monolayer limit.[15,16] Devices which have exploited the advantages and physics of 2D systems have demonstrated dramatic scaling as well as new devices paradigms.[17-19] However, edges in 2D layers still act as recombination centers and are analogous to a surface in a 3D crystal structure.[20] A recent work by Wang *et al.* demonstrated the solution synthesis of air-stable quasi-2D Te nanosheets and its high-performance for field-effect transistors.[21] Note that Te is a true one-dimensional (1D) system, which can potentially overcome some of these limitations since it consists of van der Waals bonded molecular chains.[22] As such these material systems naturally possess no dangling bonds when scaled, with the exception of the ends of the molecular chains.[22] Importantly, this material also possesses a small, thickness tunable bandgap enabling its potential use in SWIR photodetectors. Recent theoretical works have predicated an indirect gap of 0.35 eV in bulk and a direct gap of 1.04 eV in the monolayer case.[23,24]

Here, we systematically study the optical and electrical properties of solution-synthesized quasi-2D Te nanoflakes. From polarization-resolved IR transmission and reflection measurements, we experimentally extract the bandgap, absorbance, and complex refractive index of this material. Temperature-dependent electrical measurements were performed to verify the optically measured bandgap values as well as determine the carrier transport properties as a function of temperature in quasi-2D Te nanoflakes. Finally, we demonstrate SWIR photoconductive detectors based on thin (16-20 nm) quasi-2D Te nanoflakes. Although this material has low absorbance in the SWIR (6×10^5 cm^{-1} for wavelengths in the range of 2 to 3.5 μm) induced by the indirect bandgap, the Te nanoflake-based photodetectors exhibit high photoresponsivity and specific detectivity by leveraging optical cavities engineered to maximize absorption at various technologically important wavelengths in the SWIR range.

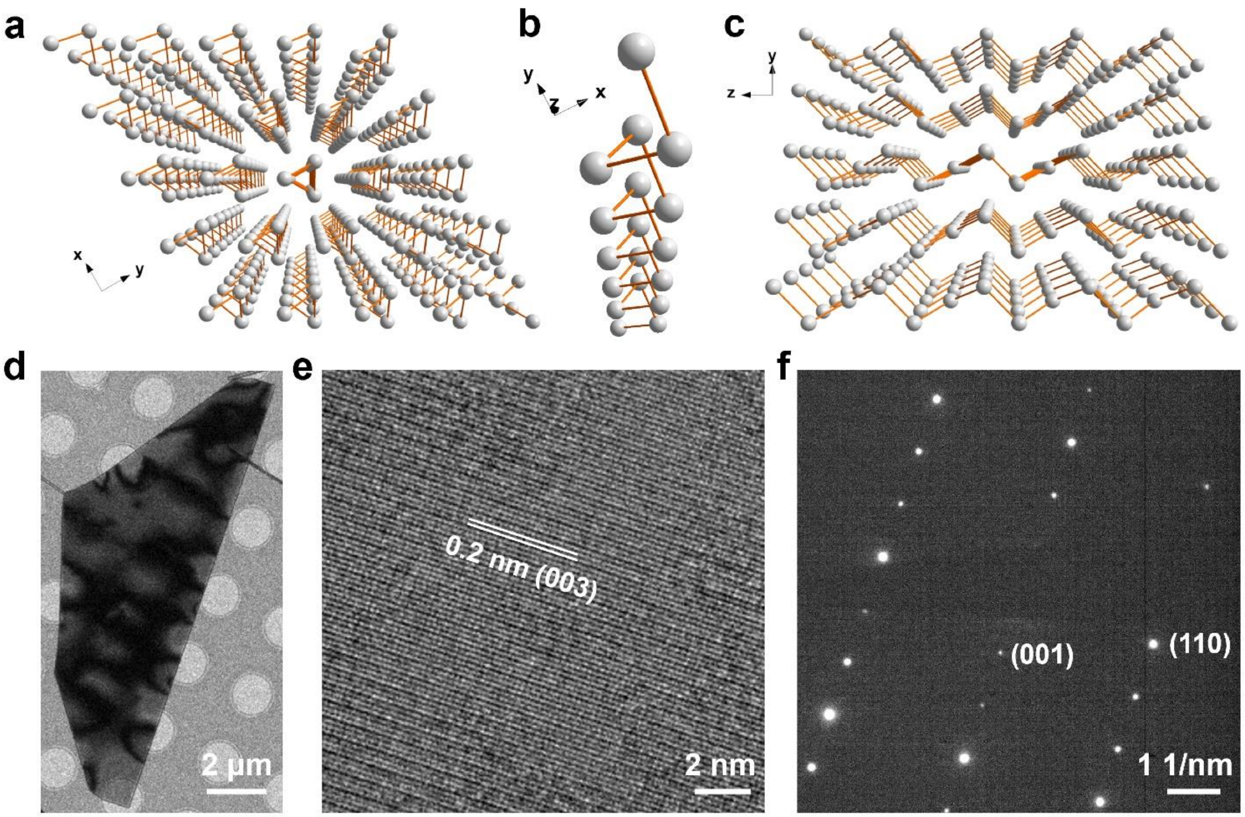

Fig. 4-3-1. Crystal structure of tellurium: (a) viewed from x-axis, (b) single-molecular chain and (c) viewed from z-axis. (d) TEM image, (e) corresponding HR-TEM image and (f) SAED pattern of a typical tellurium nanoflake.

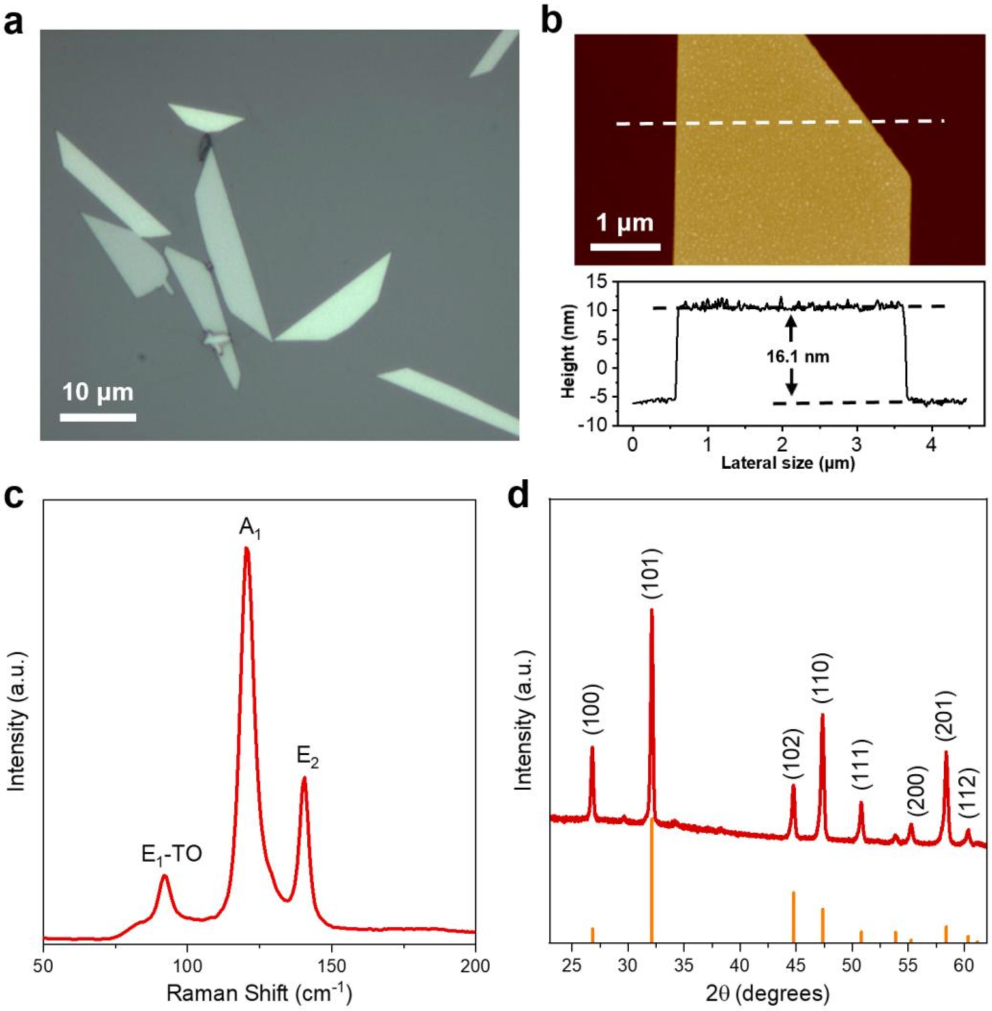

Fig. 4-3-2. (a) Optical microscope image of tellurium nanoflakes deposited on a SiO_2/Si substrate, scale bar is 10 μm. (b) AFM image of typical tellurium nanoflake (top) and the corresponding height profile (bottom), scale bar is 1 μm. (c) Raman spectrum of tellurium nanoflakes. (d) XRD pattern of dried tellurium nanoflake powder.

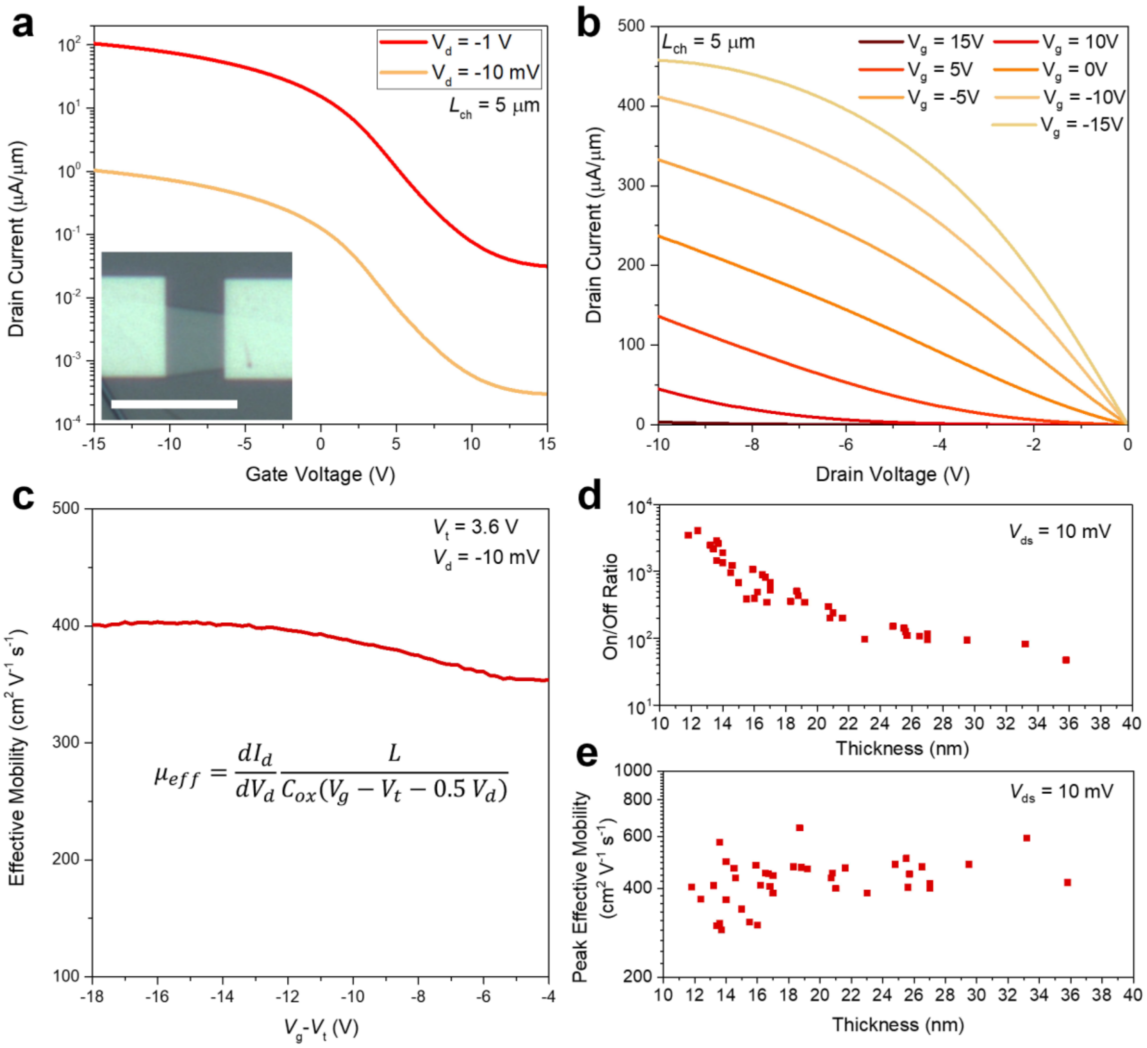

Fig. 4-3-3. (a) Back-gated I_d-V_g characteristics of a 12.3 nm thick Te nanoflake with Pd contacts on 50 nm SiO_2 measured at room temperature; inset shows optical image of the device, scale bar is 10 μm. (b) I_d-V_d measured for the same device as shown in panel (a). (c) Effective mobility as a function of gate overdrive voltage for the device shown in panel (a) under a V_d of -10 mV, giving a peak mobility value of 619 $cm^{-2}\,V^{-1}\,s^{-1}$. (d) Thickness dependence of the on/off ratio measured for Te nanoflakes of varying thickness in the range of 12-36 nm. (e) Thickness dependence of the peak effective mobility measured for Te nanoflakes of varying thickness in the range of 12-36 nm.

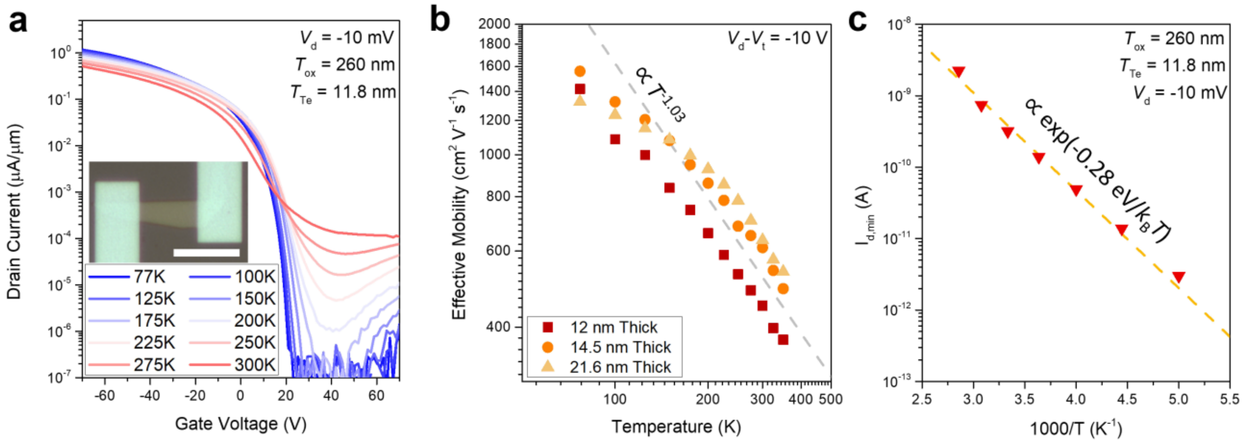

Fig. 4-3-4. (a) Temperature dependent I_d-V_g characteristics of a 12 nm thick Te nanoflake, measured at a low V_d of -10 mV. Scale bar is 5 μm. (b) Effective mobility for quasi-2D Te nanoflakes with varying thickness as a function of temperature extracted from panel (a) at a constant gate overdrive voltage of -10 V, dashed line shows a power law fit. (c) Arrhenius plot showing the minimum drain source current ($I_{d,min}$) as a function of temperature extracted from the data shown in panel (a).

Quasi-2D Te nanoflakes with varying thickness in the range of 10-200 nm were synthesized by a hydrothermal method *via* reduction of sodium tellurite with hydrazine hydrate in the presence of poly(-vinyl pyrrolidone) in an aqueous alkaline solution at 180°C for certain varying times (details are provided in methods).[21,25] The crystal structure of Te is shown in Figure 4-3-1a-c. The Te crystallizes in a structure composed of Te atomic chains in a triangular helix that are stacked together *via* van der Waals forces in a hexagonal array (Figure 4-3-1a). In this structure, Te atoms only form covalent bonds to the two nearest neighbor Te atoms in the helical chain (Figure 4-3-1b). Therefore, Te is a true 1D system rather than a 2D van der Waals crystal. When it is viewed from x-axis, the zig-zag layers are seen to be stacked together *via* van der Waals forces to form a 3D structure (Figure 4-3-1c). Figure 4-3-1d shows the transmission electron microscope (TEM) image of a typical Te nanoflake with a length of 15 μm and width of 4 μm. The corresponding high-resolution TEM (HR-TEM) image shows the continuous crystal lattice of the Te nanoflake and the measured the lattice constant is ~2 Å (Figure 4-3-1e), which is assignable to the (003) planes of the Te crystal. The corresponding selected area electron diffraction (SAED) pattern of the Te nanoflake shows bright diffraction spots with a rectangular shape, in which the nearest two spots to the diffraction center correspond to the (110) and (001) planes of the Te crystal (Figure 4-3-1f). Both the HR-TEM and SAED pattern results indicate that the solution-synthesized Te nanoflake is single-crystalline. The optical image shows that Te nanoflakes have an irregular shape with length of tens of micrometers, width of few micrometers and thickness of 10-30 nm (Figure 4-3-2a). Note that there are always some Te nanowires along Te nanoflakes in the growth solution, but Te nanowires can be partially removed from the solution by proper centrifugation (see the details in section 4-4). An atomic force microscope (AFM) image of a Te nanoflake with a thickness of 16.1 nm is shown in Figure 4-3-2b. Raman spectrum of tellurium nanoflakes gives three vibrational modes at 92, 121, 141 cm^{-1} (Figure 4-3-2c) corresponding to the E_1-TO, A_1, and E_2 peaks, which are consistent with previous literature reports.[21,26] The X-ray diffraction (XRD) peaks of Te nanoflakes match well with the simulated reference (Figure 4-3-2d). Both Raman and XRD analysis further confirm the successful preparation of Te nanoflakes.[21,25]

We now turn our attention to the electrical properties and performance of the quasi-2D Te nanoflakes. To this end, back-gated field-effect transistors were fabricated on Si/50 nm SiO_2 by patterning Pd (40 nm thick) electrodes on Te nanoflakes with thickness ranging from 10-20 nm using electron-beam lithography.[21] The I_d-V_d characteristics of a 12.3 nm thick quasi-2D Te field-effect transistor, as well as an optical image of the measured device (L = 6.8 μm, W = 1.5 μm, where L and W are length and width respectively) are shown in Figure 4-3-3a. The device shows dominantly *p*-type transport characteristics and a peak current density of 116 μA/μm at a V_d = -1 V and V_g = -20 V. It should be noted that in some devices ambipolar transport characteristics are observed, indicating that *via* proper contact engineering n-type transport could be obtained. Additionally, this device shows a current on/off ratio of $\sim 3\times10^3$, which is expected for a material with a small bulk bandgap of ~0.31 eV. The output characteristics of this device are shown in Figure 4-3-3b, and show current saturation at high drain bias, as well as linear behavior at low drain biases, indicating low contact resistance. We then utilize the square law model to calculate the effective mobility (μ_{Eff}) in this device as a function of gate field (Figure 4-3-3c) using $\mu_{Eff} = (dI_d/dV_d)/[C_{ox}(V_g - V_t - 0.5V_g)]$, where C_{ox} is the gate capacitance (69.1 nF cm^{-2} in the case of 50 nm SiO_2) and V_t is the threshold voltage. We extract a high peak μ_{Eff} of 619 $cm^2V^{-1}s^{-1}$ for holes, which is very competitive with high-performance p-type semiconductors with similar bandgaps such as InGaSb and bP, especially considering that the material is prepared by a solution-based method.[27-29] The thickness-dependent transport properties of quasi-2D Te nanoflakes were also investigated over a range of 11 to 36 nm as shown in Figure 4-3-3d and 4-3-3e. As the overall thickness of the Te nanoflakes is reduced a dramatic improvement in the ratio of the on/off currents from ~30× to ~4000× can be observed, which can be attributed to reduced gating efficiency in the device. Furthermore, over this measured thickness range, we find that there is negligible variation in the peak effective mobility which has an average value of 424±74 $cm^2V^{-1}s^{-1}$ over thirty-nine measured samples.

To better understand the transport in this material, we performed temperature-dependent electrical characterization of the devices. I_d-V_g characteristics of quasi-2D Te nanoflakes with different thicknesses measured over a temperature range of 77K to 350K are shown in Figure 4-3-4a. A clear increase in the current on/off ratio can be observed when the device is cooled, which is consistent with small bandgap materials, where thermal generation dramatically increases the carrier densities at elevated temperatures. From the temperature-dependent measurements, we extract the μ_{Eff} at a gate overdrive of -10 V as a function of temperature for different layer thicknesses as shown in Figure 4-3-4b. For all thicknesses, the mobility increases as the temperature is reduced, with the 12 nm thick device showing a μ_{Eff} of 1430 and 450 $cm^2V^{-1}s^{-1}$ at 77K and 300K respectively. For all three thicknesses, we observe the temperature dependence of mobility can be fitted with a power law, $\mu_{Eff} \propto T^{-\gamma}$, where $\gamma = -1.03$ in our case. This indicates that the mobility in this material is limited by phonon scattering and not ionized impurities.[30] Additionally, we estimate the bandgap using temperature-dependent measurements on a device prepared on a 260 nm gate oxide. In this case, the minimum drain currents, $I_{d,min}$, is determined by thermal activation of carriers over the contact Schottky barrier height.[31] The resulting data, shown in Figure 4-3-4c, can be fit using:

$$I_{\mathrm{d,min}} \propto \exp(-E_{\mathrm{g}}/kT)$$

where T is the temperature, E_g is the transport bandgap, and k is the Boltzmann constant. We extract an E_g of 280 meV for a 11.8 nm thick sample, and it is important to note that this method is expected to underestimate the bandgap due to contributions from trap states.

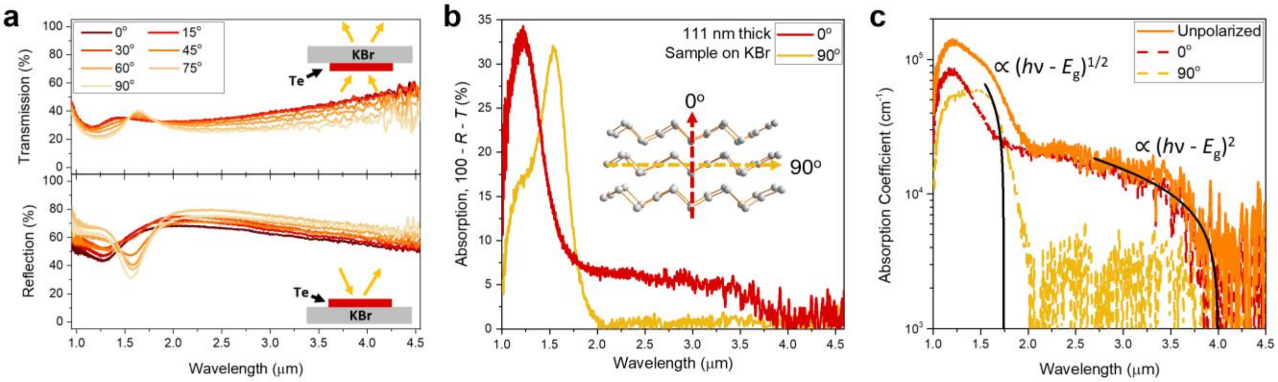

Fig. 4-3-5. (a) Polarization resolved transmission and reflection spectra measured for a 111 nm thick Te nanoflake transferred on a KBr substrate, insets show the optical configuration used during measurements. (b) Absorption spectra for the nanoflake measured in panel (a), calculated from 100%-*T*-*R*. Inset shows the Te crystal directions of 0° and 90°. (c) Absorption coefficient of tellurium for unpolarized light, as well as light aligned parallel to z-axis (0°) and y-axis (90°) of Te crystal.

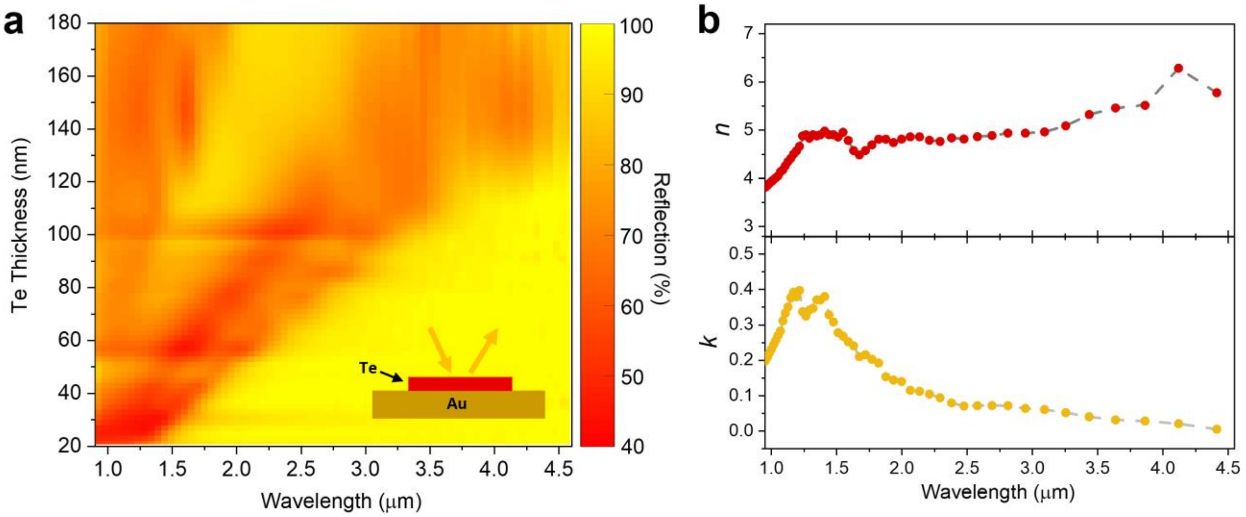

Fig. 4-3-6. (a) Reflection of quasi-2D Te nanoflakes on Au substrates, with Te thickness ranging from 20 nm to 180 nm. Plot is obtained from interpolation of spectra taken on 18 Te crystal nanoflakes of varying thicknesses. (b) Complex refractive index of quasi-2D Te nanoflakes calculated by fitting measured reflection data as a function of thickness.

To identify the optical bandgap of the quasi-2D Te nanoflakes, we performed polarization-resolved transmission and reflection measurements on Te nanoflakes which were transferred onto KBr. Polarization-resolved transmission and reflection spectra measured on a 111 nm thick sample are shown in Figure 4-3-5a. In order to accurately extract the absorption in the sample, the optical path was kept constant for both the transmission and reflection measurements, as annotated in the Figure 4-3-5a. Transmission and reflection spectra were taken in reference to the blank KBr substrate and an Au mirror, respectively. The total absorption and the corresponding absorption coefficient in the material can then be calculated as 100%-Reflection-Transmission as shown in Figure 4-3-5b and 4-3-5c. For light polarized along the direction of the Te molecular wires (defined as 90°), we measure a strong absorption that can be fitted to a direct bandgap (Figure 4-3-5c) at 0.71 eV. However, when the light is polarized perpendicular to the axis of the Te molecular wires (defined as 0°) a significantly weaker absorption edge is observed at lower wavelengths. From similar analysis, the transition can be fitted to an indirect bandgap at 0.31 eV. Importantly, while the absorption coefficient for wavelengths below 1.6 μm is high (4.5×10^6 cm^{-1}), the absorption for longer wavelengths ($1.6\ \mu m < \lambda < 3.4\ \mu m$) is an order of magnitude lower (6×10^5 cm^{-1}). As such, in order to effectively utilize this material in the full SWIR band, it is necessary to increase the absorption *via* proper optical engineering.[32]

To this end, we extracted the complex refractive index (n, k) which can be used to estimate the total absorption in the quasi-2D Te layers in combination with optical cavities, back-reflectors, or anti-reflection coatings. The refractive index was extracted using a previously established technique for nanoscale materials for unpolarized light, where reflection is measured as a function of oxide or sample thickness.[33] In our case, quasi-2D Te nanoflakes of thicknesses varying from 16 nm to 180 nm were drop-casted on Au substrates, and the reflection spectra were measured using an Fourier transform infrared spectrometer (FTIR). The resulting reflection data are plotted as a function of thickness and wavelength. (Figure 4-3-6a). To extract the complex refractive index from the reflection measurements, we utilize the transfer matrix method to fit a refractive index to the measured reflection *versus* thickness at each wavelength.[34] The extracted n and k values are plotted in Figure 4-3-6b; the extracted extinction coefficient clearly shows absorption resulting from both the indirect and direct transitions at the expected wavelengths and corroborates the results from absorption measurements shown in Figure 4-3-5c.

Based on the optical properties and electrical properties of quasi-2D Te, the device structure shown in Figure 4-3-7a was chosen to optimize photoconductive detectors targeting the SWIR spectrum. Here, we selected thicknesses in the range of 16-20 nm for the quasi-2D Te layers, which provides desired electrical characteristics, the most important of which being a low dark current.[35] To increase the absorption, an optical cavity consisting of an optically thick Au film (100 nm) and an Al_2O_3 dielectric spacer layer was utilized. The predicted absorption for an 18 nm thick Te layer as a function of wavelength and Al_2O_3 thickness was calculated using the transfer matrix method and is shown in Figure 4-3-7b. From these simulations, it can be clearly seen that by adjusting the thickness of the

Al_2O_3 layer, the peak absorption wavelength can be tuned over a large range and the total absorption in the material can be increased by over two orders of magnitude relative to a sample on Si/SiO_2. Additionally, the optical cavity simultaneously acts as the gate stack in this structure.

Figure 4-3-7c shows optical images of devices fabricated on three different Al_2O_3 spacer thickness (550 nm (i), 150 nm (ii), and 350 nm (iii)), which are selected to provide optimized absorption at 1.4 µm, 1.8 µm, and 2.2 µm, respectively. The spectral responsivity of these devices to SWIR illumination was characterized using an FTIR, by placing the devices in place of the internal detector and focusing the light source of the FTIR on the device with a CaF_2 lens. To calibrate the measurements, the internal Deuterated Triglycine Sulfate (DTGS) in the FTIR, which has a wavelength independent responsivity, was used to determine the relative intensity of the light source while a NIST traceable Ge photodiode was used to determine the absolute intensity of the illumination (further measurement details are provided in section 4-4 and ref. 35). The final responsivity (R) is then calculated as $R(\lambda) = I_{\mathrm{ph}}(\lambda)/P_{\mathrm{in}}(\lambda)$, where I_{ph} is the photocurrent and P_{in} is the incident optical power on the device. The spectral responsivity for representative devices fabricated on the three different optical cavity substrates are shown in Figure 4-3-7d. Devices fabricated on these three substrates were measured at a drain bias of $V_{\mathrm{d}} = 5$ V, and the gate voltage was adjusted to maximize the responsivity. The measured responsivity curves closely match the calculated absorption curves which further confirms the estimated refractive index values.

To further characterize the performance of these photodetectors, additional measurements were performed on an 18.8 nm thick device fabricated on a Au/150 nm Al_2O_3 substrate. The I_{d}-V_{g} characteristics of a device measured at 78K and 297K without the presence of a cold shield is shown in Figure 4-3-8a. The gate and drain bias dependence of the device at an incident wavelength of 1.7 µm are shown in Figure 4-3-8b and 4-3-8c, respectively. We can see that the photoresponse can be strongly modulated by the gate bias and is maximized when the device is biased such that drain current is minimized, similar to what has previously been observed in bP photoconductors[35,36]. This can be seen in the clear peak responsivity of 27 A/W at 78K, while the responsivity at 297K saturates with increasing gate biases to a peak measured value of 16 A/W. Additionally, the device shows an approximately linearly increasing responsivity at low V_{d}, and begins to show saturation at high V_{d}. The full spectral responsivity of the device is shown in Figure 4-3-8d. For $V_{\mathrm{d}} = 5$ V, this detector shows a peak responsivity at $\lambda = 1.7$ µm of 27 A/W and 16 A/W at 78K and 297K, respectively.

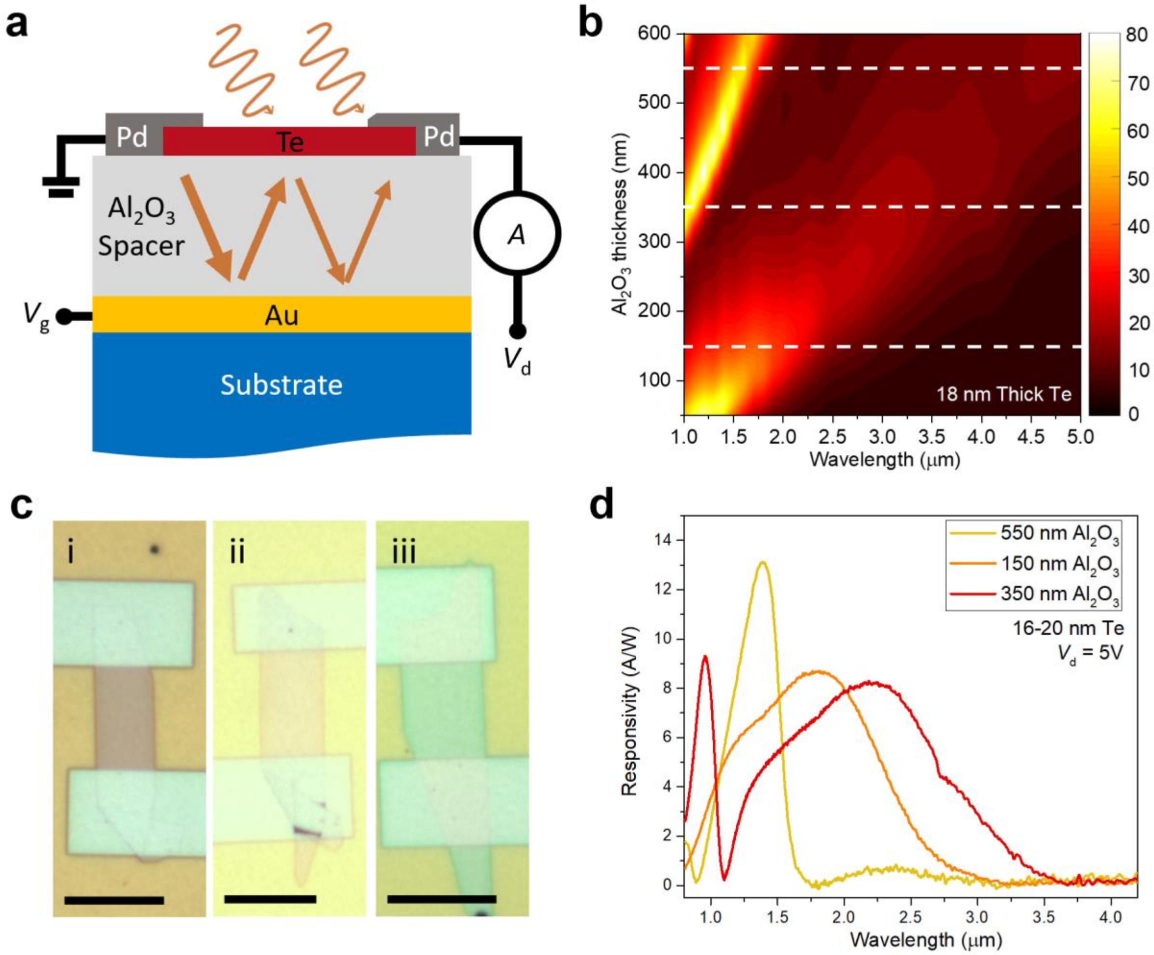

Fig. 4-3-7. (a) Schematic showing the optical cavity structure used to fabricate SWIR photoconductors from quasi-2D Te nanoflakes in this study. An evaporated Au film acts as the gate electrode and back-reflector, while a Al_2O_3 dielectric layer acts as a ~λ/4 spacer as well as the gate oxide. (b) Calculated absorption in the Te layer, as a function of wavelength and Al_2O_3 thickness for a fixed semiconductor thickness of 18 nm. (c) Optical images of SWIR photoconductors fabricated on optical cavities with Al_2O_3 thickness of 550 nm (i), 150 nm (ii), and 350 nm (iii); scale bar is 10 μm. (d) Measured responsivities of quasi-2D Te nanoflakes fabricated on optical cavities with different Al_2O_3 thicknesses.

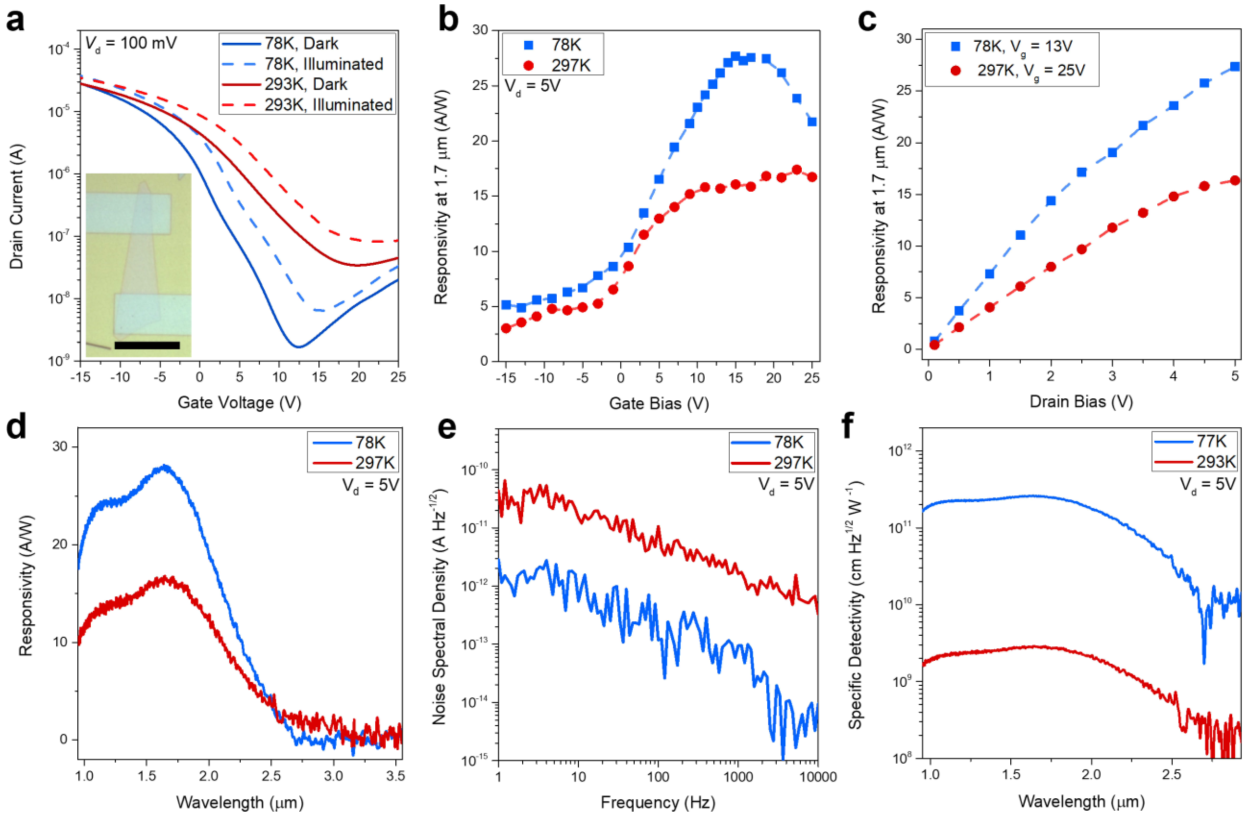

Fig. 4-3-8. (a) I_d-V_g characteristics of an 18.8 nm Te photoconductor measured at 297K and 78K under illumination and in the dark. Inset shows optical image of the measured device; scale bar is 10 μm. (b) Responsivity at 1.7 μm measured at 297K and 78K as a function of gate bias, at a constant drain bias of V_d = 5 V. (c) Responsivity at 1.7 μm measured at 297K and 78K as a function of drain bias at an optimized gate bias (V_g = 13 V at 78K and V_g = 25 V at 297K). (d) Spectral responsivity per watt of a Te photoconductor measured at 78K and 297K under optimized gate bias and V_d = 5 V. (e) Noise spectrum measured at room temperature for a Te photoconductor operated with optimized gate bias and a V_d = 5 V and optimized gate bias. (f) Specific detectivity of Te photoconductors with optimized thickness; measurements were performed under gating conditions which maximized detectivity for the specific device at room temperature. Note that an Au/Al_2O_3 substrate with an Al_2O_3 thickness of 150 nm was used for the measurements.

To calculate the specific detectivity of this device, the noise current density is measured under bias conditions which give maximum responsivity at an integration time (Δf) of one second and is shown in Figure 4-3-8e. The noise currents clearly show the expected $1/f$ (where f is frequency) flicker noise which is typically attributed to charge trapping/de-trapping. Utilizing the noise and responsivity measurements, we calculate the specific detectivity (D^*) using:

$$D^* = \frac{\sqrt{A\Delta f}}{NEP} = \frac{R\sqrt{A\Delta f}}{i_\mathrm{n}}$$

where A is the detector area, NEP is noise equivalent power, and i_n is the noise current. In the ideal case for photoconductors, the i_n is limited by shot noise and can be calculated from dark current using: $\langle i_S^2 \rangle = 2qI_{\mathrm{G-R}}\Delta f$.[37,38] This typically overestimates noise current; thus, we utilized the experimental noise currents taken at a modulation frequency of 1 kHz, which was selected to minimize the contribution of $1/f$ noise. The specific detectivity as a function of wavelength is shown in Figure 4-3-8f for both 78K and 297K. At room temperature these devices show a peak D^* of 2.9×10^9 $\mathrm{cmHz^{1/2}W^{-1}}$. This value dramatically increases at low temperatures due to the large decrease in the noise current as well as the improved responsivity to a peak value of 2.6×10^{11} $\mathrm{cmHz^{1/2}W^{-1}}$.

To characterize the speed of this device, a directly modulated laser diode (λ = 1.55 μm) was utilized to excite the photoconductor. The response of the device to a low-frequency and high-frequency square wave are shown in Figure 4-3-9a and 4-3-9b, respectively. From both of the step responses shown in Figure 4-3-9a and 4-3-9b, a slow and fast component of the rise/fall time can be observed. To more clearly characterize this behavior, the photoresponse was measured with a sinusoidally modulated incident light over a wide frequency range (100 mHz to 100 kHz) as shown in Figure 4-3-9c. Over this measured spectral range, a clear 3dB cutoff wavelength cannot be observed, indicating that it is higher than the measured range. However, the device shows a weak increase in response for light modulated at low frequencies; *i.e.* the photoresponse at a 100 kHz shows only a ~5× drop relative to the low frequency (~0.1 Hz) photoresponse. It is likely that this behavior is a result of photoconductive gain present in the device which consistent with the high responsivity and the short carrier transit time (τ_{tr}), which is calculated to be 0.4 ns according to $\tau_{\mathrm{tr}} = L^2/(\mu V_\mathrm{d})$, where L is channel length (8.9 μm) and μ in this case is 392 $\mathrm{cm^2V^{-1}s^{-1}}$. The exact mechanisms of the gain likely is a result of the population and depopulation of trap states, which show saturation at high illumination powers.[39-41] This is particularly likely given the fact that the Te nanoflakes in this work were prepared using solution-based synthesis.

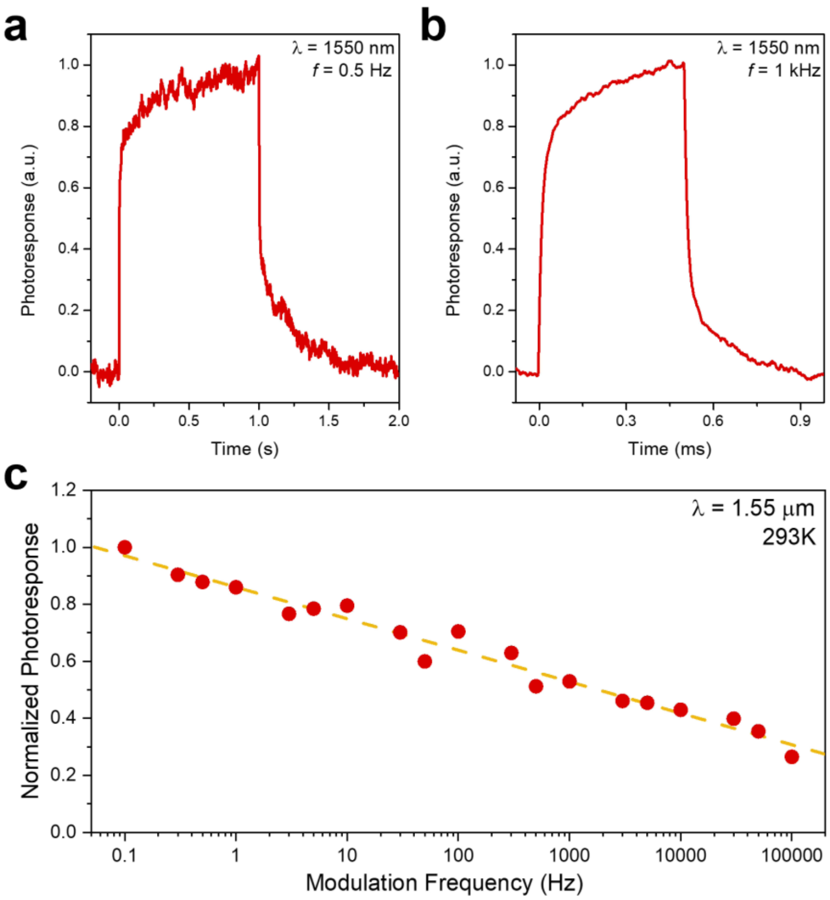

Fig. 4-3-9. (a) Room-temperature step response of an 18.8nm thick Te photoconductor, excited by a 1550-nm laser modulated by a 0.5 Hz square wave. (b) Room-temperature step response of a Te photoconductor, excited by a 1550 nm laser modulated by a 1 kHz square wave. (c) Normalized photoresponse of a Te photoconductor *versus* modulation frequency; the device is excited using a sinusoidally modulated 1550 nm laser. Note that an Au/Al_2O_3 substrate with an Al_2O_3 thickness of 150 nm was used for the measurements.

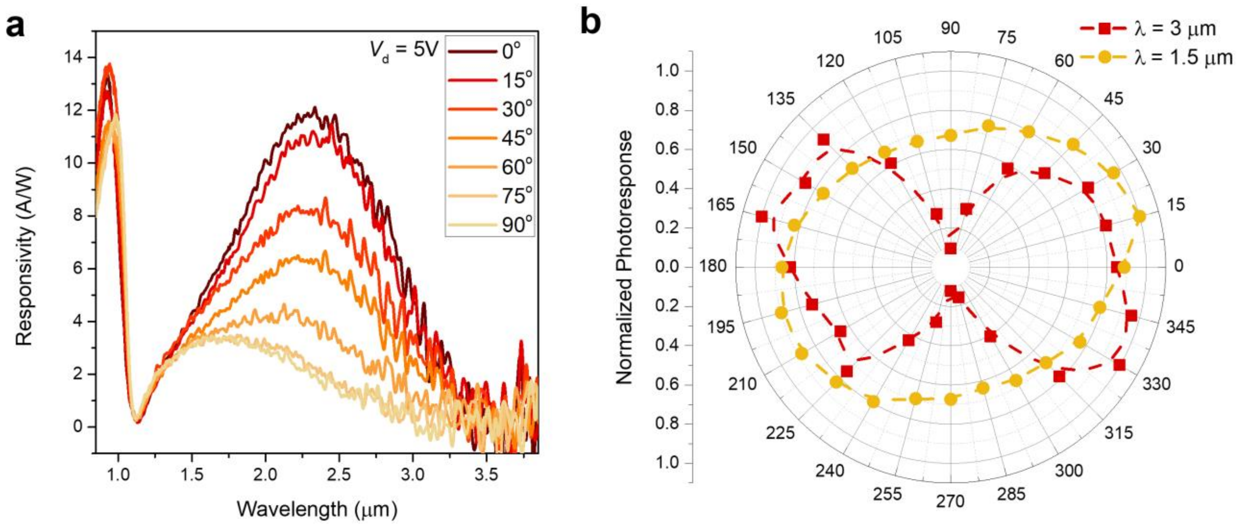

Fig. 4-3-10. (a) Polarization resolved photoresponse of an 18.8 nm thick quasi-2D Te nanoflake fabricated on an optical cavity with a 350 nm thick Al_2O_3. (b) Polar plot showing the relative response of the device shown in panel (a) at wavelengths of 3 μm and 1.5 μm as a function of polarization.

Finally, we investigated the polarization-dependent photoresponse of Te nanoflake-based photodetectors. We chose a device fabricated on a 350 nm thick Al_2O_3 substrate as an example to measure the responsivity, which provides strong absorption enhancement at wavelengths covering indirect gap band edge. Figure 4-3-10a shows the responsivity of an 18.8 nm thick Te photoconductor measured at various incident polarization angles, with 0° and 90° corresponding to light polarized perpendicular and parallel to the molecular wires, respectively. A clear drop in the responsivity for wavelengths greater 1.5 μm can be observed when the incident light is polarized at 90°, consistent with the indirect band edge. A polar plot showing the responsivity as a function of polarization at wavelengths of 3 μm and 1.5 μm is shown in Figure 4-3-10b, and clearly shows the highly anisotropic responsivity of the indirect gap, while the direct gap shows minimal dependence on the polarization of the light.

In summary, we have performed a systematic study on the electrical and optical properties of solution-synthesized quasi-2D Te, an indirect, small bandgap (0.31 eV) semiconductor. The Te nanoflake-transistor shows high effective hole mobilities of 450 and 1430 $cm^2 V^{-1} s^{-1}$ at 300K and 77K respectively. The absorbance and complex refractive index of Te were also extracted based on the polarization-resolved transmission and reflection measurements. Furthermore, the Te gated photodetectors exhibit high responsivities over the entire SWIR range with a cut-off wavelength of 3.4 μm. Importantly, using the extracted optical parameters, we dramatically enhanced the responsivity and specific detectivity of Te photodetectors using optical cavity substrates. We show that the peak wavelength can be tuned from 1.4 to 2.4 μm by changing the thickness of the Al_2O_3 cavity on Au. This simple substrate engineering technique can be a general way to significantly enhance the performance of other 2D material-based photodetectors. In addition, due to the anisotropic crystal structure of the Te nanoflakes, the devices possess a polarization-sensitive SWIR photoresponse. Our electrical and optoelectronic study indicate that Te is a promising material for high-performance and low-cost electronic and optoelectronic devices. Finally, this material has a high potential for wafer-scale production either through the assembly of solution-processed nanoflakes to form semi-continuous thin films or through techniques such as chemical vapor deposition or epitaxial growth.

References for Section 4-3

1. Alamo, J. A. Nanometre-Scale Electronics with III-V Compound Semiconductors. *Nature* **2011**, 479, 317-323.
2. Chuang, S.; Gao, Q.; Kapadia, R.; Ford, A. C.; Guo, J.; Javey, A. Ballistic InAs Nanowire Transistors. *Nano Lett.* **2012**, 13, 555-558.
3. Barve, A. V.; Lee, S. J.; Noh, S. K.; Krishna, S. Review of Current Progress in Quantum Dot Infrared Photodetectors. *Laser Photonics Rev.* **2009**, 4, 738-750.
4. Hoang, A. M.; Dehzangi, A.; Adhikary, S.; Razeghi, M. High Performance Bias-Selectable Three-Color Short-Wave/Mid-Wave/Long-Wave in Infrared Photodetecotrs based on Type-II InAs/GaSb/AlSb Superlattices. *Sci. Rep.* **2016**, 6, 24144.
5. Martyniuk, P.; Antoszewski, J.; Martyniuk, M.; Faraone, L.; Rogalski, A. New Concepts in Infrared Photodetector Designs. *Appl. Phys. Rev.* **2014**, 1, 041102.
6. Martinelli, R. U.; Zamerowski, T. J.; Longeway, P. A. 2.6 μm InGaAs Photodiodes. *Appl. Phys. Lett.* **1988**, 53, 989-991.

7. Nishida, K.; Taguchi, K.; Matsumoto, Y. InGaAsP Heterostructure Avalanche Photodiodes With High Avalanche Gain. *Appl. Phys. Lett.* **1979**, 35, 251-253.
8. Chen, K.; Kapadia, R.; Harker, A.; Desai, S.; Kang, J. S.; Chuang, S.; Tosun, M.; Sutter-Fella, C. M.; Tsang, M.; Zeng, Y.; Kiriya, D.; Hazra, J.; Madhvapathy, S. R.; Hettick, M.; Chen, Y.-Z.; Mastandrea, J.; Amani, M.; Cabrini, S.; Chueh, Y.-L.; Ager, J. W.; Chrzan, D. C.; Javey, A. Direct Growth of Single Crystalline III-V Semiconductors on Amorphous Substrates. *Nat. Commun.* **2016**, 7, 10502.
9. Ko, H.; Takei, K.; Kapadia, R.; Chuang, S.; Fang, H.; Leu, P. W.; Ganapathi, K.; Plis, E.; Chen, S.-Y.; Madsen, M.; Ford, A. C.; Chueh, Y.-L.; Krishna, S.; Salahuddin, S.; Javey, A. Ultrathin Compound Semiconductor on Insulator Layers for High-Performance Nanoscale Transistors. *Nature* **2010**, 468, 286-289.
10. Fitzgerald, E. A.; Xie, Y.-H.; Monroe, D.; Silverman, P. J.; Kuo, J. M.; Kortan, A. R.; Thiel, F. A.; Weir, B. E. Relaxed Ge_xSi_{1-x} Structures for III-V Integration with Si and High Mobility Two-Dimensional Electron Gasses in Si. *J. Vac. Sci. Technol., B* **1992**, 10, 1807-1819.
11. Kim, Y.; Cruz, S. S.; Lee, K.; Alawode, B. O.; Choi, C.; Song, Y.; Johnson, J. M.; Heidelberger, C.; Kong, W.; Choi, S.; Qiao, K.; Almansouri, I.; Fitzgerald, E. A.; Kong, J.; Kolpak, A. M.; Hwang, J.; Kim, J. Remote Epitaxy Through Graphene Enables Two-Dimensional Material-Based Layer Transfer. *Nature* **2017**, 554, 340-343.
12. Li, T.; Cheng, J.-F.; Shao, X.-M.; Deng, H.-H.; Chen, Y.; Tang, H.-J.; Li, X.; Gong, H.-M. Performance of Low Dark Current InGaAs Shortwave Infrared Detector. *Proc. SPIE.* **2012**, 8419.
13. Tan, C.; Cao, X.; Wu, X.-J.; He, Q.; Yang, J.; Zhang, X.; Chen, J.; Zhao, W.; Han, S.; Nam, G.-H.; Sindoro, M.; Zhang, H. Recent Advances in Ultrathin Two-Dimensional Materials. *Chem. Rev.* **2017**, 117, 6225-6331.
14. Lin, Z.; McCreary, A.; Briggs, N.; Subramanian, S.; Zhang, K.; Sun, Y.; Li, X.; Borys, N. J.; Yuan, H.; Fullerton-Shirey, S. K.; Chernikov, A.; Zhao, H.; McDonnell, S.; Lindenberg, A. M.; Xiao, K.; LeRoy, B. J.; Drndić, M.; Hwang, J. C.M.; Park, J.; Chhowalla, M.; *et al.* 2D Materials Advances: From Large Scale Synthesis and Controlled Heterostructures to Improved Characterization Techniques, Defects and Applications. *2D Mater.* **2016**, 3, 042001.
15. Amani, M.; Lien, D.-H.; Kiriya, D.; Xiao, J.; Azcatl, A.; Noh, J.; Madhvapathy, S. R.; Addou, R.; Kc, S.; Dubey, M.; Cho, K.; Wallace, R. M.; Lee, S.-C.; He, J.-H.; Ager, J. W.; Zhang, X.; Yablonovitch, E.; Javey, A. Near-Unity Photoluminescence Quantum Yield in MoS_2. *Science* **2015**, 350, 1065-1068.
16. Amani, M.; Taheri, P.; Addou, R.; Ahn, G. H.; Kiriya, D.; Lien, D.-H.; Ager, J. W.; Wallace, R. M.; Javey, A. Recombination Kinetics and Effects of Superacid Treatment in Sulfur- and Selenium Based Transition Metal Dichalcogenides. *Nano Lett.* **2016**, 16, 2786-2791.
17. Desai, S. B.; Madhvapathy, S. R.; Sachid, A. B.; Llinas, J. P.; Wang, Q.; Ahn, G. H.; Pitner, G.; Kim, M. J.; Bokor, J.; Hu, C.; Wong, H.-S. P.; Javey, A. MoS_2 Transistors with 1-Nanometer Gate Lengths. *Science* **2016**, 354, 99-102.
18. Lien, D.-H.; Amani, M.; Desai, S. B.; Ahn, G. H.; Han, K.; He, J.-H.; Ager, J. W.; Wu, M. C.; Javey, A. Large-Area and Bright Pulsed Electroluminescence in Monolayer Semiconductors. *Nat. Commun.* **2018**, 9, 1299.
19. Zhang, Y. J.; Oka, T.; Suzuki, R.; Ye, J. T.; Iwasa, Y. Electrically Switchable Chiral Light-Emitting Transistor. *Science* **2014**, 344, 725-728.
20. Zhao, P.; Amani, M.; Lien, D.-H.; Ahn, G. H.; Kiriya, D.; Mastandrea, J. P.; Ager, J. W.; Yablonovitch, E.; Chrzan, D. C.; Javey, A. Measuring the Edge Recombination Velocity of Monolayer Semiconductors. *Nano Lett.* **2017**, 17, 5356-5360.
21. Wang, Y.; Qiu, G.; Wang, R.; Huang, S.; Wang, Q.; Liu, Y.; Du, Y.; Goddard, W. A.; Kim, M. J.; Xu, X.; Ye, P. D.; Wu, W. Field-Effect Transistors made from Solution-Grown Two-Dimensional Tellurene. *Nat. Electron.* **2018**, 1, 228-236.
22. von Hippel, A. Structure and Conductivity in the VIb Group of the Periodic System. *J. Chem. Phys.* **1948**, 16, 372-380.
23. Yi, S.; Zhu, Z.; Cai, X.; Jia, Y.; Cho, J.-H. The Nature of Bonding in Bulk Tellurium Composed of One-Dimensional Helical Chains. *Inorg. Chem.* **2018**, 57, 5083-5088.
24. Wu, B.; Liu, X.; Yin, J.; Lee, H. Bulk β-Te to Few Layered β-Tellurenes: Indirect to Direct Band-Gap Transitions Showing Semiconductor Property. *Mater. Res. Express* **2017**, 4,095902.
25. Qian, H.; Yu, S.; Gong, J.; Luo, L.; Fei, L. High-Quality Luminescent Tellurium Nanowires of Several Nanometers in Diameter and High Aspect Ratio Synthesized by a Poly(Vinyl Pyrrolidone)-Assisted Hydrothermal Process. *Langmuir* **2006**, 22, 3830-3835
26. Du, Y.; Qiu, G.; Wang, Y.; Si, M.; Xu, X.; Wu, W.; Ye, P. D. 1D van der Waals Material Tellurium: Raman Spectroscopy under Strain and Magneto-transport Source. *Nano Lett.* **2017**, 17, 3965-3973.
27. Liu, H.; Neal, A. T.; Zhu, Z.; Luo, Z.; Xu, X.; Tomanek, D.; Ye, P. D. Phosphorene: An Unexplored 2D

Semiconductor with a High Hole Mobility. *ACS Nano* **2014**, 8, 4033-4041.

28. Li, L.; Yu, Y.; Ye, G. J.; Ge, Q.; Ou, X.; Wu, H.; Feng, D.; Chen, X. H.; Zhang, Y. Black Phosphorus Field-Effect Transistors. *Nat. Nanotechnol.* **2014**, 9, 372-377.
29. Takei, K.; Madsen, M.; Fang, H.; Kapadia, R.; Chuang, S.; Kim, H. S.; Liu, C.-H.; Plis, E.; Nah, J.; Krishna, S.; Chueh, Y.-L. Guo, J.; Javey, A. Nanoscale InGaSb Heterostructure Membranes on Si Substrates for High Hole Mobility Transistors. *Nano Lett.* **2012**¸12, 2060-2066.
30. Radisavljevic, B.; Kis A. Mobility Engineering and a Metal-Insulator Transition in Monolayer MoS_2. *Nat. Mater.* **2013**, 12, 815-820.
31. Javey, A.; Guo, J.; Farmer, D. B.; Wang, Q.; Wang, D.; Gordon, R. C.; Lundstrom, M.; Dai, H. Carbon Nanotube Field-Effect Transistors with Integrated Ohmic Contacts and High-κ Gate Dielectrics. *Nano Lett.* **2004**, 4, 447-450.
32. Lien, D.-H.; Kang, J. S.; Amani, M.; Chen, K.; Tosun, M.; Wang, H.-P.; Roy, T.; Eggleston, M. S.; Wu, M. C.; Dubey, M.; Lee, S.-C.; He, J.-H.; Javey, A. Engineering Light Outcoupling in 2D Materials. *Nano Lett.* **2015**, 15, 1356-1361.
33. Zhang, H.; Ma, Y.; Wan, Y.; Rong, X.; Xie, Z.; Wang, W.; Dai, L. Measuring the Refractive Index of Highly Crystalline, Monolayer MoS_2 with High Confidence. *Sci. Rep.* **2015**, 5, 8440.
34. Born, M.; Wolf. E. Principles of optics: Electromagnetic Theory of Propagation, Interference and Diffraction Light. Cambridge University Press, Cambridge (2002).
35. Amani, M.; Regan, E.; Bullock, J.; Ahn, G. H.; Javey, A. Mid-Wave Infrared Photoconductors based on Black Phosphorous-Arsenic Alloys. *ACS Nano* **2017**, 11, 11724-11731.
36. Guo, Q.; Pospischil, A.; Bhuiyan, M. Jiang, H.; Tian, H.; Farmer, D.; Deng, B.; Li, C.; Han, S.-J.; Wang, H.; Xia, Q.; Ma, T.-P. Mueller, T.; Xia, F. Black Phosphorus Mid-Infrared Photodetectors with High Gain. *Nano Lett.* **2016**, 16, 4648-4655.
37. Piotrowski, J.; Gawron, W. Ultimate Performance of Infrared Photodetectors and Figure of Merit of Detector Material. *Infrared Phys. Technol.* **1997**, 38, 63-68.
38. Vincent, J. D. Fundamentals of Infrared Detector Operation and Testing. Wiley, New York (1990).
39. Petritz, R. L. Theory of Photoconductivity in Semiconductor Film. *Phys. Rev.* **1956**, 104, 1508-1516.
40. Beck, W. A. Photoconductive Gain and Generation-Recombination Noise in Multiple-Quantum-Well Infrared Detectors. *Appl. Phys. Lett.* **1993**, 63, 3589-3591.
41. Ye, Z.; Campbell, J. C.; Chen, Z.; Kim, E.-T., Madhukar, A. Noise and Photoconductive Gain in InAs Quantum-Dot Infrared Photodetectors. *Appl. Phys. Lett.* **2003**, 83, 1234-1236.

4.4 – Experimental and Theoretical Methods

Black Phosphorous and Tellurium Photoconductor Fabrication

b-P and b-PAs crystals (purchased from Smart Elements and HQ Graphene, respectively) were utilized for all devices in this study. Significant effort was made during processing to minimize exposure to ambient air, due to the hydroscopic nature of b-P. Crystal were exfoliated and spin-coated with PMMA C4 in a nitrogen glovebox on p^{++} Si/SiO_2 chips with a 50 nm thick gate oxide. Following exfoliation and encapsulation with PMMA, suitable crystals were located by using an optical microscope and devices were fabricated using standard e-beam lithography techniques. After development, 40 nm thick Ni electrodes were deposited by thermal evaporation and lift-off was performed using anhydrous solvents in a nitrogen glovebox. The sample thickness was then measured in an N_2 purged AFM (Bruker) and devices were subsequently wire bonded in a 24 pin chip carrier. Samples for absorption/reflection measurements were transferred to KBr substrates using a previously established dry transfer technique and were measured in an FTIR microscope.

Black Phosphorous Photovoltaic Detector Fabrication

Photodiodes presented in this work were fabricated by a dry transfer process utilising a poly(methyl methacrylate) (PMMA) carrier. In brief, freshly exfoliated bP and MoS_2 sheets are transferred onto an Au pad creating an Au / bP / MoS_2 stack. A contact to the MoS_2 layer was then patterned by e-beam lithography and a 40 nm thick Ni film was subsequently deposited by thermal evaporation. In some devices, the heterojunction was patterned by e-beam lithography and subsequently etched in a Xactix vapor etching tool by XeF_2.[37] Finished devices were encapsulated by an ~2 nm thick AlO_x layer formed by thermal evaporation of Al.

For the polarisation resolved detector, an identical dry transfer process was used to create an MoS_2 / bP / Au stack. An additional bP flake was transferred on top of the MoS_2 layer such that its crystal orientation was orthogonal to the bottom bP layer. The crystalline orientations of the bP sheets was determined using polarised reflection measurements performed in an FTIR microscope as described above. The hole contact for the top bP device was patterned using electron beam lithography, followed by evaporation of MoO_x / Pd (4/30 nm). For all devices in this study, care was taken to reduce air exposure during fabrication of devices to minimise PO_x growth at the bP surface. Processing steps including bP exfoliation, lift-off, PMMA removal and AFM were all performed in either a glovebox or a nitrogen purged environment and all chemicals used were anhydrous.

Synthesis of tellurium nanoflakes

Tellurium nanoflakes were synthesized by a hydrothermal method according to a previously reported procedure with slight modifications. In a typical procedure, 1.5 g of PVP was first dissolved in 16 mL DI water and 46 mg of Na_2TeO_3 was then added and dissolved into the PVP solution to form a clear solution. Then, 1.66 mL of ammonium hydroxide solution and 0.838 mL of hydrazine monohydrate was added into the above solution in sequence. The solution was then transferred into a 25 mL Teflon-lined stainless-steel autoclave. The autoclave was sealed well and then placed in an oven. The autoclave was heated up to 180℃ from room temperature with ramp rate of 3 ℃/min and then maintained at 180℃ for 4 hours. After, the autoclave was removed from the oven and cooled to room temperature by running water immediately. The resulting product was purified and washed with DI water three times by centrifugation at 3000 r.p.m for 2 min. After washing and purification, the final tellurium solution is a silver-gray color. Note that there are always some Te nanowires coexisting along with Te nanoflakes and it is challenging to fully separate the nanowires from the nanoflakes. The final product was redispersed in pure ethanol before being transferred to the target substrate for characterization and device fabrication by drop-casting. Maintaining the autoclave in oven at 180℃ for 4h will produce the tellurium nanoflakes with a typical thickness in the range of 10-30 nm, with typical lateral dimensions of 10-50 μm. It is important to point out that the thickness of tellurium nanoflakes can be roughly controlled by controlling the reaction time (4-30 hours) at 180℃. The thickness of tellurium nanoflakes can be increased by prolonging the reaction.

Refractive index extraction and optical simulations

Samples for refractive index extraction were fabricated by thermally evaporating Ti / Au (5/80 nm) onto a Si/SiO_2 carrier wafer. Following this, bP (Smart Elements) was mechanically exfoliated onto the Au surface in an N_2 purged glovebox. A set of 22 bP flakes were chosen with approximately linearly spaced thickness from 50 to 500 nm, as measured by atomic force microscopy (AFM) (Bruker Dimension Icon). Polarised reflection measurements were taken using a Fourier transform infrared (FTIR) microscope (Thermo Scientific, Nicolet iS50) with a BaF_2 wire grid linear polariser (Thorlabs). The arm-chair direction of the bP absorber was determined by measuring reflection as a function of polarisation, to find the angle at which maximum absorption occurs. Implicit in this approach is the assumption that the largest absorption will occur when light is aligned to the *x*, or arm-chair direction, a fact that has been theoretically predicted and demonstrated by a number of previous studies. In all cases the minimum absorption (at 0.31 eV) was found to be offset by 90^o from this angle, corresponding to the expected zig-zag or *y*-direction. All FTIR reflection measurements in this study utilise a bare Au surface as a 100% reflection standard. The set of reflection curves in the *x*-direction were fitted using the transfer matrix method, which models the reflection of the bP / Au stack using the refractive indices of bP as the only fitting parameter. The optical simulations of the full bP / MoS_2 / Au photodiodes were also performed through the transfer matrix method utilising known refractive index values for Au, constant values for MoS_2 ($n = 4.3$, $k = 0$), as well as the refractive index values for bP measured in this work. An average of the bP absorption values over the $\lambda = 2.5$-3.8 μm range was obtained for every combination of MoS_2 and bP thicknesses.

Infrared Detector Characterization

Temperature dependent electrical measurements on b-P were performed in a flow cryo probe station (Lakeshore) using a B1500A Semiconductor Parameter Analyzer (Agilent). Spectral photoresponse measurements were performed in a FTIR spectrometer (ThermoFisher), with a customized Janis cryostat using a CaF_2 window. Prior to measurement, the wire bonded devices were loaded into the spectrometer and evacuated to a base pressure of $< 10^{-5}$ Torr. The cryostat was then placed at the auxiliary exit port of the FTIR, and the exciting illumination from the Glowbar (1000 K blackbody) source was focused on the sample using either a CaF_2 lens or 15× Schwarzschild objective. The photocurrent from the b-P/b-PAs devices was then sent to a current amplifier (Stanford Research Systems), which also provided the bias voltage, and the signal was subsequently returned to the external detector interface of the FTIR. All measurements taken with the FTIR were performed with the current amplifier operating with a gain setting such that the bandwidth was greater than 100 kHz. Bias voltage and gain were selected to maximize signal to noise ratio for the particular device under measurement, with the aforementioned condition. During measurements, the gate bias of the device was pulsed synchronously with the FTIR, in order to mitigate hysteresis in the device. The relative intensity of the illumination source was measured using the internal Deuterated Triglycine Sulfate (DTGS) detector of the FTIR with identical measurement conditions. Polarization measurements were performed by placing a BaF_2 wire grid polarizer in the beam path, the polarization response of the system was calibrated using a commercial Ge and HgCdTe detector in place of the sample. The frequency response of the devices was measured using a directly modulated 980 nm laser. To measure the specific defectivity of the devices we utilized optically chopped flood illumination from a 673 K blackbody source with no focusing optics. The net power incident on the device above the band-edge was calculated by the integration of the spectral radiant exitance of the blackbody and sample (M_{total}) according to Plank's Law:

$$M_{\text{total}}(\lambda, T) = \bar{\epsilon} \int_0^{\lambda_{co}} \frac{2\pi c}{\lambda^4 (e^{hc/\lambda kT} - 1)} d\lambda \tag{4-4-1}$$

where, $\bar{\epsilon}$ is average the emissivity, T is temperature, λ is wavelength, λ_{co} is the cut-off wavelength of the detector under test, h is Plank's constant, k is Boltzmann's constant, and c is the speed of light. The projected solid angle viewed by the detector (Ω) is calculated as:

$$\Omega = \pi \frac{r^2}{D^2 + r^2} \tag{4-4-2}$$

where r is the radius of the defining aperture and D is the distance between the aperture and sample surface. The total incident power on the detector can then be calculated according to:

(4-4-3)

$$E = \frac{\Omega}{\pi} \times (M_{\text{total,BB}} - M_{\text{total,Det}}) \times M.F. \times A$$

where $M_{\text{total,BB}}$ is the integrated photon exitance of the blackbody, $M_{\text{total,Det}}$ is the integrated photon exitance of the detector, *M.F.* is the chopper modulation factor, and *A* is the device area. The photocurrent and noise current in the device was then measured using a lock-in amplifier. For all measurements, an integration time of 1s was used and the blackbody was chopped at a frequency of 150 Hz.

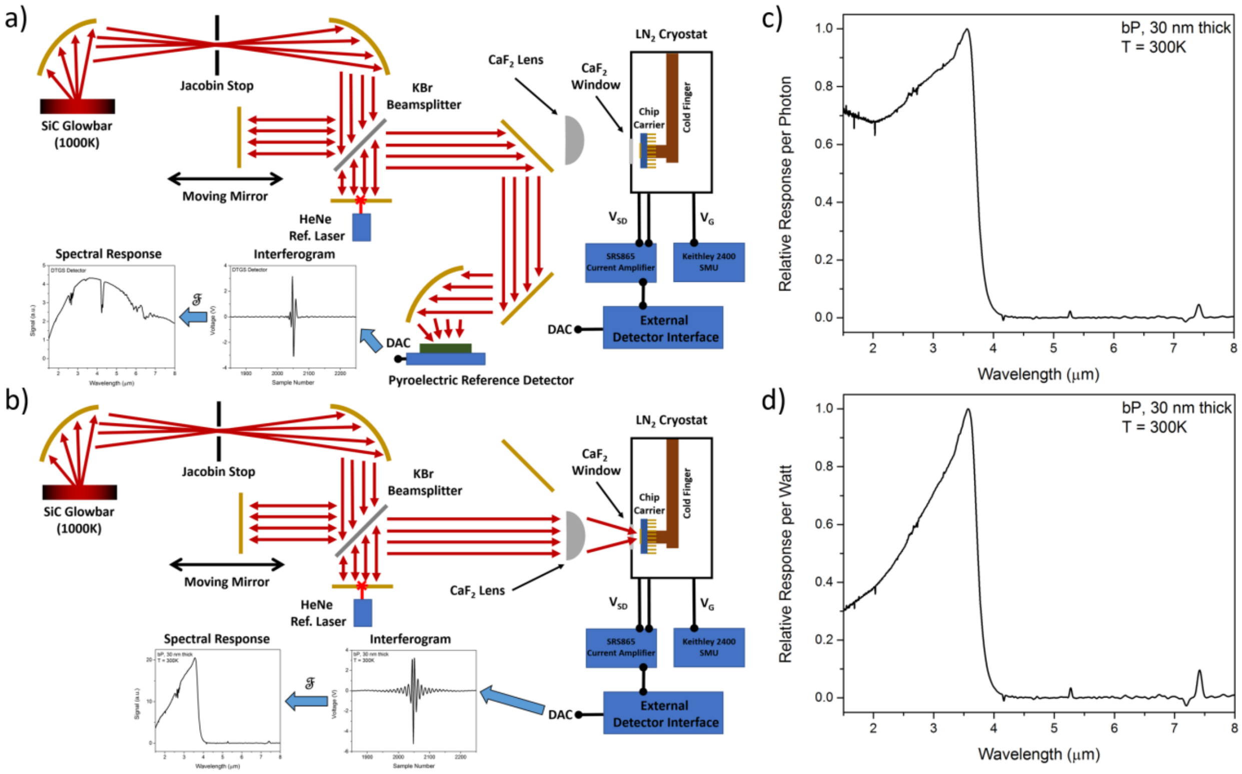

Fig. 4-4-1. (a) Schematic of measurement setup used to measure the spectral content of the incident light on the b-P detector, measurements taken using the internal pyroelectric detector of the FTIR were performed at an optical velocity of 0.15 cm/s. (b) Schematic of measurement setup used to measure the spectral response of the b-P and b-PAs gated photoconductors. Light from the FTIR Glowbar was focused on the device using either a CaF2 lens or a Schwarzschild objective. During measurements, the gate voltage was modulated from V_g during the interferometer scan to -V_g during the wait period, in order to minimize hysterics effects (timing shown in Fig. 4-4-2). (c) Relative response per photon of a b-P gated photoconductor, calculated using the ratio of response from the b-P detector to the pyroelectric reference detector. (d) Relative response per photon of a b-P gated photoconductor, calculated using the ratio of response from the b-P detector to the pyroelectric reference detector and photon energy.

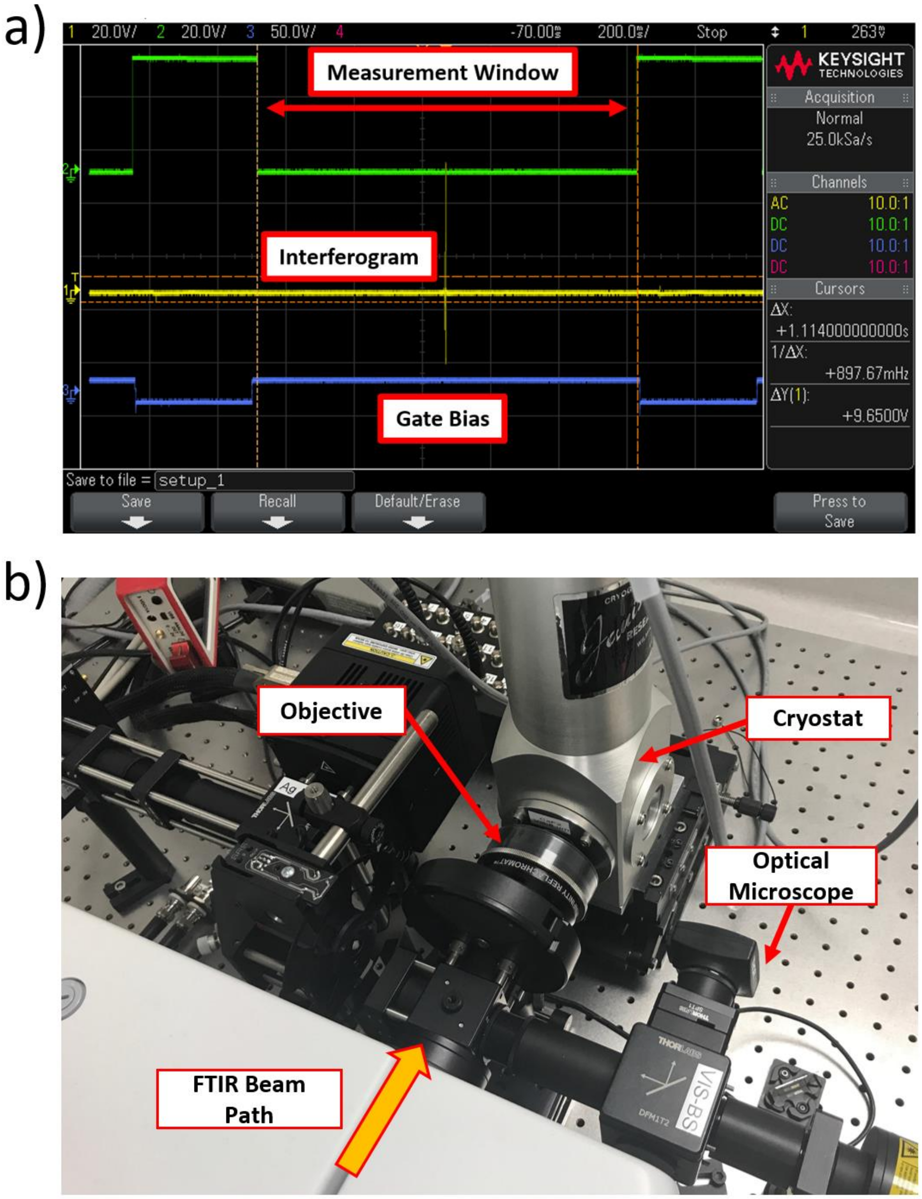

Fig. 4-4-2. (a) Timing of gate biasing during FTIR measurements. During the measurement window, which is identified by an external trigger from the FTIR, the gate is held at the desired bias potential, V_g. During the rest period, the gate bias is held at -V_g, in order to minimize hysteresis effects. (b) Photograph of the optical setup used to measure the spectral and frequency response of the b-P and b-PAs gated photoconductors. Sample is placed in a 24-pin chip carrier in the cryostat. An external microscope is setup to locate and focus light on the sample with a reflective objective or CaF_2 lens.

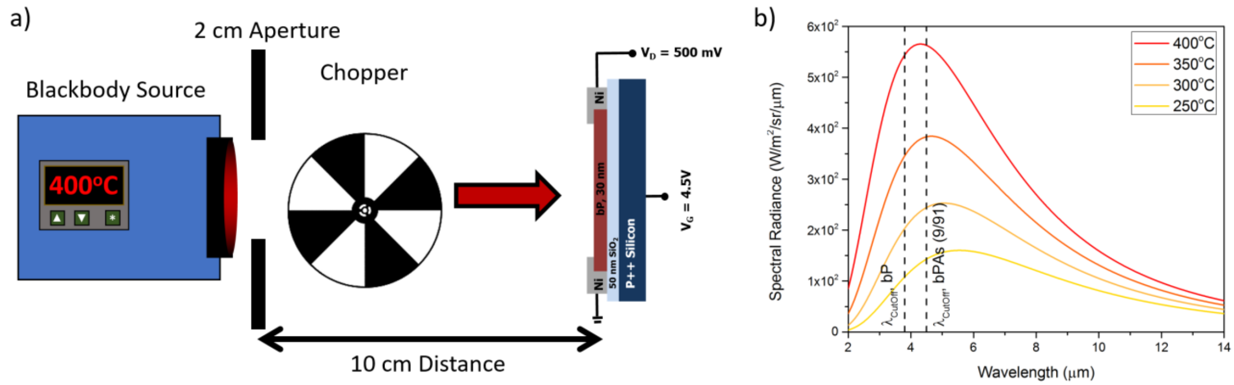

Fig. 4-4-3. (a) Schematic of the setup used to measure the absolute responsivity and detectivity of the b-P detector. The sample was illuminated by a blackbody source held at 400°C-250°C (673 K-523 K). The beam was modulated using a chopper and the response of the gated photoconductor was measured using a lock-in amplifier. (b) Spectrum of the illumination on the sample at various blackbody temperatures calculated using Plank's law. The cut-off wavelengths for b-P and b-PAs (91% As) are indicated by dashed lines.

Chapter 5

Conclusion and Future Prospects

This body of work has presented an overview of some of the potential advantages for the implementation of two-dimensional materials in optoelectronic devices. Photoluminescence (PL) quantum yield (QY) is a crucial requirement for many optoelectronic devices, and the demonstration that 2D semiconductors can obtain PL QY's approaching 100% is a key factor which opens the potential of these materials to be used in practical devices. However, the realization of new semiconductor materials and technologies require substantial advantages in device performance coupled with a viable route towards scalability. While the field of 2D semiconductors remains relatively new and questions of scalability has not been fully addressed their potential performance advantages suggest that they should be investigate further.

In chapter two, a detailed analysis of the PL QY of several monolayer 2D materials, both prepared by micro-mechanical exfoliation from bulk sources and by chemical vapor deposition was analyzed. Despite having naturally terminated surfaces with no covalent dangling bonds, as-exfoliated 2D semiconductors have poor PL QY, which is likely explained by the presence of a significant number of sulfur vacancies. We demonstrated that using chemical treatments, the PL QY of some of these materials, specifically MoS_2 and WS_2, can be increased to values approaching unity. While this is a crucial metric and can potentially enable the use of these materials in light emitting devices, numerous questions have yet to be addressed. This solution-based mechanism that was developed and utilized here is not an ideal process for integration in practical devices, as it introduces numerous process challenges for realizing light emitting devices. Furthermore, the underlying mechanism that enabled enhancement of PL QY in these materials was not successfully identified in this work, and the models developed to describe the recombination kinetics do not fully describe the behavior of the system. This is a crucial area for further research, which can also likely lead to improved methods to achieve bright materials.

In chapter three, two device structures were developed and presented to obtain electrically pumped light emission from 2D semiconductors. In the first part of this chapter, we developed a single metal-semiconductor contact electroluminescent device which is pumped using a transient injection mechanism. This permits us to largely avoid forming ohmic hole/electron contacts to the semiconductor which is exceptionally challenging for materials such as MoS_2 and WS_2. Although we are able to show that the quantum efficiency of these devices closely matches the material quantum yield it was found that biexcitonic recombination acts as a major barrier towards bright emission. Developing techniques to mitigate this issue, such as through engineering the dielectric environment of the 2D semiconductor can potentially overcome this limiting factor. In the second section, light emitting diodes based on few-layer to bulk black phosphorous were demonstrated. These devices show high quantum efficiencies (internal quantum efficiencies as high as 11%) these can still be potentially improved through defect passivation schemes similar to those developed in chapter two. Furthermore, while contact resistance does not impact the quantum efficiency in these devices, it does have a substantial detriment towards their wall plug efficiency especially at high injection levels and this can only be mitigated through the development of improved contacts as well as the development of doping schemes.

In chapter four, we investigated the potential of 2D semiconductors for their use as photodetectors. In particular, we focused on applications in the infrared spectrum, where devices are severely limited by generation-recombination noise. We demonstrated that through the reduction of detector volume, we can obtain a substantial improvement in the overall detectivity. Furthermore, this work provided a through analysis of some of the basic material properties of small bandgap 2D semiconductors. Looking forward, a key development which can improve the performance of these devices is their integration with optical structures (i.e. optical antennas) which can increase the light absorption in small volume detectors.

In summary, 2D materials possess numerous attractive properties for their implementation in future optoelectronic applications. The work outlined in this thesis has presented routes to obtain 2D semiconductors with the potential to have exceptionally high quantum efficiencies, opening numerous research opportunities to exploit this exciting material system. Additionally, several device schemes were demonstrated that can be leveraged and further improved upon in the future.